Dissertation zur Erlangung des Doktorgrades

der Fakultät für Chemie und Pharmazie

der Ludwig-Maximilians-Universität München

METHYLAMMONIUM LEAD HALIDE THIN FILM CRYSTALLIZATION FOR OPTOELECTRONIC APPLICATIONS

Nadja Giesbrecht

aus

Ekaterinowka, Russland

2018

ERKLÄRUNG

Diese Dissertation wurde im Sinne von § 7 der Promotionsordnung vom 01. Mai 2015 von Herrn Dr. Pablo Docampo betreut und von Herrn Prof. Dr. Thomas Bein von der Fakultät für Chemie und Pharmazie vertreten.

Eidesstattliche Versicherung

Diese Dissertation wurde eigenständig und ohne unerlaubte Hilfe bearbeitet.

München den 16.08.2018,

Nadja Giesbrecht

Dissertation eingereicht am 16.08.2018

1. Gutachter: Prof. Dr. Thomas Bein
2. Gutachter: Dr. Pablo Docampo

Mündliche Prüfung am 11.09.2018

Acknowledgments

Foremost I would like to thank Dr. Pablo Docampo for his advice and guidance throughout all the stages of my PhD studies. I wish to thank him for convincing me how really exciting the study of perovskites will be. I never regretted my choice, even after I had to use a glove-bag at the beginning while the same Jack Johnson song was playing for over two hours on repeat. I very much appreciate the large degree of independence and freedom given to me in the selection of my studies but with Pablo always showing excitement for my results and providing constant support.

I would also like to express my deepest gratitude to Prof. Thomas Bein for his additional supervision during my PhD studies. I am very grateful for his support and encouragement. I wish to thank Thomas for providing me with all the facilities required for the successful completion of my doctoral thesis, especially for the fully equipped new glovebox, which saved me from my fate with the glove-bag.

I would like to thank Johannes Schlipf and Prof. Peter Müller-Buschbaum for fruitful collaborations producing amazing GIWAXS patterns. I wish to thank Irene Grill for the countless ToF measurements she accomplished for my studies and Prof. Achim Hartschuh for the various studies carried out revealing remarkable insights regarding the perovskite films included in my studies. I especially thank Moritz Schultes for being excited about the nanoparticle story and working together with me on this subject.

I am very much grateful to Markus Döblinger for the introduction to be an SEM operator. Without the access to the machine and the valuable skills learned during the introduction, my studies on morphology would not have been as fruitful. I also would like to thank Markus for the remarkable TEM investigation he executed on a solar cell cross-section. I still get much admiration for the images during conferences. I also thank Steffen Schmidt that he mastered the challenging sample preparation. I am grateful to Tina Reuther for her assistance in obtaining chemicals and laboratory utilities.

I wish to thank all of my colleagues for the nice time we spent on different group events. My sincere thanks to the people from the perovskite group including Irene Grill, Andreas Binek, Michiel Petrus, Max Sirtl, Yinghong Hu and Meltem Aygüler for the great atmosphere and fun we had including both being colleagues and friends. I enjoyed the time we spent on travels to conferences and some vacations on holidays. I very much appreciated the order and cleanliness in the lab introduced and enforced by Andreas Binek. I valued the openness for discussion about

all kind of themes about and beyond the science with Michiel Petrus. I thank Max Sirtl for always coming in cheerful, which spreads all over the other people. I treasured the funny drawing Hongi made for all of the perovskite group members on their lab-coats. I still think it might be a nice strategy to encourage people to wear their lab-coats in the labs. I greatly thank Meltem Aygüler for mostly coming in on Sundays because of the regeneration of the glovebox, which I think strongly improved the conditions for the experiments for all of us. I also thank Meltem for sharing my enthusiasm for good coffee and our discussions during several coffee breaks. Therefore, I also would like to thank Nespresso delivery service, which offers delivery time slots between 7 and 9 am with actual punctual arrivals.

Most importantly I wish to thank my family and Johann Glück for believing in me, encouraging me and supporting me throughout my education and the rest of my life.

ABSTRACT

Energy efficient technologies together with renewable energy sources are necessary to cover and reduce the world's energy demand. Among renewable energy sources, sunlight is the most abundant and easily accessible. Current efforts mainly center around silicon-based photovoltaic technologies. However, the rollout of silicon is inherently slow, energy-intensive, and new technologies would be highly desirable.

Very recently, hybrid lead halide perovskite materials were found to be highly promising candidates for both light emitting diodes (LED) and solar cell applications with very cost-efficient manufacturing potential. The perovskite materials show both strong absorption and emission properties combined with solution-based fabrication. However, it turned out that in addition to other factors, the efficiency of optoelectronic devices strongly depends on perovskite thin film morphology. The present thesis reports on new perovskite synthesis procedures for application in highly efficient perovskite-based optoelectronic devices, like solar cells and LEDs.

In the work described in chapter 3, we synthesized dense layers of a wide bandgap perovskite (methylammonium lead bromide) with 10 µm large crystallites. We confirmed the perfect crystal alignment of the large grains with (100) facets parallel to the substrate by using grazing-incidence-wide angle X-ray scattering (GIWAXS). With photovoltaic devices, we showed that increased grain size and the strong preference in crystal facet alignment are beneficial for solar cell performance. This improvement led to high voltages of over 1.4 V and high photocurrents, as well as internal quantum efficiencies approaching unity.

In chapter 4 we describe a new intermediate phase, which provides the optimum crystallization conditions for iodide-based perovskite films. We validated grain sizes of over 10 µm in 450 nm thin films with high-resolution investigations in a transmission electron microscope. Similar to the bromide compound described in chapter 3, we determined pure perovskite crystal alignment in one direction via GIXAWS investigations. To investigate the influence of thin film quality on electronic properties such as charge carrier mobilities, we performed time-of-flight (TOF) measurements. Our polycrystalline thin films show superior charge carrier mobilities, comparable to single crystals, and led to the superior performance of photovoltaic devices in a like-to-like comparison.

In chapter 5, we studied the influence of perovskite crystal facet alignment on optoelectronic device applications. The strong crystal alignment in one direction of all our $MAPbX_3$ films

reveals a special case for the iodide-based compound. We discovered that substituting small amounts of highly polar solvents could be used to tune the alignment of the crystallites. Depending on the chosen reaction conditions, purely aligned films with (200) or (002) tetragonal crystal facets parallel to the substrates were obtained. To reveal the role of crystal orientation in optoelectronic devices, we investigated the charge transport with time-of-flight techniques (ToF). In the photovoltaic device application, particularly with the (200) perovskite crystal facets in combination with TiO_2, we observed an energetic barrier causing a dramatic loss in fill factor. With an additional fullerene-based interface layer on top of TiO_2, or in the inverted device architecture with fully organic interface layers, the energetic barrier at the interfaces was avoided and fill factors of 80 % were reached.

In chapter 6, we addressed one of the most challenging factors for reproducible thin film deposition from solution, namely the interaction between the solution and the substrate surface. We introduce a new interfacial treatment to enhance the reproducibility of perovskite deposition on different surfaces. This method additionally enables up-scaling to produce large area modules. To decrease the impact of substrate hydrophobicity towards polar perovskite precursor solutions, we applied small amounts of nanoparticles on top to improve surface. With contact angle measurements and scanning electron microscopy investigations, we established that approximately 1 % surface coverage of insulating nanoparticles like Al_2O_3 or SiO_2 on top of rather hydrophobic fullerene interfaces significantly improves the wetting properties. In photovoltaic device applications, the performance was not compromised by the presence of the particles at the interface.

Finally, in chapter 7 we used chloride- and bromide-based perovskite compounds for LED applications. Here, our optimized process enabled the production of very thin but homogeneous perovskite films with varying halide compositions. We characterized the films using X-ray diffraction, photothermal deflection spectroscopy, time-resolved photoluminescence, and energy dispersive X-ray measurements. We were able to tune the emission color from the blue to the green region of the visible spectrum (425–570 nm). Low voltages between 2.2–3 V were sufficient to light up the LEDs.

CONTENT

LIST OF ABBREVIATIONS

ACN	Acetonitrile
Ag	Silver
Al	Aluminium
Al_2O_3	Aluminium oxide
Au	Gold
Ca	Calcium
CB	Chlorobenzene
CdTe	Cadmium telluride
CIGS	CuInGa/S
CSD	Controlled solvent drying
CTM	Charge transport material
DSSC	Dye sensitized solar cells
DMF	Dimethylformamide
DMSO	Dimethylsulfoxide
E_{gap}	Band gap energy
EL	Electroluminescence
EQE	External quantum efficiency
ETM	Electron transporter material
F8	Poly(9,9′-dioctylfluorene)
FF	Fill Factor
FTO	Fluorine-doped tin oxide
GaAs	Gallium arsenide
GIWAXS	Grazing-incidence wide angle X-ray scattering

HTM	Hole transporter material
IL	Interface layer
IP	intermediate phase
IPA	Isopropanol
ITO	Tin-doped indium oxide
J_{Ph}	Photogenerated current density
J_{SC}	Short-circuit current
JV	Current-Voltage
LED's	Light emitting diodes
LiF	Lithium fluoride
MA	Methylammonium
MABr	Methylammonium bromide
MACl	Methylammonium chloride
MAI	Methylammonium iodide
$MAPbBr_3$	Methylammonium lead bromide
$MAPbCl_3$	Methylammonium lead chloride
$MAPbI_3$	Methylammonium lead iodide
$MAPbX_3$	Methylammonium lead halide
nm	Nanometer
OLED	Organic light emitting diodes
OPV	Organic photovoltaic
$Pb(Ac)_2$	Lead acetate
$PbBr_2$	Lead bromide
PbI_2	Lead iodide
PCBM	[6,6]-Phenyl-C_{61} butyric acid methyl ester

PCE	Power conversion efficiency
PDS	Photothermal deflection spectroscopy
PEDOT:PSS	Poly(3,4-ethylenedioxythiophene) polystyrene sulfonate
PeLEDs	perovskite light emitting diodes
PK	Perovskite
PL	Photoluminescence
PLQY	Photoluminescence quantum yield
PSC	Perovskite solar cells
PV	Photovoltaic
QD-SCs	Quantum dot solar cells
QLED	Quantum dot light emitting diodes
RT	Room temperature
SD	Solvent drying
SE	Solvent engineering
SEM	Scanning electron microscopy
SiO_2	silicon dioxide
TCSPC	Time-correlated single photon counting
TEM	Transmission electron microscopy
THTO	Tetraethylthiophene-1-oxide
ToF	Time of flight
VASP	Vapour-assisted solution process
V_{OC}	Open-circuit voltage
XRD	X-ray diffraction

1 INTRODUCTION

1.1 GLOBAL ENERGY CHALLENGE

The annual global energy consumption constantly increased by 1.8 % over the last decade.[1] Even if we assume no further increase in energy consumption, the current main energy sources, namely the fossil fuels are expected to be depleted in 113 years for coal, 52 years for natural gas and 50 years for oil.[1] The only reasonable approach to prevent this upcoming energy crisis is, on the one hand, the development of more energy efficient technologies and on the other hand, a stronger focus on renewable energy sources.

Up to date, fossil fuels fulfill over 81 % of the total energy demand (see *Figure 1 - 1a*).[2] However, the use of fossil fuels is unsustainable, and their emission products may catalyze irreversible climate change.[3] Therefore, energy production from wind and solar has been at the forefront of renewable energy research in recent decades. Both approaches are potentially cost-effective, abundant and evenly distributed in the world.[4] In particular, the sun provides about 120000 terawatts to the earth's surface and therefore potentially covers 6000 times the present world's energy consumption.[5] Covering just 0.4% of planet's surface with 15 % efficient solar panels[6] or a solar farm with 160 000 km^2 in the Sahara Desert with 25 % efficient solar panels[7] would cover the projected energy needs. Thus, the application of photovoltaic (PV) technologies has increased constantly in the last few years. Between 2012 and 2015, the amount of energy demand covered with PV was doubled from 100 GW to 200 GW[8] and was expected to be 300 GW in 2017. Such a rapid increase was only possible due to the constant increase of cost efficiency in PV systems.[9] Here, the improvement of performance in silicon-based solar cells and the reduction of its production cost turned this system into a leading PV technology with an installed capacity of over 40 GW in 2015 (see *Figure 1 - 1b*).[10]

In addition to silicon solar cells, other technologies were also developed in the past decades to address the global energy challenge with PVs. *Figure 1 – 1b* gives a summery.[11] Although GaAs reaches top efficiencies with up to 28 % on single junction solar cells, the production cost is too high to be considered for mass production.[11,12] However, one of the most competitive technologies in comparison with silicon-based PV was found to be the second-generation thin film-based PV with CdTe or $Cu(InGa)Se_2$ (CIGS). Such devices show high efficiencies of up to 22.6 % and are compatible with up-scalable techniques.[13-16] The biggest advantage of these

systems compared to crystalline silicon is a lower probability of charge recombination at grain boundaries or other traps. Therefore, a high crystal quality is not as crucial.[17] However, these devices are either too toxic or contain rather rare elements like indium, which is much less abundant and harder to extract than silicon, making large-scale deployment difficult.

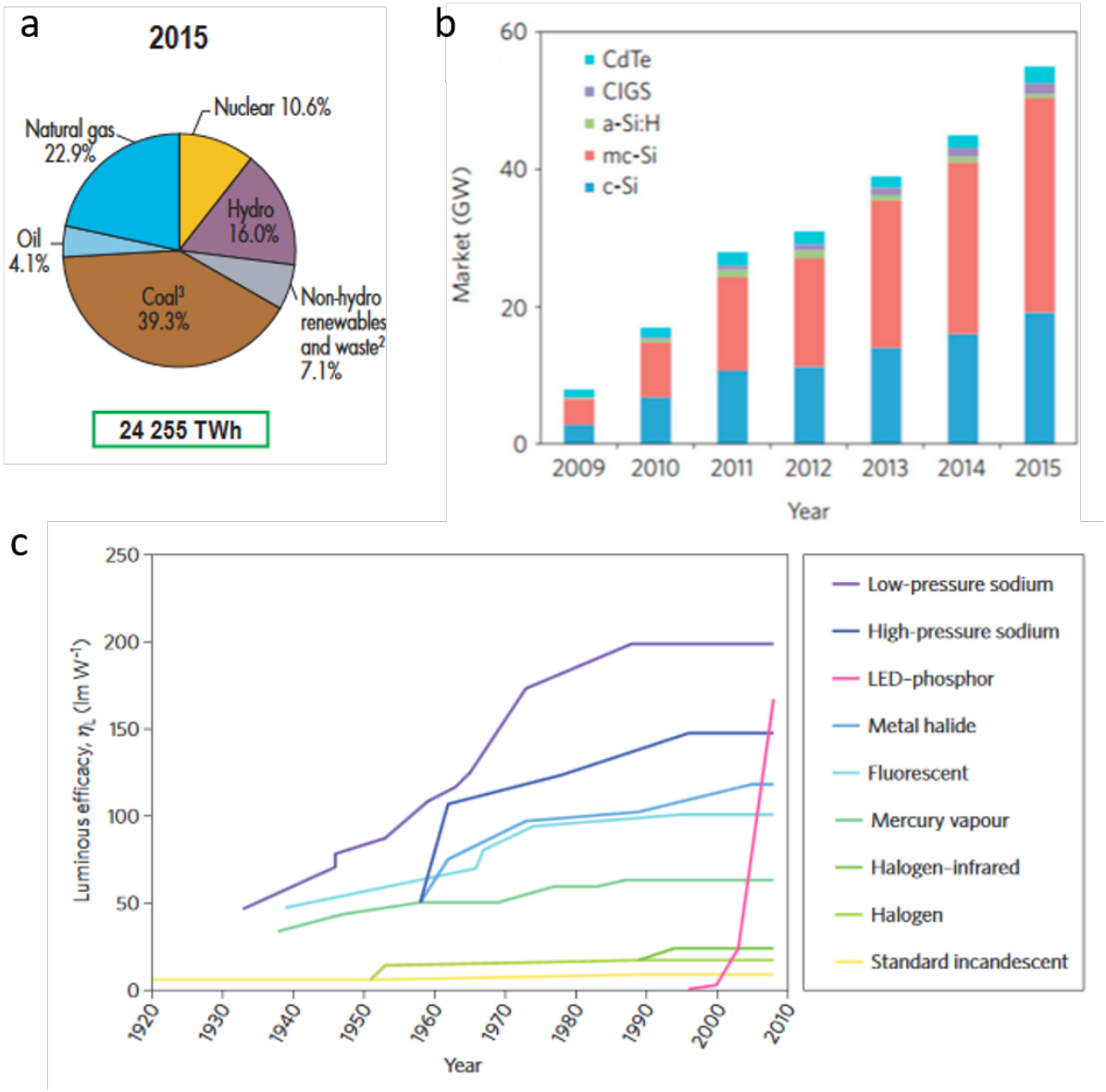

Figure 1 - 1: a) World electricity generation by source, non-hydro renewables includes geothermal, solar, wind, tide/wave/ocean, biofuels, waste, heat and other;[2] b) annual photovoltaic market demand by technology, with c-Si for crystalline silicon, mc-Si for multicrystalline silicon and a-Si:H for amorphous hydrogenated silicon;[18] c) historical development of the most common white-light sources.[19]

The driving force for the development of third-generation PV technologies was mainly the possibility of mass production without the requirement of high-temperature annealing and high vacuum during synthesis. Therefore, solution-processable solar cells gained increasing interest in organic photovoltaics (OPV),[20] dye-sensitized solar cells (DSSC)[21] or quantum dot solar cells

(QD-SC).[22] However, the photovoltaic performance is still rather limited in all these types of devices. The most efficient type, a QD-SC, presently reaches 13.4 % power conversion efficiency.[23] Typically, these devices suffer from high recombination losses associated with surface defects after ligand exchange.[24] In OPV and DSSCs, the losses associated with the thermodynamic driving force required to either dissociate strongly bound photo-generated excitons[20] or to drive electron transfer processes in a DSSC[24] inherently limit the device efficiencies. Thus, the highest efficiencies so far do not exceed 12 %.[23] With the emergence of hybrid perovskite materials in solid state thin film PV applications, the development of a highly efficient but solution processable technique seems to be imminent, but significant optimization is still required. Especially the morphology and microstructure of the perovskite material have a significant influence on photovoltaic performance, but a detailed study of their influence and further optimization is still necessary.

Although the development of new technologies to cover the world's energy demand may appear to be the most efficient and direct approach, the introduction of more energy efficient technologies tackles the problem at the source. Worldwide, 19 % of the produced electricity provides the energy for artificial light.[25] Therefore energy conservation measures are required for lighting applications. To date, light emitting diodes (LEDs) show the highest potential with the better energy efficiency of white LEDs compared to incandescent bulbs and fluorescent lamps (see *Figure 1 - 1c*).[26] LEDs show dramatic improvement in luminous efficiency compared to High-Pressure Sodium (HPS) systems in general illumination and road lighting.[27] Additionally, LEDs do not suffer from drawbacks such as exposure to mercury found in fluorescent bulbs.[19]

To date, the use of inorganic LEDs has transformed artificial lighting with significant savings in energy. Unfortunately, these semiconductors rely on high temperature, expensive vacuum-based processing with epitaxial growth on expensive and rigid substrates. Recently, OLEDs[28] and QLEDs[29] emerged as the most promising candidates in comparison with the III-V semiconductors and have already found commercial application.[30,31] However, in QLEDs the performance is limited due to large non-radiative recombination caused by the high amount of surface defects. OLEDs on the other side, are typically processed via vacuum-based sublimation, which is unsuitable for cost-effective large-area processing. Furthermore, forbidden (triplet exciton) radiative recombination fundamentally limits their intrinsic emission process to typically no more than 25%.[32] Hybrid perovskite semiconductors, however, show - despite their manufacturability from solution - low defect densities and a direct bandgap, which

results in photoluminescence quantum yields exceeding 90 %.[33,34] Still, the field of perovskite-based light emitting diodes (PeLEDs) presents some unexplored areas. Especially, the development of blue PeLEDs is desirable for lighting applications but still challenging. Blue light generation belongs to the most challenging tasks in LED development and is the emission-limiting factor in OLEDs[35,36] as well as in QLEDs[37]. However, the generation of white light by LEDs requires blue radiation to cover a large part of the emission spectrum.[25,35,38]

1.2 PEROVSKITES: A NEW CLASS OF MATERIALS FOR OPTOELECTRONIC APPLICATIONS

Recently, the hybrid perovskite halides emerged as the most promising material for low-cost photovoltaic applications. These absorber layers are the basis of the fourth generation of PV technology. In 2009 perovskites were first introduced to PV applications in DSSC devices.[39] However, the perovskite material quickly progressed as the most promising absorber layer in solid-state thin-film PV devices. After only eight years of research, the power conversion efficiencies for perovskite-based solar cells (PSCs) are exceeding 22 %.[40,41] Therefore, the photovoltaic performance of perovskite-based devices is competitive compared to the other solid-state-based PV techniques (see *Figure 3b*), while it combines the advantages of fabrication from solutions and material abundance of OPV, DSSC, and QD-SC.

The term perovskite arises from the materials crystal structure-type which was discovered with $CaTiO_3$ in 1839 and named after the mineralogist Lew Alexejewitsch Petrowski.[42] This specific crystal structure typically exhibits ABX_3 stochiometry, and its oxides like $BaBiO_3$ belong to the most studied perovskites, due to their outstanding electrical properties of ferroelectricity and superconductivity.[43] Thus, the hybrid metal halide perovskites integrate formidably into the highly interesting perovskite family. In particular, the methylammonium lead halides ($MAPbX_3$) belong to the most investigated hybrid perovskite materials due to the dark tetragonal perovskite phase that is stable at temperatures between 160 K and 330 K.[44] At higher temperatures a transformation to a cubic phase occurs with no dramatic changes of the optoelectronic properties.[44] Therefore, this compound crystallizes in a strong light absorbing phase with good charge carrier transport properties.

In the $MAPbX_3$ compound, lead (on position B) is octahedrally coordinated by the halides (on position X), while methylammonium (on position A) occupies the octahedral voids in the structure. The structure modification possibilities include both, cation- and anion-variation. The

Goldschmidt tolerance factor (t, see *Equation 1 – 1*) is a reliable tool to predict the formation of a perovskite crystal structure based on the atom-/ molecule-radii in the compound. Additionally, with the octahedral factor (μ, see *Equation 1 – 2*) the stability of the perovskite can be evaluated. The optimal range for t is considered to be between 0.813-1.107 and for μ between 0.442-0.895.[45] The high number of variation possibilities results in expanded modification options (see *Figure 1 – 2)*.[46-50]

$$t = \frac{r_A + r_X}{\sqrt{2}(r_B + r_X)} \qquad \text{(Equation 1 – 1)}$$

$$\mu = {}^{r_B}/_{r_X} \qquad \text{(Equation 1 – 2)}$$

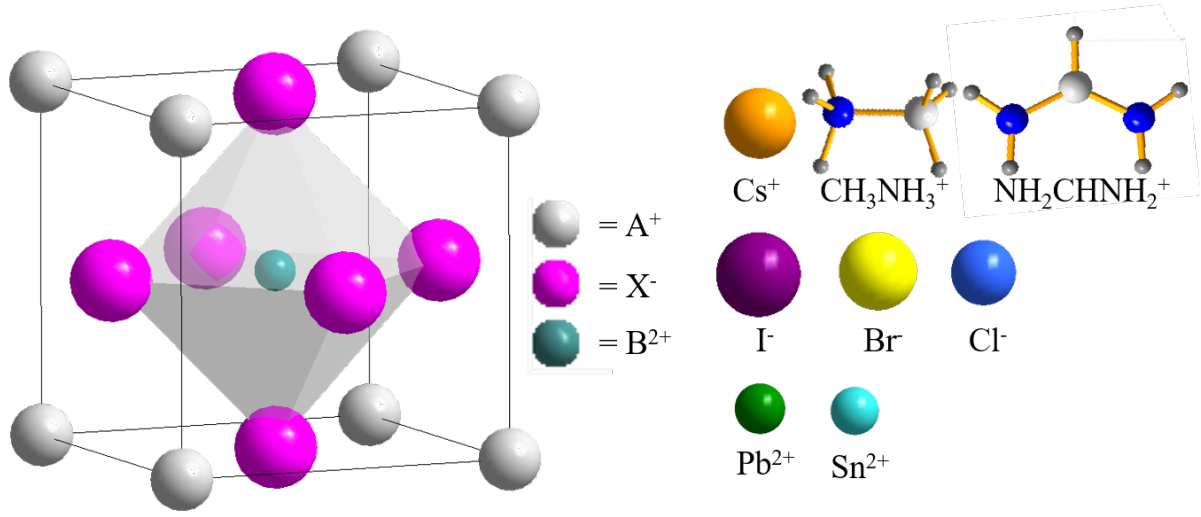

Figure 1 - 2: Schematic illustration of the halide perovskite structure and the possible ions.

1.2.1 Perovskite-Based Solar Cells (PSCs)

In PSCs, the perovskite semiconductor absorbs light and generates charges, which are transferred to the charge extraction layers and finally transported to the electrodes. The design of devices commonly matches a sandwich-like architecture. The intrinsic perovskite absorber layer is arranged in between the charge extraction layers with additional electrodes on top and bottom. Here, a "regular" architecture classifies devices with an electron-extraction layer on the bottom and hole-extraction layer on top of the perovskite thin film. Inverted devices exhibit a reversed stacking sequence. In all device configurations, the nature of the perovskite layer regarding morphology, composition, etc. in combination with the nature of the interface the perovskite layer creates with the charge extraction layers is essential for the resulting photovoltaic performance.

Generally, for solar cell applications, the key parameters of a semiconductor are the presence of a direct band gap, strong light absorption, fast and efficient charge carrier transport and a

high tolerance of defects in the structure. The perovskite fulfills all these requirements.[51-54] In particular, the optical absorption and the low degree of energetic disorder is superior to most of the other conventional thin-film solar cells and almost comparable to GaAs (see *Figure 1 – 3a*).[55] Therefore, the absorber layers can be ultrathin and concomitantly create a sufficient number of charges upon illumination, resulting in efficient extraction due to their short travel distances. However, the loss during charge extraction for perovskite solar cells is usually very low even with film thicknesses of about 500 nm, due to the shallow nature of the dominating defects in perovskite films.[56]

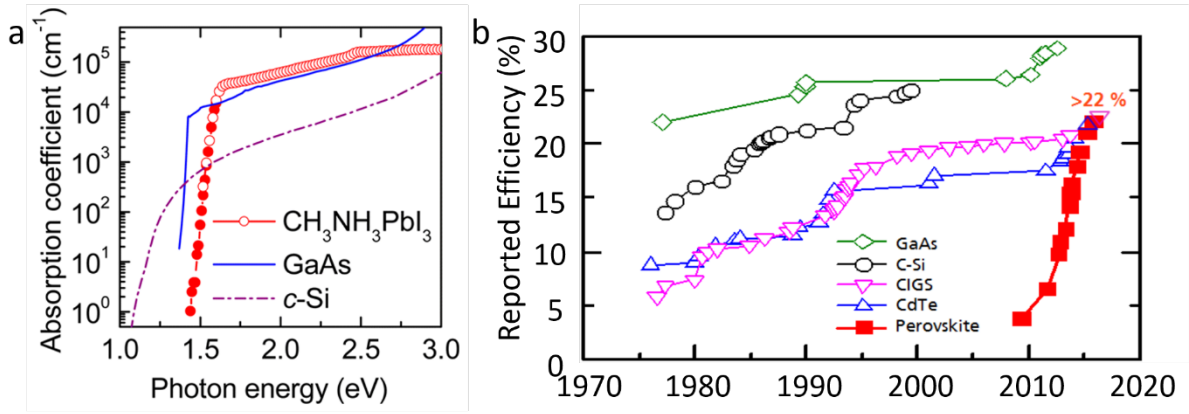

Figure 1 - 3: a) Effective absorption coefficient of a $MAPbI_3$ thin film compared to other typical photovoltaic systems;[55] b) the current status of PV technology.

This shallow nature of the defects can be attributed to their low formation energies, while deep defect levels only form at high energies in $MAPbI_3$. This unusual defect chemistry was found to be due to a strong Pb lone-pair *s* orbital and I *p* orbital antibonding coupling and the high ionicity of $MAPbI_3$ and explains the long electron-hole diffusion length and high open circuit voltages (V_{OC}).[52,56] Even though this dominating feature is considered to be responsible for the high efficiencies in perovskite solar cells, the control over the perovskite growth conditions is the key to regulate the dominant material defect doping and to approach highest solar cell efficiencies.[56,57]

The perovskite morphology and composition are crucial factors determining the photovoltaic parameters in PSCs.[58] The change in composition tunes the band-gap[47], absorption coefficient[59] or exciton binding energy[60,61]. However, the perovskite morphology affects the electron and hole diffusion lengths[62,63], ambipolar charge mobilities[64,65] and charge carrier lifetime[66].As a consequence of high-quality perovskite morphology, photovoltaic devices can approach 100 % internal quantum efficiencies[67] and exhibit remarkably high V_{OC}[68-70] and fill factors[71] approaching the Shockley-Queisser limit [72]. However, the electric properties like charge carrier

mobilities or diffusion lengths of thin nanocrystalline films are still inferior to single crystalline materials[73-80], which implies a strong need to increase the grain size in thin perovskite films. Various perovskite deposition techniques exist, but so far grain dimensions in thin films are limited to mostly 1 µm.

1.2.2 Perovskites in Light Emitting Diodes (PeLEDs)

The perovskite materials fulfill the requirements to be the key components of great solar cells and great LEDs.[72] The material shows strong photoluminescence (PL) with up to 70% quantum yield at high photon fluxes due to its low defect densities and therefore reduced non-radiative recombination pathways.[81] The advantageous electrical transport properties are crucial to achieving balanced charge-carrier densities[82], and the moderate ionization energy (IE) of the perovskite is beneficial to form stable functional interfaces[83]. In fact, good electroluminescence properties can already be observed in a solar cell device configuration.[84,85]

One of the strongest features of the perovskite for LED (peLED) applications is the tuneable color over the whole visible range.[86-88] In the ABX_3 structure, every element can be exchanged and mixed to tune the emission color. Especially the anion-based color tuning, i.e., exchanging the halides in $MAPbX_3$ with Cl^-, Br^-, I^-, gives the largest variation in bandgap from 3.1 eV to 1.6 eV.[89-92] Continuous bandgap tuning is possible by mixing the halides. However, halide segregation can occur under heat, light, etc., leading to a shift in the PL emission and loss of photoluminescence quantum yield (PLQE) in these systems.[93,94] The same applies to stacked systems with sequentially deposited films. Here, halides can migrate in-between the individual layers. Consequently, the individual PL emission of each layer is lost, which limits the engineering of white light emission.[95] With nanoparticles (NPs), embedded in a polymer matrix, no shift in PL emission occurs, and red and green emitting perovskite films on top of a GaN chip have realized white light emission.[95] However, the lack of peLEDs with a blue emitting perovskite layer hinders the development of fully perovskite-based white LEDs.

Currently, perovskite PeLEDs exhibit efficiencies similar to those of phosphorescent organic LEDs.[96] In less than two years, the efficiency of PeLEDs improved from 1% to 8% external quantum efficiencies (EQE). This improvement was mainly possible with the optimizations of perovskite emission layer morphology.[96] The morphologies of thin emission films in LED applications are desired to be twenty-five times thinner than for PV applications to achieve confinement of the charges injected into the emission layer. Synthesizing very thin perovskite films is rather challenging since they usually exhibit pinholes and other morphological defects.[97,98] Therefore, with 35 % the highest PLQE of thin films is also much lower than that

of perovskite NPs with 90 %. However, PeLEDs based on NPs suffer mostly from device degradation and efficiency drop due to heating at high current densities.[99] Additionally, the high defect densities common with NPs create similar limitations as observed in QLEDs. Therefore, the synthesis of high-quality thin films with high crystallinity but very small film thicknesses will be necessary for high-performance PeLEDs.

1.3 PEROVSKITE CRYSTALLIZATION

Studying perovskite thin film crystallization is crucial for their application in optoelectronic devices. In particular, the perovskite thin film morphology and microstructure are decisive regarding defect densities in the material and its resulting electrical properties, like charge transport under operating conditions.[100] The improvement of morphology can be obtained with increased grain sizes. However, the microstructure additionally affects the charge transfer to the charge extraction layers in devices, leading to facet-dependant photovoltaic efficiency variation of single grains in polycrystalline thin perovskite films.[101] Usually, the crystals in polycrystalline perovskite films are randomly-aligned and different facets are exposed to the charge extraction layers. Improved crystal alignment potentially decreases the defect densities in perovskite films and enables the optimization of interface engineering in the device architectures.

Interface engineering and the perovskite thin film quality are the most critical factors for optoelectronic device performance. Furthermore, perovskite crystallization strongly depends on the interface on top of the substrate.[102,103] Regarding the wetting behavior of the substrate towards the polar perovskite precursor solutions, the perovskite nucleation and crystallization are strongly altered by changes in surface roughness. Therefore, the nature of the bottom interface generally limits most perovskite crystallization techniques. These limitations need to be solved to enable a broad perovskite thin film application in various device configurations. In particular, the up-scaling to modules is an important factor for commercialization of perovskite devices.

To study perovskite crystallization in general, methylammonium lead halides ($MAPbX_3$, with $X=I^-$, Br^-, Cl^-) are some of the most suitable compounds for fundamental studies. All $MAPbX_3$ compounds show good phase purity of the perovskite structure with the tetragonal structure for the iodide compound or the cubic structure for the bromide or chloride compounds. These compounds can all be processed at low temperature and from solution. Therefore, various possibilities for perovskite conversion techniques arise, distinguished in one- or two-step

approach. In the two-step approach, a precursor is usually pre-deposited in the solid state to react with the other precursor afterward, typically in a liquid or gas environment. Whereas in the one-step approach all precursors are mixed into one precursor solution and the perovskite conversion is rather direct from solution. This method is considered to be the potentially easiest and therefore cheapest technique. Furthermore, the classification of one-step approaches has been proposed as (i) direct transition[104,105], (ii) crystallization through an intermediate phase [39,106,107] or (iii) through precursors[108]. In all methods, the nucleation occurs with induced supersaturation, such as solvent removal with isothermal heating[109-112] or addition of antisolvents[74,104,113,114].

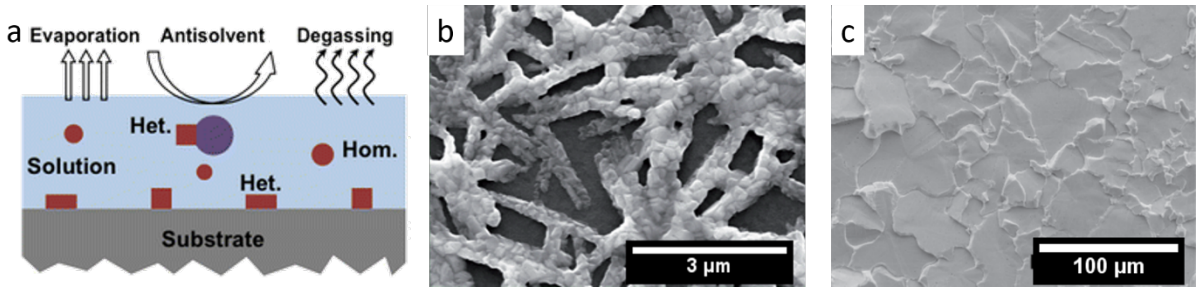

Figure 1 - 4: a) Schematic illustration of classical homogeneous and heterogeneous nucleation during supersaturation of thin film solution[115]; Top-view SEMs of $MAPbI_3$ from $MAI+PbI_2$ precursor with b) dimethylformamide (DMF) solvent[116]; c) MAF ionic liquid[117].

During the perovskite conversion process either heterogeneous or homogeneous nucleation (see *Figure 1 - 4*a) can occur. The heterogeneous nucleation on the substrate is the most desirable one to achieve uniform thin films.[115] However, the polar solvents necessary to dissolve the perovskite precursors lead to strong coordination with the divalent metal, regarding Lewis-base-adduct formation (the solvent O-atoms coordinate to the electron deficient Pb^{2+} cation). Since lead halides are known to be Lewis-acids and to form iodoplumbate anions, like $[Pb_3I_{10}]^{4-}$ and $[Pb_5I_{16}]^{6-}$ [118,119], it was also suspected that colloids form, and therefore that this would not be an ideal scenario for perovskite nucleation.[115,120] The colloids can serve as heterogeneous nucleation sites, which can assemble to form a bulk structure, leading to low nuclei distribution on the substrate, and promoting island growth with non-fully-covering films (see *Figure 1 – 4*). Thus, the main focus in process development for perovskite crystallization is to create ideal conditions for nucleation. So far, the use of an ionic liquid (methylammonium formate, MAF) presented the ideal case of nucleation for pure $MAPbI_3$ with films featuring large and highly aligned crystallites in fully-covered films.[100,117] This was attributed to the pure transition of the perovskite upon heating while the liquid remained on top.[117] However, this process condition also led to rough surfaces, which makes most device applications unfeasible.

1.3.1 The Two-Step Approach

One of the first processes introduced to avoid island formation during perovskite crystallization is the so-called two-step approach. Here, undesirable perovskite nucleation effects are prevented by pre-depositing a lead iodide layer, followed by the perovskite conversion afterward. The achievement of uniform perovskite films is even possible with a PbI_2 layer containing small pinholes, due to the healing of those pinholes during perovskite conversion.[121] Therefore, no complex thin film deposition methods are required for PbI_2 layer deposition and a process via blade coating can be efficiently used for the large-scale application.[122]

The two-step approach distinguishes between three different categories of conversion: solid-liquid[123,124], solid-solid[125] and solid-vapour[121] (see *Figure 1 – 5*). In all cases, the solid lead iodide-based layer represents the basis for the final perovskite film morphology, especially in a solid-liquid and solid-solid reaction. The conversion to the perovskite occurs through the diffusion and the subsequent intercalation of methylammonium iodide (MAI) into the lead iodide film. Therefore, the mobility of MAI must be guaranteed, either with liquid phase or by heating to facilitate ion movement. With the MAI intercalation, the PbI_2 lattice expands in volume.[126,127] This makes the process rather complex to understand or control.

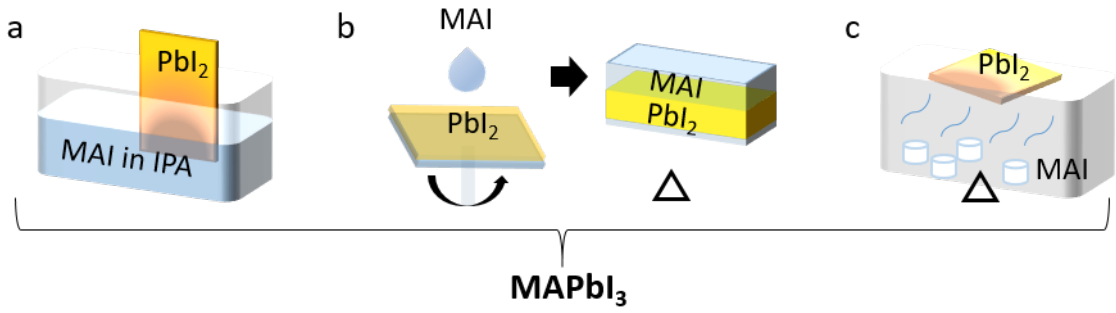

Figure 1 - 5: Schematic illustration of 2-step conversion techniques: a) solid-liquid; b) solid-solid; c) solid-vapour.

With *in situ* grazing-incidence small angle X-ray scattering (GISAXS), two main limitations for perovskite crystal growth were identified, such as thin film delamination and high roughness from grain growth constraints.[126] To overcome such limitations, the use of porous PbI_2[127] was suggested, or of density-matched adduct complexes, like the Lewis-base-adduct $PbI_2 \cdot x$DMSO[128-130]. The use of adducts belongs to be the most promising approaches due to the avoided or reduced volume expansion during the perovskite conversion.[129]

The partial substitution of MAI with MACl provides no change in the perovskite morphology, but an improvement in the photovoltaic performance.[124,131] This improvement was attributed

to the significantly decreased perovskite crystallization rate and the preferential crystals growth with (002/110) crystal facets parallel to the substrate.[132-134]

1.3.2 Antisolvent Techniques

One of the one-step approaches aiming to avoid perovskite island growth and to achieve high-quality uniform perovskite morphologies was found to be the so-called antisolvent technique. This approach stands out due to a simple process with reproducible uniform perovskite nucleation. Here, a solvent in which the perovskite shows only low solubility, i.e., an antisolvent like chlorobenzene (CB) or toluene, is added during the spin-coating process of the perovskite precursors (see *Figure 1 – 6*).[104,113] In a rapid process, the polar precursor solvent is extracted with the antisolvent and the perovskite nucleation is forced.[115] Therefore, the resulting perovskite films exhibit homogeneous coverage with ultrasmooth and fine grains.[104,114] The use of the Lewis-adduct MAI-PbI_2-DMSO established a further improvement in morphology, which now belongs to the most common perovskite deposition techniques in small lab-scale applications.[41,106,135] Similar to the two-step conversion, the DMSO-containing complex formation results in high-quality perovskite films after conversion. Especially for fast processes, such as the antisolvent technique, the Lewis-base DMSO was found to be an excellent intermediate to control to some extent the morphology and grain size of $MAPbI_3$. With these techniques, the highest recorded photovoltaic efficiencies reached up to 19.7%.[106]

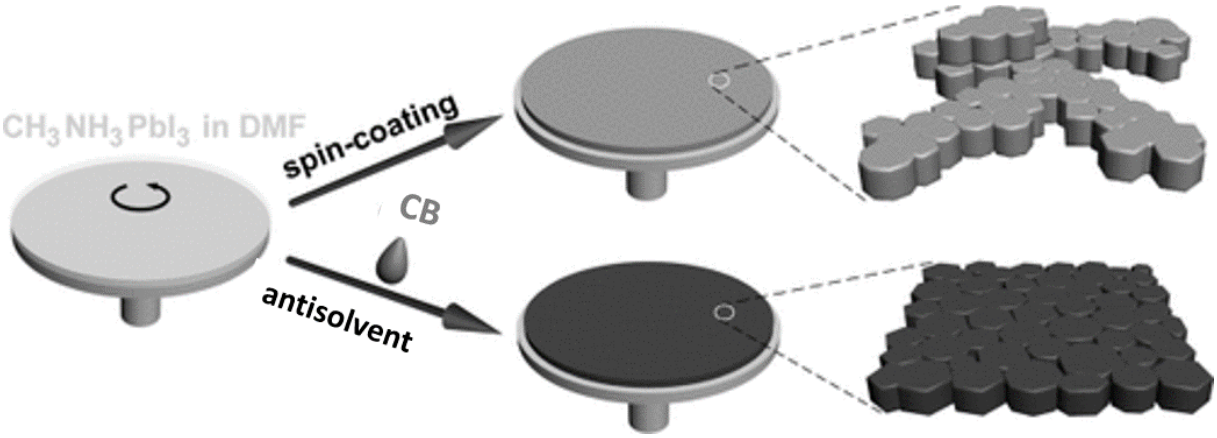

Figure 1 - 6: Schematic illustration of the antisolvent technique and conventional spin-coating process for fabricating perovskite films. Conventional spin-coating (top) results in a shiny gray film composed of large non-uniform crystals as a result of slow crystallization. In the antisolvent process (bottom), a second solvent (e.g., chlorobenzene) introduced on top of the wet film during the spin-coating process induces fast crystallization of uniformly sized perovskite grains.[104]

1.3.3 Alternative Lead Sources

Another strategy to modify the nucleation of the iodide-based compounds is to use lead sources alternative to PbI_2. Buin et al. predicted high trap densities in films synthesized with a high iodide content. As a consequence, iodide-free lead sources should have the potential for

achieving a better performance by avoiding this issue.[136] Mainly, $PbCl_2$, $Pb(Ac)_2$ and $Pb(NO_3)_2$ were suggested by Aldibaja *et al.,* and their crystallization kinetics analyzed (see *Figure 1 – 7*).[137,138] *Figure 1 – 7* shows literature-known morphologies with the largest perovskite grain sizes achieved for each precursor. However, only $PbCl_2$ and $Pb(Ac)_2$ showed satisfying perovskite nucleation behavior in a one-step process without the need for extensive optimization.[137,138] Especially in a direct comparison of PbI_2, $PbCl_2$, and $Pb(Ac)_2$ at a ratio of 1:3 with MAI, only the perovskite films from the $Pb(Ac)_2$ precursor resulted in a homogeneous layer. [139] This was attributed to a much higher nucleation density with the highly volatile excess organic salt in $Pb(Ac)_2$, as nucleation and crystallization already occurred at RT with the solvent being still on top.[138,139]

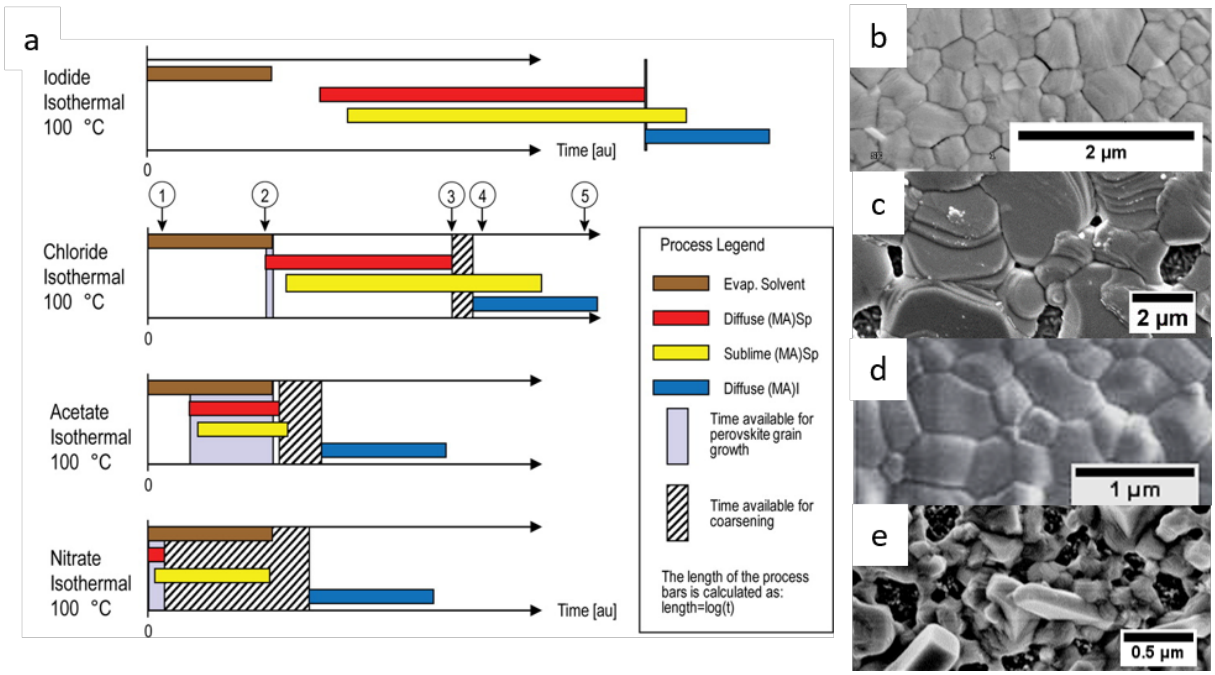

Figure 1 - 7: a) Schematic timelines for the four lead salt systems used in perovskite crystallization kinetics study.[138] The legend shows the title for each colored bar with the full explanation of the process given in the text. Although the pathway timeline is intended to be schematic, the start time and length for each process calculated from data in [108]; SEM top-view of about the best $MAPbI_3$ thin film morphologies with b) PbI_2 precursor[105]; c) $PbCl_2$ precursor[107]; d) $Pb(Ac)_2$ precursor[139]; e) $Pb(NO_3)_2$ precursor[140].

Such a fast process results in small grain sizes with up to 500 nm in dimension within the perovskite films.[139] Interestingly, the amount of hydration water in $Pb(Ac)_2$ shows a substantial impact on crystallization kinetics with slight morphological variations but significant changes in solar cell performance if the amount of hydration water is varied.[141,142] However, the origin of such effects was not revealed so far, and the grain sizes do not extend beyond 1 µm in thin films.

Using a $PbCl_2$ precursor resulted in the largest grain sizes in the µm-range. Here, the crystallization was related to the pre-formation of an intermediate phase based on a chloride-rich compound.[107] However, usually the large crystallites were disconnected and a poor surface coverage resulted. Thus, with this approach a crystal size- and surface coverage compromise was necessary.[107,131,143-145]

1.3.4 Precursor Additives

The trends described in the previous sections on perovskite crystallization mostly point toward ideal crystallization kinetics in perovskite formation through an intermediate phase. Chloride-based compounds and Lewis-base additives create such intermediate phases, and the perovskite nucleation is regulated by their stability, especially towards temperature. As described in the following, a trial and error approach with varying precursor additives was established to determine the best conditions.[146]

In the case of chloride-based compounds, the tests included either highly volatile compounds like NH_4Cl and HCl or the non-volatile compound $CaCl_2$. Here, mainly the volatile compounds led to smooth film morphologies but nanometer-sized grains.[147] With the non-volatile compound perovskite grain sizes were increased, leaving the insulating $CaCl_2$ behind. The big drawback of this approach is that no complete removal of $CaCl_2$ occurred with heat treatment as in the case of volatile compounds. Thus, devices achieved only poor performance.[148]

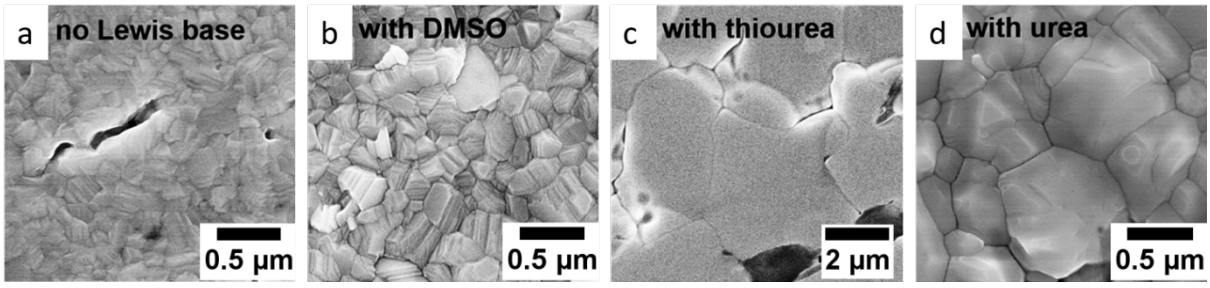

Figure 1 - 8: SEM images of $MAPbI_3$ perovskite films derived from different additives: a-d) morphological changes with variation of Lewis-base additive.[146]

Lewis-bases are considered to be the more ideal precursor additives to improve the perovskite thin film morphology. Usually, an intermediate phase forms, which directly converts to the perovskite. Therefore, homogeneous films of the Lewis-adducts can be deposited and converted to the perovskite at a slow nucleation rate while avoiding island formation. Additional studies showed increased crystal size related to the stability of the complex during perovskite conversion.[146] By choice of Lewis-bases (like DMSO, thiourea or urea), the stability could be varied by the interactions with the lead ions. Thiourea forms a more stable Lewis-base-adduct

than DMSO or urea, which results in larger grain sizes in the perovskite films (see *Figure 1 – 8*).[146] However, the stability of the Lewis-base-adducts based on thiourea entails a non-phase pure perovskite layer with low performance in photovoltaic applications.[146,149] Less stable Lewis-base adducts, such as the PbI_2-MAI-DMSO complexes are highly unstable at RT if deposited in the solid state. The instability causes barely controllable nucleation and crystallization process during perovskite conversion.[150]

1.4 OUTLINE OF THE THESIS

The preceding experience regarding perovskite crystallization points towards the elaboration of an ideal perovskite film formation through a stable intermediate perovskite phase with easily removable side products. In this thesis, we developed a new and highly stable intermediate phase with direct conversion to the pure perovskite phase under heat treatment due to highly volatile side products. We determined that this beneficial intermediate phase forms by mixing a hydrated lead acetate precursor with methylammonium halides. This method includes highly polar solvent mixtures like dimethylformamide (DMF), dimethylsulfoxide (DMSO) or tetraethylthiophene-1-oxide (THTO) and is beneficial for the deposition of iodide-, bromide- or chloride-based perovskite compounds.

The halide variation from iodide over bromide to chloride tunes the bandgap of the material, such that different applications are feasible. We used chloride- or bromide-based compounds for LED applications. Here, our process enabled the production of very thin but homogeneous perovskite films with variable halide compositions. We tuned the emission color from blue to the green region of the visible spectrum (425–570 nm), and only low voltages between 2.2-3 V were necessary to light up the LEDs. This first report on a blue perovskite LED supports the possibility of very cost-efficient lighting applications of the perovskite materials. Furthermore, our results show sharp, color-pure electroluminescence (EL), which is interesting for LEDs in display applications.

Bromide-rich compounds are also very good candidates for solar cell applications. These wide bandgap perovskites are particularly interesting materials because of their potentially high open-circuit voltage and are therefore attractive for driving electrochemical reactions like the generation of solar fuels or for multi-junction device applications. However, high-quality films are necessary for good performance in devices, and the synthesis of such planar methylammonium lead bromide thin films is very challenging. We managed to optimize the film deposition conditions with the use of a hydrated lead acetate precursor and synthesized

dense layers with large crystallites (5–10 µm in size) and perfect crystal alignment. The single junction devices exhibit high photocurrents, internal quantum efficiencies approaching unity and voltages exceeding 1.4 V. As a result, we obtained highly efficient solar cells with high open-circuit voltages.

A similar effect regarding photovoltaic performance occurred for iodide-based devices that are particularly interesting for single solar cell junctions due to their high-power conversion efficiencies. The discovered intermediate phase (IP) formed with lead acetate precursor provides optimized crystallization conditions, especially for the iodide-based compound $MAPbI_3$ due to its stability compared to the other halide systems. We obtained thin films with grain sizes of over 10 µm with pure crystal orientation with respect to the substrate. With the improved film morphology and microstructure, the electric properties were boosted and approach the ones of single crystals. Power conversion efficiencies amounted to 18.5%, higher than $MAPbI_3$-based devices prepared from standard methods in a like-to-like comparison.

All of our methylammonium lead halide films exhibit strong crystal alignment concerning the substrate. However, the role of perovskite crystal orientation in optoelectronic device application remains unclear. While all our bromide- and chloride-based compounds crystallized with the (100) cubic crystal facets preferably aligned parallel to the substrate, the crystal alignment in the iodide-based compound with a tetragonal crystal structure is tuneable. We discovered tunability of crystal facet alignment with the variation of highly polar solvent additives during synthesis, enabled by the formation of the IP from the lead acetate precursor. For the (200) and (002) tetragonal crystal facets, we can achieve almost perfect crystal alignment parallel to the substrate without changing the perovskite crystallization dynamics and morphology. In general, we observed improved charge transport with a higher degree of crystal alignment. However, the exposure of specific crystal facets to different charge extraction materials leads to changes in the interface. In particular, the (200) perovskite crystal facets in combination with TiO_2 cause an interfacial energetic barrier with severe loss in fill factor. We introduced a C_{60}-self-assembled monolayer on top of TiO_2 which removed the energetic barrier. Furthermore, inverted devices fully based on organic layers show no hint of the presence of barriers and fill factor values in such devices approach the theoretical maximum with 81 %.

The interactions between the perovskite precursor solution and the substrate limit the choice of the bottom interfaces in devices. Fullerene-based interfaces belong to the most challenging due to its hydrophobicity towards the polar perovskite precursor solutions. As a result, non-homogeneous perovskite layer coverage and its delamination usually limit the device size and

reproducibility of power conversion efficiency. To decrease the hydrophobicity and to enable a universal solution for perovskite crystallization independent from the substrate, we applied small amounts of nanoparticles, like Al_2O_3 or SiO_2 improving the wetting behavior of the surface. By adding these insulating nanoparticles, surface coverage of about 1 % at the interface already improved the wetting of polar perovskite solutions on top of fullerenes significantly (by 66 %). This way, a full and uniform film coverage was enabled. The solid-state IP from lead acetate precursor additionally provided the best conditions for large area perovskite synthesis. Following this approach, the perovskite was generated from the IP independent of the speed of the low-volatility solvent removal, and homogeneous large-grain films were obtained on a 144 cm^2 sized substrate.

1.5 LITERATURE

(1) *British Petroleum* **2017**, *66*.

(2) *International Energy Agency* **2017**.

(3) Höök, M.; Tang, X. *Energy Policy* **2013**, *52*, 797.

(4) J. Nelson; Emmott, C. J. *Trans. R. Soc. A* **2013**, *371*, 4.

(5) Grätzel, M. *Acc. Chem. Res.* **2009**, *42*, 1788.

(6) Docampo, P.; Guldin, S.; Leijtens, T.; Noel, N. K.; Steiner, U.; Snaith, H. J. *Adv. Mater.* **2014**, *26*, 4013.

(7) Fakharuddin, A.; Jose, R.; Brown, T. M.; Fabregat-Santiago, F.; Bisquert, J. *Energy Environ. Sci.* **2014**, *7*, 3952.

(8) Singh, R.; Alapatt, G. F.; Lakhtakia, A. *IEEE Journal of the Electron Devices Society* **2013**, *1*, 129.

(9) de la Tour, A.; Glachant, M.; Ménière, Y. *Energy Policy* **2011**, *39*, 761.

(10) Green, M. A. *Nature Energy* **2016**, *1*, 15015.

(11) Green, M. A.; Emery, K.; Hishikawa, Y.; Warta, W. *Progress in Photovoltaics: Research and Applications* **2010**, *18*, 346.

(12) Shah, A.; Torres, P.; Tscharner, R.; Wyrsch, N.; Keppner, H. *Science* **1999**, *285*, 692.

(13) Bhattacharya, R. N.; Contreras, M. A.; Egaas, B.; Noufi, R. N.; Kanevce, A.; Sites, J. R. *Appl. Phys. Lett.* **2006**, *89*.

(14) Sadhanala, A.; Deschler, F.; Thomas, T. H.; Dutton, S. E.; Goedel, K. C.; Hanusch, F. C.; Lai, M. L.; Steiner, U.; Bein, T.; Docampo, P.; Cahen, D.; Friend, R. H. *J. Phys. Chem. Lett.* **2014**, *5*, 2501.

(15) Ayre, J. Clean Technica, 2014.

(16) Jackson, P.; Wuerz, R.; Hariskos, D.; Lotter, E.; Witte, W.; Powalla, M. *physica status solidi (RRL) – Rapid Research Letters* **2016**, *10*, 583.

(17) Visoly-Fisher, I.; Cohen, S. R.; Ruzin, A.; Cahen, D. *Adv. Mater.* **2004**, *16*, 879.

(18) Ng, C. H.; Lim, H. N.; Hayase, S.; Zainal, Z.; Huang, N. M. *Renewable and Sustainable Energy Reviews* **2018**, *90*, 248.

(19) Pimputkar, S.; Speck, J. S.; DenBaars, S. P.; Nakamura, S. *Nature Photonics* **2009**, *3*, 180.

(20) Brabec, C. J. *Sol. Energy Mater. Sol. Cells* **2004**, *83*, 273.

(21) Grätzel, M. *Journal of Photochemistry and Photobiology C: Photochemistry Reviews* **2003**, *4*, 145.

(22) Nozik, A. J. *Physica E: Low-dimensional Systems and Nanostructures* **2002**, *14*, 115.

(23) Best Research-Cell Efficiencies (NREL, h. w. n. g. n. i. e. c. j.

(24) Ito, S.; Zakeeruddin, S. M.; Humphry-Baker, R.; Liska, P.; Charvet, R.; Comte, P.; Nazeeruddin, M. K.; Péchy, P.; Takata, M.; Miura, H.; Uchida, S.; Grätzel, M. *Adv. Mater.* **2006**, *18*, 1202.

(25) Lin, Y.-C.; Karlsson, M.; Bettinelli, M. *Top. Curr. Chem.* **2016**, *374*, 21.

(26) Uchida, Y.; Taguchi, T.; SPIE: 2005; Vol. 44, p 9.

(27) Li, F.; Chen, D.; Song, X.; Chen, Y. In *2009 Asia-Pacific Power and Energy Engineering Conference* 2009, p 1.

(28) Murawski, C.; Leo, K.; Gather, M. C. *Adv. Mater.* **2013**, *25*, 6801.

(29) Shirasaki, Y.; Supran, G. J.; Bawendi, M. G.; Bulović, V. *Nature Photonics* **2012**, *7*, 13.

(30) Supran, G. J.; Shirasaki, Y.; Song, K. W.; Caruge, J.-M.; Kazlas, P. T.; Coe-Sullivan, S.; Andrew, T. L.; Bawendi, M. G.; Bulović, V. *MRS Bull.* **2013**, *38*, 703.

(31) *Applications of Organic and Printed Electronics*; Springer US, 2013.

(32) Goushi, K.; Yoshida, K.; Sato, K.; Adachi, C. *Nature Photonics* **2012**, *6*, 253.

(33) He, H.; S., S. A.; V., K. S.; Fu, H. T.; L., R. A. *Advanced Science* **2015**, *2*, 1500194.

(34) Abhishek, S.; Ramya, C.; Kumar, R. V.; Mir, I.; Arindam, C.; Angshuman, N. *Angew. Chem.* **2015**, *127*, 15644.

(35) Reineke, S.; Lindner, F.; Schwartz, G.; Seidler, N.; Walzer, K.; Lüssem, B.; Leo, K. *Nature* **2009**, *459*, 234.

(36) Sun, Y.; Giebink, N. C.; Kanno, H.; Ma, B.; Thompson, M. E.; Forrest, S. R. *Nature* **2006**, *440*, 908.

(37) Wan Ki, B.; Jeonghun, K.; Jaehoon, L.; Donggu, L.; Min Ki, N.; Kookheon, C.; Changhee, L.; Seonghoon, L. *Nanotechnology* **2009**, *20*, 075202.

(38) Schubert, E. F.; Kim, J. K. *Science* **2005**, *308*, 1274.

(39) Kojima, A.; Teshima, K.; Shirai, Y.; Miyasaka, T. *J. Am. Chem. Soc.* **2009**, *131*, 6050.

(40) Yang, W. S.; Park, B.-W.; Jung, E. H.; Jeon, N. J.; Kim, Y. C.; Lee, D. U.; Shin, S. S.; Seo, J.; Kim, E. K.; Noh, J. H.; Seok, S. I. *Science* **2017**, *356*, 1376.

(41) Saliba, M.; Matsui, T.; Domanski, K.; Seo, J.-Y.; Ummadisingu, A.; Zakeeruddin, S. M.; Correa-Baena, J.-P.; Tress, W. R.; Abate, A.; Hagfeldt, A.; Grätzel, M. *Science* **2016**, *354*, 206.

(42) Rose, G. *De novis quibusdam fossilibus, quae in montibus uraliis inveniuntur, scripsit.* **1839**, Berlin.

(43) Yan, B.; Jansen, M.; Felser, C. *Nat Phys* **2013**, *9*, 709.

(44) Quarti, C.; Mosconi, E.; Ball, J. M.; D'Innocenzo, V.; Tao, C.; Pathak, S.; Snaith, H. J.; Petrozza, A.; De Angelis, F. *Energy Environ. Sci.* **2016**, *9*, 155.

(45) Li, C.; Lu, X.; Ding, W.; Feng, L.; Gao, Y.; Guo, Z. *Acta Crystallographica Section B* **2008**, *64*, 702.

(46) Hao, F.; Stoumpos, C. C.; Cao, D. H.; Chang, R. P. H.; Kanatzidis, M. G. *Nature Photonics* **2014**, *8*, 489.

(47) Noh, J. H.; Im, S. H.; Heo, J. H.; Mandal, T. N.; Seok, S. I. *Nano Lett.* **2013**, *13*, 1764.

(48) Eperon, G. E.; Stranks, S. D.; Menelaou, C.; Johnston, M. B.; Herz, L. M.; Snaith, H. J. *Energy Environ. Sci.* **2014**, *7*, 982.

(49) Saliba, M.; Matsui, T.; Seo, J.-Y.; Domanski, K.; Correa-Baena, J.-P.; Nazeeruddin, M. K.; Zakeeruddin, S. M.; Tress, W.; Abate, A.; Hagfeldt, A.; Gratzel, M. *Energy Environ. Sci.* **2016**, *9*, 1989.

(50) Hanusch, F. C.; Wiesenmayer, E.; Mankel, E.; Binek, A.; Angloher, P.; Fraunhofer, C.; Giesbrecht, N.; Feckl, J. M.; Jaegermann, W.; Johrendt, D.; Bein, T.; Docampo, P. *J. Phys. Chem. Lett.* **2014**, *5*, 2791.

(51) Snaith, H. J. *J. Phys. Chem. Lett.* **2013**, *4*, 3623.

(52) Yin, W.-J.; Shi, T.; Yan, Y. *Adv. Mater.* **2014**, *26*, 4653.

(53) Yin, W.-J.; Yang, J.-H.; Kang, J.; Yan, Y.; Wei, S.-H. *J. Mater. Chem. A* **2015**, 8926.

(54) Park, N.-G. *Mater. Today*.

(55) De Wolf, S.; Holovsky, J.; Moon, S.-J.; Löper, P.; Niesen, B.; Ledinsky, M.; Haug, F.-J.; Yum, J.-H.; Ballif, C. *J. Phys. Chem. Lett.* **2014**, *5*, 1035.

(56) Yin, W.-J.; Shi, T.; Yan, Y. *Appl. Phys. Lett.* **2014**, *104*, 063903.

(57) Walsh, A.; Scanlon, D. O.; Chen, S.; Gong, X. G.; Wei, S. H. *Angew. Chem. Int. Ed.* **2015**, *54*, 1791.

(58) Huang, J.; Shao, Y.; Dong, Q. *J. Phys. Chem. Lett.* **2015**, *6*, 3218.

(59) Kim, H.-S.; Lee, C.-R.; Im, J.-H.; Lee, K.-B.; Moehl, T.; Marchioro, A.; Moon, S.-J.; Humphry-Baker, R.; Yum, J.-H.; Moser, J. E.; Grätzel, M.; Park, N.-G. *Scientific Reports* **2012**, *2*, 591.

(60) Zheng, K.; Zhu, Q.; Abdellah, M.; Messing, M. E.; Zhang, W.; Generalov, A.; Niu, Y.; Ribaud, L.; Canton, S. E.; Pullerits, T. *J. Phys. Chem. Lett.* **2015**, *6*, 2969.

(61) D'Innocenzo, V.; Grancini, G.; Alcocer, M. J. P.; Kandada, A. R. S.; Stranks, S. D.; Lee, M. M.; Lanzani, G.; Snaith, H. J.; Petrozza, A. *Nat Commun* **2014**, *5*.

(62) Stranks, S. D.; Eperon, G. E.; Grancini, G.; Menelaou, C.; Alcocer, M. J. P.; Leijtens, T.; Herz, L. M.; Petrozza, A.; Snaith, H. J. *Science* **2013**, *342*, 341.

(63) Xing, G.; Mathews, N.; Sun, S.; Lim, S. S.; Lam, Y. M.; Grätzel, M.; Mhaisalkar, S.; Sum, T. C. *Science* **2013**, *342*, 344.

(64) Leijtens, T.; Stranks, S. D.; Eperon, G. E.; Lindblad, R.; Johansson, E. M. J.; McPherson, I. J.; Rensmo, H.; Ball, J. M.; Lee, M. M.; Snaith, H. J. *ACS Nano* **2014**, *8*, 7147.

(65) Chen, Y.; Peng, J.; Su, D.; Chen, X.; Liang, Z. *ACS Applied Materials & Interfaces* **2015**, *7*, 4471.

(66) Wehrenfennig, C.; Eperon, G. E.; Johnston, M. B.; Snaith, H. J.; Herz, L. M. *Adv. Mater.* **2014**, *26*, 1584.

(67) Yang, B.; Dyck, O.; Poplawsky, J.; Keum, J.; Puretzky, A.; Das, S.; Ivanov, I.; Rouleau, C.; Duscher, G.; Geohegan, D.; Xiao, K. *J. Am. Chem. Soc.* **2015**, *137*, 9210.

(68) Wolff, C. M.; Zu, F.; Paulke, A.; Toro, L. P.; Koch, N.; Neher, D. *Adv. Mater.* **2017**, *29*, 1700159.

(69) Shao, Y.; Yuan, Y.; Huang, J. *Nature Energy* **2016**, *1*, 15001.

(70) Yin, W.-J.; Yang, J.-H.; Kang, J.; Yan, Y.; Wei, S.-H. *J. Mater. Chem. A* **2015**, *3*, 8926.

(71) Stolterfoht, M.; Wolff, C. M.; Amir, Y.; Paulke, A.; Perdigon-Toro, L.; Caprioglio, P.; Neher, D. *Energy Environ. Sci.* **2017**, *10*, 1530.

(72) Shockley, W.; Queisser, H. J. *J. Appl. Phys.* **1961**, *32*, 510.

(73) Dong, Q.; Fang, Y.; Shao, Y.; Mulligan, P.; Qiu, J.; Cao, L.; Huang, J. *Science* **2015**, *347*, 967.

(74) Shi, D.; Adinolfi, V.; Comin, R.; Yuan, M.; Alarousu, E.; Buin, A.; Chen, Y.; Hoogland, S.; Rothenberger, A.; Katsiev, K.; Losovyj, Y.; Zhang, X.; Dowben, P. A.; Mohammed, O. F.; Sargent, E. H.; Bakr, O. M. *Science* **2015**, *347*, 519.

(75) Saidaminov, M. I.; Adinolfi, V.; Comin, R.; Abdelhady, A. L.; Peng, W.; Dursun, I.; Yuan, M.; Hoogland, S.; Sargent, E. H.; Bakr, O. M. *Nat Commun* **2015**, *6*.

(76) Zhumekenov, A. A.; Saidaminov, M. I.; Haque, M. A.; Alarousu, E.; Sarmah, S. P.; Murali, B.; Dursun, I.; Miao, X.-H.; Abdelhady, A. L.; Wu, T.; Mohammed, O. F.; Bakr, O. M. *ACS Energy Letters* **2016**, *1*, 32.

(77) Petrus, M. L.; Schlipf, J.; Li, C.; Gujar, T. P.; Giesbrecht, N.; Müller-Buschbaum, P.; Thelakkat, M.; Bein, T.; Hüttner, S.; Docampo, P. *Advanced Energy Materials* **2017**, *7*, 1700264.

(78) Semonin, O. E.; Elbaz, G. A.; Straus, D. B.; Hull, T. D.; Paley, D. W.; van der Zande, A. M.; Hone, J. C.; Kymissis, I.; Kagan, C. R.; Roy, X.; Owen, J. S. *J. Phys. Chem. Lett.* **2016**, *7*, 3510.

(79) Tian, W.; Zhao, C.; Leng, J.; Cui, R.; Jin, S. *J. Am. Chem. Soc.* **2015**, *137*, 12458.

(80) Handloser, K.; Giesbrecht, N.; Bein, T.; Docampo, P.; Handloser, M.; Hartschuh, A. *ACS Photonics* **2016**, *3*, 255.

(81) Deschler, F.; Price, M.; Pathak, S.; Klintberg, L. E.; Jarausch, D.-D.; Higler, R.; Hüttner, S.; Leijtens, T.; Stranks, S. D.; Snaith, H. J.; Atatüre, M.; Phillips, R. T.; Friend, R. H. *J. Phys. Chem. Lett.* **2014**, *5*, 1421.

(82) Stranks, S. D.; Snaith, H. J. *Nature Nanotechnology* **2015**, *10*, 391.

(83) Kulbak, M.; Cahen, D.; Hodes, G. *J. Phys. Chem. Lett.* **2015**, *6*, 2452.

(84) Jaramillo-Quintero, O. A.; Sanchez, R. S.; Rincon, M.; Mora-Sero, I. *J. Phys. Chem. Lett.* **2015**, *6*, 1883.

(85) Gil-Escrig, L.; Longo, G.; Pertegas, A.; Roldan-Carmona, C.; Soriano, A.; Sessolo, M.; Bolink, H. J. *Chem. Commun.* **2015**, *51*, 569.

(86) Dohner, E. R.; Hoke, E. T.; Karunadasa, H. I. *J. Am. Chem. Soc.* **2014**, *136*, 1718.

(87) Dohner, E. R.; Jaffe, A.; Bradshaw, L. R.; Karunadasa, H. I. *J. Am. Chem. Soc.* **2014**, *136*, 13154.

(88) Zhang, F.; Zhong, H.; Chen, C.; Wu, X.-g.; Hu, X.; Huang, H.; Han, J.; Zou, B.; Dong, Y. *ACS Nano* **2015**, *9*, 4533.

(89) Jang, D. M.; Park, K.; Kim, D. H.; Park, J.; Shojaei, F.; Kang, H. S.; Ahn, J.-P.; Lee, J. W.; Song, J. K. *Nano Lett.* **2015**, *15*, 5191.

(90) Akkerman, Q. A.; D'Innocenzo, V.; Accornero, S.; Scarpellini, A.; Petrozza, A.; Prato, M.; Manna, L. *J. Am. Chem. Soc.* **2015**, *137*, 10276.

(91) Nedelcu, G.; Protesescu, L.; Yakunin, S.; Bodnarchuk, M. I.; Grotevent, M. J.; Kovalenko, M. V. *Nano Lett.* **2015**, *15*, 5635.

(92) Protesescu, L.; Yakunin, S.; Bodnarchuk, M. I.; Krieg, F.; Caputo, R.; Hendon, C. H.; Yang, R. X.; Walsh, A.; Kovalenko, M. V. *Nano Lett.* **2015**, *15*, 3692.

(93) Brennan, M. C.; Draguta, S.; Kamat, P. V.; Kuno, M. *ACS Energy Letters* **2018**, *3*, 204.

(94) Sutter-Fella, C. M.; Ngo, Q. P.; Cefarin, N.; Gardner, K. L.; Tamura, N.; Stan, C. V.; Drisdell, W. S.; Javey, A.; Toma, F. M.; Sharp, I. D. *Nano Lett.* **2018**.

(95) Pathak, S.; Sakai, N.; Wisnivesky Rocca Rivarola, F.; Stranks, S. D.; Liu, J.; Eperon, G. E.; Ducati, C.; Wojciechowski, K.; Griffiths, J. T.; Haghighirad, A. A.; Pellaroque, A.; Friend, R. H.; Snaith, H. J. *Chem. Mater.* **2015**, *27*, 8066.

(96) Cho, H.; Jeong, S.-H.; Park, M.-H.; Kim, Y.-H.; Wolf, C.; Lee, C.-L.; Heo, J. H.; Sadhanala, A.; Myoung, N.; Yoo, S.; Im, S. H.; Friend, R. H.; Lee, T.-W. *Science* **2015**, *350*, 1222.

(97) Li, G.; Tan, Z.-K.; Di, D.; Lai, M. L.; Jiang, L.; Lim, J. H.-W.; Friend, R. H.; Greenham, N. C. *Nano Lett.* **2015**, *15*, 2640.

(98) Wang, J.; Wang, N.; Jin, Y.; Si, J.; Tan, Z.-K.; Du, H.; Cheng, L.; Dai, X.; Bai, S.; He, H.; Ye, Z.; Lai, M. L.; Friend, R. H.; Huang, W. *Adv. Mater.* **2015**, *27*, 2311.

(99) Tan, Z.-K.; Moghaddam, R. S.; Lai, M. L.; Docampo, P.; Higler, R.; Deschler, F.; Price, M.; Sadhanala, A.; Pazos, L. M.; Credgington, D.; Hanusch, F.; Bein, T.; Snaith, H. J.; Friend, R. H. *Nat Nano* **2014**, *9*, 687.

(100) Cho, N.; Li, F.; Turedi, B.; Sinatra, L.; Sarmah, S. P.; Parida, M. R.; Saidaminov, M. I.; Murali, B.; Burlakov, V. M.; Goriely, A.; Mohammed, O. F.; Wu, T.; Bakr, O. M. *Nature Communications* **2016**, *7*, 13407.

(101) Leblebici, S. Y.; Leppert, L.; Li, Y.; Reyes-Lillo, S. E.; Wickenburg, S.; Wong, E.; Lee, J.; Melli, M.; Ziegler, D.; Angell, D. K.; Ogletree, D. F.; Ashby, Paul D.; Toma, F. M.; Neaton, J. B.; Sharp, I. D.; Weber-Bargioni, A. *Nature Energy* **2016**, *1*, 16093.

(102) Ye, F.; Chen, H.; Xie, F.; Tang, W.; Yin, M.; He, J.; Bi, E.; Wang, Y.; Yang, X.; Han, L. *Energy Environ. Sci.* **2016**, *9*, 2295.

(103) Bi, C.; Wang, Q.; Shao, Y.; Yuan, Y.; Xiao, Z.; Huang, J. *Nature Communications* **2015**, *6*, 7747.

(104) Xiao, M.; Huang, F.; Huang, W.; Dkhissi, Y.; Zhu, Y.; Etheridge, J.; Gray-Weale, A.; Bach, U.; Cheng, Y.-B.; Spiccia, L. *Angew. Chem.* **2014**, *126*, 10056.

(105) Noel, N. K.; Habisreutinger, S. N.; Wenger, B.; Klug, M. T.; Horantner, M. T.; Johnston, M. B.; Nicholas, R. J.; Moore, D. T.; Snaith, H. J. *Energy Environ. Sci.* **2017**, *10*, 145.

(106) Ahn, N.; Son, D.-Y.; Jang, I.-H.; Kang, S. M.; Choi, M.; Park, N.-G. *J. Am. Chem. Soc.* **2015**, *137*, 8696.

(107) Binek, A.; Grill, I.; Huber, N.; Peters, K.; Hufnagel, A. G.; Handloser, M.; Docampo, P.; Hartschuh, A.; Bein, T. *Chemistry – An Asian Journal* **2016**, *11*, 1117.

(108) Munir, R.; Sheikh, A. D.; Abdelsamie, M.; Hu, H.; Yu, L.; Zhao, K.; Kim, T.; Tall, O. E.; Li, R.; Smilgies, D.-M.; Amassian, A. *Adv. Mater.* **2016**, n/a.

(109) Jung, H. S.; Park, N. G. *Small* **2015**, *11*, 10.

(110) Zhao, Y.; Zhu, K. *J. Phys. Chem. Lett.* **2014**, *5*, 4175.

(111) Stranks, S. D.; Nayak, P. K.; Zhang, W.; Stergiopoulos, T.; Snaith, H. J. *Angew. Chem. Int. Ed.* **2015**, *54*, 3240.

(112) Im, J.-H.; Kim, H.-S.; Park, N.-G. *APL Mat.* **2014**, *2*, 081510.

(113) Jeon, N. J.; Noh, J. H.; Kim, Y. C.; Yang, W. S.; Ryu, S.; Seok, S. I. *Nat. Mater.* **2014**, *13*, 897.

(114) Zhou, Y.; Yang, M.; Wu, W.; Vasiliev, A. L.; Zhu, K.; Padture, N. P. *J. Mater. Chem. A* **2015**, *3*, 8178.

(115) Zhou, Y.; Game, O. S.; Pang, S.; Padture, N. P. *J. Phys. Chem. Lett.* **2015**, *6*, 4827.

(116) Wang, Q.; Shao, Y.; Dong, Q.; Xiao, Z.; Yuan, Y.; Huang, J. *Energy Environ. Sci.* **2014**, *7*, 2359.

(117) Moore, D. T.; Tan, K. W.; Sai, H.; Barteau, K. P.; Wiesner, U.; Estroff, L. A. *Chem. Mater.* **2015**, *27*, 3197.

(118) Krautscheid, H.; Vielsack, F. *J. Chem. Soc., Dalton Trans.* **1999**, 2731.

(119) Krautscheid, H.; Vielsack, F. *Z. Anorg. Allg. Chem.* **2000**, *626*, 3.

(120) Yan, K.; Long, M.; Zhang, T.; Wei, Z.; Chen, H.; Yang, S.; Xu, J. *J. Am. Chem. Soc.* **2015**, *137*, 4460.

(121) Chen, Q.; Zhou, H.; Hong, Z.; Luo, S.; Duan, H.-S.; Wang, H.-H.; Liu, Y.; Li, G.; Yang, Y. *J. Am. Chem. Soc.* **2014**, *136*, 622.

(122) Razza, S.; Di Giacomo, F.; Matteocci, F.; Cinà, L.; Palma, A. L.; Casaluci, S.; Cameron, P.; D'Epifanio, A.; Licoccia, S.; Reale, A.; Brown, T. M.; Di Carlo, A. *J. Power Sources* **2015**, *277*, 286.

(123) Burschka, J.; Pellet, N.; Moon, S.-J.; Humphry-Baker, R.; Gao, P.; Nazeeruddin, M. K.; Gratzel, M. *Nature* **2013**, *499*, 316.

(124) Docampo, P.; Hanusch, F. C.; Stranks, S. D.; Döblinger, M.; Feckl, J. M.; Ehrensperger, M.; Minar, N. K.; Johnston, M. B.; Snaith, H. J.; Bein, T. *Advanced Energy Materials* **2014**, *4*, n/a.

(125) Xiao, Z.; Bi, C.; Shao, Y.; Dong, Q.; Wang, Q.; Yuan, Y.; Wang, C.; Gao, Y.; Huang, J. *Energy Environ. Sci.* **2014**, *7*, 2619.

(126) Schlipf, J.; Docampo, P.; Schaffer, C. J.; Körstgens, V.; Bießmann, L.; Hanusch, F.; Giesbrecht, N.; Bernstorff, S.; Bein, T.; Müller-Buschbaum, P. *J. Phys. Chem. Lett.* **2015**, *6*, 1265.

(127) Zhou, Y.; Yang, M.; Vasiliev, A. L.; Garces, H. F.; Zhao, Y.; Wang, D.; Pang, S.; Zhu, K.; Padture, N. P. *J. Mater. Chem. A* **2015**, *3*, 9249.

(128) Yang, W. S.; Noh, J. H.; Jeon, N. J.; Kim, Y. C.; Ryu, S.; Seo, J.; Seok, S. I. *Science* **2015**, *348*, 1234.

(129) Li, W.; Fan, J.; Li, J.; Mai, Y.; Wang, L. *J. Am. Chem. Soc.* **2015**, *137*, 10399.

(130) Cao, J.; Jing, X.; Yan, J.; Hu, C.; Chen, R.; Yin, J.; Li, J.; Zheng, N. *J. Am. Chem. Soc.* **2016**, *138*, 9919.

(131) Lee, M. M.; Teuscher, J.; Miyasaka, T.; Murakami, T. N.; Snaith, H. J. *Science* **2012**, *338*, 643.

(132) Grill, I.; Handloser, K.; Hanusch, F. C.; Giesbrecht, N.; Bein, T.; Docampo, P.; Handloser, M.; Hartschuh, A. *Sol. Energy Mater. Sol. Cells* **2017**, *166*, 269.

(133) Oesinghaus, L.; Schlipf, J.; Giesbrecht, N.; Song, L.; Hu, Y.; Bein, T.; Docampo, P.; Müller-Buschbaum, P. *Advanced Materials Interfaces* **2016**, *3*, 1600403.

(134) Docampo, P.; Hanusch, F. C.; Giesbrecht, N.; Angloher, P.; Ivanova, A.; Bein, T. *APL Mat.* **2014**, *2*, 081508.

(135) Zheng, X.; Chen, B.; Wu, C.; Priya, S. *Nano Energy* **2015**, *17*, 269.

(136) Buin, A.; Pietsch, P.; Xu, J.; Voznyy, O.; Ip, A. H.; Comin, R.; Sargent, E. H. *Nano Lett.* **2014**, *14*, 6281.

(137) Moore, D. T.; Sai, H.; Wee Tan, K.; Estroff, L. A.; Wiesner, U. *APL Mat.* **2014**, *2*, 081802.

(138) Moore, D. T.; Sai, H.; Tan, K. W.; Smilgies, D.-M.; Zhang, W.; Snaith, H. J.; Wiesner, U.; Estroff, L. A. *J. Am. Chem. Soc.* **2015**, *137*, 2350.

(139) Zhang, W.; Saliba, M.; Moore, D. T.; Pathak, S. K.; Hörantner, M. T.; Stergiopoulos, T.; Stranks, S. D.; Eperon, G. E.; Alexander-Webber, J. A.; Abate, A.; Sadhanala, A.; Yao, S.; Chen, Y.; Friend, R. H.; Estroff, L. A.; Wiesner, U.; Snaith, H. J. *Nat. Commun.* **2015**, *6*, 6142.

(140) Hsieh, T.-Y.; Wei, T.-C.; Wu, K.-L.; Ikegami, M.; Miyasaka, T. *Chem. Commun.* **2015**, *51*, 13294.

(141) Bai, S.; Sakai, N.; Zhang, W.; Wang, Z.; Wang, J. T. W.; Gao, F.; Snaith, H. J. *Chem. Mater.* **2017**, *29*, 462.

(142) Ling, L.; Yuan, S.; Wang, P.; Zhang, H.; Tu, L.; Wang, J.; Zhan, Y.; Zheng, L. *Adv. Funct. Mater.* **2016**, *26*, 5028.

(143) Pool, V. L.; Gold-Parker, A.; McGehee, M. D.; Toney, M. F. *Chem. Mater.* **2015**, *27*, 7240.

(144) Noel, N. K.; Abate, A.; Stranks, S. D.; Parrott, E. S.; Burlakov, V. M.; Goriely, A.; Snaith, H. J. *ACS Nano* **2014**, *8*, 9815.

(145) Ball, J. M.; Lee, M. M.; Hey, A.; Snaith, H. J. *Energy Environ. Sci.* **2013**, *6*, 1739.

(146) Zhu, L.; Xu, Y.; Zhang, P.; Shi, J.; Zhao, Y.; Zhang, H.; Wu, J.; Luo, Y.; Li, D.; Meng, Q. *J. Mater. Chem. A* **2017**, *5*, 20874.

(147) He, J.; Chen, T. *J. Mater. Chem. A* **2015**, *3*, 18514.

(148) Chen, Y.; Zhao, Y.; Liang, Z. *J. Mater. Chem. A* **2015**, *3*, 9137.

(149) Fei, C.; Li, B.; Zhang, R.; Fu, H.; Tian, J.; Cao, G. *Advanced Energy Materials* **2016**, 1602017.

(150) Guo, Y.; Shoyama, K.; Sato, W.; Matsuo, Y.; Inoue, K.; Harano, K.; Liu, C.; Tanaka, H.; Nakamura, E. *J. Am. Chem. Soc.* **2015**, *137*, 15907.

2 CHARACTERIZATION

2.1 X-RAY DIFFRACTION (XRD)

XRD is an important tool to obtain information about the crystal structure and crystallinity of a material. X-rays are generated via an electron beam targeting on a pure metal anode contained in a vacuum tube. Therefore, ground state electrons from the atoms of the target material are ejected, and holes are created. The emission of the X-rays is initiated by the refilling the ground state with the created holes. Copper or molybdenum are common anode materials with the emission of characteristic X-rays at λ = 0.154 nm for Cu-$K_{\alpha 1}$ and λ = 0.702 nm for Mo-$K_{\alpha 1}$. If these X-rays are directed onto the sample, they are diffracted by crystalline phases in the sample according to Bragg's law. Bragg's law describes the condition for constructive interference and is shown in *Equation 2 – 1* and the schematic of the process in *Figure 2 - 1*. The resolution of this technique is given by measurable angles between 0.5° 2θ and 100° 2θ, which correlate to lattice spacings of 0.1 nm to 20 nm.[1]

$$n\lambda = 2d\ sin(\theta) \qquad \text{(Equation 2 – 1)}$$

d = spacing between the atomic planes; λ = wavelength of the X-rays; θ = incident angle

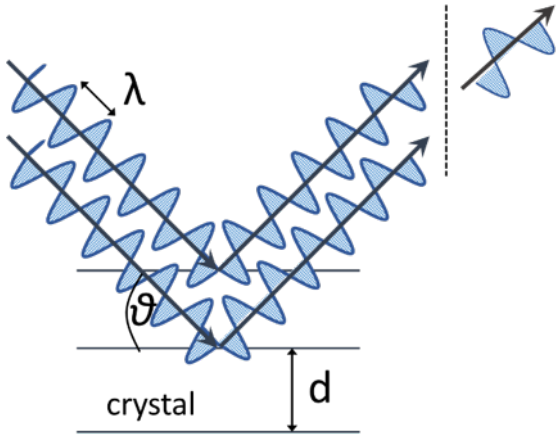

Figure 2 - 1: Diffraction process according to the Bragg's law.

2.2 GRAZING-INCIDENCE-WIDE ANGLE X-RAY SCATTERING (GIWAXS)

The principle of GIWAXS is similar to traditional X-ray diffraction, except that the incident X-ray wave vector k_i is kept at a grazing angle with respect to the sample surface to minimize the undesired background scattering (both elastic and inelastic) emanating from the bulk, and to enhance the near-surface scattering. The grazing incidence geometry is shown in *Figure 2 – 2*.

This technique captures a two-dimensional slice through reciprocal space, allowing the reconstruction of the structure and extraction of information on the orientation of the crystal planes from azimuthal intensity distribution.[2-4] Wide angle scattering allows probing the order at the atomic scale, which is the typical technique to probe the crystallographic lattice of nanostructures. In wide-angle scattering, the incident angle α_i and angle of total reflection α_f are very small, such that the scattering plane is nearly parallel with the surface and the diffracting lattice planes are perpendicular to it. Since the scattering geometry is defined by the incident beam and detector directions, a long-range periodicity parallel with the surface is probed.

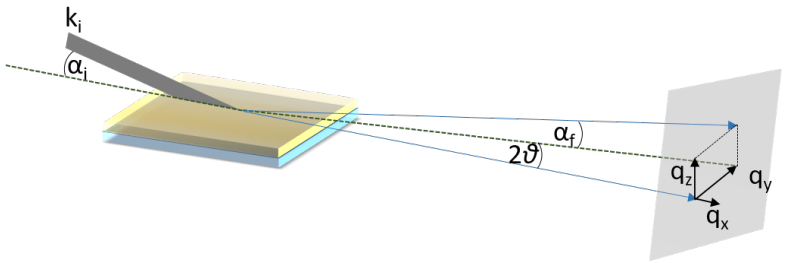

Figure 2 - 2: Grazing incidence X-ray scattering geometry, at wide angles.

In GIWAXS the angular coordinates are related to the wavevector transfer coordinates according to:

$$q_x = k_0\left[\cos(2\theta_f)\cos(\alpha_f) - \cos(\alpha_i)\right] \quad \text{(Equation 2 – 2)}$$

$$q_y = k_0\left[\sin(2\theta_f)\cos(\alpha_f)\right] \quad \text{(Equation 2 – 3)}$$

$$q_z = k_0\left[\sin(\alpha_f) + \sin(\alpha_i)\right] \quad \text{(Equation 2 – 4)}$$

$$k_0 = 2\,{}^{\pi}/_{\lambda} \quad \text{(Equation 2 – 5)}$$

q = wavevector transfer; k_0 = elastically conserved wave vector modulus; 2θ = scattering angle; α_f = angle of total reflection; α_i = incident angle; λ = is the X-ray wavelength.

The intensity measured by X-ray scattering techniques depends on the angular coordinates α_i, α_f, and $2\theta_f$. The coordinates allow building the intensity distribution in reciprocal space. If the out-of-plane and in-plane vectors differ in comparison, an independent analysis of structural properties of nanostructures such as strain, composition, and shape, without interference with the substrate is possible.[5]

2.3 SCANNING ELECTRON MICROSCOPY (SEM)

SEM is an imaging technique of a sample surface with a focused beam of electrons and gives information on topography or sample composition. This technique is capable of imaging at a

significantly higher resolution than light microscopes, due to the significantly smaller de Broglie wavelength of electrons. Here, an electron beam is scanned across the sample creating either backscattered or secondary electrons, which are then detected. The difference in the number of detected electrons at different scan positions enables the visualization of an image in the cathode-ray tube.

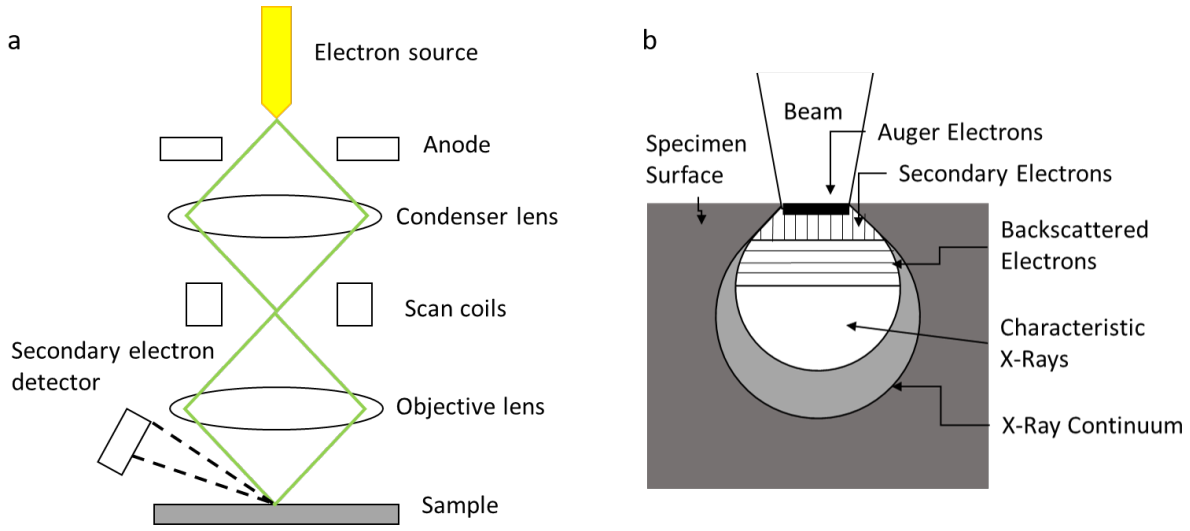

Figure 2 - 3: a) Schematic representation of basic SEM components; b) the interaction volume of an electron beam on the sample.

Two different electron source types can be used for SEM, either a thermal emitter or a field emission gun. Thus, emission of electrons is activated either thermally or with a high electrical field from a source, such as a tungsten cathode in a vacuum. Afterward, the electrons are directed to the anode. Due to electromagnetic lenses, an inhomogeneous magnetic field is created which focuses the electrons that are then scanned across the sample. The schematic of the SEM setup is shown in *Figure 2 – 3a*. If the electrons target the sample, different interactions can occur, see *Figure 2 – 3b.* The significant interactions for imaging in SEM are backscattered and secondary electrons. For electron detection, semiconductor detectors or scintillator-photomultiplier detectors are used. For example, in a semiconductor detector, a doped Si single crystal with a p-n-junction beneath the surface creates electron-hole pairs upon electron illumination. An external field or voltage is applied to separate the charge carriers, and the signal is detected and monitored. A scintillator-photomultiplier detector accelerates the electrons into the scintillator, converts the generated photons back to electrons and cascades the electrons in the photomultiplier, thus creating the signal.[6]

2.4 TRANSMISSION ELECTRON MICROSCOPY (TEM)

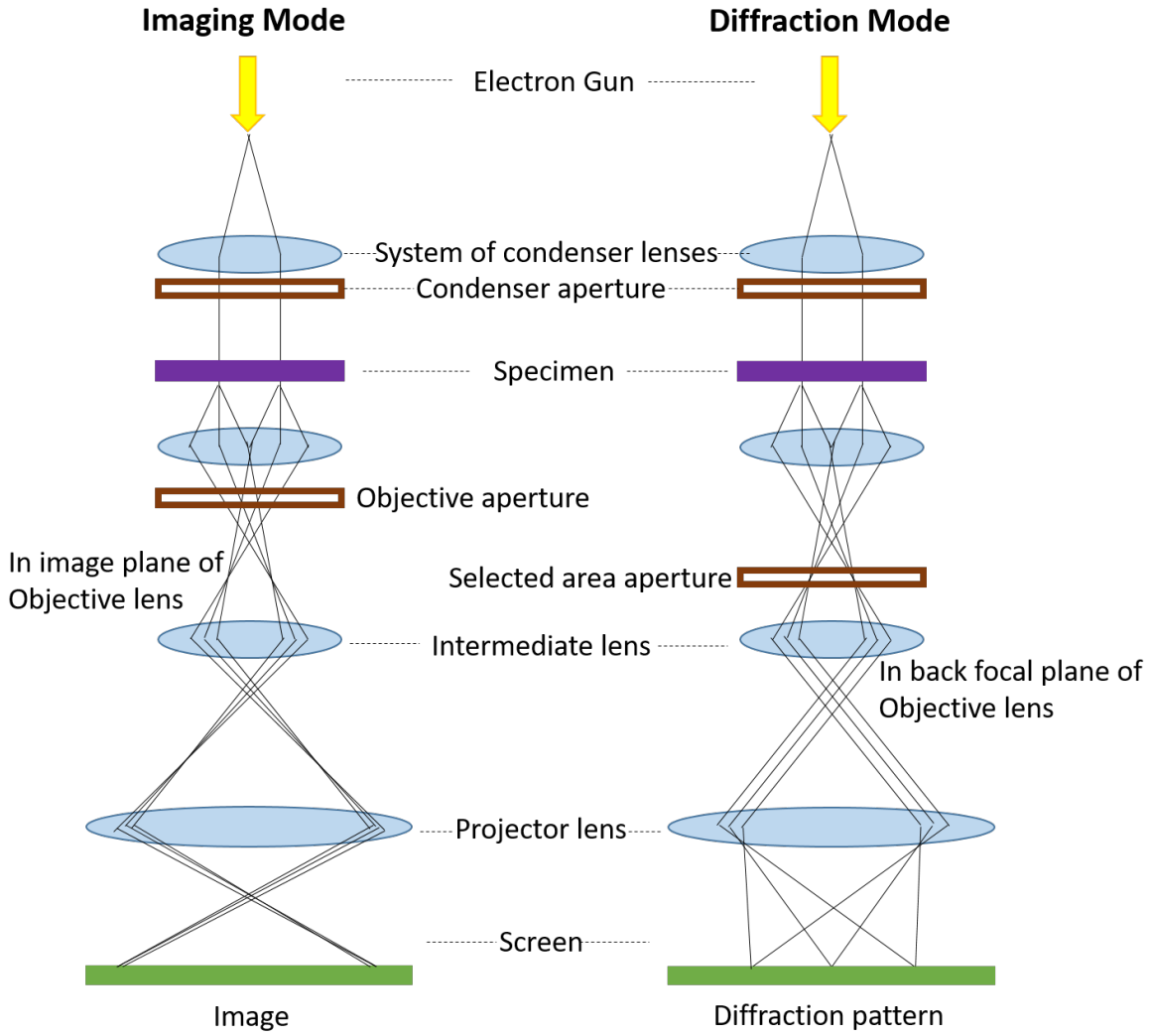

Figure 2 - 4: Schematic view of imaging and diffraction modes in TEM.

The working principle of TEM is very similar to SEM. In TEM transmitted electrons are projected onto an area detector to form an image. Here, thin samples (less than 100 nm thickness) are required, and this technique has a much higher resolution than SEM. Additionally, in contrast to classical SEM, TEM provides both image and diffraction information of the sample. The schematic view of the two different modes, which only differ in the imaging mode of the intermediate lens, is shown in *Figure 2 – 4*. For both modes, the sample is illuminated with the parallel electron beam, which is formed by condenser lenses and a condenser aperture. Either the transmitted electrons that remain un-scattered or are scattered due to interactions with the sample are detected. Inelastic scattering originates from interactions between the primary beam and the electrons of the sample, which is caused by heterogeneities like composition, morphology, etc. Therefore, electrons with various intensities are detected and are used for imaging. The diffraction information on the sample can be acquired with

elastically scattered electrons, which exhibit no energy loss. With this technique, the crystal structure can be analyzed together with the morphology.[7]

2.5 UV-VIS ABSORPTION SPECTROSCOPY

UV-vis spectroscopy is a method to determine the light absorption behavior of molecules in solution or of the bulk material. To this end, a spectrometer contains a light source, a monochromator, a sample holder and a detector. To generate a continuous spectrum, a deuterium arc lamp for the UV region and a tungsten filament or a xenon arc lamp for the visible region are usually used as light sources. The monochromator disperses the light to create a wavelength-resolved spectrum. Finally, a signal is detected by a photomultiplier, a photodiode array or a charge-coupled device.

During the measurement, the sample is illuminated. In the case of bulk materials like thin films, the measurement is dependent on the type of the incident beam and the detector. In this work transmission and reflectance of the films were measured. For the transmission measurement, the background of the substrate was subtracted, and the sample was pointed with the glass side towards the incident light. For the reflectance measurement, the background was measured with a white standard, and the sample was pointed with the film side towards the light. To eliminate the absorption of the substrate, also the transmission and reflectance were measured for each clean substrate type. To calculate the absorption from the first path of the light, *Equation 2 – 6* was used:

$$Abs\%_{PK1} = 100\% - T\% - R\% - Abs\%_{Sub} \qquad \text{(Equation 2 – 6)}$$

$Abs\%_{PK1}$ = absorption from the first path of the perovskite; T% = transmission; R% = Reflectance; $Abs\%_{SUB}$ = absorption of the substrate.

Due to the additional reflectance of the substrate during the transmission measurement, the absorption of the second path from *Equation 2 – 7* needs to be calculated to obtain the absolute absorption.

$$Abs\%_{PK2} = (100 - R\% - Abs\%_{Sub} - Abs\%_{PK1}) \cdot \frac{Abs\%_{PK1}}{100} + Abs\%_{PK1} \qquad \text{(Equation 2 – 7)}$$

$Abs\%_{PK2}$ = absorption from the second path; $Abs\%_{PK1}$ = absorption from the first path of the perovskite; T% = transmission; R% = Reflectance; $Abs\%_{SUB}$ = absorption of the substrate.

To derive the theoretical maximum current possible from the analyzed perovskite layers, we integrated the Spectrum of $Abs\%_{PK2}$.

2.6 PHOTOTHERMAL DEFLECTION SPECTROSCOPY (PDS)

PDS is a very sensitive and powerful technique to study the optical absorption of thin samples. With this technique, the change in refractive index of the sample is mainly measured. The change occurs with the heating of the medium due to absorption of the optically exciting beam and also causes a refractive index gradient in a thin layer adjacent to the sample surface. Therefore, the probe laser is refracted or bent proportional to the temperature gradient of the transparent medium near the surface. With a second beam, the deflection of the varying refractive index can be related to the optical absorption of the sample.

PDS can be performed in two variations, in collinear or transverse photothermal deflection. In the first, the gradient of the refractive index is both created and probed within the sample. For samples with the poor optical quality, the transverse photothermal deflection is more suitable since the probing of the gradient of the refraction index is accomplished in the thin layer adjacent to the sample.[8]

2.7 STEADY STATE PHOTOLUMINESCENCE (SSPL)

Photoluminescence (PL) spectroscopy is a method to analyze the photoactive material. Here, photons are used to excite the electronic states in the material and light is emitted at a wavelength specific for the material according to relaxation of the excited states.

Typically, the light source is a laser which operates in a wavelength region in which the sample absorbs photons efficiently. After the excitation of the electrons to a higher energy level, the system undergoes a fast non-radiative relaxation to a more stable excited level in which it stays for a characteristic lifetime in an excited state. Afterward, a radiative relaxation is released while the electron is returning to the ground state. Due to the non-radiative relaxation, the emitted light has longer wavelengths (lower energy) than the incident light. A fast PL emission is called fluorescence and a slow PL emission with a lifetime of 10^{-4} to 10 s is called phosphorescence, following a different relaxation mechanism. The emission of the sample is passed through an optical spectrometer to the photon detector.[9]

2.8 TIME-CORRELATED SINGLE PHOTON COUNTING (TCSPC)

If the sample emits photoluminescence, the lifetime of this emission can be analyzed with TCSPC to gain information on the recombination mechanism. Here, pulsed laser light excites the sample at a fixed repetition rate. Data collection of the number of detected photons provides a fluorescence decay profile. This technique is based on repetitive and precise time registration

of single photons, which are stored in a histogram. The time is here referred to the moment of the excitation pulse. The detection of a single photon is necessary to guarantee an accurate time-decay with the histogram, in which the x-axis represents the time difference whereas the y-axis is the number of photons detected in this period between laser pulses, as shown in *Figure 2 - 5*. After the data collection is complete, the histogram represents a waveform of the decay. With the decay data obtained during the measurement, the actual lifetime of excitons or charges before recombination can be fitted with appropriate models. The typical result in time-resolved fluorescence experiments is a histogram with an exponential drop of counts towards later times.

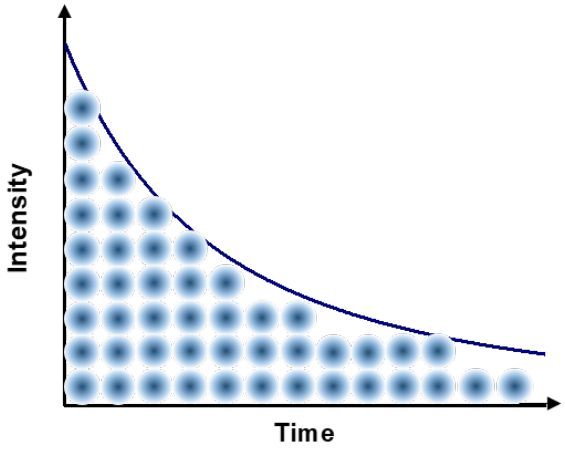

Figure 2 - 5: Schematic illustration of the number of photons counted with increasing time and its resulting typical PL decay curve.

In this study, the PL decay data were fitted according to the calculations below:

In *Equation 2 – 8* and *2 – 9* the recombination dynamics are described.

$$\mathrm{d}n(t)\mathrm{dt} = -k_3 n^3 - k_2 n^2 - k_1 n^1 \qquad \text{(Equation 2 – 8)}$$

$$n = \tilde{n} \cdot \emptyset \qquad \text{(Equation 2 – 9)}$$

n = carrier density; Ø = PL quantum yield; ñ = number of charge carriers; k3 = decay constants of Auger recombination; k2 = of bimolecular recombination; k1 = monomolecular process.

In the case of bimolecular recombination, the charge carrier dynamics can be represented by *Equation 2 – 10* and fitted with *Equation 2 – 11*.

$$\mathrm{d}n(t)\mathrm{dt} \approx -k_2 n^2 \qquad \text{(Equation 2 – 10)}$$

$$f(t) = 1a + bt \qquad \text{(Equation 2 – 11)}$$

a = parameter; b is equal to Øk₂

The monomolecular recombination can be represented by *Equation 2 – 12* and fitted with *Equation 2 – 13*.

$$\mathrm{d}n(t)\mathrm{dt} \approx -k_1 n^1 \qquad \text{(Equation 2 – 12)}$$

$$f(t) = at \qquad \text{(Equation 2 – 13)}$$

a is equal to Øk_1

The calculation of k_1 or k_2 is possible if the PLQY is known.[10]

2.9 ELECTROLUMINESCENCE (EL)

The electroluminescence spectroscopy is used to analyze luminescence properties of materials, under an applied electric field or current. Excited electrons release the energy as photons during the recombination with holes, and therefore the sample emits light through electroluminescence at specific wavelengths.[11]

2.10 CURRENT-VOLTAGE MEASUREMENTS

This chapter is based on the publication [12] and [13]. Photovoltaic devices are characterized via a current(density)-voltage (*JV*)-curve. The most important parameters describing the *JV*-curve from *Figure 2 – 6* are the power conversion efficiency (PCE), the open-circuit voltage (V_{OC}) and the short-circuit current density (J_{SC}). For convenience, the current density is often simply referred to as current.

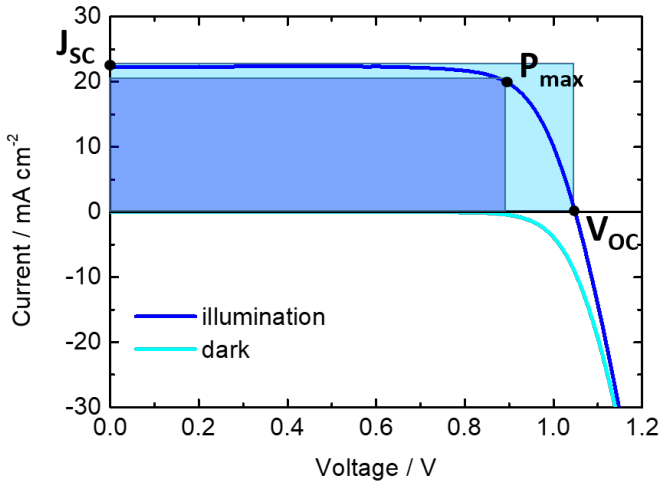

Figure 2 - 6: Typical *JV*-curve of perovskite-based devices.

The maximum limit for the J_{SC} is given by the photogenerated current density J_{Ph}. At zero ohmic losses $J_{Ph} = J_{SC}$ applies. V_{OC} is dependent on the Fermi levels of the hole- and electron

selective layers and also depends on the charge recombination rate. The fill factor (*FF*) defines the shape of the *JV*-curve and gives information on the ideality of the device, which is 100 % if the curve would exhibit a rectangular shape. In *Equation 2 – 11* the mathematical expression for the *FF* is shown.

$$FF = \frac{I_{max}V_{max}}{I_{SC}V_{OC}} \qquad \text{(Equation 2 – 11)}$$

$I_{max}V_{max} = P_{max}$ *(maximum power output)*

The resulting power conversion efficiency is defined in *Equation 2 – 12*, where P_{in} is the power input:

$$PCE = \frac{J_{SC}V_{OC}FF}{P_{in}} \qquad \text{(Equation 2 – 12)}$$

2.11 TIME OF FLIGHT MEASUREMENTS (TOF)

ToF is an experimental technique for mobility measurements and most established in organic disordered systems, such as polymers. A schematic of the experimental ToF setup is shown in *Figure 2 – 7*. This technique is based on the measurement of the carrier transit time (τ). The transit time is the time required of photogenerated charge carriers near one electrode to drift to the other electrode under an applied electric field. The charges are generated by short pulsed light irradiation at a wavelength falling into an absorption band of the material. Since the charges are created locally near one electrode, the polarity of the applied E-field defines whether electron- or hole-transport across the material is observed.

The electrode configuration is most commonly in a vertical configuration with top- and bottom electrodes and the transit time is measured with respect to the film thickness of the analyzed material. However, perovskite-based material crystallization is restricting the film thickness to usually below 500 nm, which can lead to transit times below the resolution limit of our employed setup (~2 ns). [14] Therefore, we used a sample architecture with varying electrode spacing *d*, as shown in *Figure 2 – 7*. We used a sample layout with laterally contacted electrodes with spacing *d* in the range of 20 µm to 80 µm.

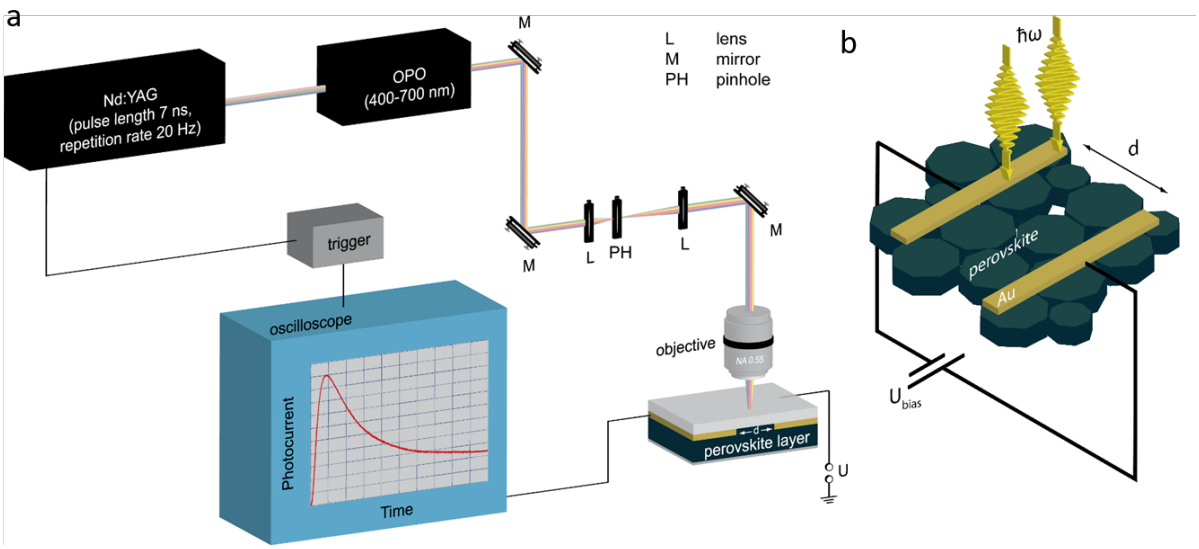

Figure 2 - 7: a) Scheme of the experimental ToF setup; b) scheme of lateral device architecture.

The charge carrier mobilities can be derived from *Equation 2 – 13* determined by the different electrode spacing *d*:[15]

$$\mu = \frac{d}{E\tau} \qquad \text{(Equation 2 – 13)}$$

μ= carrier drift mobility; E = applied electric field; τ = transit time; d = electrode spacings

2.12 LITERATURE

(1) *Proceedings of the Royal Society of London. Series A* **1913**, *88*, 428.

(2) Saliba, M.; Tan, K. W.; Sai, H.; Moore, D. T.; Scott, T.; Zhang, W.; Estroff, L. A.; Wiesner, U.; Snaith, H. J. *J. Phys. Chem. C* **2014**, *118*, 17171.

(3) Giesbrecht, N.; Schlipf, J.; Oesinghaus, L.; Binek, A.; Bein, T.; Müller-Buschbaum, P.; Docampo, P. *ACS Energy Letters* **2016**, *1*, 150.

(4) Müller-Buschbaum, P. *Adv. Mater.* **2014**, *26*, 7692.

(5) Renaud, G.; Lazzari, R.; Leroy, F. *Surf. Sci. Rep.* **2009**, *64*, 255.

(6) Goldstein, J. I.; Newbury, D. E.; Michael, J. R.; Ritchie, N. W. M.; Scott, J. H. J.; Joy, D. C. *Scanning Electron Microscopy and X-Ray Microanalysis*; Springer-Verlag New York, 2018; Vol. 4.

(7) Fultz, B.; Howe, J. M. *Transmission Electron Microscopy and Diffractometry of Materials*; 4 ed.; Springer-Verlag Berlin Heidelberg, 2013.

(8) Jackson, W. B.; Amer, N. M.; Boccara, A. C.; Fournier, D. *Appl. Opt.* **1981**, *20*, 1333.

(9) Perkowitz, S. *Optical characterization of semiconductors: infrared, raman, and photoluminescence spectroscopy*; Academic Press, 1993.

(10) O'Connor, D. V.; Phillips, D. *Time-correlated single photon counting*; Academic Press, London, 1984.

(11) Ivan Pelant; Valenta, J. *Luminescence Spectroscopy of Semiconductors*; Oxford University Press, 2016.

(12) Bucher, E. *Appl. Phys.* **1978**, *17*, 1.

(13) Shah, A.; Torres, P.; Tscharner, R.; Wyrsch, N.; Keppner, H. *Science* **1999**, *285*, 692.

(14) Grill, I.; Aygüler, M. F.; Bein, T.; Docampo, P.; Hartmann, N. F.; Handloser, M.; Hartschuh, A. *ACS Applied Materials & Interfaces* **2017**, *9*, 37655.

(15) Tiwari, S.; Greenham, N. C. *Optical and Quantum Electronics* **2009**, *41*, 69.

3 SYNTHESIS OF PERFECTLY ORIENTED AND MICROMETER-SIZED $MAPbBr_3$ PEROVSKITE CRYSTALS FOR THIN FILM PHOTOVOLTAIC APPLICATIONS

This chapter is based on the following publication:

Nadja Giesbrecht, Johannes Schlipf, Lukas Oesinghaus, Andreas Binek, Thomas Bein, Peter Müller-Buschbaum, Pablo Docampo *ACS Energy Lett.* **2016**, *1*, 150-154.

3.1 INTRODUCTION

Perovskite-based solar-cell development has been very impressive with power conversion efficiencies already exceeding 20 % after only a few years of development.[1] This fast development can be attributed to the excellent properties of the perovskite material, mainly its very high absorption coefficient[2] and long charge carrier diffusion length.[3,4] Furthermore, the perovskite material is easy to process from solution, with no high-temperature steps required.[5] Although alternatives based on the exchange of iodide for bromide are interesting for applications in multijunction and photoelectrochemical devices, their fabrication has not been studied in detail.[6-9] Bromide-based compounds are interesting since they exhibit a wider bandgap of approximately 2.3 eV and thus can achieve much higher values compared to the iodide counterpart.[6,8]

To date, the most efficient devices employing methylammonium lead bromide ($MAPbBr_3$) utilize a mesoscopic titania scaffold as the electron extraction layer.[6,8] However, a planar architecture provides higher flexibility for device optimization, multijunction construction and thus can be employed in a wider variety of applications.[10,11] The main challenges for planar heterojunction solar cells, which we will focus on, are the perovskite film coverage, grain size, and crystal orientation.[12]

Recent studies have highlighted the importance of the perovskite morphology, which determines to a large extent the performance of the final device.[13] In particular, further understanding of the crystallization processes has been the driving force behind the recent impressive device performance improvements in the iodide perovskite system.[14-17] Thus, a wide

variety of deposition techniques has been developed, such as the fast deposition-crystallization procedure, vapor-assisted solution process, or the interdiffusion of solution-processed precursor stacking layers, respectively.[13,18,19] To improve the solar cell performance in the bromide perovskite system, a similar improvement in morphology is expected to be necessary.

Recently, we have highlighted the importance of perovskite crystal orientation in the performance of the assembled devices.[20] A higher degree of preferential orientation of the crystallites in the perovskite film generally leads to higher device photocurrents and more reproducible solar cells overall.[20] Therefore, further understanding on the crystallization process for the bromide system will not only provide a path to enhanced performance with higher voltages of this system but will also give insights applicable to other hybrid halide perovskite structures.

In this work, we introduce a new synthesis approach for $MAPbBr_3$ and incorporate this material into a planar device structure. We achieve extended control over crystallization such that the perovskite film exhibits densely packed and highly-ordered grains with crystallite sizes between 5 and 10 µm. We present the first grazing-incidence wide-angle X-ray scattering (GIWAXS) investigation of the $MAPbBr_3$ perovskite and the highest orientation of the crystallites in a perovskite film ever reported for this family of materials. Such highly-ordered crystallites, in combination with the perovskite film quality in solar devices, maximize the charge collection efficiency leading to internal quantum efficiencies of over 95%.

3.2 RESULTS AND DISCUSSION

In order to understand the impact of morphology and crystal orientation of methylammonium lead bromide based solar cells, we have prepared films via the state-of-the-art spin-coating the $PbBr_2$ and MABr precursors from γ-butyrolactone:dimethylsulfoxide solution (BD),[8] vapor-assisted solution process (VASP)[18] and via spin-coating from a lead acetate precursor, which we have termed controlled solvent drying (CSD). To deposit the perovskite via the state-of-the-art process, referred to as BD from here on, we spin-coated the perovskite from the precursor solution and added toluene during the spin-coating process with a subsequent heating step.[8] The deposition steps for the VASP technique are illustrated in *Figure 3 – 1b*. In this case, an initial lead bromide layer is deposited directly on TiO_2-coated ITO substrates and afterward converted to the perovskite phase with methylammonium bromide (MABr) vapor.[18]

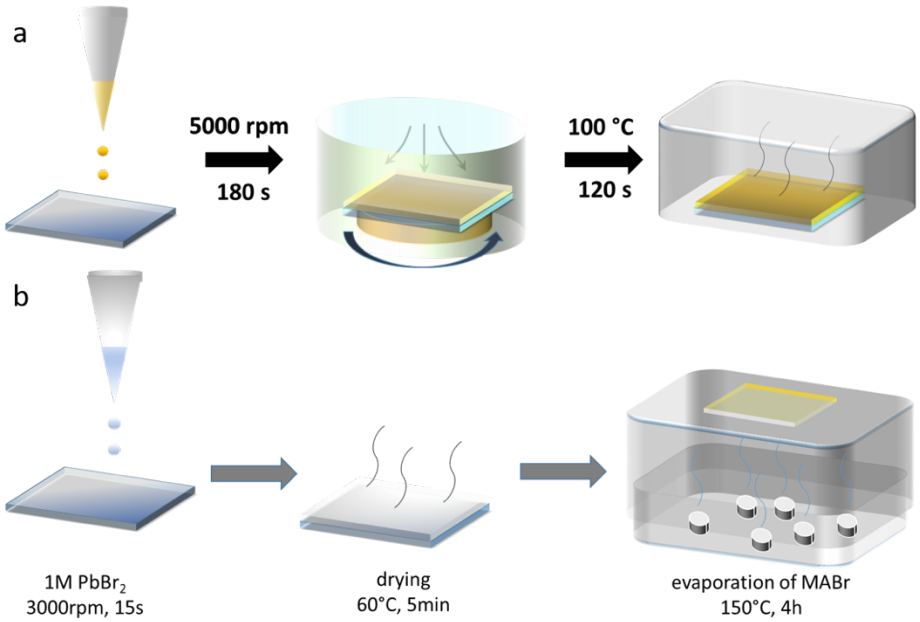

Figure 3 - 1: a) Schematic illustration of the perovskite-layer synthesis approach via CSD; b) Schematic illustration of the perovskite-layer synthesis approach via evaporation; first: $PbBr_2$ was deposited via spin-coating; second: the $PbBr_2$ film was dried on a hotplate; third: conversion of the $PbBr_2$ to the perovskite in a MABr vapor.

In *Figure 3 – 1a* we show a schematic illustration of the deposition-route via the CSD process. Our approach involves two stages wherein the solution of $Pb(Ac)_2$ and MABr precursors is spin-coated in a nitrogen-rich environment and is annealed under a glass cover. Here, we find that control of the solvent atmosphere during the whole crystallization process is crucial to maximizing crystal size. In particular, films undergo gentle solvent annealing during the 3 minute spin-coating process as a result of the solvent coating the walls of the spin-coater. To achieve high-quality films, an excess of solvent in the spin-coater must be removed between samples. Exposure to too much solvent or traces of alcoholic solvents such as methanol leads to secondary nucleation and inhomogeneous films, as shown in *Figure 3 – 2*.

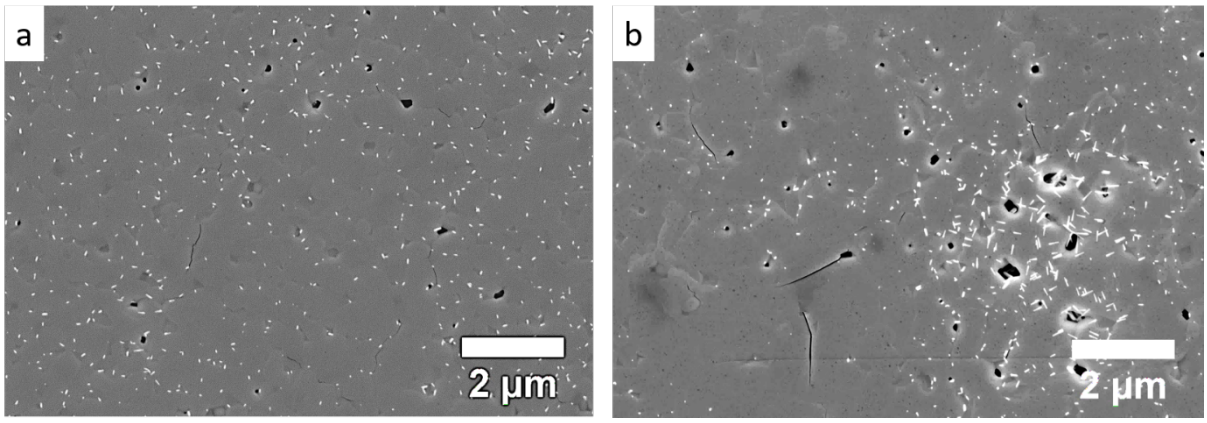

Figure 3 - 2: SEM top views of $MAPbBr_3$ perovskite films deposited via CSD; a) film deposited with an excess of perovskite solution, b) film deposited in a MeOH containing environment in the glove-box.

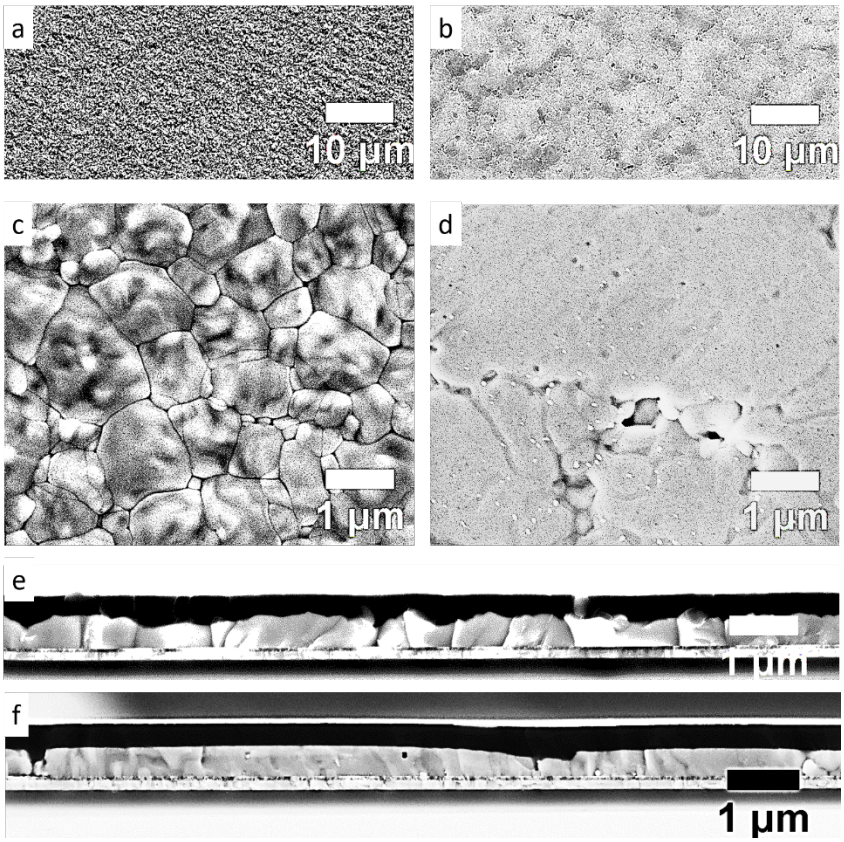

Figure 3 - 3: SEM top-view and cross-sectional images of $MAPbBr_3$ perovskite-film a, c, e) deposited on a TiO_2/ITO substrate by VASP, and b, d, f) deposited on TiO_2/ITO by spin-coating with a lead acetate precursor.

In *Figure 3 – 3a, c, e* we illustrate the morphology of the perovskite films prepared via VASP which has been shown in previous studies to achieve high performance when employed in solar cells.[7,21] This morphology is comparable with the state-of-the-art films deposited on a mesoporous scaffold with full surface coverage and grain sizes of approximately 1 µm and is similar to that achieved for the iodide system.[18,21] On the other hand, films deposited via the CSD method are very smooth and also achieve full surface coverage with large crystals between 5 and 10 µm, as shown in *Figure 3 – 3* and *3 – 4a*. We have also prepared films through the BD process, as shown in *Figure 3 – 5*. In this case, the crystal sizes are very small, in the range of 100 nm.[8]

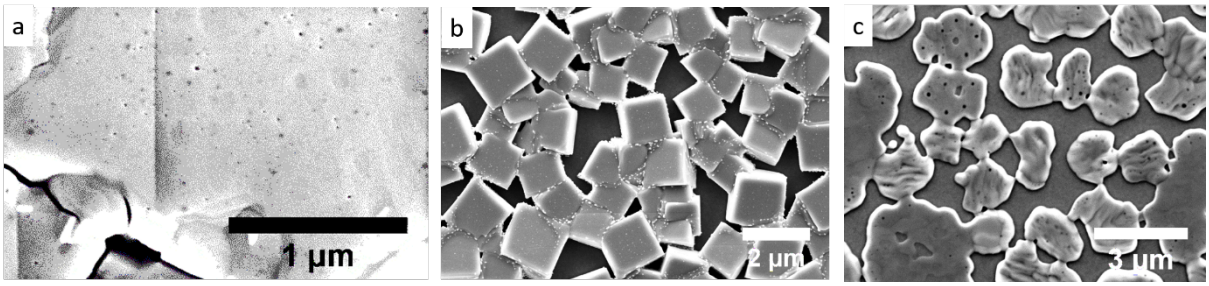

Figure 3 - 4: a) SEM images of $MAPbBr_3$ perovskite films deposited via CSD, b) SEM top-view of $MAPbBr_3$ perovskite-film deposited by spin-coating from lead acetate precursor with a short spin-coating duration of 30 s, c) SEM top view of $FAPbBr_3$ deposited with the CSD method on TiO_2/ITO coated glass.

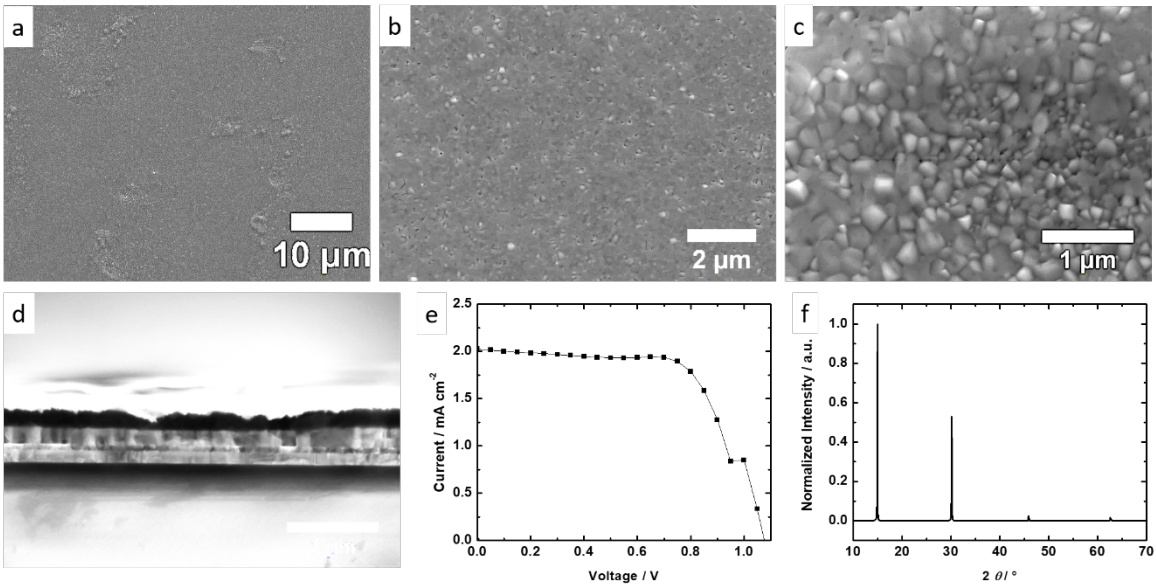

Figure 3 - 5: SEM images of $MAPbBr_3$ perovskite films deposited via the state-of-the-art BD method; a,b,c) top view on a film prepared on ITO, d) cross-sectional image of a solar cell device prepared on ITO, e) J-V curve under AM 1.5 solar irradiation conditions of the best performing device, f) XRD pattern normalized to the reflex at 2 ϑ = 14.9 °.

We attribute the full surface coverage and large grain size to our newly developed synthesis approach, which results in improved control over the crystallization of the perovskite. Low volatile solvents, such as dimethylformamide (DMF) are good candidates to grow large crystals at temperatures around 100 °C. However, achieving perovskite films with full surface coverage is challenging.[22,23] In our developed CSD method $Pb(Ac)_2$ and MABr react to form the perovskite structure, and the excess organic components react to form methylammonium acetate, methylamine, and acetic acid. All the expected organic components formed during the reaction are liquid at room temperature which keeps the films wet during the process. This in turn likely allows a certain degree of precursor mobility and enables the very large and highly oriented crystal growth observed in the final films. Further evidence that this is the case is given by the structurally related formamidinium lead halide perovskite ($FAPbX_3$). Here, a solid formamidinium acetate salt is formed, and thus the films completely dry within the spin-coating

step. In turn, this results in the formation of a non-continuous perovskite film with large voids between the crystals (see *Figure 3 – 4*).

To further investigate the crystalline quality of the films with the large domains, X-ray diffraction (XRD) experiments were performed for both CSD and VASP derived films. The X-ray patterns, shown in *Figure 3 - 6a*, confirm for both films a phase-pure $MAPbBr_3$ compound crystallized in the cubic $Pm\bar{3}m$ structure type. However, most of the reflections for the CSD sample are not present, which indicates a high degree of crystal orientation. A good tool to fully determine this parameter is grazing incidence wide-angle X-ray scattering (GIWAXS) which captures a two-dimensional slice through reciprocal space, allowing the reconstruction of the crystal structure and extraction of information on the orientation of the crystal planes from the azimuthal intensity distribution.[24,25] In *Figure 3 – 6b* and *3 – 6d* we show GIWAXS data for VASP and CSD derived perovskite films. For VASP films, very homogeneous rings with no pronounced peaks are found. This implies no preferential orientation of the crystallites in the perovskite film. In contrast, films fabricated via the CSD process show very intense Bragg peaks and no rings. This implies that all crystallites are very well oriented with the (001) planes parallel to the glass substrate. This is remarkable for a thin polycrystalline film processed from solution. The orientation distribution is shown schematically in *Figure 3 – 6c*. We suggest that such a high degree of order is derived from the pre-crystallization step in the presence of a solvent layer on top. We note that a similar effect was observed for the iodide system when an ionic liquid was used to crystallize the perovskite.[26]

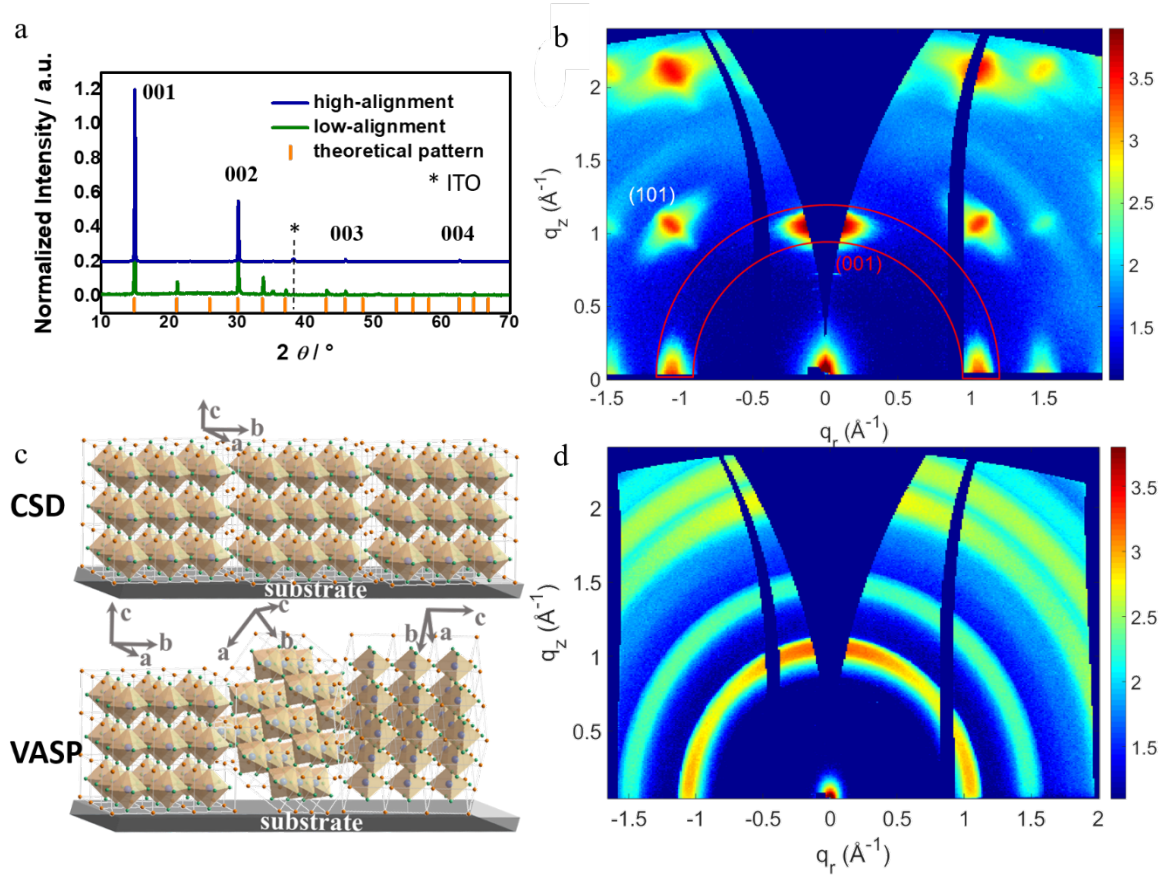

Figure 3 - 6: a) XRD patterns normalized to the reflex at 2 ϑ = 14.9 °, perovskite-film prepared via CSD and via VASP and the theoretical pattern, b) 2D GIWAXS patterns of the sample produced via CSD ((001) and (101) peaks are marked in red and white, respectively. The data are corrected as outlined in the experimental section.), c) schematic illustration of the crystal orientation of the perovskite film prepared via CSD and disorder of the film prepared via VASP, d) 2D GIWAXS pattern of the sample produced via VASP.

To correlate the effect of morphology and crystal orientation with the solar cell performance, we prepared devices with the developed perovskite layer in the standard device configuration, employing TiO_2 and Spiro-OMeTAD as the charge extraction layers, as shown schematically in *Figure* 3 - 6a. To exclude variations in the optical absorption of the films due to different perovskite film thicknesses, we have fixed this value for both techniques to 350 nm. The corresponding photovoltaic performance for perovskite films deposited via CSD and VASP is shown in *Figure 3 – 7* and the data are summarized in *Table 3 – 1*. In general, the performance of devices employing VASP-derived films is lower compared to those employing CSD-derived films. In *Figure 3 – 7c, 7d* and in *Figure 3 – 8* we show the distribution of the photovoltaic performance for the fabricated devices. The difference in device performance may arise from the different crystallization processes of the film leading to disparities in perovskite surface and defect density. However, the VASP technique leads to the highest performance reported,[21] thus we expect the number of defects to not be the major factor behind the variation in device performance.

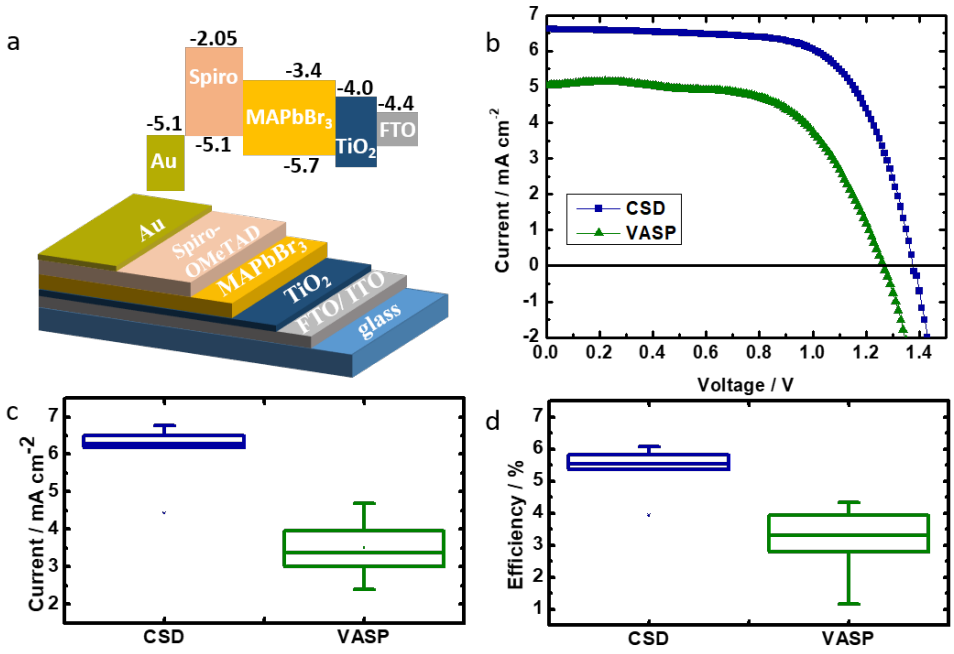

Figure 3 - 7: a) Scheme of the regular solar cell layout and energy diagram, b) J-V curves under AM 1.5 solar irradiation conditions for solar cell employing $MAPbBr_3$ derived from CSD or VASP processes, c) photocurrent and d) efficiency box plots of 20 devices employing VASP- or CSD-derived perovskite films. The edges of the box represent the 25/75 percentile, while the horizontal line represents the median value. Whiskers represent the minimum and maximum values.

Method	V_{OC} / V	J_{SC} / mA cm^{-2}	FF / %	PCE / %
CSD	1.38	6.60	67	6.08
VASP	1.26	5.05	62	4.00

Table 3 - 1: Photovoltaic performance data of devices employing CSD- or VASP-derived perovskite films.

Here, devices employing perfectly oriented perovskite films, derived via the CSD process, exhibit photocurrents between 6 and 7 mA cm^{-2}, which is twice the average value found for devices employing non-oriented perovskite crystals, prepared via the VASP process. We note that the theoretical limit for the short-circuit current extracted from light absorption measurements on devices is 7.15 mA cm^{-2} which implies an internal quantum efficiency of over 95% (c.f. *Figure 3 – 8*).

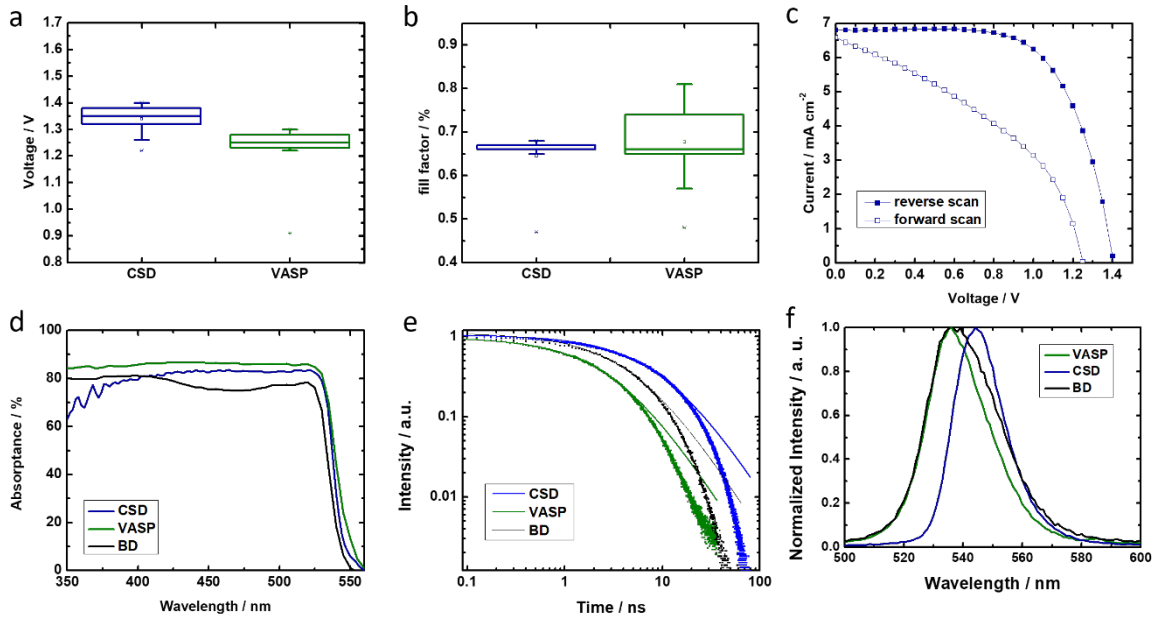

Figure 3 - 8: Distribution of device performance data of 20 devices with perovskite films prepared via VASP or spin-coating from a lead acetate precursor (CSD), a) open circuit voltage, b) fill factor, c) forward and reverse scanning results for solar cells employing $MAPbBr_3$ derived from CSD, d) Absorptance of $MAPbBr_3$ prepared via VASP or spin-coating from lead acetate precursor, e) PL decay curves for $MAPbBr_3$ prepared via VASP or spin-coating from lead acetate precursor. The samples were illuminated at 510 nm with a pump fluence of ~0.3 μJcm^{-2}; the emission was monitored at the maximum of PL emission at 549.5 nm for CSD and 540 nm for VASP; f) PL emission.

To further understand the differences in crystalline quality between films obtained from the CSD process and VASP derived films, we performed time-correlated single photon counting (TCSPC) to obtain the lifetime of the photoexcited species. Recent investigations showed that time-resolved photoluminescence (PL) measurements yield not only important information about the diffusion length of the photoexcited species in the devices but also correlate with the perovskite layer morphology. In particular, larger crystals present narrower band gaps and longer lifetimes, which points towards a smaller radiative bimolecular recombination coefficient.[27] Our results presented in *Figure 3 – 8* agree with these findings since we also observed a red shift of the steady-state PL maximum for the CSD-derived sample concerning the BD- and VASP-derived sample. We also observed a slower bimolecular recombination process for films prepared with CSD, which is a strong indicator of good crystalline quality with fewer defects and lower disorder compared to BD- and VASP-derived films.[28,29]

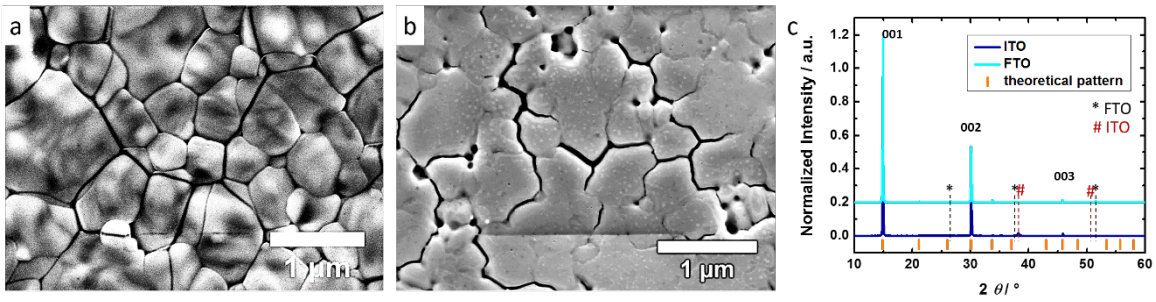

Figure 3 - 9: a) SEM top views of $MAPbBr_3$ perovskite films deposited via VASP, b) SEM top views of $MAPbBr_3$ perovskite films deposited via CSD on FTO, c) XRD pattern normalized to the reflex at 2 ϑ = 14.9 °.

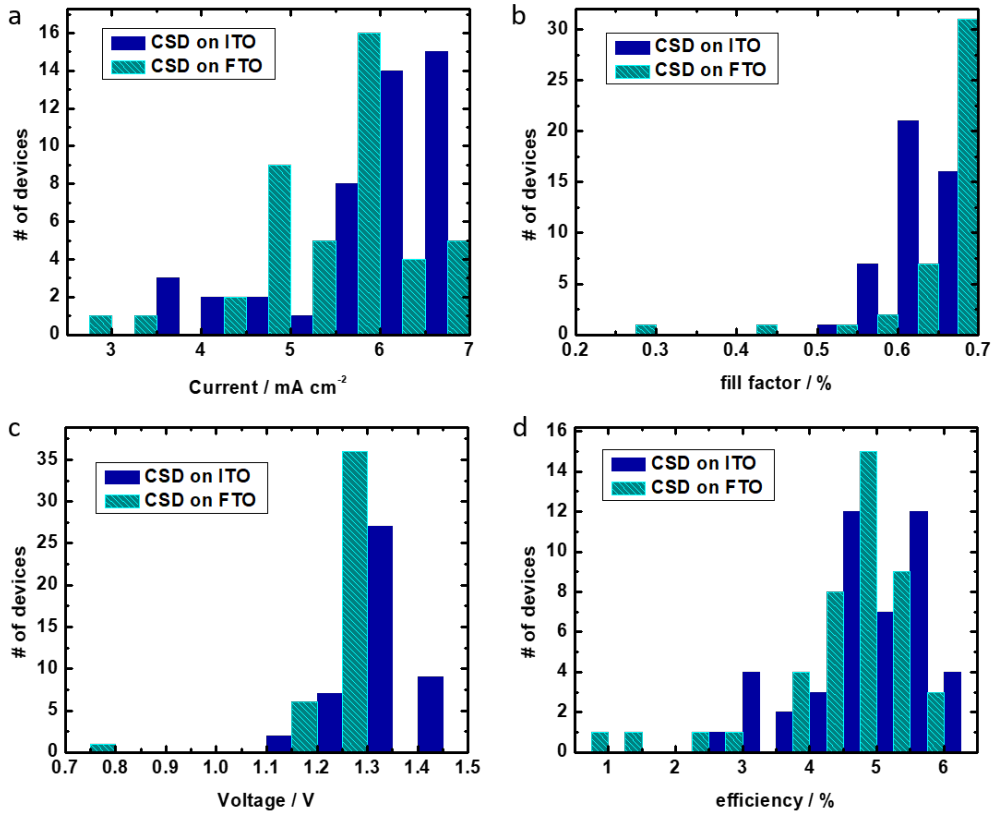

Figure 3 - 10: Distribution of device performance data of 45 devices with perovskite films prepared via spin-coating from a lead acetate precursor (CSD) with an FTO- or ITO-coated substrate, a) short circuit current output, b) fill factor, c) open circuit voltage, d) power conversion efficiencies

The higher current for our CSD-derived films may be a result of either their larger crystal size or their enhanced crystal order, as compared to those deposited via the VASP technique. To investigate this further, we have prepared devices with the rougher bottom contact FTO. This enhanced surface roughness hinders horizontal crystal growth and reduces the domain sizes in the perovskite layer, leading to crystal sizes comparable to those derived with the VASP approach, as shown in *Figure 3 – 9*. However, these films maintain their high degree of orientation with the (001) plane parallel to the substrate, allowing us to discriminate between

effects arising from the crystal size or the crystal orientation. We show histograms of all photovoltaic parameters in *Figure 3 – 10*. Here, we observe that the short circuit current is not affected by the crystal size of the films, leading us to postulate that the degree of crystal order in the film is the parameter affecting the short circuit current. This may be a result of a lower number of defects at the grain boundaries as all neighboring crystals exhibit the same facets with the same orientation.

3.3 CONCLUSION

In summary, we have studied the role of morphology and crystal order in the photovoltaic performance of $MAPbBr_3$ deposited via three different deposition techniques. We developed a new fabrication method based on solvent drying with a halide-free lead precursor controlling the crystallization atmosphere. Here, the reaction of the precursors yields liquid organic by-products at RT which enable large crystal growth with perfectly oriented crystal planes parallel to the substrate as shown by GIWAXS measurements. Our results show that large crystal sizes can only be achieved for smooth ITO substrates, whereas perovskite films on FTO result in crystals limited to hundreds of nanometers due to the enhanced surface roughness which limits horizontal growth. Also, we examined the role of perovskite crystallite orientation in planar heterojunction solar cells by comparing non-oriented VASP-derived films with our newly developed oriented CSD-derived films. We show that this perfect alignment of the cubic crystal planes parallel to the substrate of the CSD-derived film leads to a reproducible and high device performance. Additionally, we show enhanced short circuit currents approaching 7 mA cm^{-2}, their theoretical limit, compared to non-oriented VASP-derived perovskite films. The photocurrents generated in these devices correlate with the degree of crystal orientation rather than the crystal size. Thus, this work demonstrates that crystal orientation and morphology are key parameters to maximize the short-circuit current and thus the performance of perovskite solar cells.

3.4 LITERATURE

(1) Yang, W. S.; Noh, J. H.; Jeon, N. J.; Kim, Y. C.; Ryu, S.; Seo, J.; Seok, S. I. *Science* **2015**, *348*, 1234.

(2) De Wolf, S.; Holovsky, J.; Moon, S.-J.; Löper, P.; Niesen, B.; Ledinsky, M.; Haug, F.-J.; Yum, J.-H.; Ballif, C. *J. Phys. Chem. Lett.* **2014**, *5*, 1035.

(3) Stranks, S. D.; Eperon, G. E.; Grancini, G.; Menelaou, C.; Alcocer, M. J. P.; Leijtens, T.; Herz, L. M.; Petrozza, A.; Snaith, H. J. *Science* **2013**, *342*, 341.

(4) Xing, G.; Mathews, N.; Sun, S.; Lim, S. S.; Lam, Y. M.; Grätzel, M.; Mhaisalkar, S.; Sum, T. C. *Science* **2013**, *342*, 344.

(5) Liu, D.; Kelly, T. L. *Nat. Photon.* **2014**, *8*, 133.

(6) Edri, E.; Kirmayer, S.; Cahen, D.; Hodes, G. *J. Phys. Chem. Lett.* **2013**, *4*, 897.

(7) Hanusch, F. C.; Wiesenmayer, E.; Mankel, E.; Binek, A.; Angloher, P.; Fraunhofer, C.; Giesbrecht, N.; Feckl, J. M.; Jaegermann, W.; Johrendt, D.; Bein, T.; Docampo, P. *J. Phys. Chem. Lett.* **2014**, *5*, 2791.

(8) Ryu, S.; Noh, J. H.; Jeon, N. J.; Chan Kim, Y.; Yang, W. S.; Seo, J.; Seok, S. I. *Energy Environ. Sci.* **2014**, *7*, 2614.

(9) Noh, J. H.; Im, S. H.; Heo, J. H.; Mandal, T. N.; Seok, S. I. *Nano Lett.* **2013**, *13*, 1764.

(10) Docampo, P.; Ball, J. M.; Darwich, M.; Eperon, G. E.; Snaith, H. J. *Nat. Commun.* **2013**, *4*, 2761.

(11) Bailie, C. D.; Christoforo, M. G.; Mailoa, J. P.; Bowring, A. R.; Unger, E. L.; Nguyen, W. H.; Burschka, J.; Pellet, N.; Lee, J. Z.; Gratzel, M.; Noufi, R.; Buonassisi, T.; Salleo, A.; McGehee, M. D. *Energy Environ. Sci.* **2015**, *8*, 956.

(12) Yin, W.-J.; Yang, J.-H.; Kang, J.; Yan, Y.; Wei, S.-H. *J. Mater. Chem. A* **2015**, 8926.

(13) Xiao, M.; Huang, F.; Huang, W.; Dkhissi, Y.; Zhu, Y.; Etheridge, J.; Gray-Weale, A.; Bach, U.; Cheng, Y.-B.; Spiccia, L. *Angew. Chem.* **2014**, *126*, 10056.

(14) Im, J.-H.; Jang, I.-H.; Pellet, N.; Grätzel, M.; Park, N.-G. *Nat. Nano* **2014**, *9*, 927.

(15) Jeon, N. J.; Noh, J. H.; Yang, W. S.; Kim, Y. C.; Ryu, S.; Seo, J.; Seok, S. I. *Nature* **2015**, *517*, 476.

(16) Jeon, N. J.; Noh, J. H.; Kim, Y. C.; Yang, W. S.; Ryu, S.; Seok, S. I. *Nat. Mater.* **2014**, *13*, 897.

(17) Ahn, N.; Son, D.-Y.; Jang, I.-H.; Kang, S. M.; Choi, M.; Park, N.-G. *J. Am. Chem. Soc.* **2015**, *137*, 8696.

(18) Chen, Q.; Zhou, H.; Hong, Z.; Luo, S.; Duan, H.-S.; Wang, H.-H.; Liu, Y.; Li, G.; Yang, Y. *J. Am. Chem. Soc.* **2013**, *136*, 622.

(19) Xiao, Z.; Bi, C.; Shao, Y.; Dong, Q.; Wang, Q.; Yuan, Y.; Wang, C.; Gao, Y.; Huang, J. *Energy Environ. Sci.* **2014**, *7*, 2619.

(20) Docampo, P.; Hanusch, F. C.; Giesbrecht, N.; Angloher, P.; Ivanova, A.; Bein, T. *APL Mat.* **2014**, *2*, 081508.

(21) Sheng, R.; Ho-Baillie, A.; Huang, S.; Chen, S.; Wen, X.; Hao, X.; Green, M. A. *J. Phys. Chem. C* **2015**, *119*, 3545.

(22) Xie, F. X.; Zhang, D.; Su, H.; Ren, X.; Wong, K. S.; Grätzel, M.; Choy, W. C. H. *ACS Nano* **2014**, 639.

(23) Zhang, W.; Saliba, M.; Moore, D. T.; Pathak, S. K.; Hörantner, M. T.; Stergiopoulos, T.; Stranks, S. D.; Eperon, G. E.; Alexander-Webber, J. A.; Abate, A.; Sadhanala, A.; Yao, S.; Chen, Y.; Friend, R. H.; Estroff, L. A.; Wiesner, U.; Snaith, H. J. *Nat. Commun.* **2015**, *6*, 6142.

(24) Saliba, M.; Tan, K. W.; Sai, H.; Moore, D. T.; Scott, T.; Zhang, W.; Estroff, L. A.; Wiesner, U.; Snaith, H. J. *J. Phys. Chem. C* **2014**, *118*, 17171.

(25) Müller-Buschbaum, P. *Adv. Mater.* **2014**, *26*, 7692.

(26) Moore, D. T.; Tan, K. W.; Sai, H.; Barteau, K. P.; Wiesner, U.; Estroff, L. A. *Chem. Mater.* **2015**, *27*, 3197.

(27) D'Innocenzo, V.; Srimath Kandada, A. R.; De Bastiani, M.; Gandini, M.; Petrozza, A. *J. Am. Chem. Soc.* **2014**, *136*, 17730.

(28) de Quilettes, D. W.; Vorpahl, S. M.; Stranks, S. D.; Nagaoka, H.; Eperon, G. E.; Ziffer, M. E.; Snaith, H. J.; Ginger, D. S. *Science* **2015**, *348*, 683.

(29) Wu, X.; Trinh, M. T.; Niesner, D.; Zhu, H.; Norman, Z.; Owen, J. S.; Yaffe, O.; Kudisch, B. J.; Zhu, X. Y. *J. Am. Chem. Soc.* **2015**, *137*, 2089.

4 SINGLE-CRYSTAL-LIKE OPTOELECTRONIC-PROPERTIES OF $MAPbI_3$ PEROVSKITE POLYCRYSTALLINE THIN FILMS

This chapter is based on the following publication:

Nadja Giesbrecht, Johannes Schlipf, Irene Grill, Philipp Rieder, Vladimir Dyakonov, Thomas Bein, Achim Hartschuh, Peter Müller-Buschbaum, Pablo Docampo *J. Mater. Chem. A* **2018**, *6*, 4822.

4.1 INTRODUCTION

Hybrid halide perovskite materials have galvanized the photovoltaic community due to their unprecedented easy and low-cost fabrication combined with remarkable optoelectronic properties, reminiscent of GaAs.[1,2] Polycrystalline perovskite-based photovoltaic devices already reach efficiencies above 22 % after extensive optimization of the perovskite film morphology and composition and engineering of the film interfaces.[3-6] However, the density of grain boundaries in those polycrystalline perovskite films is still rather high, which places a constraint on the charge transport properties of the perovskite films and ultimately will limit the maximum achievable device performance.[7]

Single crystals of perovskite materials show a dramatic improvement of all properties, including charge carrier mobility, charge carrier diffusion length, and a substantially reduced defect density.[8-11] Therefore, higher performance can be expected with single crystalline perovskite absorber layers, as is the case for Si- or GaAs-based photovoltaic devices.[12] However, the growth of single crystalline thin perovskite films is challenging[13-15], and the forced lateral architecture with sequentially deposited electrodes, charge extraction material, and buffer layers is usually required. Such devices to date do not show competitive efficiencies.[13,16] Instead, the main improvement to perovskite solar cells has risen as a result of the development of novel synthesis methods focussing on polycrystalline films with vertical device stack architectures.[3,17] Nevertheless, to facilitate further progress in the performance of perovskite solar cells, we must tap into the full potential of perovskite materials by targeting thin films that exhibit properties similar to those of single crystals, i.e., macroscopic crystal grains and minimum disorder at the grain boundaries.

To this end, precise control of orientation and morphology of polycrystalline films will be necessary. Currently, a plethora of deposition methods are being developed and studied for the methylammonium lead iodide ($MAPbI_3$) compound. In particular, the crystallization kinetics and dynamics were investigated with different lead(II)-precursors and different methylammonium iodide (MAI) ratios[18-21] or different solvents for the precursor solution, in both one and two-step approaches.[22-27] In general, the crystallization kinetics can be divided into three categories: (i) direct formation of the perovskite material from a precursor solution mixture, (ii) sequential addition of the perovskite components or (iii) formation of an intermediate crystalline or amorphous phase which is then converted into the perovskite phase. Employing the first method leads to little control of the morphology, albeit rather large crystals can be formed if an ionic liquid or the anti-solvent technique is used.[28,29] Employing a sequential deposition approach (ii) generally leads to small grain sizes in the range of hundreds of nanometres.[30] The formation of an intermediate phase (iii), especially the Pb-Dimethylsulfoxide (DMSO) complex[3] so far resulted in perovskite films showing highest efficiencies in perovskite solar cells. However, the intermediate phase is formed from the solution and is highly unstable.[31] Therefore, this approach usually lacks fine control of perovskite phase formation and does not lead to perovskite grain sizes exceeding 1 µm.[3,22-24,32]

Larger grain sizes have been already reached for $MAPbBr_3$ based thin films in our previous work based on the use of the lead acetate precursor.[33] Grain sizes larger than 10 µm were achieved in a smooth, thin film comprising perfectly aligned crystals with respect to the substrate. For $MAPbI_3$ films, so far only crystal sizes in the nanometer range were synthesized with the use of the lead acetate precursor. However, two independent studies showed that if using the $PbAc_2$ precursor, the amount of hydration water during perovskite synthesis is essential for the optimized photovoltaic performance of the employed perovskite films in devices.[34,35] Thus, the role of the hydration water for the perovskite synthesis needs to be understood to improve this synthesis strategy further.

In this paper, we introduce a new crystallization strategy based on lead acetate trihydrate. Dissolving this precursor mixture in a highly polar solvent, such as tetrahydrothiophene 1-oxide, leads to the formation of an air-stable intermediate phase that can be converted into the perovskite phase upon heating. We controlled the crystallization process by reducing the nucleation rate significantly and triggering fast perovskite crystal growth with the annealing step, leading to grain sizes of over 10 µm in a homogeneous thin film. Such an increase in grain size and orientation leads to remarkably enhanced electrical properties of the polycrystalline

perovskite films reaching single-crystalline properties, such as charge carrier mobility values in the range of 40 cm^2/Vs. When introduced into devices, polycrystalline films were grown using the new approach resulted in power conversion efficiency values above 18.5 %, significantly above those found for traditional approaches in a like-to-like comparison.

4.2 RESULTS AND DISCUSSION

The $MAPbI_3$ thin films developed in this work are based on a new synthetic protocol using lead acetate trihydrate in combination with a highly polar solvent, tetrahydrothiophene-1-oxide (THTO). Briefly, the solid precursors are mixed in the solid form, and then the solvent mixture Dimethylformamide (DMF)/ THTO is added. To form the $MAPbI_3$ films the solution was spin-coated at 5000 rpm for 180 s on top of the substrate and annealed at 130 °C for 5 min (see chapter 9 for all details).

The crucial step in the film formation process is mixing the precursor in the solid state before adding the solvent mixture. As shown in *Figure 4 – 1a*, the colorless precursor mixture becomes yellow after manually shaking the vial. This leads to the formation of a highly crystalline intermediate phase (IP) with the crystal structure shown in *Figure 4 – 1b*. In the XRD pattern of the new phase, we see no presence of the precursor phases, indicating a phase-pure new compound that can be indexed to an orthorhombic structure with a space group similar to *P*222 with lattice parameters a=6.4 Å, b=15.935 Å, and c=27.805 Å. We note that the formation of the IP relies on the presence of hydration water in the lead acetate precursor. The XRD analysis in *Figure 4 – 2* of the precursor mixture using dehydrated $PbAc_2$ shows that no new phase is formed. This is not unexpected, as different groups found hydration water in the lead acetate precursor to be necessary to crystallize high-performing perovskite films in photovoltaic devices.[34,35]

To further study this new IP and its structure we crystallized it from the water. We found that the crystals growth is anisotropic with very long lengths in the mm range but widths in the nm range as shown in *Figure 4 – 1c* and in *Figure 4 – 2d*). Our 2D XRD data show similarity to an $(MA^+)_2(PbI_3^-)_2PbI_2 \cdot 2DMSO$ phase from a synthesis via a polymeric plumbate(II) fiber identified by Guo *et al.* [31] We note that this approach can also be used for bromide instead iodide, as shown in *Figure 4 – 2c*. In contrast to the Pb-DMSO complex, the IP shown here is very stable at ambient conditions and directly converts to the perovskite phase, if heated to at least 80 °C.

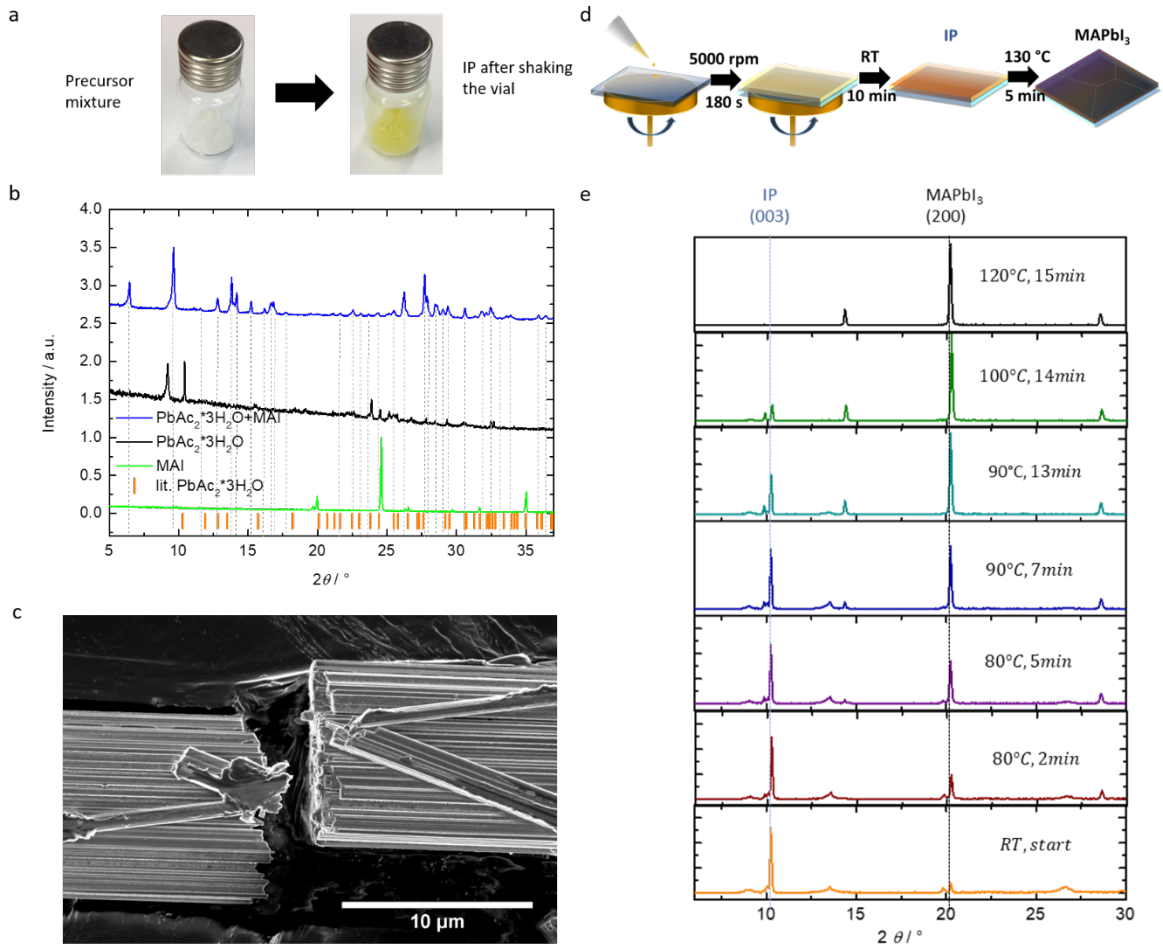

Figure 4 - 1: Figure 4 - 1. a) photos of the precursor mixtures before and after shaking of the vial;b) Comparison of the precursors MAI and (hydrated) $PbAc_2*3H_2O$ with resulting new intermediate phase (IP)compound from mixing both solids; c) SEM image of the needle-shaped crystals from the IP; d) Schematic illustration of the spin-coating process; e) *in situ* XRD while annealing the substrate with the spin-coated precursor solution.

To deposit the IP from the solution the choice of solvent is highly important. The most commonly used solvents such as DMF or γ-butyrolactone (GBL) do not favor the formation of the IP[18,34,36] but instead result in fast perovskite crystallization, as can be seen in *Figure 4 – 3a*.[21] Therefore, the solvent mixture needs to be modified to promote the crystallization of the IP rather than the perovskite phase. This is achieved by simply increasing the solubility of the perovskite compared to the solubility of the IP. Foley *et al.* predicted with Mayer bond order calculations a slightly more negative enthalpy of perovskite solvation for DMSO compared to DMF and a much more negative enthalpy of solvation for THTO.[27]To find a suitable solvent mixture, we studied the crystallization behaviour from a range of solvents via *in-situ* XRD measurements at ambient conditions right after spin-coating the films in a nitrogen-filled glovebox. DMF-based solutions lead to a highly crystalline perovskite phase immediately after spin-coating. However a weak reflection at around 9.6 °, 2θ indicates the presence of a second phase which corresponds to the IP. Employing DMSO, as shown in *Figure 4 - 3b* leads to

slower perovskite crystallization and a higher amount of the intermediate phase. Here, increasing the DMSO concentration leads to a competition of the lead-DMSO complex as shown in *Figure 4 – 3* and therefore inhibited crystallization of the new IP. Finally, THTO does not form any additional intermediate phases from the perovskite precursor solution, and small concentrations around 10-13 vol% are already sufficient to prevent perovskite nucleation before the IP is fully crystallized (*see Figure 4 – 3c-f*). In *Figure 4 – 1d* a schematic illustration of the final synthesis process through the IP phase is illustrated.

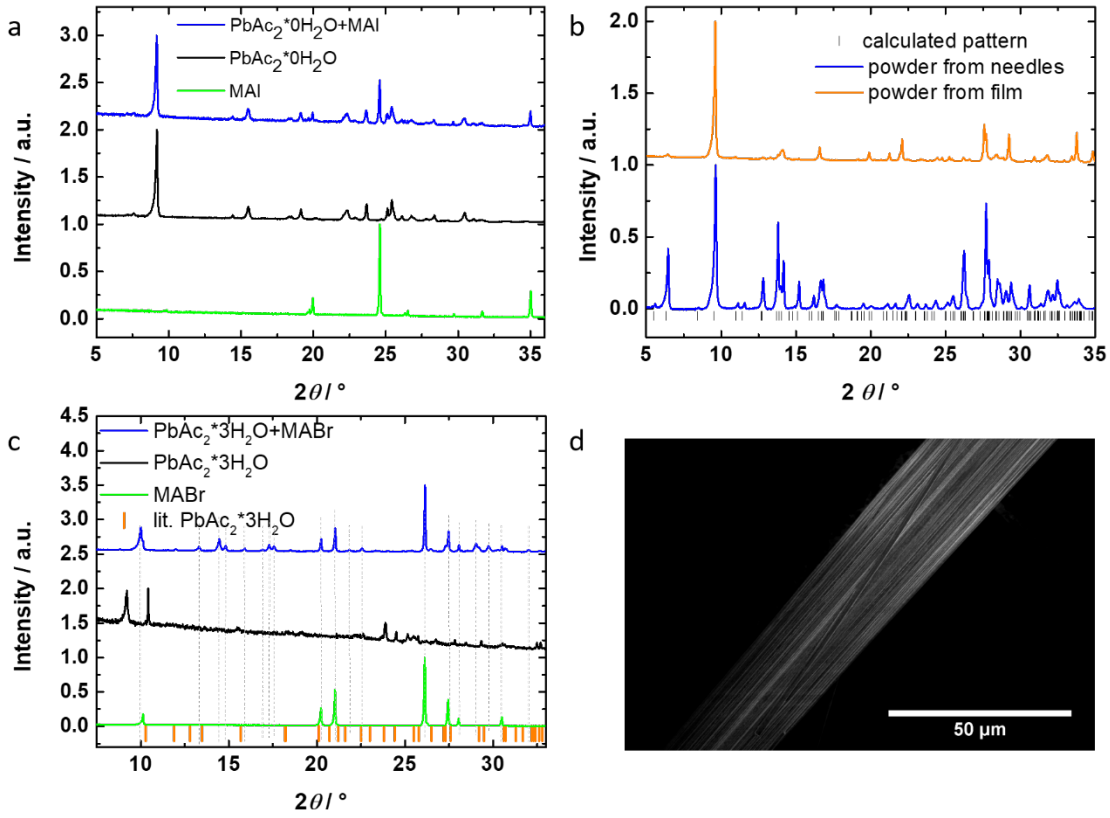

Figure 4 - 2: PXDR Analysis: a) comparison of the precursors MAI and anhydrous PbAc2 with the mixture of both, which does not form a new phase; b) comparison of in water fully converted new phase from (hydrated) $PbAc_2$•$3H_2O$ and MAI needle-shaped bright yellow crystallites and the powder scratched off from deposited film from precursor solution with 13 vol% THTO. Both agree very well with a calculated pattern in the *P222* structure type; c) comparison of the precursors MABr and hydrated $PbAc_2$ with resulting new compound from mixing both solids which also agree with an orthorhombic structure type; d) SEM images of the synthesized needles of the IP.

The *in situ* XRD data collected in *Figure 4 – 1e* clearly show the direct transformation of the (003) reflection of the IP to the (200) reflection of the perovskite. Initially, the IP shows the (003) reflection at 10°, which shifts to 9.6° upon complete drying as shown in *Figure 4 – 3*. At this stage, the IP is completely stable under ambient conditions with the same structure as from solid state reaction from the precursors. We note that the IP in the film is highly oriented and therefore mainly the reflection at 9.6 ° is visible. To confirm that the IP is the same in both

cases, we have compared the XRD between powder from the precursor mixture, and powder scraped off from the film, showing the same crystallographic pattern (see *Figure 4 – 2b*).

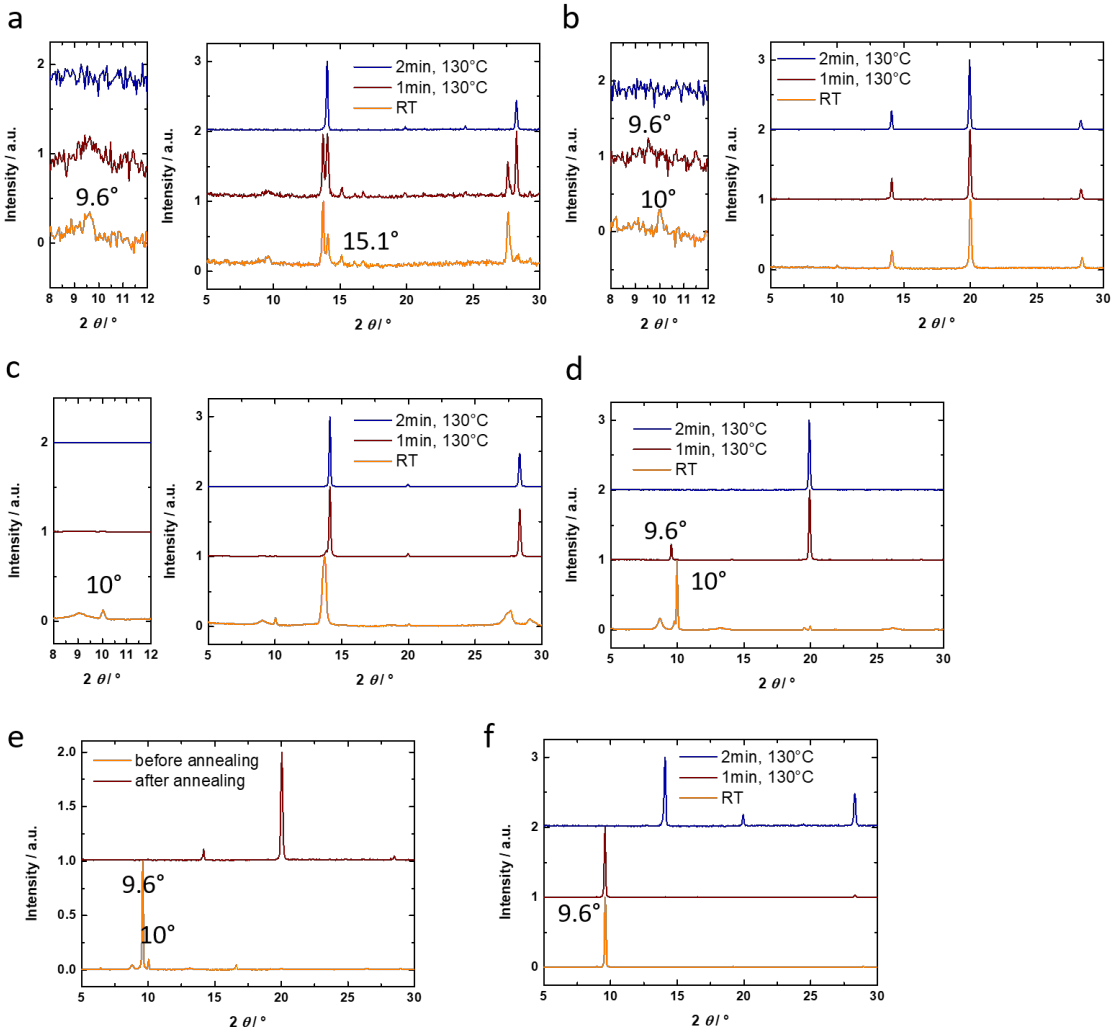

Figure 4 - 3: In-situ XRD of spin-coated films, before and while annealing: a) film prepared from DMF solution; b) films prepared from DMF-based solution containing 20 vol% DMSO; c) films prepared from DMF based solution containing 9 vol% THTO; d) films prepared from DMF-based solution containing 13 vol% THTO; e) films prepared from DMF-based solution containing 13 vol% THTO and dried at RT for 6 h; f) films prepared from DMF based solution containing 26 vol% THTO; e) films prepared from DMF-based solution containing 30 vol% DMSO, Pb_3I_8 complex appears in XRD at 6.6°, 7.2°, 9.2° agreeing with [24].

To inhibit the perovskite nucleation and promote the crystallization of the IP from the solution, the addition of THTO to the solvent mixture is crucial. This, in turn, influences the resulting grain size by determining the number of potential nucleation points for perovskite phase conversion as shown in *Figure 4 – 4*. Grain sizes of up to 100 µm can be reached with 26 vol% THTO additive, but the films show poor grain interconnection and smoothness. We found the best compromise between grain size and overall film quality to be reached with perovskite films obtained from 13 vol% THTO. This mixture leads to grain sizes of above 10 µm in a very dense

and smooth film when annealed at 130 °C. Somewhat surprisingly, lower annealing temperatures and longer conversion times lead to smaller crystallites as shown in *Figure 4 – 5*.

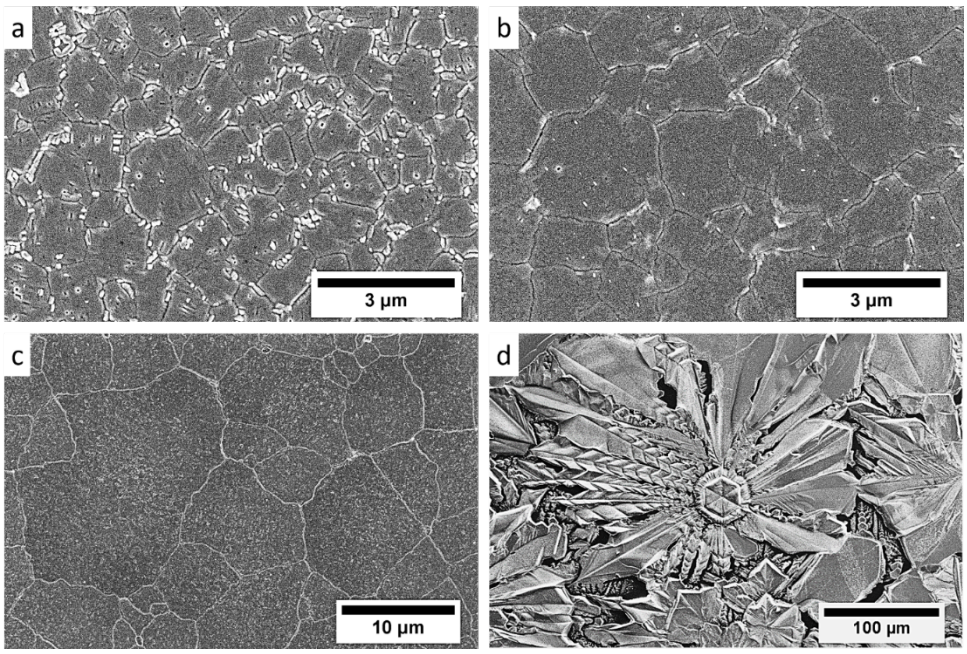

Figure 4 - 4: SEM images of perovskite films prepared from different THTO concentrations: a) 7 vol% THTO; b) 10 vol% THTO; c) 13 vol% THTO; d) 26 vol% THTO.

To obtain more insights regarding crystal orientation we performed grazing-incidence wide-angle X-ray scattering (GIWAXS) measurements, see *Figure 4 – 6a*. GIWAXS is a powerful method for evaluation of crystal orientation in thin films due to the high statistical relevance and the possibility to extract quantitative information about the crystalline part of the sample.[37-39] A typical sample based on lead acetate and employing DMF solvent usually shows no preferential orientation as shown in literature and the *Figure 4 – 7* for films prepared under our synthesis conditions.[35,36,40] As shown earlier by Foley *et al.*, the solvent THTO, on the other hand, can be used to achieve a high degree of orientation in $MAPbI_3$ films.[27] They argue that homogeneous nucleation is suppressed and instead heterogeneous nucleation starting at the substrate is responsible for this orientation. Here the synthesis parameters are different since the perovskite is formed through an IP.

However, with increased THTO concentration, the perovskite crystal alignment within the film is confined to the (200) facet parallel to the substrate as explained in the following: *Figure 4 – 6a* shows the 2D GIWAXS pattern of a film with 13 vol% THTO. The strong preferential orientation of the $MAPbI_3$ crystallites is apparent from the individual scattering reflections which are labeled according to the crystal planes from which they originate. The splitting of the cubic (110) and (111) peaks gives rise to the (112)/(200) and the (211)/(202) pair of peaks,

respectively, and shows that the sample is in tetragonal phase. In comparison, in the 2D GIWAXS pattern of the sample prepared from pure DMF solvent, the reflections adopt the form of Debye-Scherrer rings indicating no preferential crystal orientation (cf. *Figure 4 – 7*).

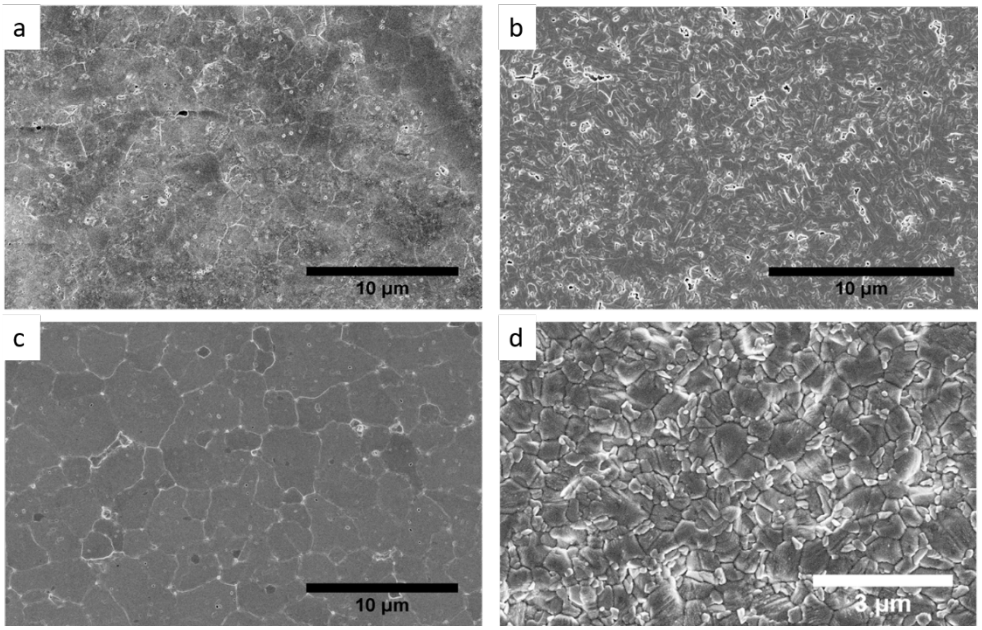

Figure 4 - 5: SEM top-view images of films deposited on TiO_2/FTO-coated glass. a) intermediate phase 1 day after deposition; b) perovskite converted at RT over 1 week from intermediate phase; c) perovskite deposited from solution with 13 vol% THTO and annealed at 100 °C; d) perovskite deposited from solution with pure DMF solution (0 vol% THTO).

The azimuthal line cuts around the q range of the (002)/(110) and their second order peaks (004)/(220) of the 13 vol% THTO data are plotted with intensity vs. azimuthal angle γ in *Figure 4 – 7b*. From the intensity distribution in these cuts, the orientation of crystals in the film can be evaluated statistically. Therefore, the peaks were fitted with Voigt functions and their positions was determined to be 44.8(3) °. These peak positions verify that the sample is oriented with the (200) facet parallel to the substrate which can be imagined as a cuboid lying on its side. The extremely narrow FWHM of 2.0(7) ° of these Voigt functions shows how well the $MAPbI_3$ crystals are aligned inside the film. As seen in *Figure 4 – 7*, already 10 vol% of THTO additive is sufficient for strong crystal alignment and 13 vol% THTO is optimal for pure crystal alignment verifying the GIWAXS result.

To determine the actual grain size within the perovskite film, we performed high-resolution transmission electron microscopy (HRTEM) on a cross-section of a photovoltaic device. To this end, we cut a 45 µm long lamella with a focused ion beam from a complete solar cell device in FTO/TiO_2/$MAPbI_3$/Spiro-OMeTAD/Au architecture. In *Figure 4 – 6* we show a representative area of a 16 µm long TEM cross-section. Here, HRTEM images from four different spots are shown together with their fast Fourier transform (FFT). A change in pattern

can only be observed in bright regions between the grains. Thus, we assume the bright lines to be the grain boundaries. In the image, the FFT pattern along the 12 µm distance between the bright areas does not change, indicating that it is indeed a single crystal. Our results show that there are mainly two distinct crystal orientations in the in-plane direction in this sample, confirming the high degree of order in the material. We note that the samples are highly sensitive to the electron beam and particularly the grain boundaries become broader with longer illumination times.

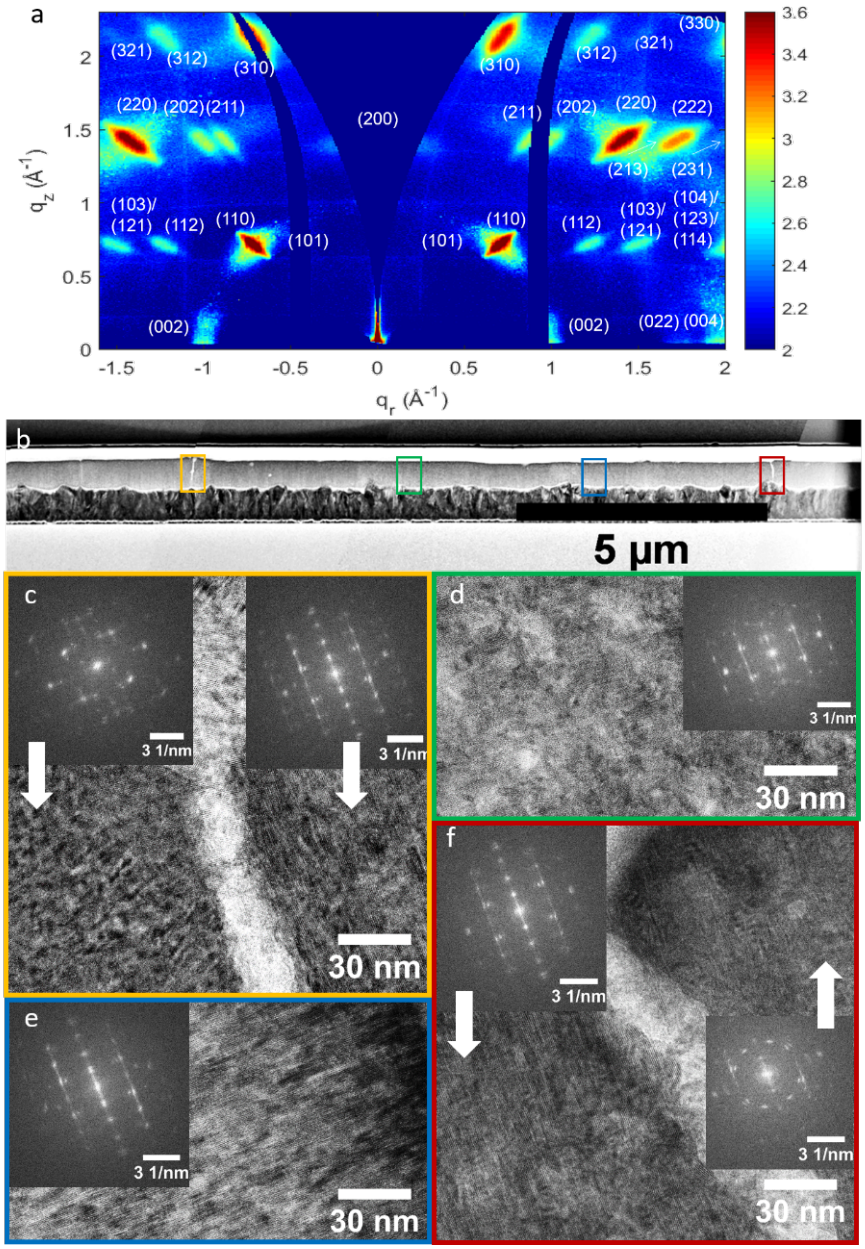

Figure 4 - 6: a) 2D GIWAXS pattern of a sample prepared from 13 vol% THTO solvent additive to the precursor solution shown in q_r-q_z representation; b) TEM cross-section of the lamella incorporating a $MAPbI_3$ film deposited from 13 vol% THTO; c-f) HRTEM's and their FFT's from the spots marked in b).

To additionally classify the different layers in the cross-section, we performed energy-dispersive X-ray spectroscopy (EDX) during the TEM investigation, as shown in *Figure 4 – 7*. Here, we can clearly distinguish between our different layers in the stack with the distribution of different atoms present and detectable. We see no heterogeneity in our perovskite layers, confirming their high quality.

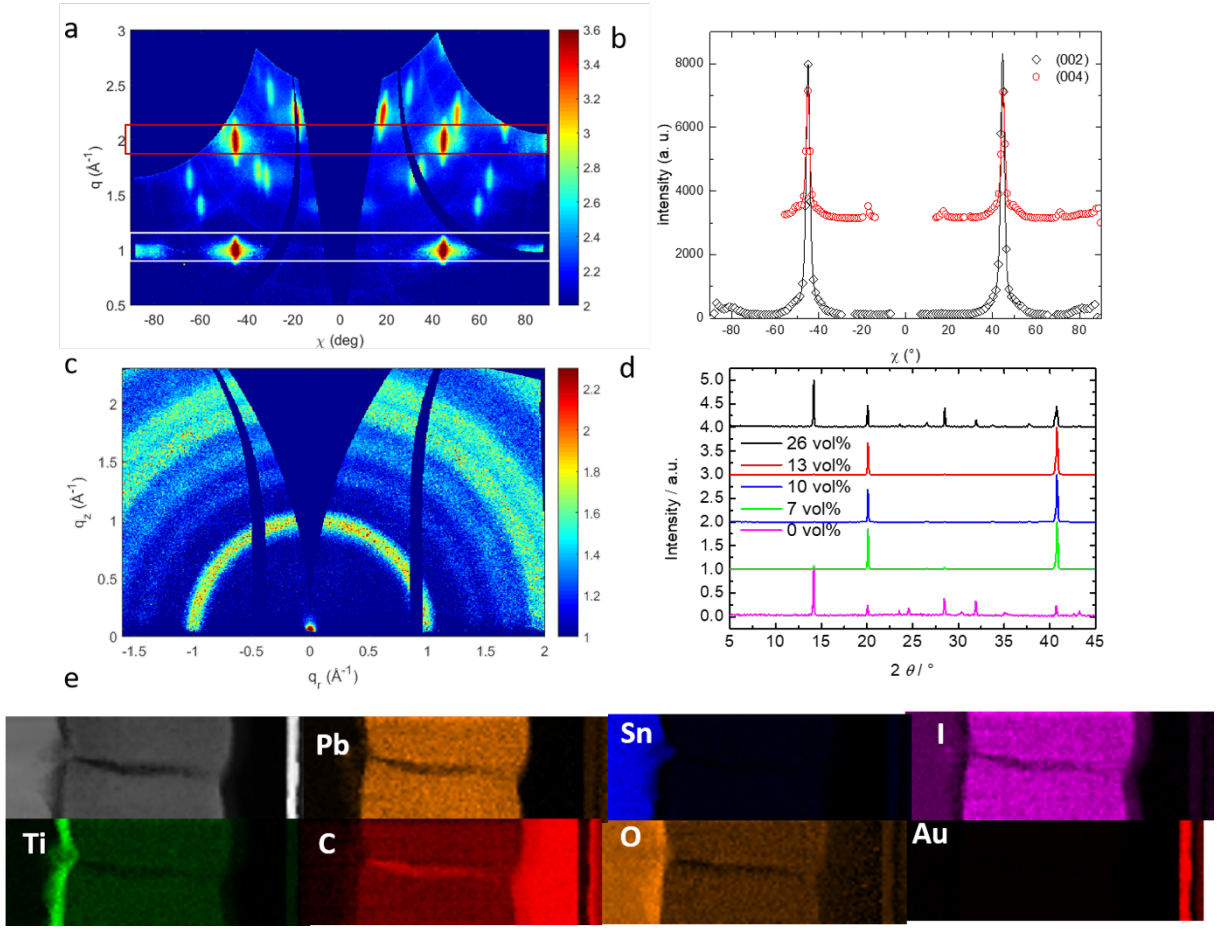

Figure 4 - 7: 2D GIWAXS investigation: a) 2D GIWAXS pattern of samples prepared from 13 vol% THTO solvent additive to the precursor solution, the boxes mark the positions for the cuts around the (002) and (004) reflection presented in b) Voigt functions were fitted at 44.8(3)° with FWHM = 2.0(7)° showing extremely narrow peaks and hence very narrow distribution of crystal orientations; c) 2D GIWAXS pattern of a film produced with pure DMF solvent (measured for 1 h); d) XRD investigation of $MAPbI_3$ films prepared from different THTO concentrations; e) EDX mapping in TEM.

To quantify the improvement in optoelectronic properties with larger grains in our polycrystalline films we performed Time of Flight (ToF) measurements as shown in *Figure 4 – 8*. ToF measurements were performed in a lateral sample configuration where the different $MAPbI_3$ films were deposited on top of an in-plane gold contact pattern. Here, the photogenerated carriers can be extracted from the electrodes with varying spacing *d* in the range of several tens of micrometers. Charge carrier generation is induced upon pulsed laser excitation at the margin of one contact while drift of the charges occurs due to an external DC field (E = 5 kV/cm) which is applied only during the short measurement period of the *j-t* profile. Since

the charges are created locally near one electrode, the polarity of the E-field defines whether electron or hole transport across the material is observed. A detailed description of the employed setup can be found in chapter 9.

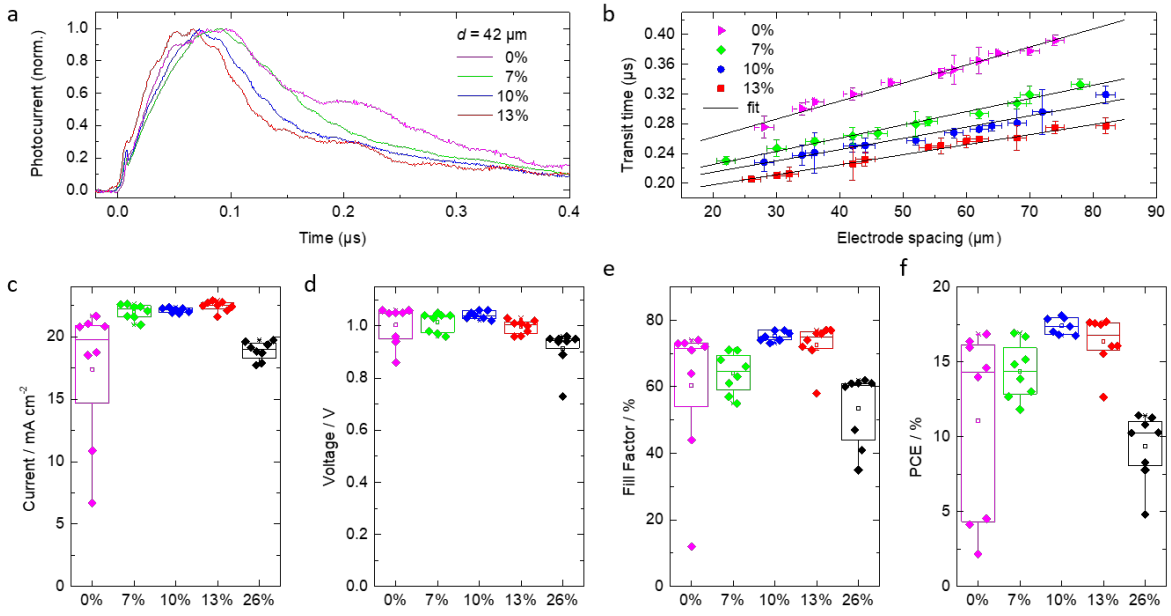

Figure 4 - 8: a) Representative transients obtained at 42 µm spacing; b) Extracted transit times for holes from ToF with perovskite films deposited from different THTO concentrations; c-f) device performance deviation of devices in the architecture FTO/TiO_2/C_{60}/Al_2O_3/$MAPbI_3$/Spiro-OMeTAD/Au employing perovskite films deposited from different THTO concentrations.

THTO conc. / vol%	Hole mobility / $cm^2 (Vs)^{-1}$	Electron mobility / $cm^2 (Vs)^{-1}$	Stand. Dev. / $cm^2 (Vs)^{-1}$	Sum / $cm^2 (Vs)^{-1}$
0	8	9	1	17
7	11	12	1	23
10	13	13	1	26
13	15	17	1	32
26*	17*	23*		40*

Table 4 - 1: Extracted mobility values from ToF measurement showing increasing charge mobility with grain size. The 26 vol% sample (*) was measured with a different procedure as discussed in the Supporting Information.

Representative transients obtained for different electrode spacings are shown in *Figure 4 – 8a*. Following a fitting procedure for ToF transients[41], the transit time t_{tr} was extracted and plotted as a function of d for every investigated material (*Figure 4 – 8b*). Because of the linear dependence of t_{tr} on d, the mobility can be calculated from the respective fit according to $\mu = d/(E \cdot t_{tr})$. The determined values are listed in *Table 4 – 1*. Clearly, an influence of the grain size is observable. With increasing grain size the mobility values increase, indicating improved transport properties due to a reduced number of grain boundaries which represent potential recombination sites.[7] We note that a full analysis of the 26 vol% THTO sample was not possible due to a large number of pinholes in the film. Therefore, the photocurrent in this device was

only measurable for a small number of different electrode spacings with no representative trend from the obtained transients. The value presented here was obtained from a voltage series performed on a fixed gap size where the photocurrent was detectable (see *Figure 4 – 9*) and represents a lower limit of the mobility. We further note that the transport measurement in the lateral configuration is essential to gain information on the optoelectronic properties of the perovskite layer, while vertical in-plane devices show several limitations for data acquisition.[42] Additionally, our sample configuration allows for the measurement of charge transport on a macroscopic scale over several micrometers reflecting the influence of grain boundaries and defects, which directly affects charge carrier transport.

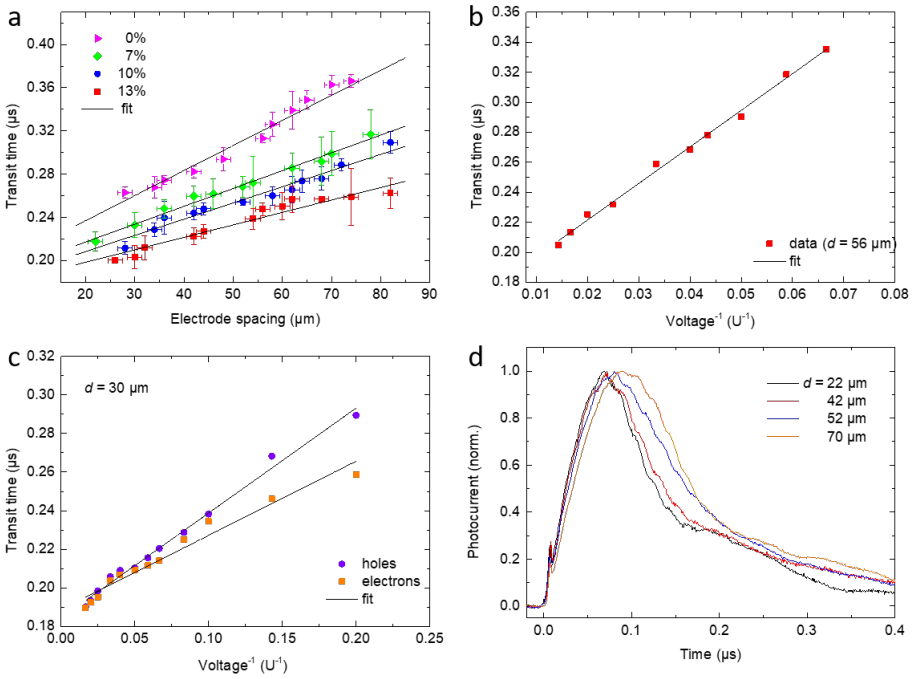

Figure 4 - 9: ToF analysis data: a) Extracted transit times for electrons from ToF analysis for perovskite films deposited with different THTO concentrations; b) Voltage series for 13 vol% THTO sample for a proof-of-principle for the acquired data in c); c) Voltage series for fixed gap sizes with 26 vol% THTO sample; c) representative transients for different electrode spacing for 13 vol% THTO sample.

To study the effect of crystal size on solar cell performance, we prepared devices in a planar heterojunction configuration (FTO/TiO_2/C_{60}/Al_2O_3/$MAPbI_3$/Spiro-OMeTAD/Au). We show a box plot distribution of the device performance of at least 8 devices for the different perovskite films in *Figure 4 – 8*. Here, we mainly observe an increase in fill factor (*FF*), correlating with the improved electrical properties of the bigger crystal films. We note that for devices fabricated from films with crystal sizes above 3 µm (namely 10 vol% and 13 vol% THTO), no significant difference in device performance occurs. The performance of these two samples is in fact within the experimental error of the system and show the highest value at 18.5 % as well as the

highest reproducibility. The high short-circuit current densities above 22 mA/cm^2, which are gained in these devices correlate perfectly with the current calculated from EQE measurement of 22.45 mA/cm^2 (see *Figure 4 – 10*). We, however, note that all the devices employing architectures as shown in *Figure 4 – 10a* have high hysteresis with non-stabilized power output. This instability is probably related to the charge extraction layers and not the perovskite layer, since with devices employing different transport materials such as Poly(3,4-ethylenedioxythiophene)-poly(styrenesulfonate) (PEDOT:PSS) or [6,6]-Phenyl C_{61} butyric acid methyl ester (PCBM) demonstrated minimal hysteresis and stabilized power output, as can be seen in *Figure 4 -10*.

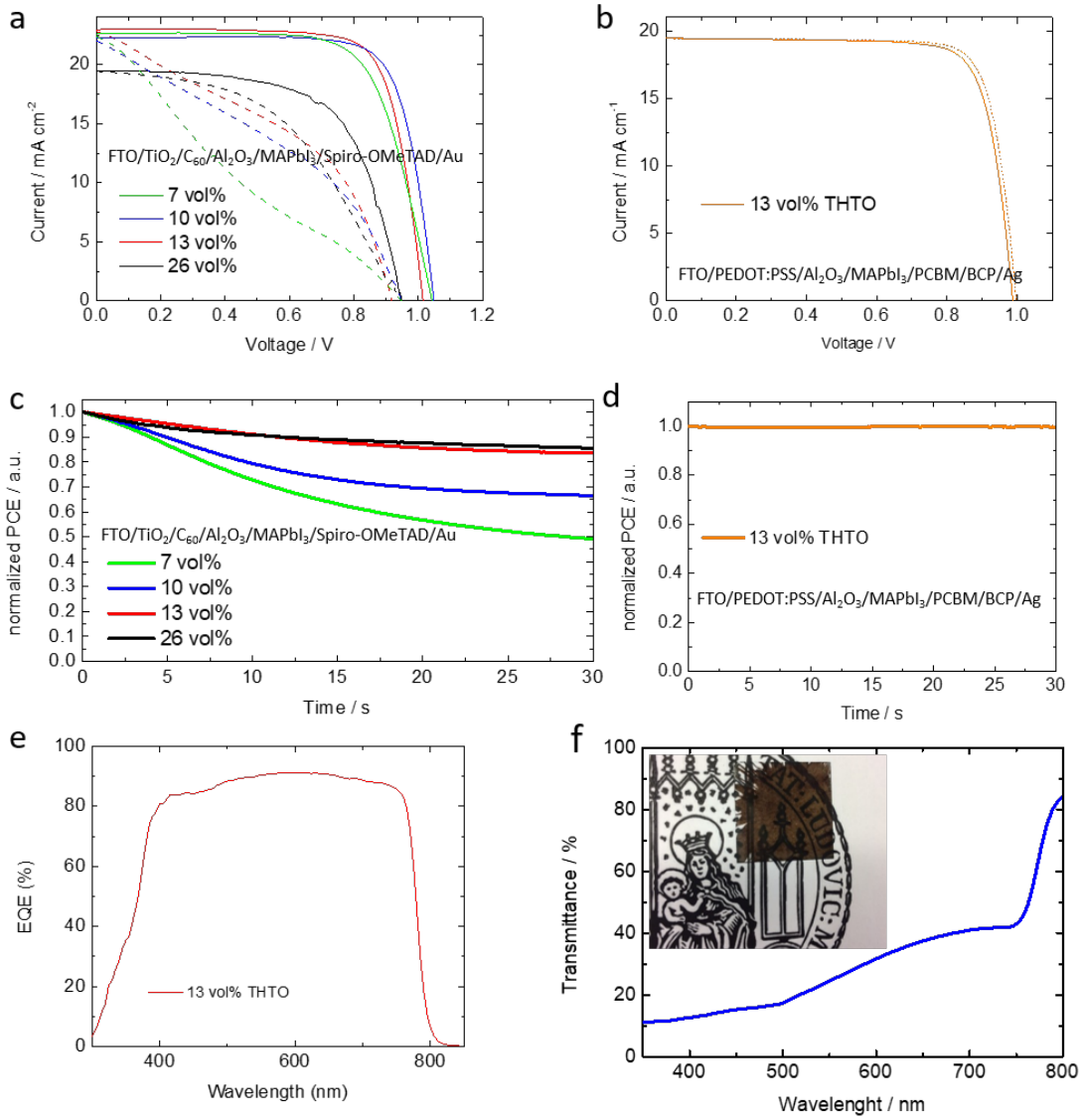

Figure 4 - 10: a+b) *JV*-curves of devices in different device architecture with straight lines for forward scan and dashed lines for reverse scan; c+d) Steady-state power output under applied bias for different perovskite films and device architectures; e) EQE of a device with a perovskite film from 13 vol% THTO in the device architecture: FTO/TiO2/C60/Al2O3/MAPbI3/Spiro-OMeTAD/Au; f) transmittance spectrum obtained from a film synthesized with 26 vol% THTO with photo of the same film.

The perovskite films with the largest grain sizes contain a large number of pinholes which leads to semi-transparent films with an average transmittance of about 28 % in the visible range, as shown in *Figure 4 – 10f*. Therefore the device properties drop if these films are incorporated. However, the current density in these devices is extremely high with 19 mA/cm^{-2} on average which is much higher than for any reported semitransparent $MAPbI_3$-based solar cells with a transmittance of about 20-30 %.[43-46] Hence, the device efficiency reaches very high values with the maximum of 12 %, which is 4 % higher than that of device shown in the literature with semitransparent appearance due to pinholes.[43]

4.3 CONCLUSION

In this work, we introduce a new route to deposit hybrid perovskite films with extremely large and perfectly oriented crystalline domains of 10-40 µm in size. To achieve this, we targeted a new, highly stable intermediate phase based on lead acetate trihydrate. Importantly, we find that a highly polar solvent, such as tetrahydrothiophene 1-oxide is necessary to inhibit the perovskite phase growth and to favor the crystallization of the IP. With HRTEM we can clearly identify the grain boundaries and verify high crystallinity and order within the perovskite film. The newly developed films show charge transport properties similar to those found in perovskite single crystals with very high mobility values in the 40 cm^2/Vs range. We capitalized on these improved properties by fabricating solar cells with a planar heterojunction architecture. The highly oriented and large grains lead to a power conversion efficiency of 18.5 %, higher than what is achieved with standard fabrication in a like-to-like comparison.

4.4 LITERATURE

(1) Snaith, H. J. *J. Phys. Chem. Lett.* **2013**, *4*, 3623.

(2) Bauhuis, G. J.; Mulder, P.; Haverkamp, E. J.; Huijben, J. C. C. M.; Schermer, J. J. *Sol. Energy Mater. Sol. Cells* **2009**, *93*, 1488.

(3) Yang, W. S.; Park, B.-W.; Jung, E. H.; Jeon, N. J.; Kim, Y. C.; Lee, D. U.; Shin, S. S.; Seo, J.; Kim, E. K.; Noh, J. H.; Seok, S. I. *Science* **2017**, *356*, 1376.

(4) Tan, H.; Jain, A.; Voznyy, O.; Lan, X.; García de Arquer, F. P.; Fan, J. Z.; Quintero-Bermudez, R.; Yuan, M.; Zhang, B.; Zhao, Y.; Fan, F.; Li, P.; Quan, L. N.; Zhao, Y.; Lu, Z.-H.; Yang, Z.; Hoogland, S.; Sargent, E. H. *Science* **2017**, *355*, 722.

(5) Correa-Baena, J.-P.; Tress, W.; Domanski, K.; Anaraki, E. H.; Turren-Cruz, S.-H.; Roose, B.; Boix, P. P.; Gratzel, M.; Saliba, M.; Abate, A.; Hagfeldt, A. *Energy Environ. Sci.* **2017**, *10*, 1207.

(6) He, M.; Li, B.; Cui, X.; Jiang, B.; He, Y.; Chen, Y.; O'Neil, D.; Szymanski, P.; Ei-Sayed, M. A.; Huang, J.; Lin, Z. *Nature Communications* **2017**, *8*, 16045.

(7) Cho, N.; Li, F.; Turedi, B.; Sinatra, L.; Sarmah, S. P.; Parida, M. R.; Saidaminov, M. I.; Murali, B.; Burlakov, V. M.; Goriely, A.; Mohammed, O. F.; Wu, T.; Bakr, O. M. *Nature Communications* **2016**, *7*, 13407.

(8) Dong, Q.; Fang, Y.; Shao, Y.; Mulligan, P.; Qiu, J.; Cao, L.; Huang, J. *Science* **2015**, *347*, 967.

(9) Shi, D.; Adinolfi, V.; Comin, R.; Yuan, M.; Alarousu, E.; Buin, A.; Chen, Y.; Hoogland, S.; Rothenberger, A.; Katsiev, K.; Losovyj, Y.; Zhang, X.; Dowben, P. A.; Mohammed, O. F.; Sargent, E. H.; Bakr, O. M. *Science* **2015**, *347*, 519.

(10) Saidaminov, M. I.; Adinolfi, V.; Comin, R.; Abdelhady, A. L.; Peng, W.; Dursun, I.; Yuan, M.; Hoogland, S.; Sargent, E. H.; Bakr, O. M. *Nat Commun* **2015**, *6*.

(11) Zhumekenov, A. A.; Saidaminov, M. I.; Haque, M. A.; Alarousu, E.; Sarmah, S. P.; Murali, B.; Dursun, I.; Miao, X.-H.; Abdelhady, A. L.; Wu, T.; Mohammed, O. F.; Bakr, O. M. *ACS Energy Letters* **2016**, *1*, 32.

(12) *NREL* **2017**.

(13) Lee, L.; Baek, J.; Park, K. S.; Lee, Y.-E.; Shrestha, N. K.; Sung, M. M. *Nature Communications* **2017**, *8*, 15882.

(14) Wei, W.; Zhang, Y.; Xu, Q.; Wei, H.; Fang, Y.; Wang, Q.; Deng, Y.; Li, T.; Gruverman, A.; Cao, L.; Huang, J. **2017**, *11*, 315.

(15) Chen, J.; Morrow, D. J.; Fu, Y.; Zheng, W.; Zhao, Y.; Dang, L.; Stolt, M. J.; Kohler, D. D.; Wang, X.; Czech, K. J.; Hautzinger, M. P.; Shen, S.; Guo, L.; Pan, A.; Wright, J. C.; Jin, S. *J. Am. Chem. Soc.* **2017**, *139*, 13525.

(16) Jumabekov, A. N.; Della Gaspera, E.; Xu, Z. Q.; Chesman, A. S. R.; van Embden, J.; Bonke, S. A.; Bao, Q.; Vak, D.; Bach, U. *Journal of Materials Chemistry C* **2016**, *4*, 3125.

(17) Wu, Y.; Xie, F.; Chen, H.; Yang, X.; Su, H.; Cai, M.; Zhou, Z.; Noda, T.; Han, L. *Adv. Mater.* **2017**, *29*, 1701073.

(18) Zhang, W.; Saliba, M.; Moore, D. T.; Pathak, S. K.; Hörantner, M. T.; Stergiopoulos, T.; Stranks, S. D.; Eperon, G. E.; Alexander-Webber, J. A.; Abate, A.; Sadhanala, A.; Yao, S.; Chen, Y.; Friend, R. H.; Estroff, L. A.; Wiesner, U.; Snaith, H. J. *Nat. Commun.* **2015**, *6*, 6142.

(19) Aldibaja, F. K.; Badia, L.; Mas-Marza, E.; Sanchez, R. S.; Barea, E. M.; Mora-Sero, I. *J. Mater. Chem. A* **2015**.

(20) Munir, R.; Sheikh, A. D.; Abdelsamie, M.; Hu, H.; Yu, L.; Zhao, K.; Kim, T.; Tall, O. E.; Li, R.; Smilgies, D.-M.; Amassian, A. *Adv. Mater.* **2016**, n/a.

(21) Moore, D. T.; Sai, H.; Tan, K. W.; Smilgies, D.-M.; Zhang, W.; Snaith, H. J.; Wiesner, U.; Estroff, L. A. *J. Am. Chem. Soc.* **2015**, *137*, 2350.

(22) Yang, W. S.; Noh, J. H.; Jeon, N. J.; Kim, Y. C.; Ryu, S.; Seo, J.; Seok, S. I. *Science* **2015**, *348*, 1234.

(23) Jeon, N. J.; Noh, J. H.; Kim, Y. C.; Yang, W. S.; Ryu, S.; Seok, S. I. *Nat. Mater.* **2014**, *13*, 897.

(24) Cao, J.; Jing, X.; Yan, J.; Hu, C.; Chen, R.; Yin, J.; Li, J.; Zheng, N. *J. Am. Chem. Soc.* **2016**.

(25) Ahn, N.; Son, D.-Y.; Jang, I.-H.; Kang, S. M.; Choi, M.; Park, N.-G. *J. Am. Chem. Soc.* **2015**, *137*, 8696.

(26) Fei, C.; Li, B.; Zhang, R.; Fu, H.; Tian, J.; Cao, G. *Advanced Energy Materials* **2016**, 1602017.

(27) Foley, B. J.; Girard, J.; Sorenson, B. A.; Chen, A. Z.; Scott Niezgoda, J.; Alpert, M. R.; Harper, A. F.; Smilgies, D.-M.; Clancy, P.; Saidi, W. A.; Choi, J. J. *J. Mater. Chem. A* **2017**, *5*, 113.

(28) Moore, D. T.; Tan, K. W.; Sai, H.; Barteau, K. P.; Wiesner, U.; Estroff, L. A. *Chem. Mater.* **2015**, *27*, 3197.

(29) Xiao, M.; Huang, F.; Huang, W.; Dkhissi, Y.; Zhu, Y.; Etheridge, J.; Gray-Weale, A.; Bach, U.; Cheng, Y.-B.; Spiccia, L. *Angew. Chem.* **2014**, *126*, 10056.

(30) Docampo, P.; Hanusch, F. C.; Stranks, S. D.; Döblinger, M.; Feckl, J. M.; Ehrensperger, M.; Minar, N. K.; Johnston, M. B.; Snaith, H. J.; Bein, T. *Advanced Energy Materials* **2014**, *4*, n/a.

(31) Guo, Y.; Shoyama, K.; Sato, W.; Matsuo, Y.; Inoue, K.; Harano, K.; Liu, C.; Tanaka, H.; Nakamura, E. *J. Am. Chem. Soc.* **2015**, *137*, 15907.

(32) Li, X.; Bi, D.; Yi, C.; Décoppet, J.-D.; Luo, J.; Zakeeruddin, S. M.; Hagfeldt, A.; Grätzel, M. *Science* **2016**, *353*, 58.

(33) Giesbrecht, N.; Schlipf, J.; Oesinghaus, L.; Binek, A.; Bein, T.; Müller-Buschbaum, P.; Docampo, P. *ACS Energy Letters* **2016**, *1*, 150.

(34) Bai, S.; Sakai, N.; Zhang, W.; Wang, Z.; Wang, J. T. W.; Gao, F.; Snaith, H. J. *Chem. Mater.* **2017**, *29*, 462.

(35) Ling, L.; Yuan, S.; Wang, P.; Zhang, H.; Tu, L.; Wang, J.; Zhan, Y.; Zheng, L. *Adv. Funct. Mater.* **2016**, *26*, 5028.

(36) Forgacs, D.; Sessolo, M.; Bolink, H. J. *J. Mater. Chem. A* **2015**, *3*, 14121.

(37) Oesinghaus, L.; Schlipf, J.; Giesbrecht, N.; Song, L.; Hu, Y.; Bein, T.; Docampo, P.; Müller-Buschbaum, P. *Advanced Materials Interfaces* **2016**, *3*, 1600403.

(38) Hexemer, A.; Muller-Buschbaum, P. *IUCrJ* **2015**, *2*, 106.

(39) Schlipf, J.; Müller-Buschbaum, P. *Advanced Energy Materials* **2017**, *7*, 1700131.

(40) Zhao, L.; Luo, D.; Wu, J.; Hu, Q.; Zhang, W.; Chen, K.; Liu, T.; Liu, Y.; Zhang, Y.; Liu, F.; Russell, T. P.; Snaith, H. J.; Zhu, R.; Gong, Q. *Adv. Funct. Mater.* **2016**, *26*, 3508.

(41) Scher, H.; Montroll, E. W. *Physical Review B* **1975**, *12*, 2455.

(42) Grill, I.; Aygüler, M. F.; Bein, T.; Docampo, P.; Hartmann, N. F.; Handloser, M.; Hartschuh, A. *ACS Applied Materials & Interfaces* **2017**, *9*, 37655.

(43) Eperon, G. E.; Burlakov, V. M.; Goriely, A.; Snaith, H. J. *ACS Nano* **2014**, *8*, 591.

(44) Jung, J. W.; Chueh, C.-C.; Jen, A. K. Y. *Advanced Energy Materials* **2015**, *5*, 1500486.

(45) Fu, F.; Feurer, T.; Jäger, T.; Avancini, E.; Bissig, B.; Yoon, S.; Buecheler, S.; Tiwari, A. N. *Nature Communications* **2015**, *6*, 8932.

(46) Roldan-Carmona, C.; Malinkiewicz, O.; Betancur, R.; Longo, G.; Momblona, C.; Jaramillo, F.; Camacho, L.; Bolink, H. J. *Energy Environ. Sci.* **2014**, *7*, 2968.

5 PEROVSKITE CRYSTAL FACETS: DO THEY MATTER?

This chapter is based on a publication in preparation:

Nadja Giesbrecht, Eline Hutter, Irene Grill, Johannes Schlipf, Alexander Hufnagel, Peter Müller-Buschbaum, Achim Hartschuh, Thomas Bein, Tom Savenije, Pablo Docampo

5.1 INTRODUCTION

In recent years, hybrid halide perovskite compounds have evolved extremely attractive for optoelectronic applications. Photovoltaic devices employing methylammonium lead iodide ($MAPbI_3$) as absorber material nowadays reach power conversion efficiencies (PCE) over 20 %, while mixed anion and cation perovskite materials can yield PCEs of over 22 %.[1-4] Beyond compositional optimization of perovskite films and their morphology, interface engineering is critical to achieving high efficiencies and in fact, has played a significant role in the rapid development of the photovoltaic device efficiency.[2,5-10] However, the efficiency loss mechanism in optoelectronic devices is still not fully understood. Further optimization of perovskite-based optoelectronic device efficiencies requires the understanding of these fundamental characteristics.

Perovskite materials exhibit a surprisingly high defect tolerance, where polycrystalline films with crystal sizes in the nanometre range still show high charge carrier mobilities and lifetimes.[11-14] The significantly more pronounced non-radiative charge carrier recombination locates at interfaces of the perovskite layer rather than bulk and grain boundaries.[15] In this setting, perovskite surface film passivation via the introduction of molecules that can bind to the perovskite crystal is one of the main strategies to address the issue of surface recombination.[4,5,16,17] However, typical polycrystalline perovskite films exhibit a rather heterogeneous surface, with a pronounced degree of crystal facet disorder. In perovskite films with crystal facet disorder, the photoluminescence and cathodoluminescence strongly alter with the investigated grain.[18,19] The same trend applies for photovoltaic efficiency with observable intra-grain heterogeneities.[20]

In the latter study, Leblebici *et al.* suggested perovskite crystal facet-dependency of photovoltaic devices due to variations in defect densities for different crystal facets.[20] A

possible explanation for how different crystal facets might influence the solar cell performance was suggested by Yin *et al.* in a theoretical study.[21] Here, interfacial charge transfer anisotropy between different perovskite facets was proposed where hole- or electron injection varies for (200) and (002) perovskite crystal facets exposed to the charge extraction layers.[21] However, a direct correlation between perovskite crystal termination and their optoelectronic features is still missing.

Here, we investigated the impact of perovskite crystal facet termination on the behavior of optoelectronic devices. We show substantial heterogeneity in device performance under applied bias. In particular, (200) perovskite crystal facets contacted with a TiO_2 or SnO_2 interface in devices exhibit *JV*-curves with a significant s-shape indicating an energetic interfacial barrier. Analyzing the corresponding Schottky diodes, we confirmed a more pronounced energetic barrier between the (200) perovskite crystal facet and a metal oxide electron transfer layer than for the (002) facet. When fullerenes are deposited over the metal oxide interface or in inverted devices with organic interfaces, a barrier was not observable for both different perovskite crystal alignments. Interestingly, devices fabricated with perovskite films oriented with (200) facets exposed, result in fill factors which approach theoretical limitations, showcasing the importance of interfacial order to maximize charge transfer in the system. However, with time-resolved microwave conductivity (TRMC) measurements no significant difference of photoconductance was observed if (200) or (002) perovskite crystal facet was terminated at a quartz or TiO_2 interface, indicating no change in defect densities for different crystal facets.

5.2 RESULTS AND DISCUSSION

Tuning crystal orientation is challenging and usually requires different synthesis procedures.[22] We recently demonstrated a new synthesis approach for purely aligned $MAPbI_3$ perovskite crystallites where the (200) planes are parallel to the surface in thin films.[23] We attribute this high degree of crystal orientation mainly to the formation of an already highly oriented non-perovskite intermediate phase, which then converts into the perovskite structure. Therefore, the stability of the intermediate pre-perovskite-phase has a substantial impact on the final alignment of the perovskite crystallites in the layer. The addition of highly polar solvents, such as dimethylsulfoxide (DMSO) and tetrahydrothiophene-1-oxide (THTO), to the precursor solution, helps with the stabilization of the highly aligned intermediate phase. In contrast to the THTO additive, DMSO tends to form complexes with lead-based precursors, which usually leads to the high alignment of the perovskite crystals with their (002) plane parallel to the

surface.[24] Thus, the concentration of DMSO solvent additive tunes perovskite crystal alignment.

In *Figure 5 – 1c and 1f*, we show the schematics of the two main differences in the perovskite facet alignments studied here. To analyze the type and degree of perovskite crystal alignment with respect to the substrate, we performed grazing incidence wide-angle X-ray scattering (GIWAXS) experiments. This technique captures a two-dimensional slice through reciprocal space, allowing for the reconstruction of the structure and extraction of information on the orientation of the crystal planes from the azimuthal intensity distribution.[25-27] Hence, with the GIWAXS patterns in *Figure 5 – 1b* and *1e,* we can confirm the synthesis of perovskite films with strong alignment of (002) facets parallel to the substrate with 10 vol% DMSO additive, hereon termed (002) facets; or pure alignment of the (200) crystal facet parallel to the substrate with 20 vol% DMSO, hereon termed (200) facets.

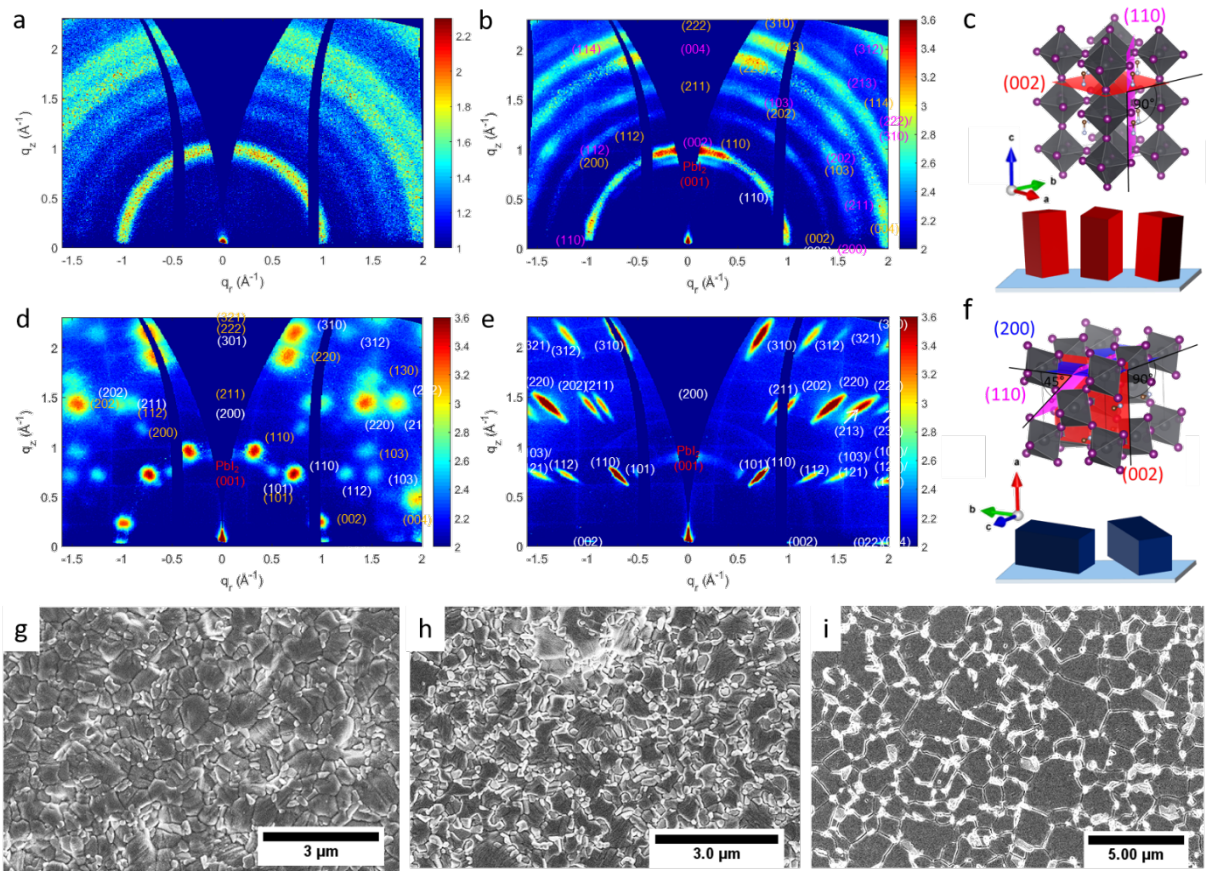

Figure 5 - 1: a) 2D GIWAXS image of non-oriented perovskite films with pure DMF-based solution; b) 2D GIWAXS image of the perovskite film with (002) facet parallel to the substrate with 10 vol% DMSO additive; c) schematic illustration of the (002) crystal facets parallel to the substrate; d) 2D GIWAXS image of the perovskite film with (200) and (321) facet parallel to the substrate with 15 vol% DMSO additive; e) 2D GIWAXS image of the perovskite film with (200) facet parallel to the substrate with 20 vol% DMSO additive; f) schematic illustration of the (002) crystal facets parallel to the substrate; g) SEM image of the non-oriented films with pure DMF-based solution; h) SEM image of the with (002) facet aligned films with 10 vol% DMSO additive; i) SEM image of the with (200) facet aligned films with 20 vol% DMSO additive.

Multiple facet alignment degrees are also possible with no preference in crystal alignment with a fully DMF-based solution (*Figure 5 – 1a*), and a mixed arrangement of (321) facets together with (200) facets in the same perovskite film with 15 vol% DMSO (see *Figure 5 – 1d*). Hence, the variation of the DMSO solvent additive between 0-20 vol% tunes the crystal alignment a large extent. We note here that the variety is highly reproducible and was confirmed with GIWAXS and XRD studies (see *Figure 5 – 2*). The change in overall film morphology, however, remained negligible and for all films, grain sizes between 1-3 µm were achieved with DMSO additive variation (see *Figure 5 – 1g-i*). When using the THTO additive instead of DMSO, we could additionally increase the grain sizes significantly to values over 10 µm in films with pure crystal alignment of (200) facets, as shown in our previous work described in chapter 4.[23]

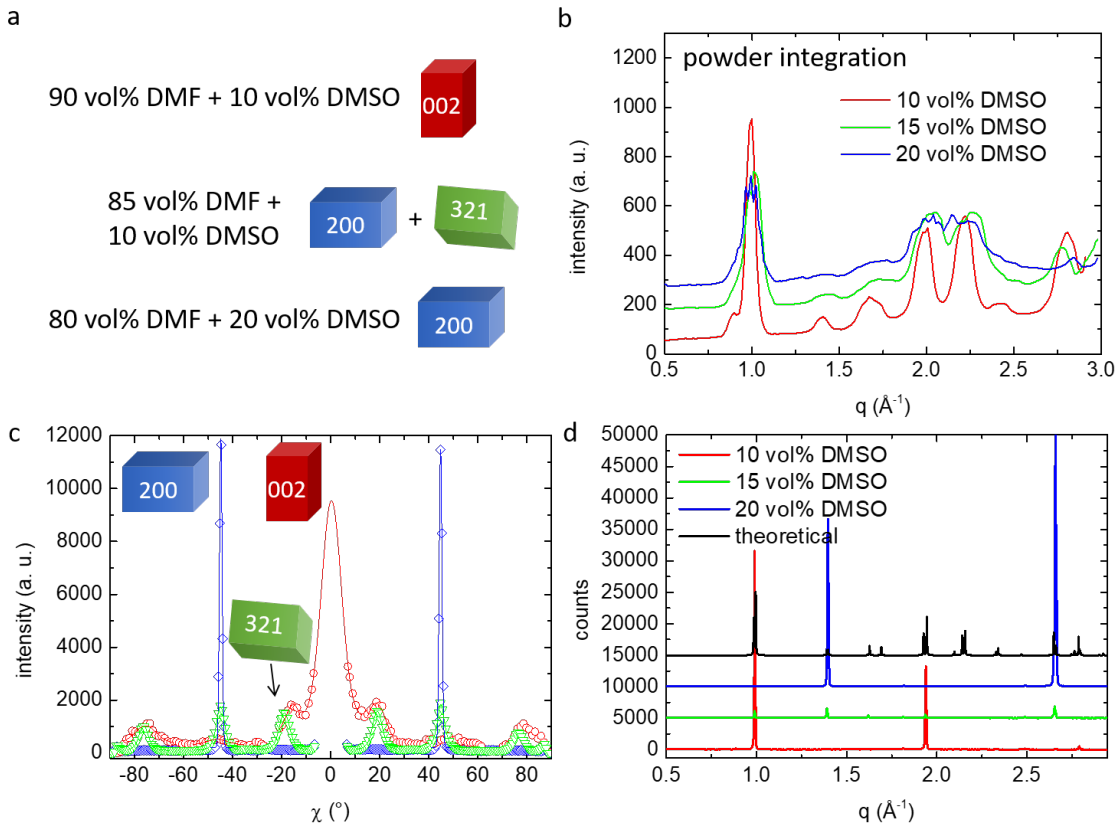

Figure 5 - 2: a) Schematic illustration of the resulting crystal alignment from the corresponding solvent mixtures; b) 1D integration of scattering data from GIWAXS results; c) azimuthal cut at q~1Å^{-1} from GIWAXS results; d) XRD results on thin films investigated with GIWAXS.

To study the impact of crystal orientation on the photovoltaic performance, we prepared devices in the regular architecture with the perovskite layers sandwiched between TiO_2 and Spiro-OMeTAD as displayed in *Figure 5 – 3a*. In *Figure 5 – 3b* and *5 – 3c* we show representative *JV*-curves of devices implementing the (002) and the (200) perovskite crystal facets at the

interface with the charge transport materials (CTMs). Here, the most significant difference appeared in the shape of the *JV*-curve close to open-circuit voltage (V_{OC}). This s-shape repeatedly appears in devices with the (200) plane facing TiO_2 and Spiro-OMeTAD resulting in lower V_{OC} and fill factor (*FF*) if directly compared to similar architectures with (002) perovskite crystal facet terminal to the substrate.

To further examine the effect of facet disorder, we prepared samples with equally strong (200) and (321) crystal facet alignment parallel to the substrate as shown in the XRD pattern and the GIWAXS investigation in *Figure 5 – 2*. Application of these films sandwiched between TiO_2 and Spiro-OMeTAD show no s-kink in the *JV*-curve. The device open circuit voltages are higher than those fabricated from pure (002) or (200) facets, similar to samples exhibiting no preferential crystal alignment (see *Figure 5 – 3*). Therefore, we can conclude that only pure perovskite crystal alignment shows a significant energetic barrier in solar cells, indicating a facet-dependent charge injection from the perovskite material to the CTMs.

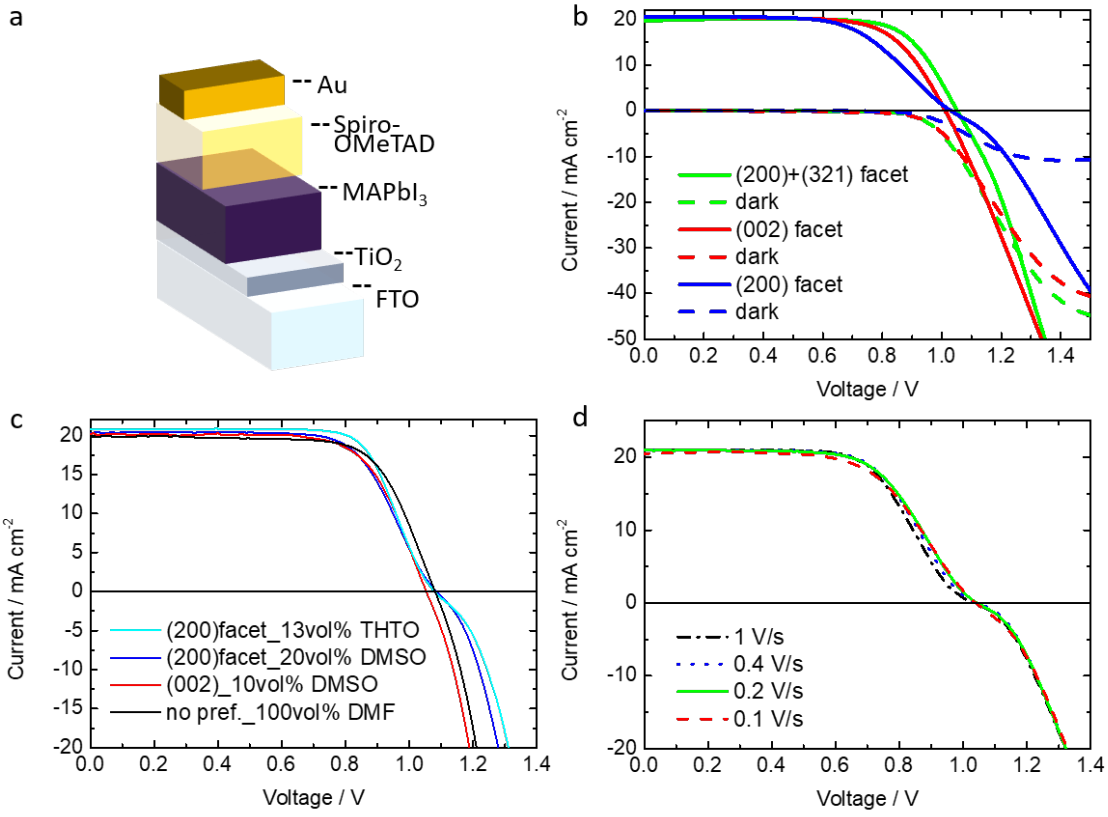

Figure 5 - 3: a) Schematic illustration of the device architecture studied in this work; b) *JV*-curves of devices employing perovskite films with (200), (002) or (200) with (321) facets parallel to the substrate in the dark and under radiation; c) *JV* curves of devices employing perovskite films made with different solvent mixtures and crystal facet alignments; d) *JV*-curves obtained with different scan speeds of devices containing perovskite films with the (200) facets parallel to the substrate.

S-shapes in the *JV*-curve are already well known and discussed in the literature for organic photovoltaic (OPV). In most cases, energy barriers at the interfaces constitute the respective kink.[28] Furthermore, the much lower dark current for the devices employing the (200) facets compared to devices with the (002) facets indicates the presence of an injection barrier, see *Figure 5 – 3b*. With a change in scan speed, the shape of the *JV*-curve remains as shown in *Figure 5 – 3d*, which indicates that the s-kink is not an electronic phenomenon due to light soaking or capacitive effects arising from ion migration.

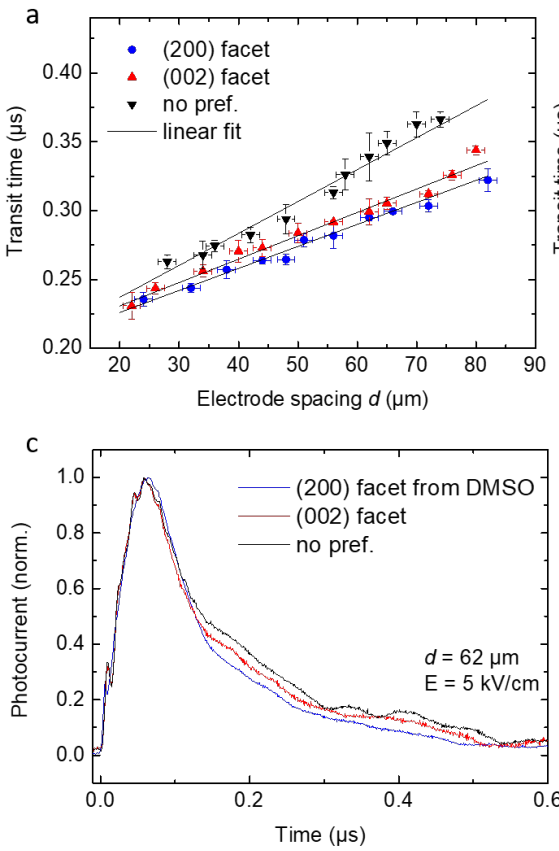

d

Crystal Facet Alignment	Hole Mobility / $cm^2(Vs)^{-1}$	Electron Mobility / $cm^2(Vs)^{-1}$	Standard deviation / $cm^2(Vs)^{-1}$
(200) from THTO	15	16	1
(200) from DMSO	12	13	1
(002)	11	12	1
No. pref	8	9	1

Figure 5 - 4: ToF analysis data of perovskite films prepared from different DMSO concentrations: a) extracted transit times for holes from ToF analysis; b) extracted transit times for electrons from ToF; c) representative transients at fixed electrode spacing with 62 µm; d) table of the extracted electron- and hole-mobility from ToF measurement.

In OPV the formation of such barriers is attributed to a variety of effects, from imbalance in charge carrier mobilities or energetic injection and extraction barriers between the photoactive layer and the electrodes.[28] Here, the s-kink arises or vanishes simply by changing the crystal alignment of the perovskite in the thin film. Therefore, we studied charge carrier mobilities of the differently aligned perovskite films with Time-of-Flight (ToF) transient photoconductivity measurements (see *Figure 5 – 4*). This technique allows the determination of charge carrier mobility upon pulsed laser excitation. To this end, we employed a lateral sample layout, which enables us to perform photocurrent measurements for varying electrode spacings *d* at constant

external voltage E (here: 5 kV/cm). By illuminating the sample at the edge of one contact, charge carriers are created locally and extracted at the opposite electrode. Hence, the polarity of the applied field determines the type of charges probed (holes or electrons). The obtained transients were plotted on a double log scale while the intersection of the pre- and post-transit defines the transit time t_{tr}, which is needed to calculate the mobility according to:

$$\mu = d/(E \cdot t_{tr}) \qquad \text{(Equation 5 – 1)}$$

A detailed description of the ToF-setup can be found in chapter 9.

From the laterally contacted perovskite films, we extracted charge carrier mobility values shown in *Figure 5 – 4d*. Representative transients, as well as the determination of the mobility from the transit time as a function of electrode spacing, are shown in *Figure 5 – 4*. We measured perovskite films with no preference in orientation and with (200) or (002) perovskite crystal facet parallel to the substrate. Grain sizes in all layers were very similar and therefore are not expected to have a substantial impact on charge transport. In all cases, we have high-quality perovskite films with balanced hole- and electron-mobilities with values over 15 $cm^2\ Vs^{-1}$ and the difference between electron- and hole-mobility was within the standard deviation, excluding an imbalance in charge carrier mobility as a possible reason for the energy barrier in devices with (200) perovskite facet.[29]

Our results show that a significant improvement of at least 35 % in mobility occurs with a higher degree of crystal alignment in the perovskite films if the grain size is similar for both crystal facet alignments, indicating the benefits of purely aligned polycrystalline films, see *Figure 5 – 4d*. In our measurements, we see no clear trend according to anisotropy in charge transport of differently aligned perovskite films. Here, the films were measured laterally, while the high alignment of our samples is in the out-of-plane direction rather than in-plane. On the other hand, ToF measurements in the vertical direction of the film (thickness around 450 nm) do not provide any meaningful information as charge transport in this direction occurs on a faster timescale than the temporal resolution of our ToF setup, which is approximately two ns.[30] Nevertheless, the correlation between higher orientational order and higher mobility is significant and reproducible.

To further explore and tailor the origin of the energetic barrier in our solar cells with (200) aligned perovskite films, we investigated interfaces to different charge transport material. We tested different Hole-Transporting Materials (HTMs) and Electron-Transporting Materials (ETMs) with the (200) perovskite interface, as shown in *Figure 5 – 5*. Here, for both HTMs,

Spiro-OMeTAD and EDOT-OMeTPA, an s-kink arises in the *JV*-curve. In the case of the ETMs, the s-kink appeared with a metal oxide interface, such as TiO_2 or SnO_2, but disappeared with the deposition of a fullerene layer between the metal oxide and the perovskite interface. In either case, with a thin PCBM layer or a C_{60}-self-assembled monolayer (SAM), the devices showed improved V_{OC} values and *FFs* and a correspondingly enhanced device performance. Most importantly, in these cases no s-shape of the *JV*-curve was visible.

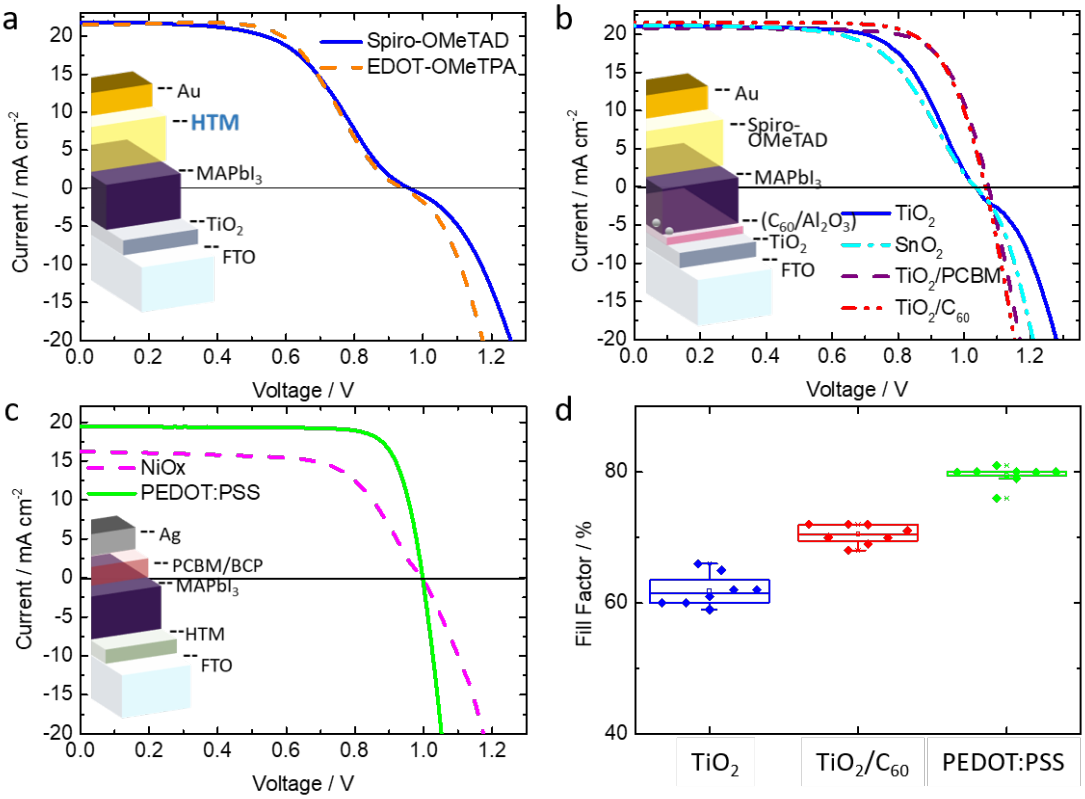

Figure 5 - 5: (200) Perovskite facets applied in different device architectures, each schematic of the architecture is shown inside the plot: a) *JV*-curves of devices in the configuration with different HTMs; b) *JV*-curves of devices in the architecture with different ETMs; c) *JV*-curves of devices in inverted architecture with different HTMs; d) deviation of fill factor with different bottom CTMs.

A similar trend is observed with inverted devices for different HTMs, as shown in *Figure 5 – 5d*. In the representative *JV*-curves of devices employing NiO_x as HTM, the (200) perovskite shows a slight s-shape that is not present with PEDOT:PSS at the interface. In particular, devices with inverted architectures with the (200) facet exposed to PEDOT:PSS and PCBM reach a fill factor of 81 %, approaching the theoretical maximum of 89 %.[31] These fill factor values are 10 % higher than the ones obtained with a C_{60} layer at the interface and about 20 % higher than with devices employing a TiO_2-interface with s-kink in the *JV*-curves (see *Figure 5 – 5d*).

To quantify the barrier heights of the contacts between (200) or (002) perovskite crystal facets in combination with a metal oxide interface like SnO_2, we prepared Schottky diodes with PCBM and silver on top (see *Figure 5 – 7a*). We fitted the *JV*-curves to the Schottky diode equations:

$$J = J_S e^{\frac{qV}{kT-1}} \qquad \text{(Equation 5 – 2)}$$

$$J_S = A^* T^2 e^{\frac{-\varphi_B}{kT}} \qquad \text{(Equation 5 – 3)}$$

J is current density; J_s is the saturation current which is extrapolated from the current density at 0V; V is applied bias; q is the electron charge; k the Bolzmann constant; T the temperature; A is the Richardson constant for thermionic emission; φ_B is the Schottky barrier height.*

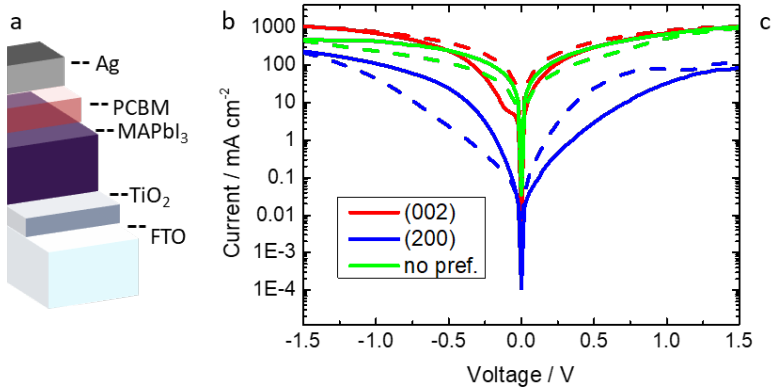

c

Device	Dark ϕ_B(eV) Reverse scan	Dark ϕ_B(eV) Forward scan
(200) Facet	0.23±0.02	0.17±0.02
(002) Facet	0.13±0.02	0.08±0.01
No pref.	0.10±0.02	0.11±0.01

Figure 5 - 6: a) Schematic illustration of the Schottky diode architecture; b) *JV*-curves of the Schottky diodes in dark, measured from 1.5 V to -1.5 V to 1.5 V, the current obtained from 1.5 V to 0 V was multiplied by -1, full lines for reverse scan and dashed lines for forward scan; c) table containing Schottky barrier heights for diodes estimated by fitting the *JV*-curves in b) with *Equation 5 – 3*.

This approach assumes that all the injection current is via thermionic emission, ignores the shape of the barrier and tunneling currents and assumes band-bending in the perovskite layer. We used $A^* = 1.54 \cdot 10^{-5}$ A cm^{-2} K^{-2} for the Richardson constant, as was approximated for a $MAPbI_3$-$MAPbBr_3$ heterojunction.[34] The values were not derived explicitly for our system. Therefore, our obtained barrier heights are considered to be rough estimates. We calculated the barrier heights from the fits shown in *Figure 5 – 6b* and summarized the values in *Figure 5 – 6c*. Here, the estimated barrier heights follow the trend observed in the *JV*-curves of devices containing different perovskite crystal facets exposed to a metal oxide interface (TiO_2 or SnO_2) with significantly more pronounced barrier heights for the (200) facet/ SnO_2 interface. Additionally, a definite kink is present in the forward scan around 1 V for the diode containing (200) facet, similar to the s-kink in solar cells.

5.3 CONCLUSION

In this work, we showed how the $MAPbI_3$ perovskite crystal termination impacts photovoltaic device performance. We studied the (200) and (002) crystal facet terminations in polycrystalline perovskite thin films accomplished by a new approach switching crystal alignment within the same layer synthesis approach. With this method, the charge transport was improved in both highly ordered films compared to films with the disorder in crystal alignment. However, photovoltaic devices revealed a perovskite crystal facet-dependent anisotropy in performance. In particular, perovskite films with (200) facets exposed to a metal oxide CTM show a highly pronounced s-shape in the *JV*-curve, leading to a loss in V_{OC} and *FF*. With a C_{60} monolayer at the metal oxide interface the energetic barrier was removed, and the *FF* improved. Especially with the use of inverted devices with PEDOT:PSS and PCBM as CTMs and (200) perovskite facet at the interfaces, the *FF* increased close to its theoretical limit without hysteresis in device performance. With our results, we prove and specify the impact of different perovskite crystal facets and emphasize the importance of perovskite crystal facet dependent interface engineering for highly efficient perovskite solar cells.

5.4 LITERATURE

(1) Ahn, N.; Son, D.-Y.; Jang, I.-H.; Kang, S. M.; Choi, M.; Park, N.-G. *J. Am. Chem. Soc.* **2015**, *137*, 8696.

(2) Yang, W. S.; Park, B.-W.; Jung, E. H.; Jeon, N. J.; Kim, Y. C.; Lee, D. U.; Shin, S. S.; Seo, J.; Kim, E. K.; Noh, J. H.; Seok, S. I. *Science* **2017**, *356*, 1376.

(3) Best Research-Cell Efficiencies (NREL, h. w. n. g. n. i. e. c. j.

(4) Zhang, H.; Wu, Y.; Shen, C.; Li, E.; Yan, C.; Zhang, W.; Tian, H.; Han, L.; Zhu, W.-H. *Advanced Energy Materials* **2019**, *9*, 1803573.

(5) Tan, H.; Jain, A.; Voznyy, O.; Lan, X.; García de Arquer, F. P.; Fan, J. Z.; Quintero-Bermudez, R.; Yuan, M.; Zhang, B.; Zhao, Y.; Fan, F.; Li, P.; Quan, L. N.; Zhao, Y.; Lu, Z.-H.; Yang, Z.; Hoogland, S.; Sargent, E. H. *Science* **2017**, *355*, 722.

(6) Correa-Baena, J.-P.; Tress, W.; Domanski, K.; Anaraki, E. H.; Turren-Cruz, S.-H.; Roose, B.; Boix, P. P.; Gratzel, M.; Saliba, M.; Abate, A.; Hagfeldt, A. *Energy Environ. Sci.* **2017**, *10*, 1207.

(7) He, M.; Li, B.; Cui, X.; Jiang, B.; He, Y.; Chen, Y.; O'Neil, D.; Szymanski, P.; Ei-Sayed, M. A.; Huang, J.; Lin, Z. *Nature Communications* **2017**, *8*, 16045.

(8) Zhou, H.; Chen, Q.; Li, G.; Luo, S.; Song, T.-b.; Duan, H.-S.; Hong, Z.; You, J.; Liu, Y.; Yang, Y. *Science* **2014**, *345*, 542.

(9) Shao, Y.; Yuan, Y.; Huang, J. *Nature Energy* **2016**, *1*, 15001.

(10) Ahmadi, M.; Hsiao, Y.-C.; Wu, T.; Liu, Q.; Qin, W.; Hu, B. *Advanced Energy Materials* **2017**, *7*, 1601575.

(11) Stranks, S. D.; Eperon, G. E.; Grancini, G.; Menelaou, C.; Alcocer, M. J. P.; Leijtens, T.; Herz, L. M.; Petrozza, A.; Snaith, H. J. *Science* **2013**, *342*, 341.

(12) Xing, G.; Mathews, N.; Sun, S.; Lim, S. S.; Lam, Y. M.; Grätzel, M.; Mhaisalkar, S.; Sum, T. C. *Science* **2013**, *342*, 344.

(13) Dong, Q.; Fang, Y.; Shao, Y.; Mulligan, P.; Qiu, J.; Cao, L.; Huang, J. *Science* **2015**, *347*, 967.

(14) Wehrenfennig, C.; Eperon, G. E.; Johnston, M. B.; Snaith, H. J.; Herz, L. M. *Adv. Mater.* **2014**, *26*, 1584.

(15) Yang, Y.; Yang, M.; Moore, David T.; Yan, Y.; Miller, Elisa M.; Zhu, K.; Beard, Matthew C. *Nature Energy* **2017**, *2*, 16207.

(16) Shao, Y.; Xiao, Z.; Bi, C.; Yuan, Y.; Huang, J. *Nature Communications* **2014**, *5*, 5784.

(17) Noel, N. K.; Abate, A.; Stranks, S. D.; Parrott, E. S.; Burlakov, V. M.; Goriely, A.; Snaith, H. J. *ACS Nano* **2014**, *8*, 9815.

(18) Bischak, C. G.; Sanehira, E. M.; Precht, J. T.; Luther, J. M.; Ginsberg, N. S. *Nano Lett.* **2015**, *15*, 4799.

(19) de Quilettes, D. W.; Vorpahl, S. M.; Stranks, S. D.; Nagaoka, H.; Eperon, G. E.; Ziffer, M. E.; Snaith, H. J.; Ginger, D. S. *Science* **2015**, *348*, 683.

(20) Leblebici, S. Y.; Leppert, L.; Li, Y.; Reyes-Lillo, S. E.; Wickenburg, S.; Wong, E.; Lee, J.; Melli, M.; Ziegler, D.; Angell, D. K.; Ogletree, D. F.; Ashby, Paul D.; Toma, F. M.; Neaton, J. B.; Sharp, I. D.; Weber-Bargioni, A. *Nature Energy* **2016**, *1*, 16093.

(21) Yin, J.; Cortecchia, D.; Krishna, A.; Chen, S.; Mathews, N.; Grimsdale, A. C.; Soci, C. *J. Phys. Chem. Lett.* **2015**, *6*, 1396.

(22) Oesinghaus, L.; Schlipf, J.; Giesbrecht, N.; Song, L.; Hu, Y.; Bein, T.; Docampo, P.; Müller-Buschbaum, P. *Advanced Materials Interfaces* **2016**, *3*, 1600403.

(23) Giesbrecht, N.; Schlipf, J.; Grill, I.; Rieder, P.; Dyakonov, V.; Bein, T.; Hartschuh, A.; Muller-Buschbaum, P.; Docampo, P. *J. Mater. Chem. A* **2018**, *6*, 4822.

(24) Cao, J.; Jing, X.; Yan, J.; Hu, C.; Chen, R.; Yin, J.; Li, J.; Zheng, N. *J. Am. Chem. Soc.* **2016**, *138*, 9919.

(25) Saliba, M.; Tan, K. W.; Sai, H.; Moore, D. T.; Scott, T.; Zhang, W.; Estroff, L. A.; Wiesner, U.; Snaith, H. J. *J. Phys. Chem. C* **2014**, *118*, 17171.

(26) Giesbrecht, N.; Schlipf, J.; Oesinghaus, L.; Binek, A.; Bein, T.; Müller-Buschbaum, P.; Docampo, P. *ACS Energy Letters* **2016**, *1*, 150.

(27) Müller-Buschbaum, P. *Adv. Mater.* **2014**, *26*, 7692.

(28) Wagner, J.; Gruber, M.; Wilke, A.; Tanaka, Y.; Topczak, K.; Steindamm, A.; Hörmann, U.; Opitz, A.; Nakayama, Y.; Ishii, H.; Pflaum, J.; Koch, N.; Brütting, W. *J. Appl. Phys.* **2012**, *111*, 054509.

(29) Tress, W.; Petrich, A.; Hummert, M.; Hein, M.; Leo, K.; Riede, M. *Appl. Phys. Lett.* **2011**, *98*, 063301.

(30) Grill, I.; Aygüler, M. F.; Bein, T.; Docampo, P.; Hartmann, N. F.; Handloser, M.; Hartschuh, A. *ACS Applied Materials & Interfaces* **2017**, *9*, 37655.

(31) Baloch, A. A. B.; Hossain, M. I.; Tabet, N.; Alharbi, F. H. *J. Phys. Chem. Lett.* **2018**, *9*, 426.

(32) Guo, Q.; Cocks, I.; Williams, E. M. *Surf. Sci.* **1997**, *393*, 1.

(33) J., K.; U., B.; M., G. *Adv. Mater.* **2000**, *12*, 447.

(34) Murali, B.; Saidaminov, M. I.; Abdelhady, A. L.; Peng, W.; Liu, J.; Pan, J.; Bakr, O. M.; Mohammed, O. F. *Journal of Materials Chemistry C* **2016**, *4*, 2545.

6 UNIVERSAL NANOPARTICLE WETTING AGENT FOR UPSCALING PEROVSKITE SOLAR CELLS

This chapter is based on the following publication:

Nadja Giesbrecht*, Moritz Schultes*, Johannes Küffner, Michael Powalla, Thomas Bein, Erik Ahlswede, Pablo Docampo *ACS Appl. Mater. Interfaces*, **2019**, 11, *12948*.

*Authors contributed equally to this work.

6.1 INTRODUCTION

Hybrid lead halide-based perovskites have recently emerged as a serious contender to established technologies for photovoltaic applications. Perovskite solar cells combine record power conversion efficiencies (PCEs), comparable to record values of multi-crystalline silicon or Cu(In,Ga)Se_2 at over 22 %,[1,2] with low cost deposition methods from precursor solutions or inks, typically deposited via spin coating.[3-6] These exciting characteristics have led to extensive research efforts to fabricate large area devices in order to enable their commercialization through upscalable solution-based techniques such as spray-coating,[7] inkjet printing,[8] doctor-blading,[9] slot-die coating,[10] or drop casting.[11]

However, module fabrication is challenging and solution-based processes of stacked layers may be limited by two major technical constraints: i) re-dissolving the underlying layer has to be avoided by the use of orthogonal solvents, and ii) de-wetting of the subsequent layer has to be controlled by suitable means. The first issue constrains the number of suitable solvents, while the second issue leaves few options to form uniform perovskite films limiting possible stack architectures at present to a few traditionally used routes.

The planar n-i-p (standard) architecture mostly uses substrates with electron selective bilayers of oxides such as TiO_2 and fullerenes such as C_{60}-SAMs (self-assembled monolayers) or phenyl-C_{61}-butyric acid methyl ester (PCBM),[12-16] since they offer good contact and passivation against hysteresis effects[15-18] compared to single oxide layers.[19] The fullerenes have a low surface energy of < 40 mJm^{-2} [20,21] making the surface hydrophobic and leading to severe de-wetting issues in the subsequent perovskite layer.[22] On one hand, it was shown that hydrophobic

interfaces improve the solar cell performance by increasing the crystallite size.[23] On the other hand it is very difficult to produce large scale homogeneous layers without uncovered areas on the hydrophobic fullerene interfaces, which strongly inhibit the upscaling possibilities of these devices. In the p-i-n (inverted) architecture, large area devices could be printed on well wetting hole transport materials such as Poly(3,4-ethylenedioxythiophene)-poly(styrenesulfonate) (PEDOT:PSS),[24] but there are other more promising materials available, which are often very hydrophobic such as Poly(3-hexylthiophen-2,5-diyl) (P3HT) or Poly(triaryl amine) (PTAA).[25]

In order to overcome these issues a methodical step is needed, which enables good wetting, yet does not alter the morphology, complies with any printing technique and plays only a passive role in the solar cell performance. Testing solvent pre-treatment of the hydrophobic material on our samples showed only little effect. Plasma etching is also an option for surface activation and usually can improve the wetting, but the risk of damaging the sensitive organic layer is high. Furthermore, surface treatments such as plasma etching do not prevent a change in crystallization dynamics caused by different surfaces.[26] Selective linkers have been used to specifically increase the surface energy of certain materials,[27] but this is of course very demanding to develop for any new material.

This work demonstrates a universal wetting strategy enabling the deposition of perovskite thin films independent of deposition technique or nature and size of the substrate. This method comprises the deposition of electrically inert metal oxide nanoparticles (NPs) (≤50 nm) such as aluminum oxide (Al_2O_3) or silicon oxide (SiO_2) at the problematic interfaces, e.g. C_{60}-SAMs or P3HT. We show that the insulating nature of the nanoparticles ensures a passive application without interrupting the functionality of the interface whether it is p-type or n-type. Notably, already 14 % surface coverage with the NPs improves the wetting behavior of the perovskite dramatically and facilitates a homogeneous spread of the precursor film. Consequently, high-quality perovskite film morphologies with 5-10 µm grain sizes as previously introduced[28] are feasible in the same quality for 144 cm^2 large area devices in standard (n-i-p) geometry with a low-surface-energy fullerene bottom-contact and for modules with about 24 cm^2 active area dimension. Moreover, the wetting promotion by the particles can be adapted for various other hydrophobic interfaces and is not only limited to perovskite deposition.

6.2 RESULTS AND DISCUSSION

Improved Wetting by Nanoparticles

In order to understand how nanoparticles improve the wetting on variant low-energy surfaces, we have carried out contact angle measurements with perovskite precursors based on different solvents. Following Young's theory, the contact angle of a liquid droplet directly relates to the surface energy and therefore is an indicator for the surface wettability by perovskite solutions.[29] From these investigations we can conclude that the density of particle distribution on the surface and the particle size have the strongest influence on the wettability. *Figure 6 – 1a* illustrates the general mechanism how the nanoparticles decrease the contact angle and improve the droplet spreading that results in homogeneous perovskite layers without de-wetting issues regardless of the solution deposition technique.

To prove the strong effect of the distribution of nanoparticles on the surface, we deposited commercially available Al_2O_3 nanoparticles by spin coating from differently diluted alcoholic dispersions. *Figure 6 – 1b* shows scanning electron microscopy (SEM) images of a fullerene (PCBM) surface and the spatial distribution of nanoparticles deposited from a 0.2 wt% in isopropanol (IPA) solution, which corresponds to a covered area of 14 %. The Al_2O_3 nanoparticles have a mean diameter of 35 nm (±26 nm) (see SEM images and size distribution in *Figure 6 – 2a* and *Figure 6 – 2b*). Following the graphs in *Figure 6 – 1c*, different combinations of organic interlayers (PCBM or C_{60}-SAM) and two perovskite precursors based on the solvents dimethyl formamide (DMF) and tetrahydrothiophene-1-oxide (THTO) in the volume ratio of 87:13 and γ-butyrolactone (GBL) and dimethyl sulfoxide (DMSO) (70:30) reveal the strong decrease of the contact angle with increase of the nanoparticle concentration. In all cases, increasing the nanoparticle concentration and overcoming a critical surface coverage leads to contact angle reduction to less than 10° and a change in the droplet wetting behavior. The perovskite precursor solution then spreads almost perfectly flat on top of the substrate.

Furthermore, we observed that particles with a smaller diameter lead to a stronger decline of the contact angle (*Figure 6 – 1d*). For this study, ethanol-based dispersions with 0.4 and 0.6 wt% concentration of SiO_2 nanospheres of diameters of 20, 40 and 60 nm (see *Figure 6 – 2b*) were synthesized following Bogush et al.[30] References with untreated- and ethanol pre-treated PCBM surfaces have both high contact angles of about 45°, indicating a weak effect of pure solvent pre-treatment. In our experience, alternative perovskite solvents such as DMF, GBL and DMSO or switching between isopropanol or ethanol for diluting the nanoparticles has only

little influence on the contact angle. Our results indicate that the wetting behavior is mainly influenced by concentration and size of the nanoparticles. Here, the contact angle declines below 10° in case of the smallest particles (10 nm) at 0.6 wt% concentration. Notably the variation of the diameter has a stronger effect on the contact angle than increasing the concentration. The same relation between contact angle and nanoparticle size is shown by Munshi et al.[31]

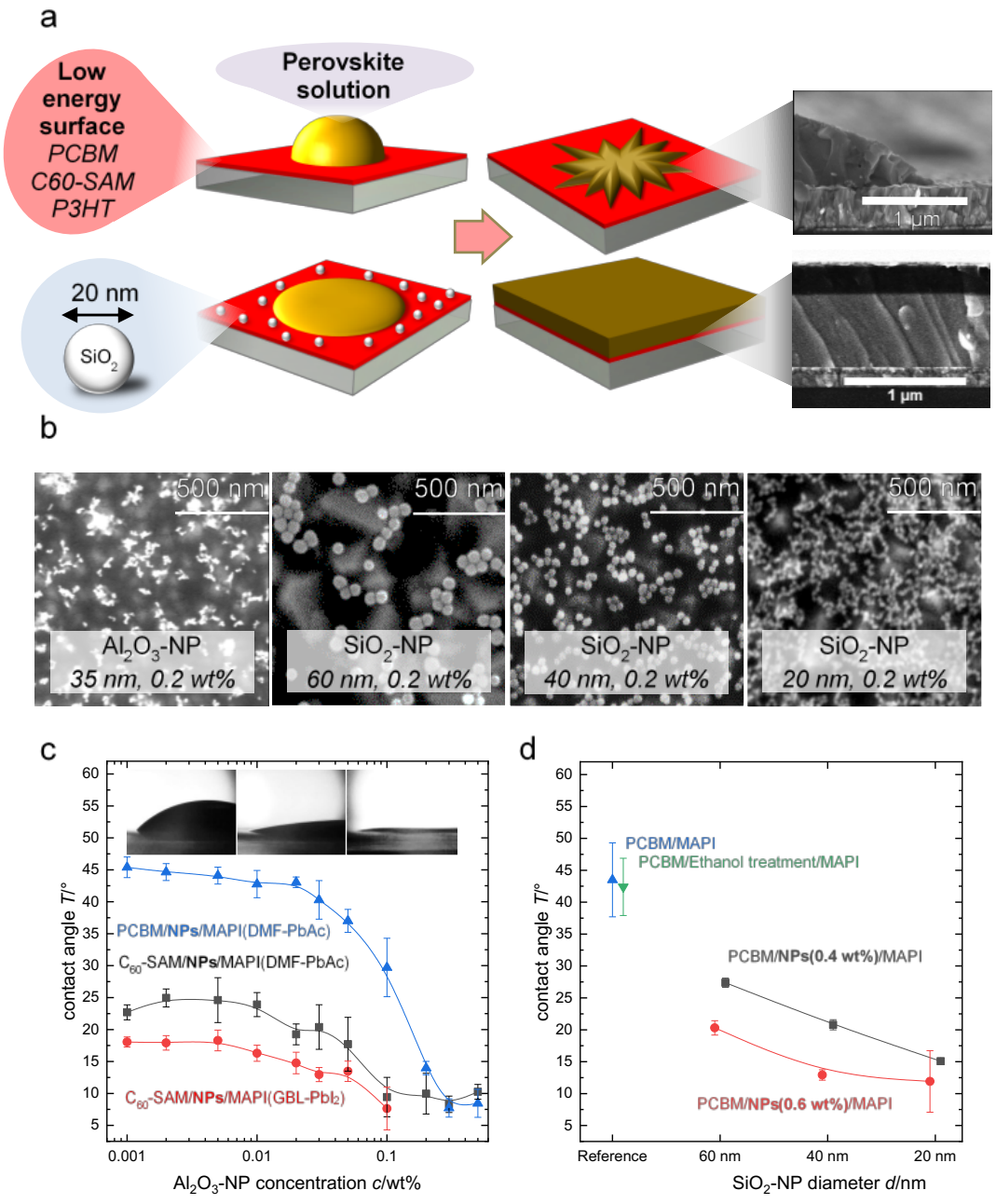

Figure 6 - 1: a) Schematic illustration of the wetting improvement by nanoparticles; b) SEM micrographs of various nanoparticles on PCBM-surface; c) contact angles of DMF/THTO+PbAc or GBL/DMSO+PbI_2-based perovskite solutions on fullerene interface (PCBM or C_{60}-SAM) covered with Al_2O_3-NPs from differently concentrated solutions; d) contact angle of a DMF/THTO+PbAc-based perovskite solution on PCBM interface covered with differently sized SiO_2-NPs.

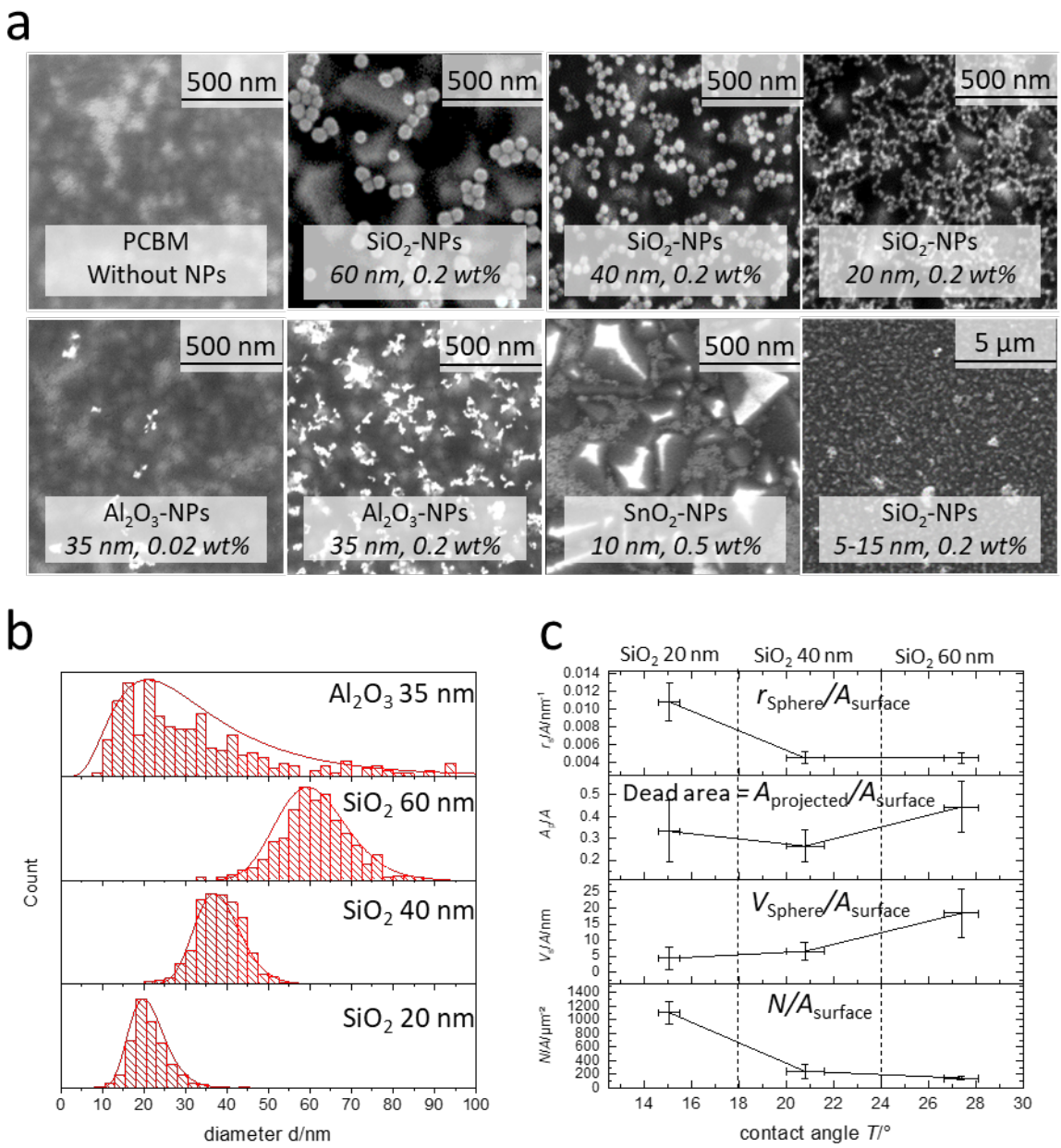

Figure 6 - 2: a) SEM micrographs of various nanoparticles on top of FTO/TiO_2/PCBM-surface; the roughness of the FTO surface effects the morphology of the PCBM and the distribution of the nanoparticles b) distribution of calculated diameters of different NPs; c) Particle quantity, volume, area and radii (normalized to surface area) of different sized SiO_2-NPs as function of contact angle.

The well-established contact angle theories of Wenzel and Cassie predict that the roughness has a strong influence on the contact angle. They describe also the transitions from the non-wetting Cassie state, in which the droplet sits on top a rough morphology with air trapped underneath, to a wetting Wenzel state, where the droplet completely penetrates the surface.[32,33] In our case, a rising number of nanoparticles increases the roughness of the interface and leads to a direct decline of the wetting angle. In consequence, we propose here wetting behavior relates to a Wenzel-like mechanism, at which the high surface energetic oxide particles increase the overall

surface energy dominated by the fullerenes and act as capillary features that force the liquid to spread in between the gaps of the energetically favored particles. Other fields of research, e.g. the fabrication of solution-processable organic transistors on hydrophobic surfaces, confirmed the validity of the Wenzel-like wetting mechanism.[34-36]

There are two reasons why a decrease of the particle diameter favors the wetting even more. By keeping the mass concentration in the precursor dispersion constant, a reduction of the particle diameter leads to a significantly increased particle density at the interface. This can be observed as a higher surface roughness, which generally improves the wetting mechanism.[31,37] Furthermore, the additional rise in free surface energy, due to the high surface-to-volume ratio and the increased number of gaps between smaller particles exhibits a strong capillary force and therefore enable the perovskite solution to spread more easily. On the other hand, nanoparticles smaller than 20 nm may show negative effects on the wetting. Due to their increased surface energy, the particles tend to agglomerate (see *Figure 6 – 2a*) and thereby the capillary action is inhibited by the large distance between the clusters.

Perovskite layer formation

In solar cell applications, the perovskite film formation is critical and usually depends strongly on the bottom layer surface.[23] For investigation of the surface coverage of Al_2O_3-NPs and the influence on the wetting, the final nucleation and crystallization behavior of the perovskite thin films, we analyzed top-view SEM images. We used the same lead acetate-based (PbAc) perovskite fabrication for large-grained $MAPbI_3$ thin films as introduced in our previous work.[38] The favorable morphology with about 5 µm sized crystallites is obtained for perovskite films directly deposited on TiO_2 and can be reproduced on top of non-wetting TiO_2/C_{60}-SAM, when varying surface coverages of Al_2O_3-NPs (see *Figure 6 – 3a-d*) are applied. Since the grain diameter is much larger than the average distance between the particles, it is very unlikely that the nanoparticles act as nucleation centers. Additionally, all related XRD patterns show no significant differences in crystallinity and crystal alignment (see *Figure 6 – 3e*).

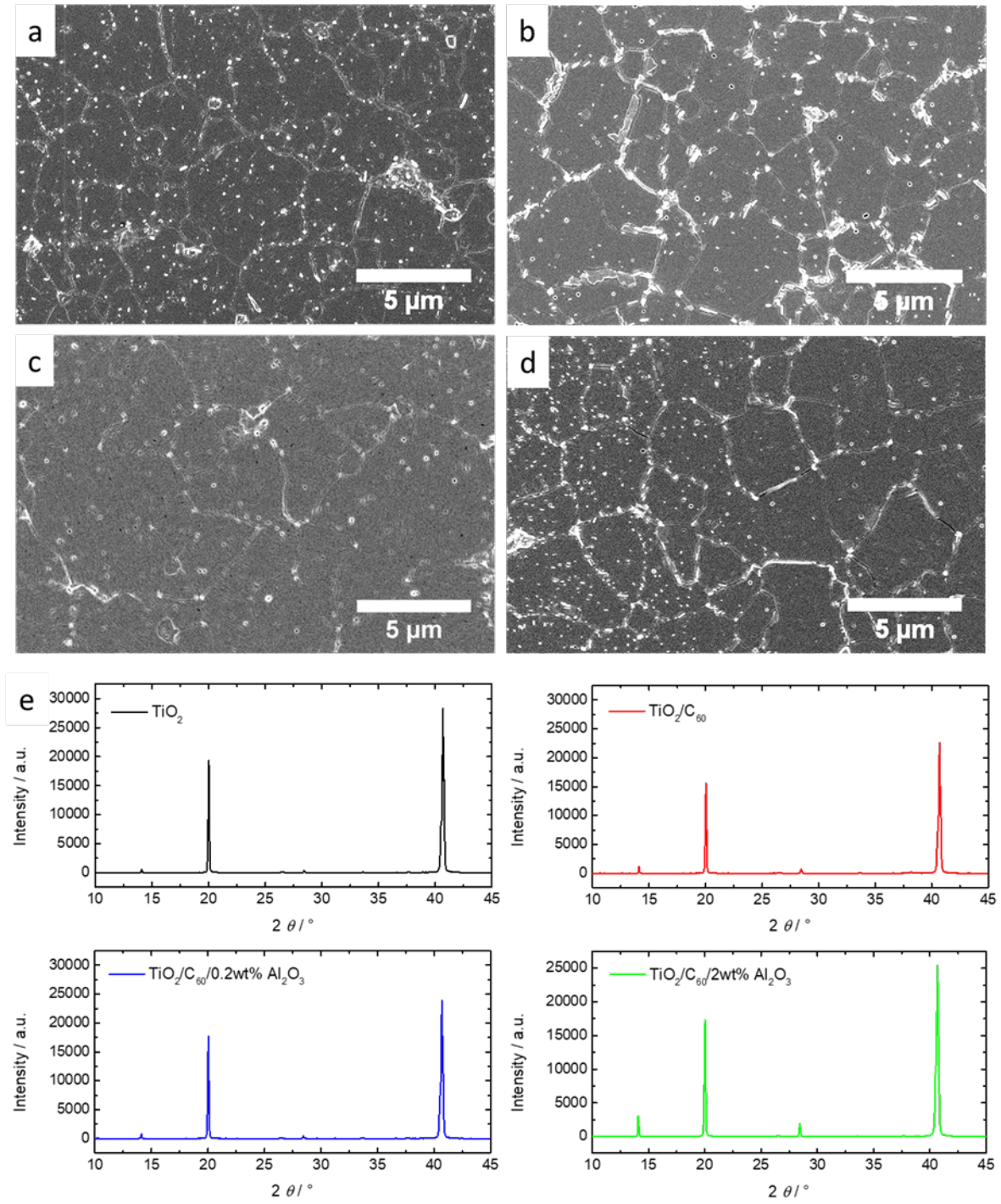

Figure 6 - 3: SEM top-views of perovskite films on top of: a) FTO/TiO_2; b) FTO/TiO_2/C_{60}-SAM/0.02 wt% Al_2O_3; c) FTO/TiO_2/C_{60}-SAM /0.2 wt% Al_2O_3; d) FTO/TiO_2/C_{60}-SAM /2 wt% Al_2O_3; e) XRD pattern of perovskite thin films crystallized on top of different interfaces.

Furthermore, we studied the effect of substrate surface dependent perovskite crystallization on microscopic glass or silicon wafers with and without nanoparticle wetting agent. These substrates used for analytical means should demonstrate the same perovskite morphology from the solar cell stack with TiO_2 interface. An additional plasma-etching step was needed to enable full surface coverage on reference surfaces without nanoparticles. Both plasma treated glass

and silicon substrates result in perovskite films with morphological defects (see the red marks in *Figure 6 – 4*), but the application of Al_2O_3-NPs at the interface enable comparable and high quality perovskite morphologies in both cases (see *Figure 6 – 4b* and *Figure 6 – 4d*). These results indicate that not only the wetting improves but also the perovskite morphology is well controlled when using additional oxide nanoparticles on any substrate surface.

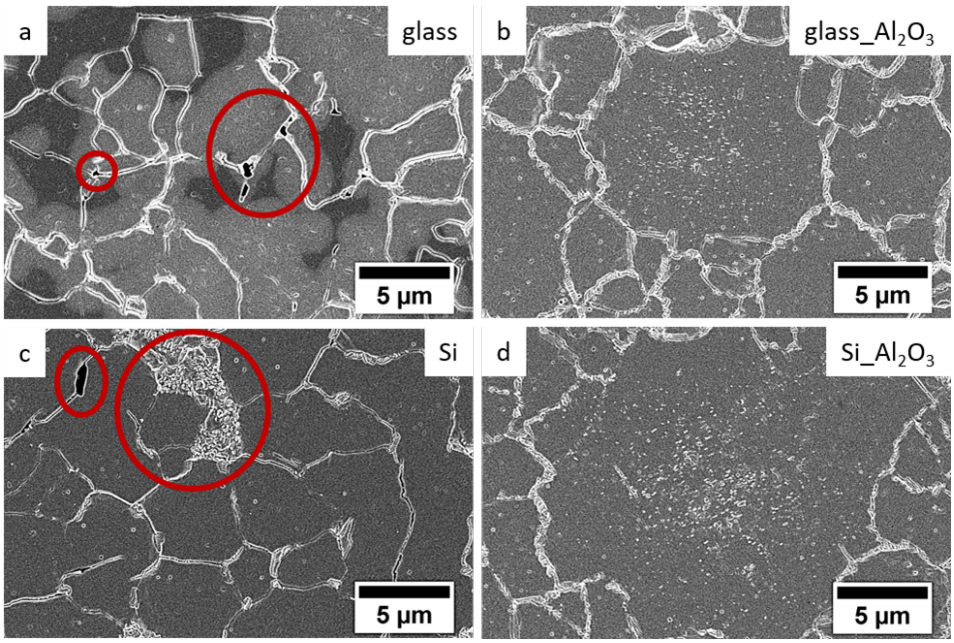

Figure 6 - 4: SEM top-views of perovskite films on top of: a) plasma etched microscopic glass; b) glass/0.02 wt% Al_2O_3-NPs; c) plasma etched silicon; d) silicon/2 wt% Al_2O_3-NPs.

In order to study the impact of the wetting strategy on the solar cell performance, we prepared full device stacks with variation in type, size and distribution of NPs. The device stack of the investigated n-i-p architecture was FTO/TiO_2/C_{60}-SAMs/NPs/$MAPbI_3$/Spiro-OMeTAD/Au (compare also *Figure 6 – 12c*).

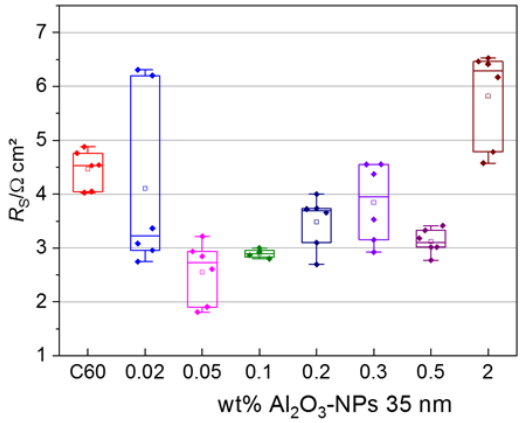

Figure 6 - 5: Series resistance of devices (ITO/TiO_2/C_{60}-SAM/Al_2O_3-NPs/$MAPbI_3$/Spiro-OMeTAD/Au) employing Al_2O_3 nanoparticles from dispersions with different concentrations. The series resistance was calculated from one diode equivalent circuit model fits to the dark *JV*-response and the reverse *JV*-scan under one sun illumination.

Figure 6 – 6b shows that the C_{60}-SAMs at the interface improve the power conversion efficiency of the devices compared to non-treated TiO_2 interfaces. We attribute this to the improved fill factor (see *Figure 6 – 7c*), but we observe a bad reproducibility due to the poor wetting properties. This is overcome with the application of the metal oxide NPs at the interface and the best compromise between perovskite surface coverage and efficiency (18%) was achieved with 0.2 wt% Al_2O_3-NP in solution (IPA) with an average particle size of 35 nm and resulting surface coverage of 14 % (see *Figure 6 – 2a*). Only a rather concentrated 2 wt% solution of Al_2O_3-NPs leads to a drop of PCE. Analyzing the *JV*-data (*Figure 6 – 7*) reveals significant losses in J_{sc} and *FF* due to the complete coverage of the interface by the insulating metal-oxide particles. In all other cases with only fractions of the surface covered, the solar cells reached J_{sc} values larger than 22 mA cm^{-2}, which is close to the theoretical maximum of the $MAPbI_3$ perovskite material. This confirms the transparency of the non-conducting SiO_2 or Al_2O_3 nanoparticles and that their presence neither results in dark areas nor that they inhibit charge transport. As shown in our previous work[38] the achieved short-circuit current density values correlate perfectly with the value of 22.45 mA cm^{-2} determined from an external quantum efficiency measurement.

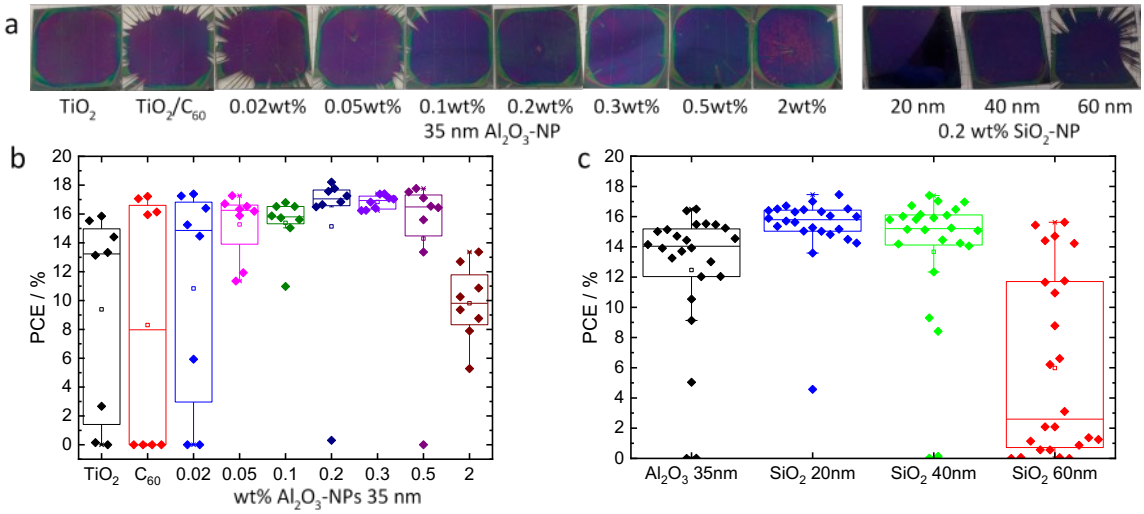

Figure 6 - 6: a) Photographs of perovskite film coverage in devices (without electrodes) with different NP concentrations at the C_{60}-SAM-interface; b) Boxplots of performance values from devices employing different surface coverage of Al_2O_3-NPs at the interface; c) Boxplots of performance values from devices employing Al_2O_3 or SiO_2 nanoparticles with different particle sizes from 0.2 wt% solution. Shown values were measured reversely from + 1.5 to 0 V at a scan speed of 0.2 V/s.

Further analysis of the dark and light *JV*-curves by fitting a one-diode equivalent circuit model revealed, that devices with a simple C_{60}-SAM interface suffer from higher series resistances of 4 to 5 Ωcm² compared to devices employing nanoparticles (see *Figure 6 – 5*). Concluding from the previous observations, the capillary forces seem to aid the formation of a better interface with less defects between the fullerenes and the perovskite, by which the mean series resistance

of the devices could be decreased to 2 to 4 Ωcm² for nanoparticle concentrations between 0.05 to 0.5 wt%. Once again, applying a too high concentration of nanoparticles of 2 wt% leads to an increased series resistance due to the insulation of the interface.

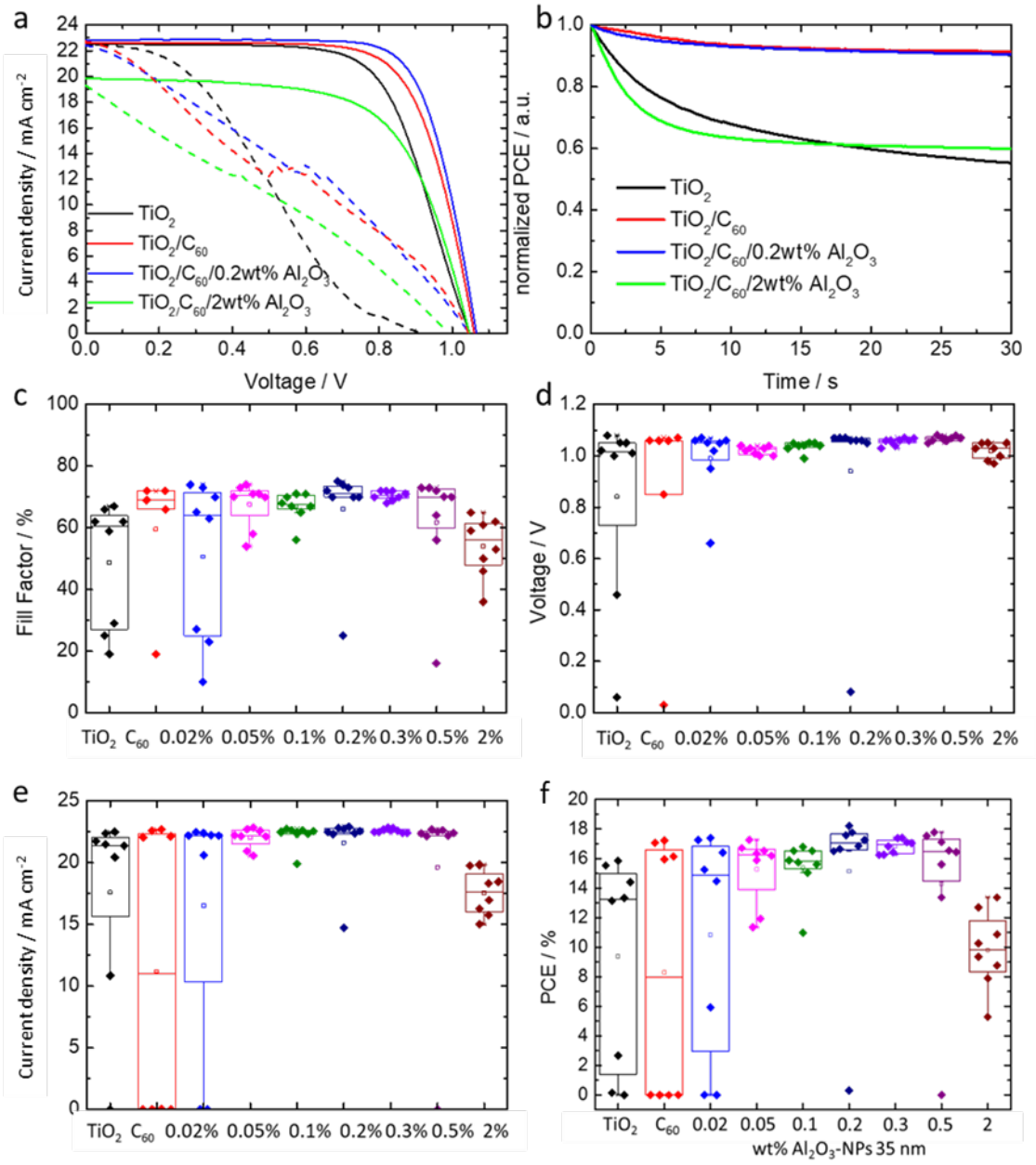

Figure 6 - 7: a) JV-curves of devices with different bottom interfaces (in configuration ITO/bottom interface/$MAPbI_3$/Spiro-OMeTAD/Au), straight lines for reverse scan and dashed lines for forward scan; c-e) box plots of performance for devices employing Al_2O_3 nanoparticles from dispersions with different concentrations: c) fill factor FF; d) open circuit voltage V_{oc}; e) short circuit current density J_{sc}; f) power conversion efficiency.

The devices of this work show rather strong hysteresis as visible in *Figure 6 – 7a* due to the large preferential orientation of the perovskite crystals as described in our previous work.[38] However, stabilized PCE values at maximum power point of up to 16.5 % are achieved due to the additional fullerene interface with NPs - a significant improvement compared to reference

samples with a simple TiO_2 layer (see *Figure 6 – 7b*). Low concentrations of Al_2O_3-NPs at the fullerene interface maintain the power output stability of the devices and in general the NPs do not affect the hysteresis negatively, indicating that they do not inflict additional charge accumulation.

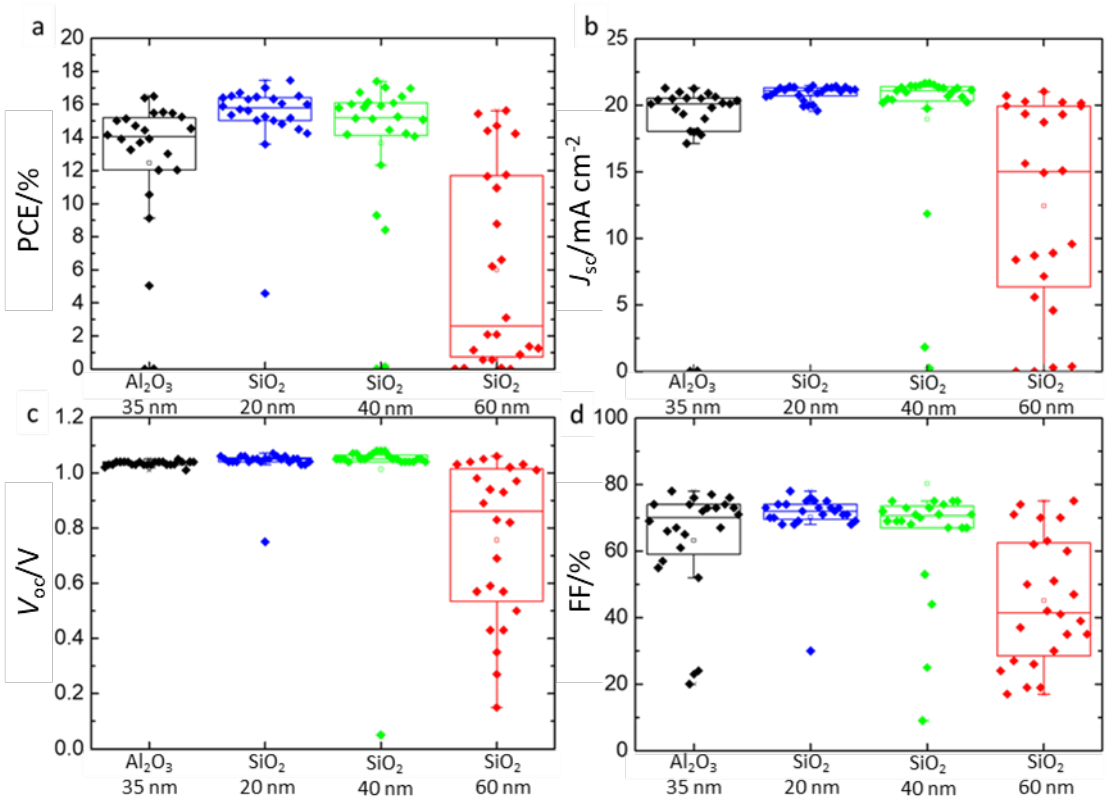

Figure 6 - 8: Box plots of performance for devices employing Al_2O_3 or SiO_2 nanoparticles with different particle sizes: a) PCE; b) short circuit current density J_{sc}; c) open circuit voltage V_{oc}; d) fill factor FF.

An additional experiment was designed to evaluate the influence of the NP-material choice as well as the wetting-impact of the size of the individual particles, by using the previously introduced SiO_2 nanoparticles with very narrowly distributed average diameters of 20, 40, and 60 nm, respectively (*Figure 6 – 2b*). As expected from the contact angle studies, the wetting benefits from a decrease in NP-size. In particular, 20 nm sized SiO_2-particles at the interface usually show better photovoltaic performance in comparison to larger particles (*Figure 6 – 6c* and *Figure 6 – 8*) originating from the generally improved reproducibility of high performing devices. Bad wetting and poor layer quality lead to a large scattering of the performance, when the largest particles (60 nm) are employed. Providing good wetting conditions by choosing a preferably small particle size and an appropriate concentration, the choice of the insulating oxide material, here Al_2O_3 or SiO_2, does not affect solar cell parameters significantly (see

Figure 6 – 8), which repeatedly confirms the passive role of the NPs in the solar cell functionality.

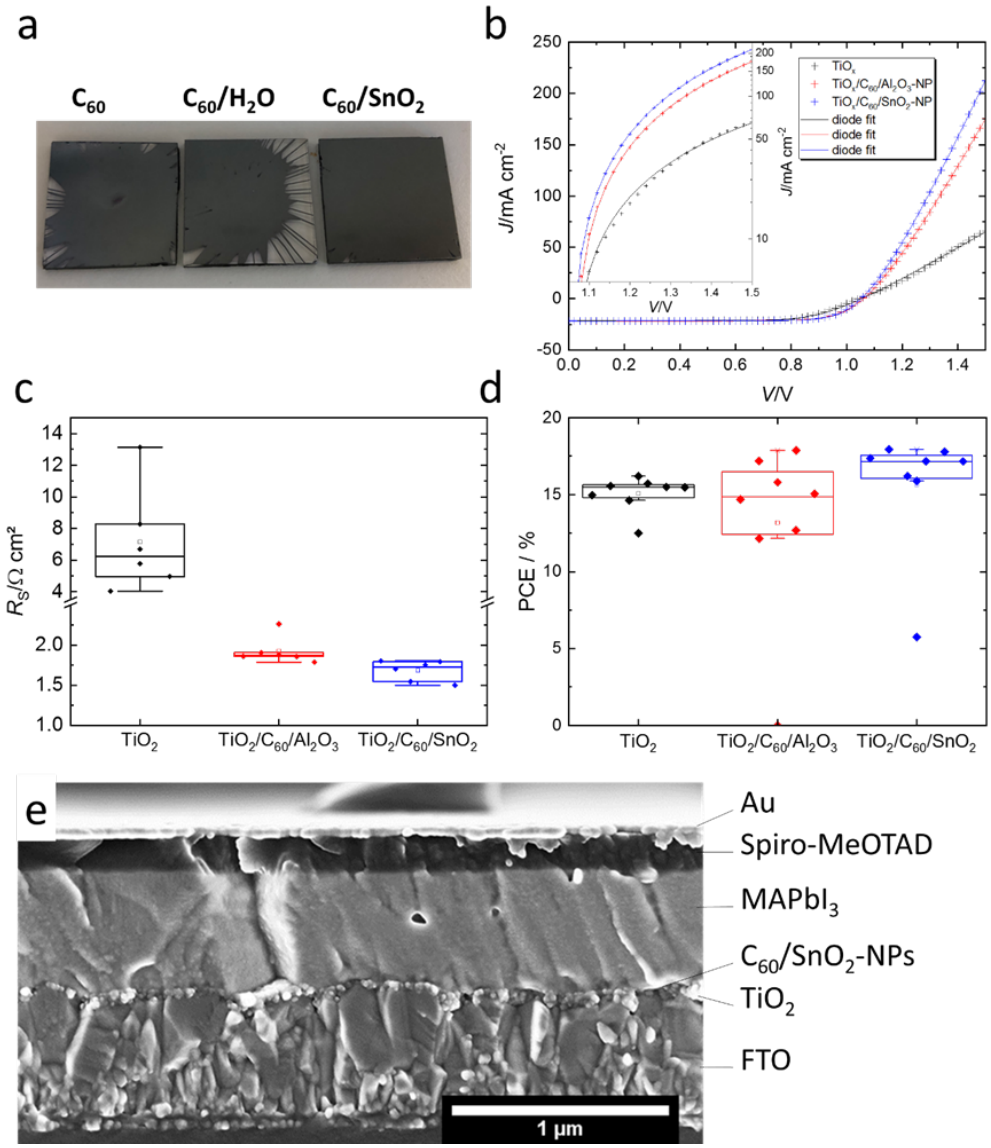

Figure 6 - 9: a) Photographs of perovskite devices with different interfaces (FTO/TiO_2/Interface/$MAPbI_3$), the center sample was treated with an H_2O dripping, in order to rule out any wetting effects by the H_2O from the aqueous SnO_2-NP dispersion; b) *JV*-curves from similar devices with different NP interfaces fitted by a one diode equivalent circuit model in order to determine the series resistance; c) and d) boxplot of the corresponding device efficiencies (experimental) and series resistance (simulated fits); e) cross sectional SEM micrograph of a device with SnO_2 based wetting agent.

In special applications, it may be beneficial to turn the passive NPs into active contributors. Tin oxide (SnO_2) is widely used in perovskite solar cells as a n-type semiconductor and is commercially available as nanoparticle dispersions, thus making these n-type NPs a perfect candidate for their application on n-type fullerene interfaces. As expected from the previous findings, these 10-15 nm oxide-NPs from a 0.5 wt% aqueous dispersion improve the wetting equally well compared to the insulating nanoparticles, but as an electron selective charge conductor, the SnO_2-NPs improve the solar cell performance actively. Analysis of the *JV*-

response proves the active role of the SnO_2, because the additional gathering and transfer of charges through the nanoparticles enlarges the contact area and leads to a reduction of the device series resistance down to 15 Ωcm² (*Figure 6 – 9*). However, these may not be universally applicable to other interfaces that require a passive wetting agent, whereas on p-type interfaces other p-semiconducting oxides such as NiO_x might facilitate the wetting as well as the electrical contact improvement.

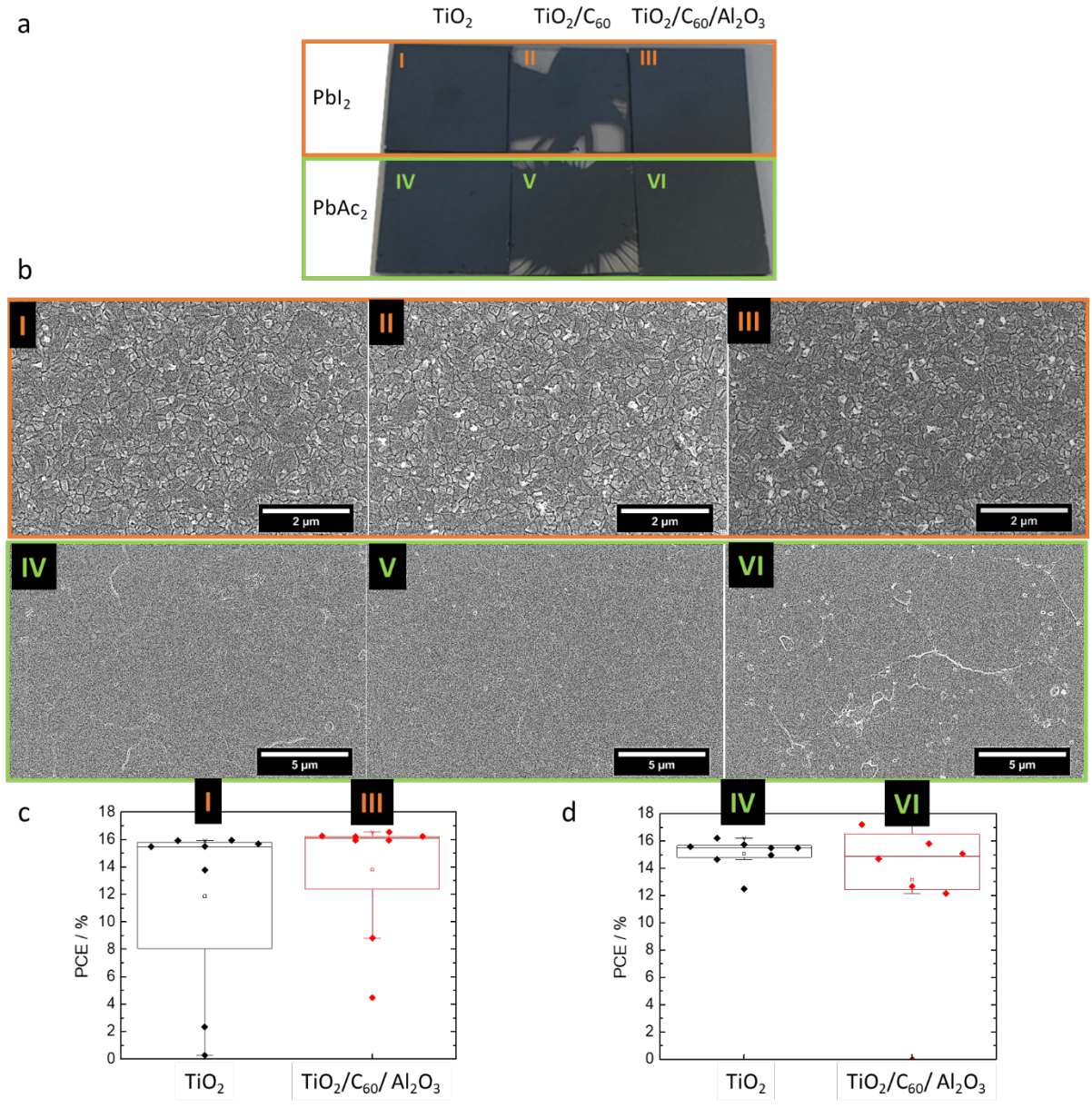

Figure 6 - 10: a) Photographs of different perovskite layers on different interfaces FTO/TiO_2/Interface/$MAPbI_3$. The perovskite was deposited in different approaches (orange) by a one-step PbAc based process and (green) by a PbI_2 based anti-solvent dripping method; b) corresponding SEM top view micrographs show the uniform morphology on the different interfaces marked by roman numbers; Boxplots of the power conversion efficiency of the corresponding devices with c) PbI_2 based precursor and d) PbAc based precursor.

Besides the previously discussed one-step PbAc-based deposition method with the large grain morphology, various other perovskite recipes could possibly benefit from the wetting agent.

For demonstrating this, we chose a PbI_2-based perovskite deposition method including the formation of the Pb-DMSO complex together with an anti-solvent initiated nucleation, resulting in grain sizes smaller than 1 µm.[39] This method is commonly applied and usually shows less dependency on substrate surface interactions compared to the PbAc deposition technique without anti-solvent, which is used in this work for large area deposition.[40] In direct comparison between both methods, in each case the application of nanoparticles is mandatory in order to get complete coverage of the FTO/TiO_2/C_{60}-SAM substrates (*Figure 6 – 10a*). As we already demonstrated for the PbAc-based perovskite, also the small grain morphology of the PbI_2-based perovskite can be reproduced on either wetting oxide-, non-wetting fullerene-, or wetting fullerene-surfaces after nanoparticles have been applied to it (*Figure 6 – 10*). In contrast to earlier reports[23] a facilitated grain growth due to the non-wetting C_{60}-SAMs interface is not observable in our studies.

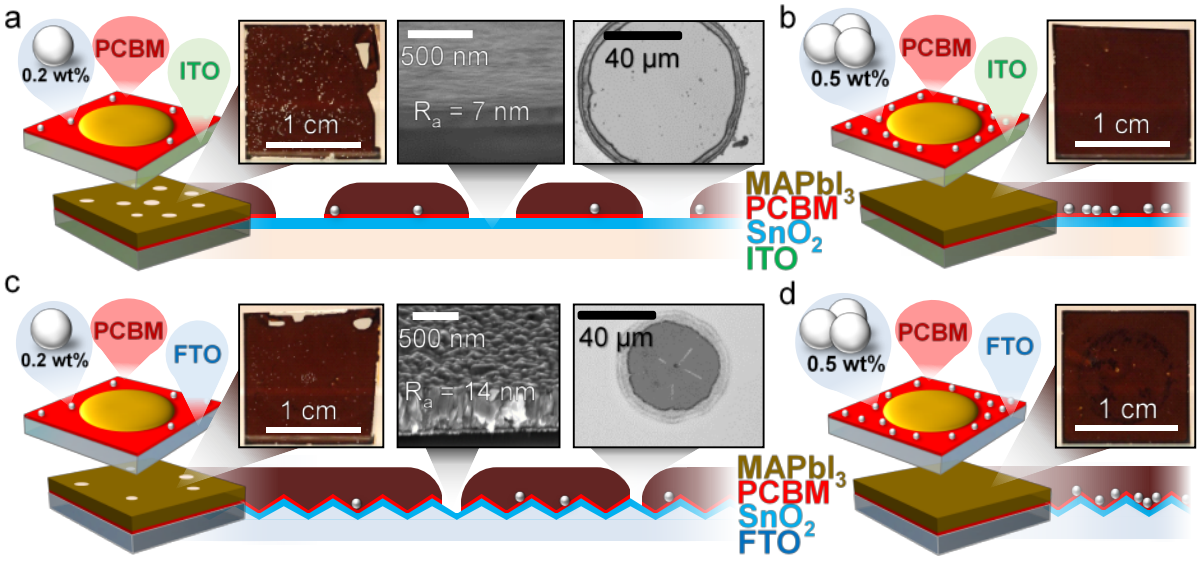

Figure 6 - 11: a-d) Demonstration of pinhole defect suppression by the application of Al_2O_3 nanoparticles on different substrates (ITO/SnO_2, FTO/SnO_2) with PCBM as fullerene layer.

However, when dealing with even more hydrophobic materials like PCBM instead of C_{60}-SAMs and further reduce the surface energy by a decreased surface roughness, pinhole formation in the perovskite layer is often an issue, which is highly critical for upscaling perovskite solar cells.[4] In order to analyze this effect in more detail, two substrates, one with a low (ITO) and one with high surface roughness (FTO), have been spin coated with GBL/DMSO+PbI_2-based perovskite along with a toluene anti-solvent step.

Despite the enhanced wetting through the 0.2 wt% Al_2O_3-NP layer *Figure 6 – 11a* and *11c* shows the formation of macroscopic pinholes in the crystallized perovskite layer in the top-

view photographs and confocal micrographs after spin coating. The smooth surface of ITO/SnO_2/PCBM has a very low surface energy and exhibits more and larger pinholes than the second rougher FTO/SnO_2/PCBM sample. The pinholes form due to de-wetting of the still-wet precursor solution during spin coating. During the nucleation step, the toluene cast dissolves and removes the PCBM from the pinhole bottom. This example shows how substrate morphology, choice of materials and solvents can lead to different wetting issues. In both cases however, the pinholes could be effectively suppressed by increasing the surface energy with the application of a higher concentration of Al_2O_3-NPs of 0.5 wt% as shown in *Figure 6 – 11b* and *11d*.

Large area spin coating and module fabrication

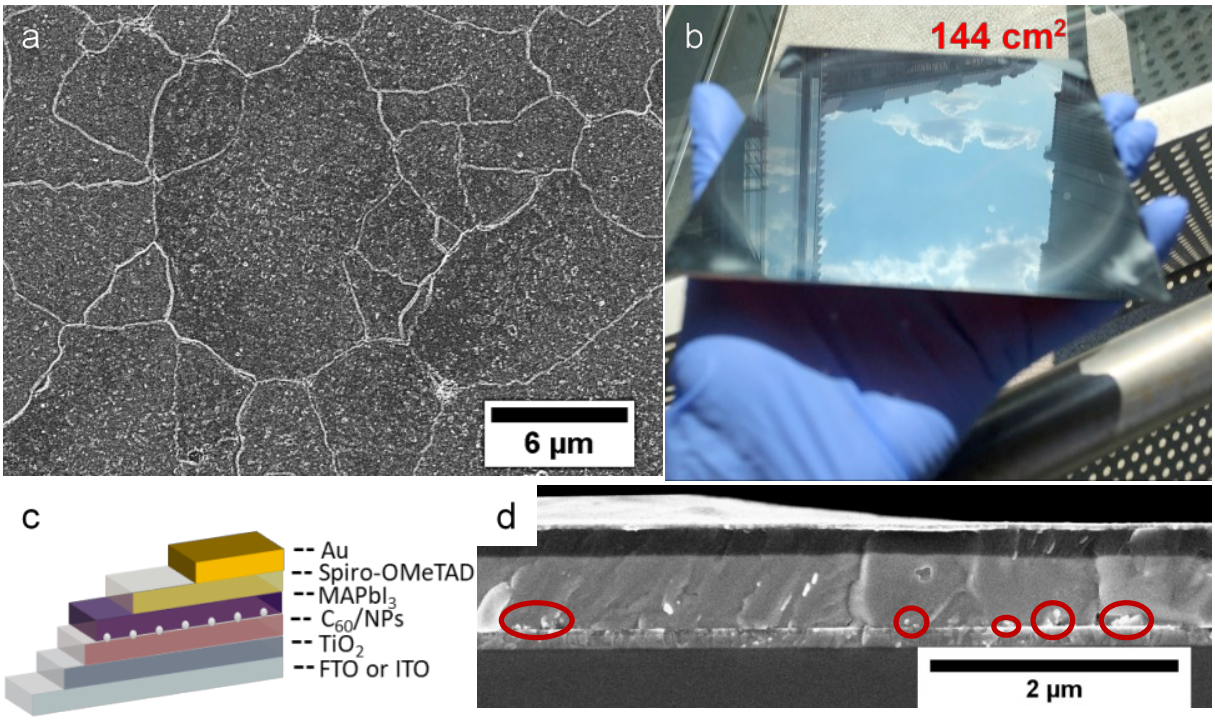

Figure 6 - 12: a) SEM image of perovskite film morphology; b) photograph of 144 cm^2 sized substrate covered with thin perovskite film; c) schematic illustration of the device stack; d) SEM cross-section of devices from large scale deposition with NPs marked in red circles.

With proper control of the wetting behavior, it is possible to push the substrate size to the technical limit of the spin coater, in our case to sample diameters of 17 cm. Even then, the application of the nanoparticle wetting agent enables complete coverage and furthermore provides control of the perovskite morphology. Consequently, we proved this by the usage of the PbAc-based, one-step spin coating procedure that produces perovskite films with characteristic 5 µm large grains and scaled it up from 9 cm^2 to a 144 cm^2 substrate (*Figure 6 – 12a* and *12b*) in a setup with ITO/TiO_2/C_{60}-SAMs and NP treatment. As shown in *Figure*

6 – 13b-f the perovskite grain size and coverage remains homogeneous even on the 16-times larger substrate.

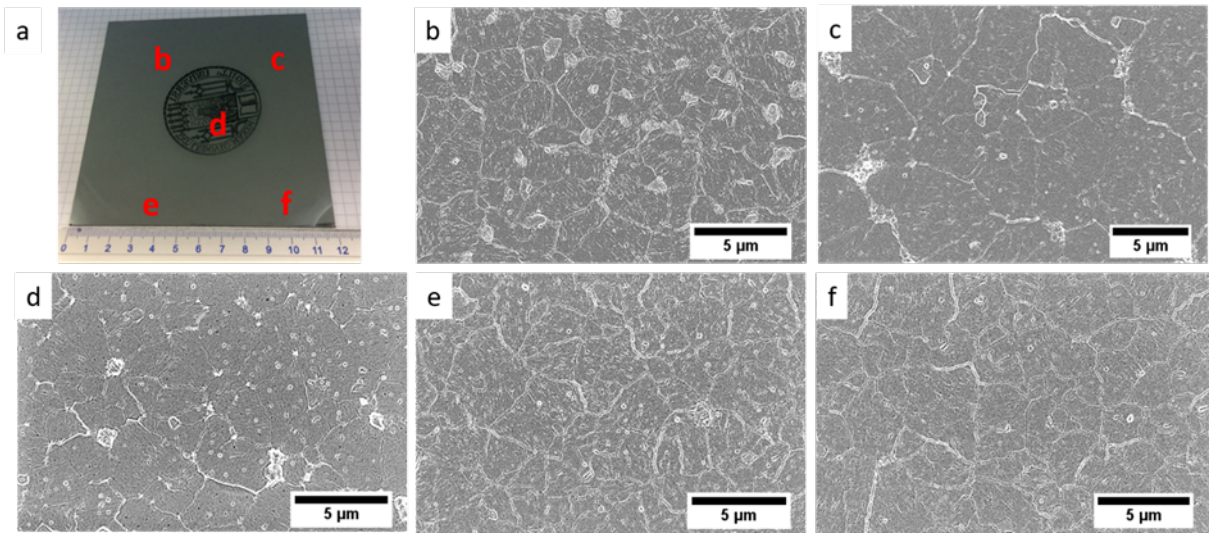

Figure 6 - 13: a) Photograph of 144 cm² substrate with perovskite on top, letters in red mark the different spots of SEM investigation; b-f) SEM images of perovskite morphology in different spots of the large area thin film.

In order to demonstrate that the device performance can be maintained on larger substrate sizes, full devices composed of ITO/TiO_2/C_{60}-SAM/NPs/$MAPbI_3$/Spiro-OMeTAD/Au (see *Figure 6 – 12c* and *12d* were prepared on a 144 cm^2 area. Afterwards, the sample was cut into 16 pieces to match our standard test device structure (30 x 30 mm² substrate area) defining 12 cells with an active area of 0.0831 cm^2 each (*Figure 6 – 14a* and *14b*). Device efficiencies of approximately 16 % on average are similar to the ones reached by processing small-sized, standard test devices in the same device architecture. Comparing the devices out of the lower left quadrant of the 144 cm^2 substrate (*Figure 6 – 14a*), only minor variations in device performance are apparent (*Figure 6 – 14c-f*) indicating a homogeneous deposition of the total of all layers on the large device area. However, we note that our hotplate used for the perovskite annealing at 130 °C step was only about 14 cm in diameter, and the corners of the large substrate reached beyond the hotplate. Therefore, the corners of the substrate show inhomogeneity and were discarded from the investigation.

Reproducible perovskite deposition on increased substrate sizes is particularly desirable for the fabrication of modules. Insufficient wetting interactions of perovskite precursor solutions on top of fullerene interfaces have limited the module fabrication in this configuration so far. Here, we present a large area module in ITO/TiO_2/C_{60}-SAM/NPs/$MAPbI_3$/Spiro-OMeTAD/Au architecture with an aperture area of 23.65 cm². The overall efficiency of the device containing 11 cells with 2.15 cm^2 active area each is 5.7 %, with evenly distributed individual cell

performance between 5-7 % (see black curves in *Figure 6 – 15a*). The narrow distribution in performance indicates a homogeneous perovskite layer quality over the full area of the module. Furthermore, we confirmed the perovskite layer quality by light-induced current (LBIC) mappings (*Figure 6 – 15c* and *15d*). The mappings show evenly colored areas that indicate a homogeneous charge carrier generation and extraction throughout the complete film. Small shunts would already result in a current drop over the complete cell area, as it is the case for cell number 10 and 11 in *Figure 6 – 15c*. Little inhomogeneity originates from comet-like defects induced by the spin coating process.

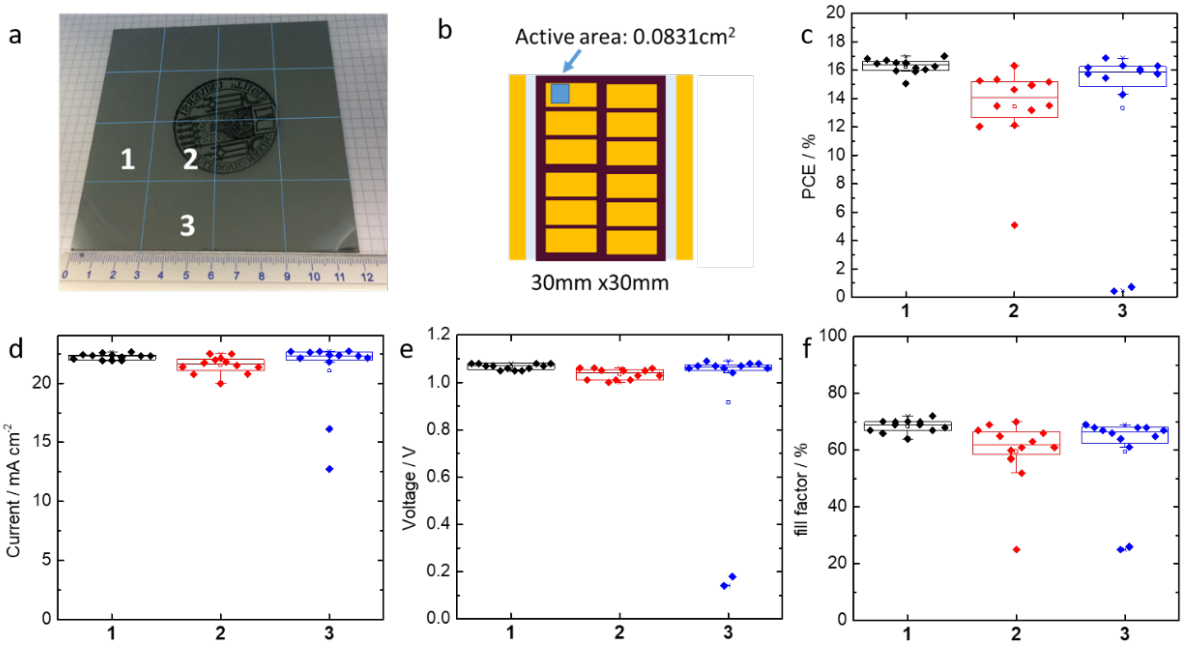

Figure 6 - 14: a) Photograph of 144 cm² sized substrate covered with thin perovskite film, lines in blue indicate the cuts for 9 cm² devices. The numbers correspond to the device pieces characterized in photovoltaic efficiency with each 12 pixels as schematically shown in b); c-f) Box plots of photovoltaic device parameters. Corresponding devices marked in a).

The performance loss of modules compared to small area devices mostly derives from a significantly reduced fill factor (FF). With increased device area, the series resistance at the interconnections becomes more dominant. Therefore, the smaller device (red curves) with an active area of 2.8 cm² shows the potential of the setup with a higher power conversion efficiency of 10.7 %. Both modules exhibit high open circuit voltages of V_{OC} = 1050 mV, which add up almost loss-free in the serial interconnection (*Figure 6 – 15b*) to a total open circuit voltage of 10.4 V of the large module.

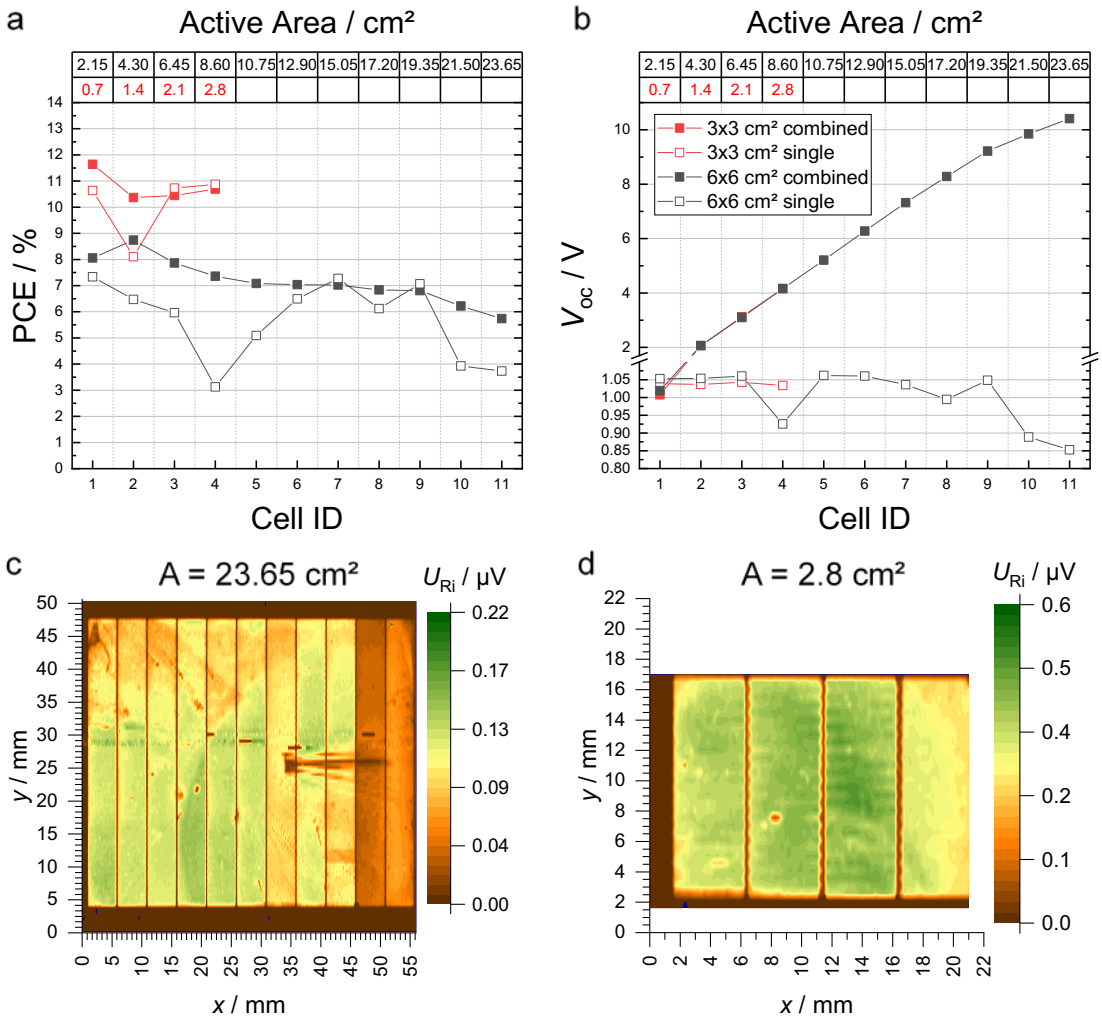

Figure 6 - 15: a) PCE chart of 2.8 cm² (red) and 23.65 cm² modules (black). Filled dots: measurements of cells in serial connection; white dots: measurements of individual cells; b) open circuit voltage V_{oc}; c) and d) light beam induced current (LBIC) mappings of each module.

Extended application for upscaling

Wetting challenges of the perovskite precursor on different types of thin films are inherent of the technique utilized for its deposition, but our nanoparticle wetting agent is truly universal for upscaling any sort of perovskite solar cell stack. Having already demonstrated successful wetting of hydrophobic polymers, molecules and inorganic surfaces by spin coating, we show how upscalable solution-based printing techniques benefit from our solution as well. Therefore, we chose doctor blading as a representative upscaling method to deposit a DMF+PbAc-based perovskite layer on top of a poly-3-hexylthiophene (P3HT) interface with the aid of SiO_2-NPs. The polymeric hole transport material P3HT is a candidate for the p-i-n architecture, but can hardly be used underneath a perovskite layer due to its extremely low surface energy of below 30 mJ m^{-2}.[20] Initially, the doctor blade forces the DMF-based perovskite solution to wet the

P3HT interface, but the super-hydrophobicity leads to immediate de-wetting of the film and the solution remains in the meniscus of the blade. The result of the non-coated P3HT surface is observable from the cross-section SEM image in *Figure 6 – 12d*. Only the application of SiO_2-NP at the interface allows for sufficient wetting of the perovskite solution and the subsequent formation of a uniform crystalline layer (*Figure 6 – 16b*). Comparing to reference p-i stacks with (PEDOT:PSS), that can also be coated without the aid of NPs due to its higher surface energy of over 70 mJ m^{-2} [41] (*Figure 6 – 16c* and *16d*), we conclude that the morphology and film thickness is again well controlled by the wetting agent. These results show high potential of our nanoparticle-induced wetting strategy to promote the fabrication of perovskite solar cells by scalable printing techniques such as blade coating.

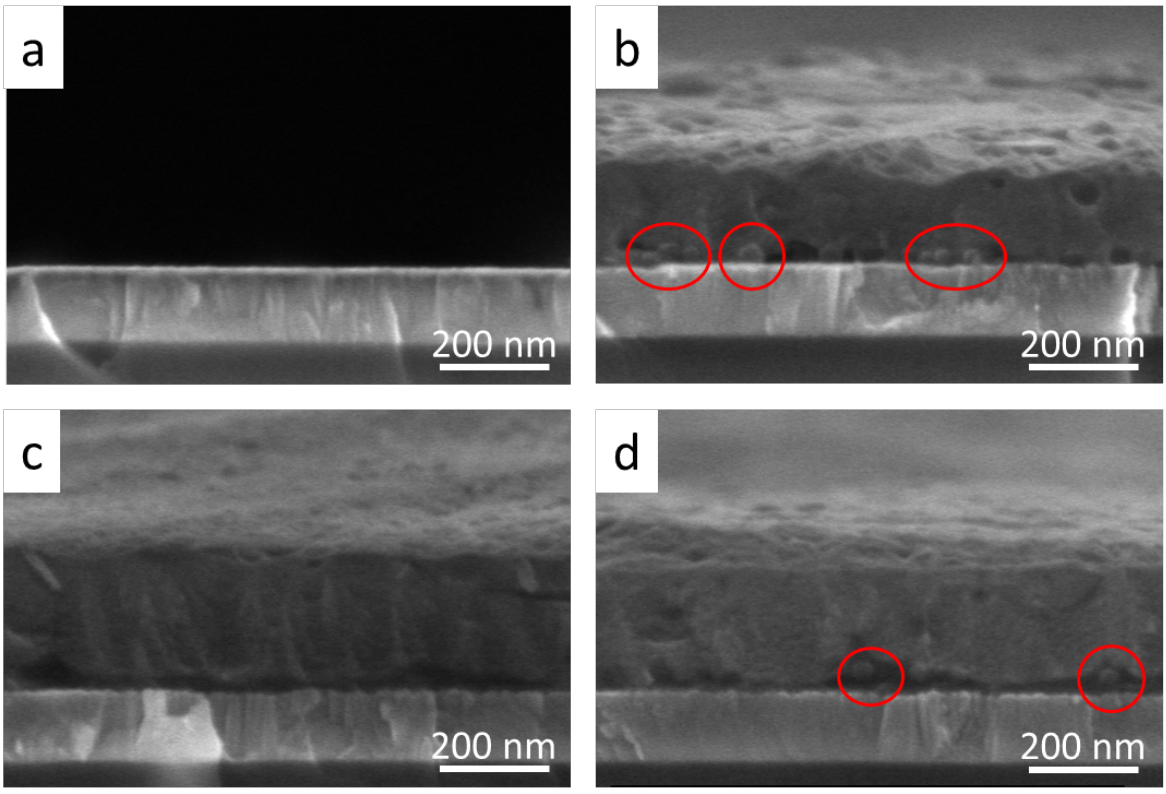

Figure 6 - 16: SEM cross-sections of blade coated perovskite layers on top of a) ITO/P3HT (due to de-wetting, no perovskite remained on the surface); b) ITO/P3HT/SiO_2-NPs (red circles); c) ITO/PEDOT-PSS; d) ITO/PEDOT-PSS/SiO_2-NPs (red circles).

Not only perovskite film deposition suffers from wetting challenges but also various other applications. The use of NPs to improve wetting on low-energy surfaces show potential to be a universally valid solution. In our experience, extremely smooth $MAPbBr_3$ films with large grain sizes[28] show non-wetting behavior towards Spiro-OMeTAD from chlorobenzene solutions (see *Figure 6 – 17a*). Thus, pinholes in the Spiro-OMeTAD layer regularly appear and the devices

suffer mostly from local voids in the hole-transporting layer. When Al_2O_3-NPs from a 0.2 wt% solution cover the surface of the $MAPbBr_3$ perovskite film we can deposit a homogenous Spiro-OMeTAD layer on top (see *Figure 6 – 17b*). As a result, the number of completely HTL-covered functional devices is increased along with an increase in performance (see *Figure 6 – 17c*).

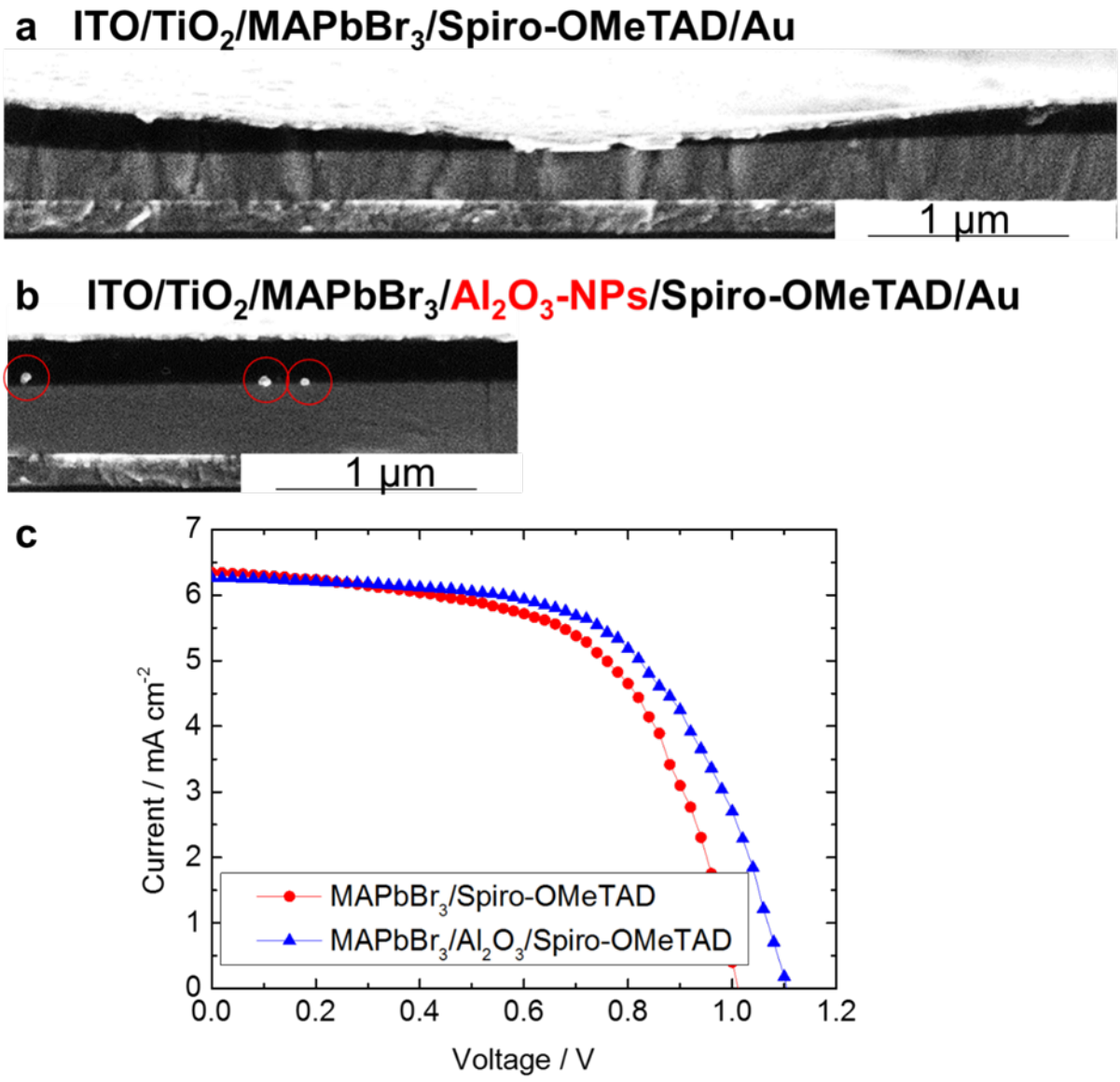

Figure 6 - 17 a) SEM cross-section of ITO/TiO_2/$MAPbBr_3$/Spiro-OMeTAD/Au and b) the same setup but with Al_2O_3-NPs at the perovskite/HTL interface; c) JV-curves of devices with ITO/TiO_2/$MAPbBr_3$/Spiro-OMeTAD/Au or ITO TiO_2/$MAPbBr_3$/Al_2O_3-NPs/Spiro-OMeTAD/Au architecture, measured reversely from 1.5 to 0 V.

6.3 CONCLUSION

In this work, we present a universally applicable wetting agent for perovskite deposition on non-wetting, low-energy surfaces. Electrically inert metal oxide nanoparticles such as Al_2O_3 or SiO_2 with diameters between 20 and 60 nm promote the wetting of perovskite precursor solutions on various surfaces. In the special case of n-type contacts SnO_2-NPs can improve both the wetting and electrical contact formation. Even hardly-wetting, low energetic surfaces e.g. PCBM, C_{60}-SAMS or P3HT are covered homogeneously and defect-free by solution-based perovskite deposition when the nanoparticles are pre-applied at the interface. Furthermore, the nanoparticles do not significantly interfere with the dominant perovskite grain growth mechanism as we demonstrate for different prominent perovskite synthesis routes. In particular, the wetting agent strategy allowed the homogeneous deposition of a perovskite film with 5 µm grains by spin coating on a 144 cm^2 large, non-wetting C_{60}-SAM interface and the fabrication of 24 cm^2 modules of the same. Interfaces with less than 30 % NP coverage provide full photovoltaic functionality. Efficiencies in the range of 16-18 % were obtained for small area perovskite solar cells deposited on 9 cm^2 and 144 cm^2 large substrates. Our route to enhance wetting on problematic surfaces provides an extremely useful tool for all solution-based deposition processes. Three major applications are conceivable: 1) Implementation of hydrophobic materials with controlled formation of subsequent perovskite layers or other functional films, 2) achieving superior results when upscaling thin film processing, and 3) realization of perovskite layers with representative morphology on any hydrophobic substrate for analytical research.

6.4 LITERATURE

(1) Yang, W. S.; Park, B.-W.; Jung, E. H.; Jeon, N. J.; Kim, Y. C.; Lee, D. U.; Shin, S. S.; Seo, J.; Kim, E. K.; Noh, J. H.; Seok, S. I. *Science* **2017**, *356*, 1376.

(2) *NREL* **2017**.

(3) Manoj, J.; Weiming, Q.; Maarten, v. E.; Tom, A.; Robert, G.; Maarten, D.; W., P. U.; Jef, P. *Advanced Energy Materials* **2017**, *7*, 1602807.

(4) Qiu, W.; Merckx, T.; Jaysankar, M.; Masse de la Huerta, C.; Rakocevic, L.; Zhang, W.; Paetzold, U. W.; Gehlhaar, R.; Froyen, L.; Poortmans, J.; Cheyns, D.; Snaith, H. J.; Heremans, P. *Energy Environ. Sci.* **2016**, *9*, 484.

(5) Yang, Z.; Zhang, S.; Li, L.; Chen, W. *Journal of Materiomics* **2017**, *3*, 231.

(6) Jaysankar, M.; Filipič, M.; Zielinski, B.; Schmager, R.; Song, W.; Qiu, W.; Paetzold, U. W.; Aernouts, T.; Debucquoy, M.; Gehlhaar, R.; Poortmans, J. *Energy Environ. Sci.* **2018**, *11*, 1489.

(7) Das, S.; Yang, B.; Gu, G.; Joshi, P. C.; Ivanov, I. N.; Rouleau, C. M.; Aytug, T.; Geohegan, D. B.; Xiao, K. *ACS Photonics* **2015**, *2*, 680.

(8) Wei, Z.; Chen, H.; Yan, K.; Yang, S. *Angew. Chem.* **2014**, *126*, 13455.

(9) Deng, Y.; Peng, E.; Shao, Y.; Xiao, Z.; Dong, Q.; Huang, J. *Energy Environ. Sci.* **2015**, *8*, 1544.

(10) Hwang, K.; Jung, Y. S.; Heo, Y. J.; Scholes, F. H.; Watkins, S. E.; Subbiah, J.; Jones, D. J.; Kim, D. Y.; Vak, D. *Adv. Mater.* **2015**, *27*, 1241.

(11) Mei, A.; Li, X.; Liu, L.; Ku, Z.; Liu, T.; Rong, Y.; Xu, M.; Hu, M.; Chen, J.; Yang, Y.; Grätzel, M.; Han, H. *Science* **2014**, *345*, 295.

(12) Tao, C.; Neutzner, S.; Colella, L.; Marras, S.; Srimath Kandada, A. R.; Gandini, M.; Bastiani, M. D.; Pace, G.; Manna, L.; Caironi, M.; Bertarelli, C.; Petrozza, A. *Energy Environ. Sci.* **2015**, *8*, 2365.

(13) Wojciechowski, K.; Stranks, S. D.; Abate, A.; Sadoughi, G.; Sadhanala, A.; Kopidakis, N.; Rumbles, G.; Li, C.-Z.; Friend, R. H.; Jen, A. K. Y.; Snaith, H. J. *ACS Nano* **2014**, *8*, 12701.

(14) Wojciechowski, K.; Leijtens, T.; Siprova, S.; Schlueter, C.; Hörantner, M. T.; Wang, J. T.-W.; Li, C.-Z.; Jen, A. K. Y.; Lee, T.-L.; Snaith, H. J. *J. Phys. Chem. Lett.* **2015**, *6*, 2399.

(15) Kegelmann, L.; Wolff, C. M.; Awino, C.; Lang, F.; Unger, E. L.; Korte, L.; Dittrich, T.; Neher, D.; Rech, B.; Albrecht, S. *ACS Applied Materials & Interfaces* **2017**, *9*, 17245.

(16) Li, Y.; Zhao, Y.; Chen, Q.; Yang, Y.; Liu, Y.; Hong, Z.; Liu, Z.; Hsieh, Y.-T.; Meng, L.; Li, Y.; Yang, Y. *J. Am. Chem. Soc.* **2015**, *137*, 15540.

(17) Hou, Y.; Du, X.; Scheiner, S.; McMeekin, D. P.; Wang, Z.; Li, N.; Killian, M. S.; Chen, H.; Richter, M.; Levchuk, I.; Schrenker, N.; Spiecker, E.; Stubhan, T.; Luechinger, N. A.; Hirsch, A.; Schmuki, P.; Steinrück, H.-P.; Fink, R. H.; Halik, M.; Snaith, H. J.; Brabec, C. J. *Science* **2017**, *358*, 1192.

(18) Yi, H.; Simon, S.; Xiaofeng, T.; Nicola, G.; Moses, R.; Ning, L.; Peter, S.; Shi, C.; Haiwei, C.; Ramirez, Q. C. O.; Xiaoyan, D.; J., M. G.; Andres, O.; Erdmann, S.; H., F. R.; Andreas, H.; Marcus, H.; J., B. C. *Advanced Materials Interfaces* **2017**, *4*, 1700007.

(19) Aygüler, M. F.; Hufnagel, A. G.; Rieder, P.; Wussler, M.; Jaegermann, W.; Bein, T.; Dyakonov, V.; Petrus, M. L.; Baumann, A.; Docampo, P. *ACS Applied Materials & Interfaces* **2018**, *10*, 11414.

(20) Dashan, Q.; Wenbo, W.; Mingxia, W.; Song, J.; Jidong, Z. *Semicond. Sci. Technol.* **2014**, *29*, 125011.

(21) Xu, H.; Wada, T.; Ohkita, H.; Benten, H.; Ito, S. *Scientific Reports* **2015**, *5*, 9321.

(22) Ye, F.; Chen, H.; Xie, F.; Tang, W.; Yin, M.; He, J.; Bi, E.; Wang, Y.; Yang, X.; Han, L. *Energy Environ. Sci.* **2016**, *9*, 2295.

(23) Bi, C.; Wang, Q.; Shao, Y.; Yuan, Y.; Xiao, Z.; Huang, J. *Nature Communications* **2015**, *6*, 7747.

(24) Mallajosyula, A. T.; Fernando, K.; Bhatt, S.; Singh, A.; Alphenaar, B. W.; Blancon, J.-C.; Nie, W.; Gupta, G.; Mohite, A. D. *Applied Materials Today* **2016**, *3*, 96.

(25) Luo, D.; Yang, W.; Wang, Z.; Sadhanala, A.; Hu, Q.; Su, R.; Shivanna, R.; Trindade, G. F.; Watts, J. F.; Xu, Z.; Liu, T.; Chen, K.; Ye, F.; Wu, P.; Zhao, L.; Wu, J.; Tu, Y.; Zhang, Y.; Yang, X.; Zhang, W.; Friend, R. H.; Gong, Q.; Snaith, H. J.; Zhu, R. *Science* **2018**, *360*, 1442.

(26) Burschka, J.; Pellet, N.; Moon, S.-J.; Humphry-Baker, R.; Gao, P.; Nazeeruddin, M. K.; Gratzel, M. *Nature* **2013**, *499*, 316.

(27) Lee, J.; Kang, H.; Kim, G.; Back, H.; Kim, J.; Hong, S.; Park, B.; Lee, E.; Lee, K. *Adv. Mater.* **2017**, *29*, 1606363.

(28) Giesbrecht, N.; Schlipf, J.; Oesinghaus, L.; Binek, A.; Bein, T.; Müller-Buschbaum, P.; Docampo, P. *ACS Energy Letters* **2016**, *1*, 150.

(29) Young, T. *Philos. Trans. R. Soc. London* **1805**, *95*, 65.

(30) G. H. Bogush, M. A. T., C. F. Zukoski *J. Non-Cryst. Solids* **1988**, 95.

(31) Munshi, A. M.; Singh, V. N.; Kumar, M.; Singh, J. P. *J. Appl. Phys.* **2008**, *103*, 084315.

(32) Ishino, C.; Okumura, K. *The European Physical Journal E* **2008**, *25*, 415.

(33) Marmur, A. *Langmuir* **2003**, *19*, 8343.

(34) L, T. C., S. *Journal of Thermodynamics & Catalysis* **2017**, *8*, 1.

(35) Haapanen, J.; Aromaa, M.; Teisala, H.; Tuominen, M.; Stepien, M.; Saarinen, J. J.; Heikkilä, M.; Toivakka, M.; Kuusipalo, J.; Mäkelä, J. M. *Mater. Chem. Phys.* **2015**, *149-150*, 230.

(36) Nagase, T.; Yoshikawa, M.; Yamazaki, S.; Kobayashi, T.; Michiwaki, Y.; Watase, S.; Watanabe, M.; Matsukawa, K.; Naito, H. *J. Polym. Sci., Part B: Polym. Phys.* **2016**, *54*, 509.

(37) Vafaei, S.; Borca-Tasciuc, T.; Podowski, M. Z.; Purkayastha, A.; Ramanath, G.; Ajayan, P. M. *Nanotechnology* **2006**, *17*, 2523.

(38) Giesbrecht, N.; Schlipf, J.; Grill, I.; Rieder, P.; Dyakonov, V.; Bein, T.; Hartschuh, A.; Muller-Buschbaum, P.; Docampo, P. *J. Mater. Chem. A* **2018**, *6*, 4822.

(39) Petrus, M. L.; Hu, Y.; Moia, D.; Calado, P.; Leguy, A. M. A.; Barnes, P. R. F.; Docampo, P. *ChemSusChem* **2016**, *9*, 2699.

(40) Zhou, Y.; Game, O. S.; Pang, S.; Padture, N. P. *J. Phys. Chem. Lett.* **2015**, *6*, 4827.

(41) Petrosino, M.; Rubino, A. *Synth. Met.* **2012**, *161*, 2714.

7 BLUE-GREEN COLOUR TUNABLE PEROVSKITE LEDS

This chapter is based on the following publication:

Aditya Sadhanala, Shahab Ahmad, Baodan Zhao, Nadja Giesbrecht, Phoebe M. Pearce, Felix Deschler, Robert L. Z. Hoye, Karl C. Goedel, Thomas Bein, Pablo Docampo, Siân E. Dutton, Michael F.L. De Volder, Richard H. Friend *Nano Lett.* **2015**, *15*, 6095.

Initial experiments and optical characterization were performed by Aditya Sadhanala, Shahab Ahmad, Baodan Zhao and Phoebe Pearce. Nadja Giesbrecht was additionally involved in optimization of perovskite film deposition including morphology and composition and application in LEDs and also performed structural characterization of the perovskite composites. The optical characterization was done by Felix Deschler and optimization of ALD-deposited injection layers was done by Robert Hoye.

7.1 INTRODUCTION

The field of solution processed organic-inorganic halide perovskite-based optoelectronics has emerged in the last couple of years.[1-6] This was initially driven by solar cells based on organo-lead halide perovskite that now demonstrates power conversion efficiencies of above 20%.[7] Thin films based on the mixed-halide $CH_3NH_3Pb(I_xCl_{1-x})_3$ version of these perovskite materials also feature high photoluminescence quantum yield (PLQE).[8] The demonstration of these high radiative emission efficiencies led to the development of bright light-emitting diodes (LEDs) and optically pumped lasers.[5,8,9] There are recent reports that the optical bandgap of lead halide perovskites can be tuned in the visible range of ~550–780 nm through the use of solid solutions of bromide-iodide mixed halides.[10-12] These solid solution based thin films can be easily prepared by varying the ratio of the two individual pure trihalide perovskite solutions mixed (for example, $CH_3NH_3PbI_3$ and $CH_3NH_3PbBr_3$). However, tuning the bandgap in the blue-green region using solution processed chloride–bromide mixed halide perovskites has been a challenging task, given the low solubility of the chloride containing precursor materials (CH_3NH_3Cl and $PbCl_2$) in regularly used solvents like *N*,*N*-dimethylformamide (DMF). We here make use of mixed solvents DMF and dimethyl sulfoxide (DMSO) along with an organic lead source of lead acetate $Pb(CH_3COO)_2$ to achieve the solution processability of the chloride

containing precursor materials. Realizing such large bandgap solution-processed semiconductors is of great importance given their utility in making tandem solar cells and making LEDs which emit in the blue-green range of the visible spectrum.

Here, we demonstrate bandgap tuning of the $CH_3NH_3Pb(Br_xCl_{1-x})_3$ [$0 \leq x \leq 1$] perovskites in the UV–visible (UV–vis) range of ~3.1–2.3 eV. We tuned the bandgap in this range by varying the chloride to bromide ratios in the $CH_3NH_3Pb(Br_xCl_{1-x})_3$ [$0 \leq x \leq 1$] perovskites, which are solution processed from their respective precursor solutions. This solution processed mixed chloride–bromide films were further characterized using X-ray diffraction (XRD), photothermal deflection spectroscopy (PDS), time-resolved photoluminescence (TRPL), and energy dispersive X-ray (EDX) measurements. These mixed chloride–bromide perovskites provide a way to realize solution processed large bandgap perovskite solar cells to combine with small bandgap perovskite solar cells in tandem architecture. Furthermore, these perovskites allow blue LEDs to be realized, which have proven to be a difficult task with gallium nitride (GaN) being the only widely used option for commercial application. We here demonstrate the use of the $CH_3NH_3Pb(Br_xCl_{1-x})_3$ perovskites in the fabrication of LEDs with color tunability dependent on the composition, and for $CH_3NH_3Pb(Br_xCl_{1-x})_3$ [$x < 0.6$] we demonstrate blue LEDs with narrow emission full-width at half maxima (FWHM).

7.2 RESULTS AND DISCUSSION

Bandgap tuning in the $CH_3NH_3Pb(Br_xCl_{1-x})_3$ [$0 \leq x \leq 1$] perovskites was achieved by substitution of Br and Cl ions in the precursor solutions. We prepared perovskite precursor solutions with two different organic (CH_3NH_3X) to inorganic ($Pb(CH_3COO)_2$) molar ratios 3:1 and 5:1 organic to inorganic (for a detailed description of material preparation refer to chapter 9. We note that these ratios correspond respectively to (1) a stoichiometric solution and (2) one with an excess of CH_3NH_3X, and these are analogous to the 1:1 and 3:1 ratios for methylammonium halide and lead halide starting materials typically used.[5,13,14] The photophysical properties of the 3:1 molar starting ratio perovskite samples are summarized in the *Figures 7 – 1, 7 – 2, and 7 – 3*). In brief, we observe a monotonic blue shift in the bandgap with decreasing bromide content and increasing chloride content in the $CH_3NH_3Pb(Br_xCl_{1-x})_3$ [$0 \leq x \leq 1$] perovskites. X-ray diffraction of the $CH_3NH_3Pb(Br_xCl_{1-x})_3$ films formed using the stoichiometric solution indicates the formation of a cubic perovskite, space group *Pm3m*, across the entire composition range [$0 \leq x \leq 1$]. In agreement with Vegard's law, a monotonic decrease in the lattice parameter with increasing chloride content is observed. These 3:1 molar staring ratio perovskite materials could be useful in solar cell applications as their band-edges are sharper with clean sub-bandgap and

narrow XRD diffraction peaks (see *Figures 7 – 1, 7 – 2, and 7 – 3* for PDS and XRD spectra). However, for luminescence applications, we use 5:1 organic to inorganic molar starting ratio perovskite materials analogous to the materials used to make efficient perovskite LEDs previously,[5,14-17] and these are described in detail as follows.

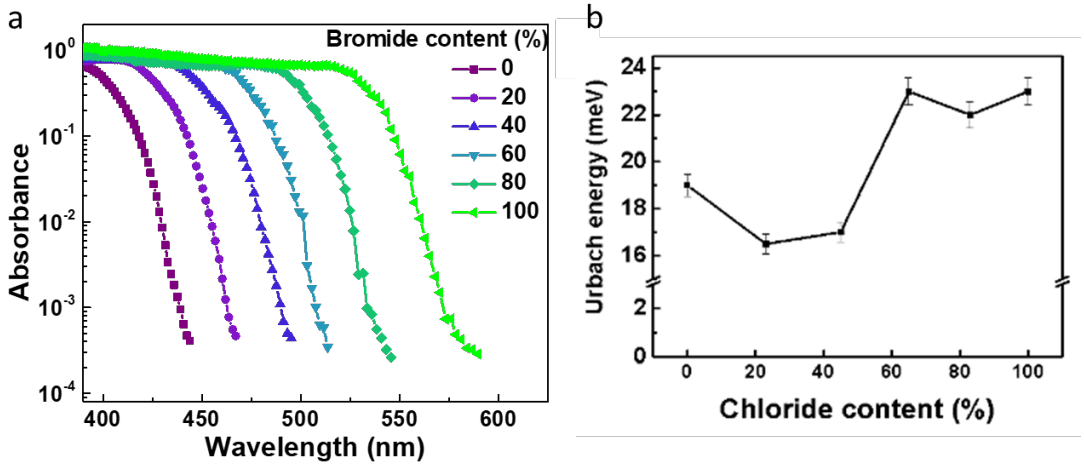

Figure 7 - 1: a) PDS absorption data for the 3:1 molar starting ratio $CH_3NH_3Pb(Br_xCl_{1-x})_3$ [$0 \leq x \leq 1$] perovskite thin films with different chloride-bromide ratios as indicated, showing monotonic bandgap; tuning with changing composition. They also demonstrate sharp band-edges and clean sub-bandgap. b) Urbach energy for all the samples showing low disorder. The 24 and 45% chloride samples demonstrate the lowest Urbach energy of ~ 17 meV and the samples with no chloride content shows Urbach energy of ~19 meV and the remaining samples with chloride content higher than 45% showed higher Urbach energies of ~23 meV. These Urbach energy values are much lower than those obtained for the 5:1 molar starting ratio $CH_3NH_3Pb(Br_xCl_{1-x})_3$ [$0 \leq x \leq 1$] perovskite thin films, which makes them more useful for solar cell applications.

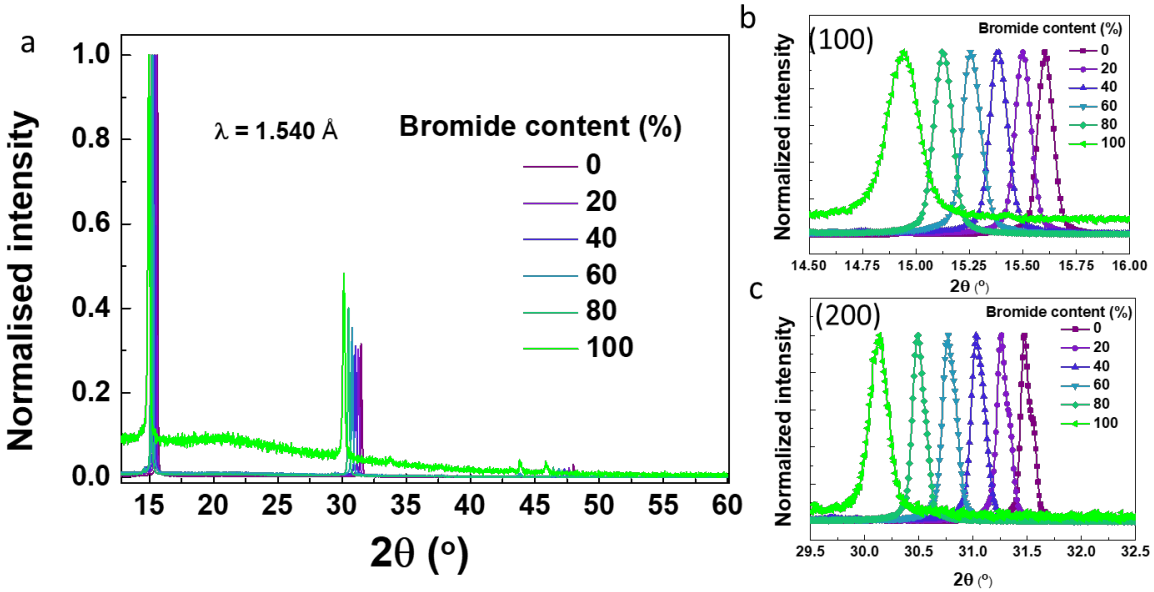

Figure 7 - 2: a) XRD patterns as a function of composition for 3:1 organic to inorganic molar starting ratio $CH_3NH_3Pb(Br_xCl_{1-x})_3$ [$0 \leq x \leq 1$] perovskite thin films showing diffraction pattern shift to higher scattering angle, 2q with decreasing bromide content. b) and c) Show the evolution of the normalized XRD patterns for the (100) and (200) reflection respectively as a function of composition for the same thin films.

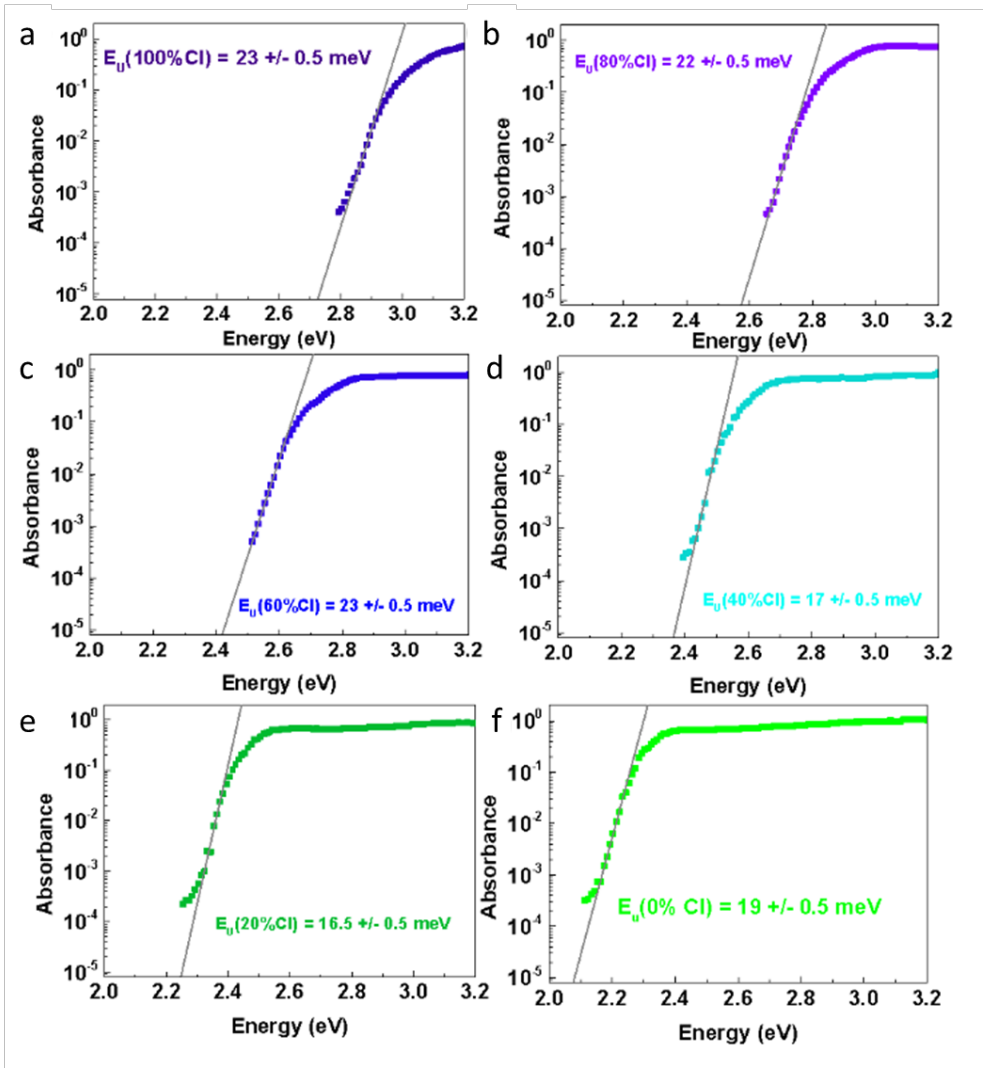

Figure 7 - 3: a-f) PDS spectra for the 3:1 molar starting ratio $CH_3NH_3Pb(Br_xCl_{1-x})_3$ [$0 \leq x \leq 1$] perovskite thin films with different chloride-bromide ratios as indicated. The grey lines in each plot are the linear fits to the Urbach tail used to calculate the Urbach energy and the obtained Urbach energy 'Eu' which is indicated for each sample.

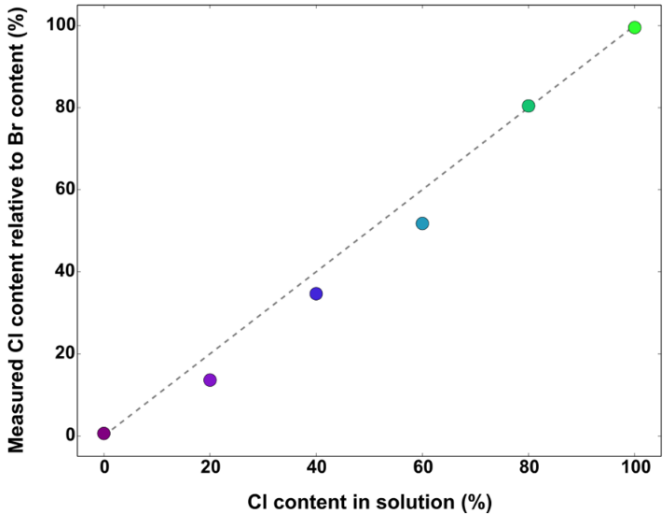

Figure 7 - 4: Energy dispersive X-ray spectroscopy (EDX) data for the 5:1 molar starting ratio $CH_3NH_3Pb(Br_xCl_{1-x})_3$ [$0 \leq x \leq 1$] perovskite solid solutions based thin films with different chloride-bromide ratios as indicated showing a close match between the concentration in solution and that in thin films.

EDX measurements were performed (see *Figure 7 – 4*) to determine the nominal halide composition in the 5:1 organic-to-inorganic molar starting ratio based $CH_3NH_3Pb(Br_xCl_{1-x})_3$ [$0 \leq x \leq 1$] perovskite films spin-coated onto quartz substrates, and it was found that the halide content in films is similar to that in the precursor mixture solutions within the detection error limits of the measurement (±5%). Henceforth, the composition indicated in the rest of the manuscript is that of the respective perovskite films.

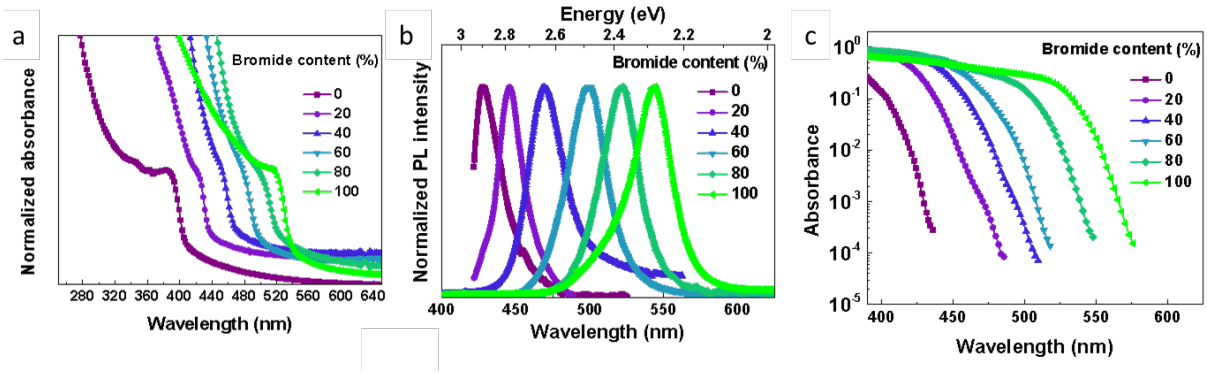

Figure 7 - 5: (a) UV–visible absorption spectra and (b) normalized photoluminescence spectra for the 5:1 organic to inorganic molar starting ratio $CH_3NH_3Pb(Br_xCl_{1-x})_3$ [$0 \leq x \leq 1$] perovskite thin films with different chloride–bromide ratios as indicated. Excitation for PL was performed with a pulsed laser system at 3.1 eV photon energy and 100 fs pulse length, and PL spectra have been normalized to the peak emission. (c) PDS spectra are showing sharp band edges and a clean bandgap.

The optical properties of 5:1 organic-to-inorganic molar starting ratio based $CH_3NH_3Pb(Br_xCl_{1-x})_3$ [$0 \leq x \leq 1$] perovskite films spin-coated onto quartz substrates were measured. The absorption spectra in *Figure 7 – 5a* shows a monotonic blue shift in the bandgap of these films with decreasing bromide content (or increasing chloride content), from a band-edge of around 530 nm for 0% chloride sample ($CH_3NH_3PbBr_3$) to 400 nm for the 100 % chloride sample ($CH_3NH_3PbCl_3$). To analyze the quality of a semiconductor formed, we performed PDS measurements to probe the sub-bandgap absorption of our perovskite films. PDS is a highly sensitive absorption measurement technique capable of measuring absorbances down to 10^{-5} and is not subject to optical effects, such as light scattering, reflection, and interference effects at the substrate/material interface. PDS has been extensively used to study various organo-metal halide perovskites to measure the sub-bandgap defect states, degradation, and energetic disorder in the form of Urbach energy.[5,12,13,18-20] The PDS spectra for the 5:1 organic to inorganic molar starting ratio $CH_3NH_3Pb(Br_xCl_{1-x})_3$ [$0 \leq x \leq 1$] perovskite films are shown in *Figure 7 – 5c*, which shows a blue shift in the bandgap with increasing chloride content in the perovskite films. We find that all of these perovskite films have sharp band edges and clean sub-bandgap absorption indicating the superior quality of the semiconductor formed. Steady-state PL spectra of the 5:1 organic to inorganic molar starting ratio $CH_3NH_3Pb(Br_xCl_{1-x})_3$ [$0 \leq x \leq 1$] perovskites were measured (*Figure 7 – 5b*). We observe a systematic blue shift in the PL spectra with increasing

chloride content from 543 nm for 0 % chloride perovskite ($CH_3NH_3PbBr_3$) to 428 nm for 100% chloride perovskite ($CH_3NH_3PbCl_3$). The PL and the PDS spectra demonstrate that the resulting $CH_3NH_3Pb(Br_xCl_{1-x})_3$ [$0 \leq x \leq 1$] perovskite films demonstrate a single optically active phase. This finding supports our observation of a clean bandgap in these films.

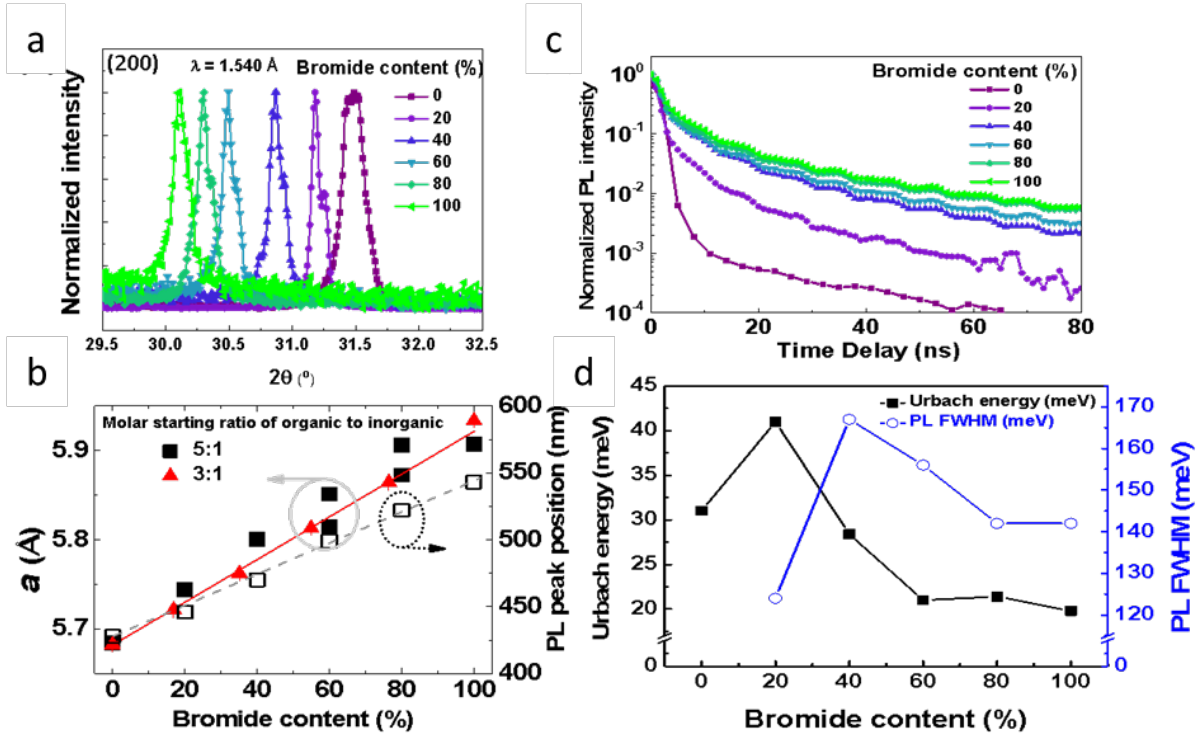

Figure 7 - 6: (a) XRD patterns showing the evolution of the (200) reflection as a function of composition for 5:1 molar starting ratio $CH_3NH_3Pb(Br_xCl_{1-x})_3$ [$0 \leq x \leq 1$] perovskite thin films showing diffraction pattern shift to higher scattering angle, 2θ with increasing chloride content. (b) Changes of normalized lattice parameters for 5:1 (closed squares) and 3:1 (closed triangles) organic-to-inorganic molar starting ratio $CH_3NH_3Pb(Br_xCl_{1-x})_3$ [$0 \leq x \leq 1$] perovskite thin films and PL peak position with a change in composition for the same films. (c) The plot of normalized PL intensity versus time for the same films. (d) Comparison of the change in FWHM of the PL emission peak, (200) XRD reflection, and the Urbach energy calculated from PDS measurements for the same films. The normalized lattice parameter and XRD FWHM show two data points for 20 % and 40 % chloride samples each, and these values are for the split phases observed in the XRD of these samples. Excitation for PL was performed with a pulsed laser system at 3.1 eV photon energy and 100 fs pulse length.

XRD studies of the $CH_3NH_3Pb(Br_xCl_{1-x})_3$ [$0 \leq x \leq 1$] perovskite films formed using the 5:1 molar starting ratio solutions (*Figure 7 – 6a*), indicate the formation of a cubic phase, space group $Pm\bar{3}m$, across the composition range (for full XRD spectra see *Figure 7 – 7*). Quantitative analysis to determine the lattice parameters was carried out using a Le Bail analysis,[21] in the Fullprof suite of programmes;[22] preferential alignment in the films prevents a full analysis of the crystal structure. As the chloride content increases, the peaks in the diffraction pattern shift to higher scattering angle, 2θ, as would be expected when bromide is replaced by smaller chloride ions. At low chloride concentrations (20–40 % Cl) the high angle peaks at 30–31.5° 2θ (*Figure 7 – 6a*) are observed to split, indicating the formation of cubic perovskites with more than one lattice parameter. Given the monotonic variation in the lattice parameters in the 3:1 films with composition, this is most likely to arise as a result of bulk phase segregation into

perovskite crystals with different ratios of halides with a composition within 10 % of the initial starting solution. From the current analysis, it is not possible to determine the relative phase fraction of the perovskites formed, and so it is not possible to quantify the extent of the phase segregation. At higher chloride concentrations (x>0.4) a single perovskite phase is seen in the XRD patterns; however, the broadening of the reflections may indicate some less extensive phase segregation.

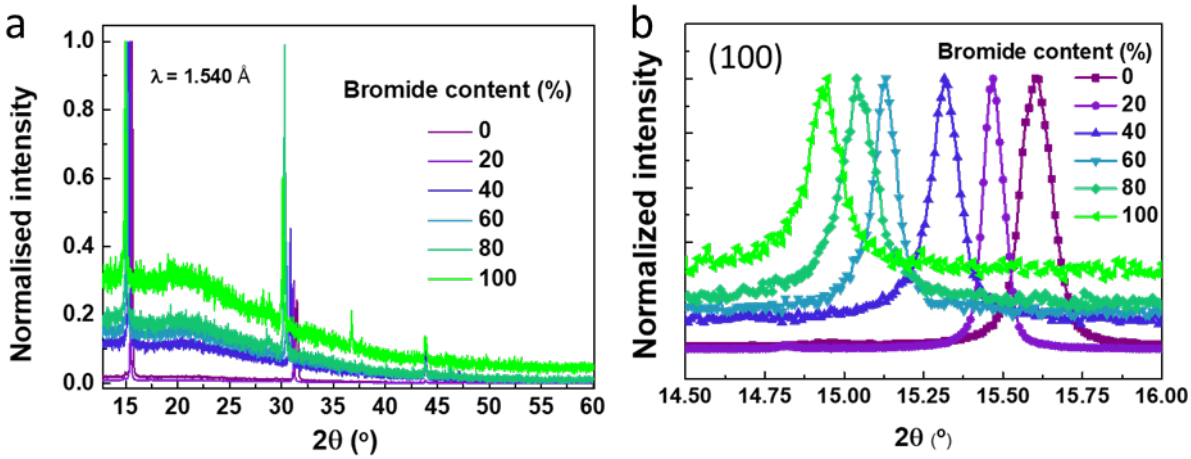

Figure 7 - 7: a) X-ray diffraction (XRD) data for the 5:1 molar starting ratio $CH_3NH_3Pb(Br_xCl_{1-x})_3$[0≤x ≤1] perovskite thin films with different chloride-bromide ratios as indicated. b) XRD patterns are showing the evolution of the (100) reflection as a function of composition for the same samples.

In *Figure 7 – 6b*, we compare the change in the PL peak positions alongside the extracted normalized lattice parameters, where both follow a linear trend with the changing chloride fraction for the 5:1 organic to inorganic molar starting ratio $CH_3NH_3Pb(Br_xCl_{1-x})_3$ [0≤x≤1] perovskite films. We further measured the photoluminescence kinetics of the 5:1 organic to inorganic molar starting ratio $CH_3NH_3Pb(Br_xCl_{1-x})_3$ [0 ≤ x ≤1] perovskite films (*Figure 7 – 6c*) which show single bimolecular decays for the 0 % chloride film ($CH_3NH_3PbBr_3$) and also for films down to 60 % chloride sample, similar to what was reported previously for bromide–iodide mixed halide perovskite materials.[8,12] Films with 80% and 100% chloride content both show faster kinetics than the films with lower chloride content.

The Urbach energies were measured for all of the 5:1 organic to inorganic molar starting ratio $CH_3NH_3Pb(Br_xCl_{1-x})_3$ [0≤x≤1] perovskite films using the PDS spectra. Urbach energy "E_U" is an empirical parameter that indicates the energetic disorder for a given semiconductor.[23,24] The Urbach energy is derived from the PDS absorption data by using the following expression: $A = A_0 \exp((E - E_g)/E_U)$, where A is the absorbance, A_0 is a constant, and E_g is the bandgap of the material.[12,24,25] *Figure 7 – 6d* shows the correlation between the extracted Urbach energies and

the full width at half maxima (FWHM) of the PL spectra and the (200) XRD reflection of the 5:1 organic to inorganic molar starting ratio $CH_3NH_3Pb(Br_xCl_{1-x})_3$ [$0 \leq x \leq 1$] perovskite films with various chloride content. It can be seen that the Urbach energy is the lowest for the 0 % chloride ($CH_3NH_3PbBr_3$) sample at 20 meV and increases monotonically with increasing chloride content to 41 meV for the 80 % chloride film and then drops down to 31 meV for the 100% chloride sample ($CH_3NH_3PbCl_3$). We also observe a similar trend in the PL with a minimum for the 0 % chloride ($CH_3NH_3PbBr_3$) and 80 % chloride ($CH_3NH_3Pb(Br_{0.2}Cl_{0.8})_3$) samples at 142 and 124 meV, respectively. Furthermore, the PL FWHM increases monotonically with increasing chloride content in the films to reach a maximum of 167 meV for 60 % chloride sample ($CH_3NH_3Pb(Br_{0.4}Cl_{0.6})_3$). The FWHM of a process (absorption and emission) is generally indicative of the magnitude of disorder experienced by the excited carriers in the energetic landscape around them. Interestingly, the FWHM of the (200) reflection XRD shows a similar trend to the PL FWHM and Urbach energy. This similarity in the trends between Urbach energy, PL FWHM, and XRD FWHM, indicates the possibility that the energetic disorder experienced by the absorptive and emissive species are similar and are related to the structural disorder.

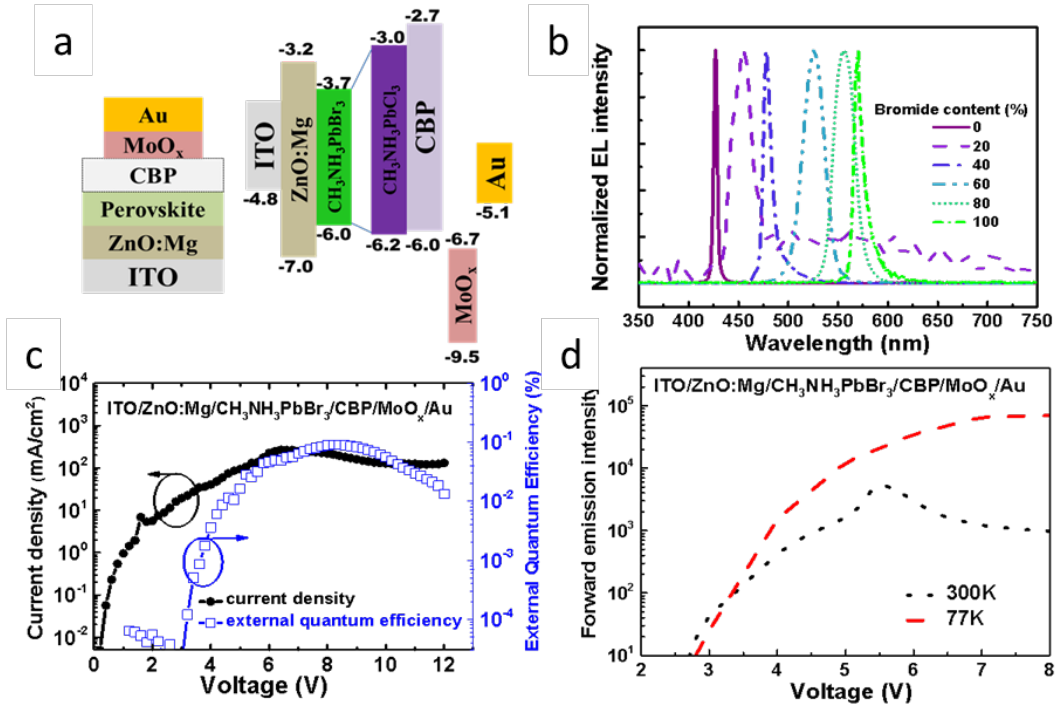

Figure 7 - 8: (a) Device structure of the perovskite LEDs. (b) Normalized EL spectra of the 5:1 organic to inorganic molar starting ratio $CH_3NH_3Pb(Br_xCl_{1-x})_3$ [$0 \leq x \leq 1$] perovskite thin film based LEDs with different chloride–bromide ratios as indicated and measured at 77 K. These LEDs were fabricated in a device structure comprising of ITO/Mg:ZnO/perovskite/CBP/MoO_x/Au and they demonstrate high color purity and emission tunability with a change in composition. (c) Current density and external quantum efficiency curves for the 0% chloride ($CH_3NH_3PbBr_3$) LED measured at room temperature (300 K) and (d) the forward emission of this LED with respect to a bias voltage for the same device at room (300 K) and liquid nitrogen (77 K) temperatures.

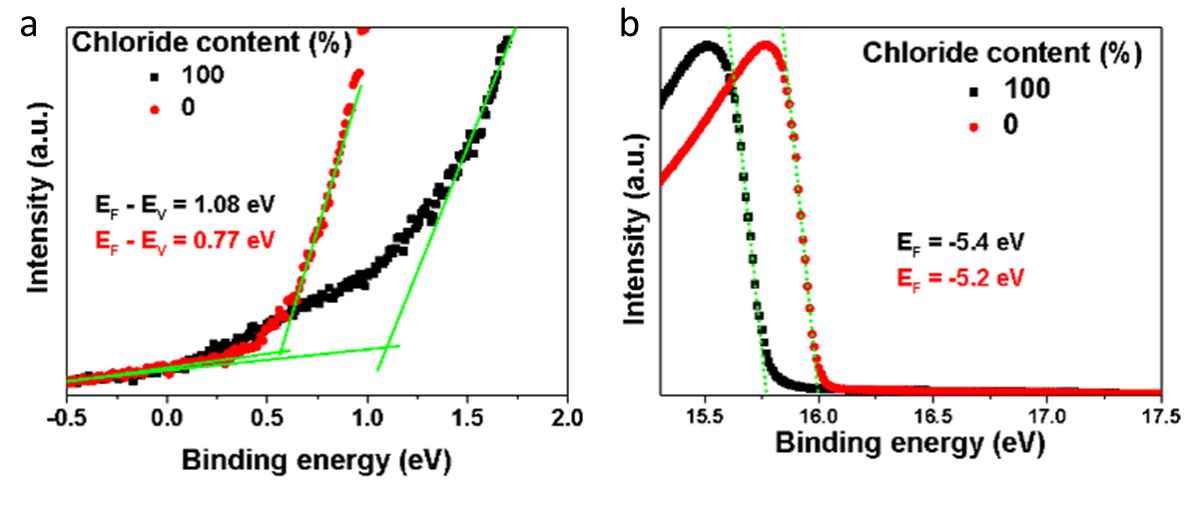

Figure 7 - 9: UPS spectra of the 5:1 molar starting ratio $CH_3NH_3Pb(Br_xCl_{1-x})_3[0\leq x\leq 1]$ different chloride-bromide ratios as indicated, on a gold substrate. a) UPS spectra of the top of the Valance band maxima (EV) for the perovskite samples as a function of composition giving the difference between the Fermi energy level (EF) and EV of around 1.08 eV and 0.77 eV for 100 % and 0 % chloride samples respectively. b) Photoemission cut-off for the perovskite samples as a function of composition, from which the vacuum level of the film is extracted. The EF for 100 % and 0 % chloride samples are -5.4 eV and -5.2 eV respectively.

In order to demonstrate the potential application of these $CH_3NH_3Pb(Br_xCl_{1-x})_3$ $[0\leq x\leq 1]$ perovskite films in optoelectronic devices, we fabricated light-emitting diodes using these 5:1 organic to inorganic molar starting ratio $CH_3NH_3Pb(Br_xCl_{1-x})_3$ $[0\leq x\leq 1]$ perovskite films. The device structure used in this work is ITO/Mg:ZnO/$CH_3NH_3Pb(Br_xCl_{1-x})_3$/CBP/$MoO_x$/Au, where a combination of indium tin oxide (ITO) coated glass substrate and 50 nm ZnO followed by 10 nm zinc magnesium oxide (Mg:ZnO) forms the electron selective contact and the combination of 25 nm 4,4′-Bis(*N*-carbazolyl)-1,1′-biphenyl (CBP), 15 nm molybdenum trioxide, and 100 nm gold (Au) electrode act as a hole-selective contact. This device structure is depicted in *Figure 7 – 8a* along with the energy levels. The energy levels of the perovskite films were measured using Ultraviolet photoelectron spectroscopy (UPS) (see *Figure 7 – 9*), and all other energy levels were obtained from various literature reports. [26,27] We measured the electroluminescence (EL) spectra for devices with varying chloride content, $CH_3NH_3Pb(Br_xCl_{1-x})_3$ $[0\leq x\leq 1]$ (*Figure 7 – 8b*). At room temperature weak or no EL could be measured except for the 0% chloride ($CH_3NH_3PbBr_3$) based perovskite LED device which gave us a peak external quantum efficiency (EQE) of around 0.1 % at ~6 V which is comparable to previous reports.[5,28] This LED demonstrated a near bandgap turn on at around 2.2 V indicating efficient and balanced charge injection in the device. The other LEDs containing different chloride content other than 0 % chloride did not show weak or no measurable EL emission at room temperature. However, on cooling below 200 K, EL is observed in devices containing the mixed halide, 5:1 organic to inorganic molar starting ratio $CH_3NH_3Pb(Br_xCl_{1-x})_3$ $[0\leq x<1]$, perovskite films. The EQE could not be measured at low temperatures due to experimental

difficulties. Nevertheless, we compare the peak forward emission intensity of the 100 % bromide ($CH_3NH_3PbBr_3$) device at room temperature and 77 K (*Figure 7 – 8b*) which is indicative of the device performance at the measured temperatures. From *Figure 7 – 8c* and *d*, we observe that the turn-on voltage remains at 2.2–3 V even at 77 K similar to what we observe at room temperature. This is an interesting observation given the device turn-on voltages for conventional organic LEDs (OLEDs) increases with decreases in temperature.[29] The forward emission intensity of this device also increases at low temperatures, indicating the improvement in the photoluminescence quantum efficiency (PLQE) at low temperatures due to a potential reduction in nonradiative recombination pathways at low temperatures.[30]

In *Figure 7 – 8b* we demonstrate the ability to tune the bandgap and emission wavelength of the LEDs based on the mixed halide, 5:1 organic-to-inorganic molar starting ratio $CH_3NH_3Pb(Br_xCl_{1-x})_3$ [$0 \leq x < 1$], perovskite films which were measured at liquid nitrogen temperatures (77 K). The EL emission wavelength monotonically changes from 570 nm for 0 % chloride ($CH_3NH_3PbBr_3$) based LED to 427 nm for the 100% chloride LED ($CH_3NH_3PbCl_3$). One notable observation is the narrow 5 nm EL FWHM for the 100% chloride ($CH_3NH_3PbCl_3$) perovskite-based LED, which to our knowledge is one of the lowest FWHM observed to date for any solution processed material.[5,14,16,28,31]

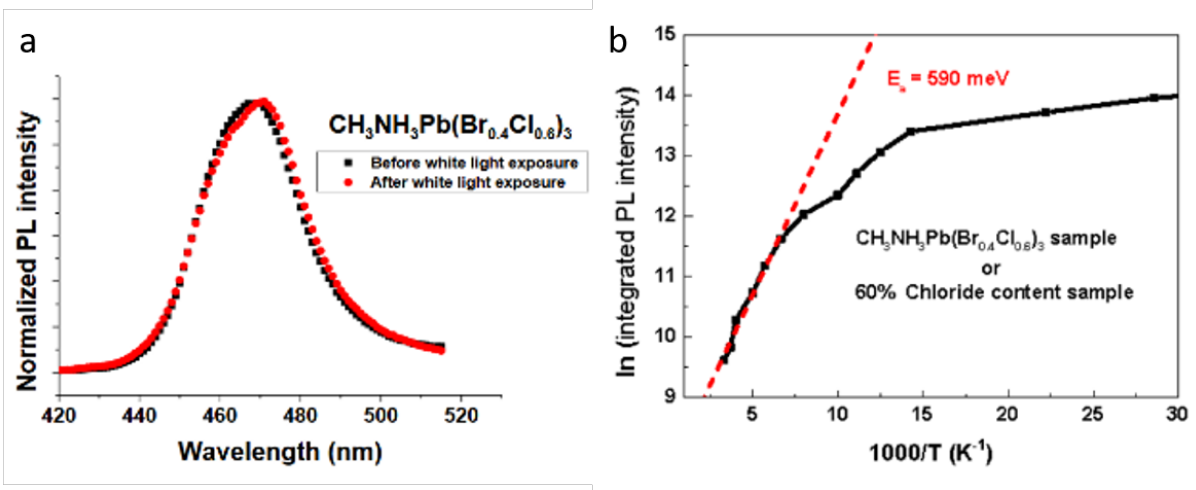

Figure 7 - 10: PL spectra for the 60 % chloride content sample ($CH_3NH_3Pb(Br0.4Cl_{0.6})_3$) measured before and immediately after exposure to 1sun intensity (100 mW/cm2) demonstrating no change in the PL peak position proving the photo-stability of these materials; b) Plot of the natural log of the PL Vs inverse temperature for the 5:1 molar starting ratio $CH_3NH_3Pb(Br_{0.4}Cl_{0.6})_3$ perovskite thin films showing high integrated PL at lower temperatures and high activation energies in the range of ~590 meV for this thermally-activated PL quenching process.

The reason for the materials with large bandgap not showing any EL at room temperature could probably be the optical instability of these perovskite films. Recently, it was reported that the mixed halide bromide-iodide perovskite show optical instability under solar illumination (100 mW/cm^2).[32] To rule out any such optical instability in these perovskites, we performed PL

measurements on the 60% chloride ($CH_3NH_3Pb(Br_{0.4}Cl_{0.6})_3$) sample before and immediately after a 10 min exposure under 1 sun illumination (100 mW/cm^2) (see *Figure 7 – 10*). We found that the PL peak position does not change before and after illumination, which suggests that these 5:1 organic-to-inorganic molar starting ratio $CH_3NH_3Pb(Br_xCl_{1-x})_3$ [$0 \leq x < 1$] perovskite films are optically stable. One other reason behind the lack of EL at room temperature from the LEDs fabricated using large bandgap perovskite films could be the low PLQE. We investigated this by measuring the integrated PL from the 60 % chloride ($CH_3NH_3Pb(Br_{0.4}Cl_{0.6})_3$) perovskite film at low temperatures. The integrated PL from this film increases with a decrease in temperature from room temperature (300 K) down to liquid nitrogen temperature (77 K). This can be inferred as an increase in PLQE at low temperatures, and this can be further inferred from the PL activation curve (see *Figure 7– 9*). We observe an increase in the integrated PL intensity for the 60 % chloride sample with decreasing temperature indicating the presence of efficient nonradiative processes at room temperature which is suppressed on cooling.[30] We estimate activation energies in the range of ∼590 meV for this thermally activated PL quenching.

Nevertheless, the fact that the LEDs based on these perovskite materials demonstrate narrow emission and low turn-on voltages at low temperatures along with the color tunability is a step forward to realize high color purity tunable LEDs. Further investigation into increasing the quality and PLQE of perovskite materials can help us realize blue LEDs operating at room temperature, and this could become a potential alternative to the current industrial standard gallium nitride (GaN) based blue LEDs.

7.3 CONCLUSION

In summary, we demonstrate bandgap is tuning in the green to blue region of the visible spectrum using solution-processed $CH_3NH_3Pb(Br_xCl_{1-x})_3$ [$0 \leq x < 1$] perovskites. We overcame the challenge of incorporating chloride into perovskite structures containing bromide by using mixed solvent approach and organic source of lead. These color tunable materials have been used to fabricate high color-purity, tunable LEDs with narrow FWHM emission and low turn-on voltages. With further investigation into increasing the quality of mixed chloride–bromide perovskites, $CH_3NH_3Pb(Br_xCl_{1-x})_3$, to enhance the PLQE, these materials may offer an alternative to current gallium nitride (GaN) based blue LED technologies.

7.4 LITERATURE

(1) Lee, M. M.; Teuscher, J.; Miyasaka, T.; Murakami, T. N.; Snaith, H. J. *Science* **2012**, *338*, 643.

(2) Kim, H.-S.; Lee, C.-R.; Im, J.-H.; Lee, K.-B.; Moehl, T.; Marchioro, A.; Moon, S.-J.; Humphry-Baker, R.; Yum, J.-H.; Moser, J. E.; Grätzel, M.; Park, N.-G. *Scientific Reports* **2012**, *2*, 591.

(3) Luo, J.; Im, J.-H.; Mayer, M. T.; Schreier, M.; Nazeeruddin, M. K.; Park, N.-G.; Tilley, S. D.; Fan, H. J.; Grätzel, M. *Science* **2014**, *345*, 1593.

(4) Zhou, H.; Chen, Q.; Li, G.; Luo, S.; Song, T.-b.; Duan, H.-S.; Hong, Z.; You, J.; Liu, Y.; Yang, Y. *Science* **2014**, *345*, 542.

(5) Tan, Z.-K.; Moghaddam, R. S.; Lai, M. L.; Docampo, P.; Higler, R.; Deschler, F.; Price, M.; Sadhanala, A.; Pazos, L. M.; Credgington, D.; Hanusch, F.; Bein, T.; Snaith, H. J.; Friend, R. H. *Nat Nano* **2014**, *9*, 687.

(6) Green, M. A.; Ho-Baillie, A.; Snaith, H. J. *Nature Photonics* **2014**, *8*, 506.

(7) Yang, W. S.; Noh, J. H.; Jeon, N. J.; Kim, Y. C.; Ryu, S.; Seo, J.; Seok, S. I. *Science* **2015**, *348*, 1234.

(8) Deschler, F.; Price, M.; Pathak, S.; Klintberg, L. E.; Jarausch, D.-D.; Higler, R.; Hüttner, S.; Leijtens, T.; Stranks, S. D.; Snaith, H. J.; Atatüre, M.; Phillips, R. T.; Friend, R. H. *J. Phys. Chem. Lett.* **2014**, *5*, 1421.

(9) Xing, G.; Mathews, N.; Lim, S. S.; Yantara, N.; Liu, X.; Sabba, D.; Grätzel, M.; Mhaisalkar, S.; Sum, T. C. *Nat Mater* **2014**, *13*, 476.

(10) Noh, J. H.; Im, S. H.; Heo, J. H.; Mandal, T. N.; Seok, S. I. *Nano Lett.* **2013**, *13*, 1764.

(11) Eperon, G. E.; Stranks, S. D.; Menelaou, C.; Johnston, M. B.; Herz, L. M.; Snaith, H. J. *Energy Environ. Sci.* **2014**, *7*, 982.

(12) Sadhanala, A.; Deschler, F.; Thomas, T. H.; Dutton, S. E.; Goedel, K. C.; Hanusch, F. C.; Lai, M. L.; Steiner, U.; Bein, T.; Docampo, P.; Cahen, D.; Friend, R. H. *J. Phys. Chem. Lett.* **2014**, *5*, 2501.

(13) Zhang, W.; Saliba, M.; Moore, D. T.; Pathak, S. K.; Hörantner, M. T.; Stergiopoulos, T.; Stranks, S. D.; Eperon, G. E.; Alexander-Webber, J. A.; Abate, A.; Sadhanala, A.; Yao, S.; Chen, Y.; Friend, R. H.; Estroff, L. A.; Wiesner, U.; Snaith, H. J. *Nat. Commun.* **2015**, *6*, 6142.

(14) Wang, J.; Wang, N.; Jin, Y.; Si, J.; Tan, Z.-K.; Du, H.; Cheng, L.; Dai, X.; Bai, S.; He, H.; Ye, Z.; Lai, M. L.; Friend, R. H.; Huang, W. *Adv. Mater.* **2015**, *27*, 2311.

(15) Li, G.; Tan, Z.-K.; Di, D.; Lai, M. L.; Jiang, L.; Lim, J. H.-W.; Friend, R. H.; Greenham, N. C. *Nano Lett.* **2015**, *15*, 2640.

(16) Hoye, R. L. Z.; Chua, M. R.; Musselman, K. P.; Li, G.; Lai, M. L.; Tan, Z. K.; Greenham, N. C.; MacManus-Driscoll, J. L.; Friend, R. H.; Credgington, D. *Adv. Mater.* **2015**, *27*, 1414.

(17) Kumawat, N. K.; Dey, A.; Narasimhan, K. L.; Kabra, D. *ACS Photonics* **2015**, *2*, 349.

(18) Noel, N. K.; Stranks, S. D.; Abate, A.; Wehrenfennig, C.; Guarnera, S.; Haghighirad, A.-A.; Sadhanala, A.; Eperon, G. E.; Pathak, S. K.; Johnston, M. B.; Petrozza, A.; Herz, L. M.; Snaith, H. J. *Energy Environ. Sci.* **2014**, *7*, 3061.

(19) Di, D.; Musselman, K. P.; Li, G.; Sadhanala, A.; Ievskaya, Y.; Song, Q.; Tan, Z.-K.; Lai, M. L.; MacManus-Driscoll, J. L.; Greenham, N. C.; Friend, R. H. *J. Phys. Chem. Lett.* **2015**, *6*, 446.

(20) Sadhanala, A.; Kumar, A.; Pathak, S.; Rao, A.; Steiner, U.; Greenham, N. C.; Snaith, H. J.; Friend, R. H. *Advanced Electronic Materials* **2015**, *1*, 1500008.

(21) Le Bail, A.; Duroy, H.; Fourquet, J. L. *Mater. Res. Bull.* **1988**, *23*, 447.

(22) Rodriguez-Carvajal, J.; Fernandez-Diaz, M. T.; Martinez, J. L. *J. Phys.: Condens. Matter* **1991**, *3*, 3215.

(23) Urbach, F. *Phys. Rev.* **1953**, *92*, 1324.

(24) Venkateshvaran, D.; Nikolka, M.; Sadhanala, A.; Lemaur, V.; Zelazny, M.; Kepa, M.; Hurhangee, M.; Kronemeijer, A. J.; Pecunia, V.; Nasrallah, I.; Romanov, I.; Broch, K.; McCulloch, I.; Emin, D.; Olivier, Y.; Cornil, J.; Beljonne, D.; Sirringhaus, H. *Nature* **2014**, *515*, 384.

(25) Kronemeijer, A. J.; Pecunia, V.; Venkateshvaran, D.; Nikolka, M.; Sadhanala, A.; Moriarty, J.; Szumilo, M.; Sirringhaus, H. *Adv. Mater.* **2014**, *26*, 728.

(26) Greiner, M. T.; Helander, M. G.; Tang, W.-M.; Wang, Z.-B.; Qiu, J.; Lu, Z.-H. *Nature Materials* **2011**, *11*, 76.

(27) Hoye, R. L. Z.; Ehrler, B.; Böhm, M. L.; Muñoz-Rojas, D.; Altamimi, R. M.; Alyamani, A. Y.; Vaynzof, Y.; Sadhanala, A.; Ercolano, G.; Greenham, N. C.; Friend, R. H.; MacManus-Driscoll, J. L.; Musselman, K. P. *Advanced Energy Materials* **2014**, *4*, 1301544.

(28) Kim, Y. H.; Cho, H.; Heo, J. H.; Kim, T. S.; Myoung, N.; Lee, C. L.; Im, S. H.; Lee, T. W. *Adv. Mater.* **2015**, *27*, 1248.

(29) Hayer, A.; Köhler, A.; Arisi, E.; Bergenti, I.; Dediu, A.; Taliani, C.; Al-Suti, M.; Khan, M. S. *Synth. Met.* **2004**, *147*, 155.

(30) Stranks, S. D.; Burlakov, V. M.; Leijtens, T.; Ball, J. M.; Goriely, A.; Snaith, H. J. *Physical Review Applied* **2014**, *2*, 034007.

(31) Dai, X.; Zhang, Z.; Jin, Y.; Niu, Y.; Cao, H.; Liang, X.; Chen, L.; Wang, J.; Peng, X. *Nature* **2014**, *515*, 96.

(32) Hoke, E. T.; Slotcavage, D. J.; Dohner, E. R.; Bowring, A. R.; Karunadasa, H. I.; McGehee, M. D. *Chemical Science* **2015**, *6*, 613.

8 CONCLUSION AND OUTLOOK

In this thesis, we discovered a new and highly stable intermediate perovskite-like phase that allowed us to fabricate high-quality perovskite $MAPbX_3$ films with grain sizes exceeding 10 µm and pure crystal alignment. In the first part, we developed a new method to process the wide-bandgap perovskite $MAPbBr_3$. This perovskite compound is especially interesting as a green light emitting layer in LEDs or as an absorber for high voltage solar cells. In the course of this work, the optimized deposition conditions led to high-quality thin films with crystal sizes of up to 10 µm and pure alignment of the crystallites. In photovoltaic devices, these film qualities boosted the power conversion efficiency significantly, compared to thin films with smaller grain sizes and no preference in crystal alignment. In particular, the $MAPbBr_3$ thin films presented here exhibit high photocurrents in single-junction devices, in combination with high voltages of over 1.4 V.

The high stability of the intermediate perovskite-like phase (IP) in the iodide-based compounds creates rather optimal synthesis conditions for the perovskite formation. To deposit the IP from the solution, we found the use of highly polar solvent additives to be necessary. In particular, the additive tetrahydrothiophene-1-oxide (THTO) enabled the crystallization of the phase-pure IP from solution. This precursor enabled a highly controlled conversion to perovskite from the crystalline IP, such that we obtained grain sizes of over 10 µm with pure crystal orientation with respect to the substrate. Therefore, the electronic properties of these films approached the ones of single crystals, leading to very high solar power conversion efficiencies for this compound with 18.5 %.

Moreover, the formation of the IP makes tuning of crystal alignment possible if the Lewis-base DMSO was used as a solvent additive. By varying the amount of DMSO additive in the range of 10 vol%, the crystal alignment was flipped from strong alignment with the long c-axis perpendicular to the substrate to pure alignment of the long c-axis parallel to the substrate. These findings enabled a study on the influence of crystal facet alignment in perovskite thin films in optoelectronic devices. We found that a higher crystal alignment most likely decreases defect densities within the perovskite films and generally leads to improved charge carrier mobility. However, the most significant impact in solar cells was provided by the interface between different crystal facets and charge extraction materials (CTMs). In particular, interfacial energetic barriers were formed under applied bias for the (002) perovskite crystal facets and TiO_2. The barrier between the (200) facets and TiO_2 vanished with an additional

fullerene-layer at the interface. In contrast, with the use of inverted devices with fully organic CTMs, no the energetic barrier was observable. Therefore, charge transfer and consequently the device performance in perovskite solar cells was notably optimized with pure perovskite facet alignment and by matching interfaces with the charge extraction materials.

The limitation of the perovskite crystallization to suitable bottom interfaces is very unfavorable for flexible interface engineering or up-scaling of devices to produce modules. In this thesis, we developed a deposition method for adhesion promoters at the interfaces to increase the surface roughness and improve the wetting behavior of various interfaces. We used electrically inert oxide nanoparticles (NPs), such as $Al2O_3$ or SiO_2. Already with 1 % surface coverage of the NPs, we significantly improved the surface wetting of highly hydrophobic interfaces like fullerenes. This improvement enabled up-scaling of spin-coating processes with homogeneous coverage of diverse perovskite precursor solution variations up to substrate sizes of 144 cm^2 with no loss in performance of devices. The NPs serving as adhesion promoters were not limited to perovskite deposition but enabled various other processes using hydrophilic solutions on top of hydrophobic surfaces. In the case of the deposition of lead acetate-based precursor mixtures, film deposition of similar morphologies on substrate sizes between 9 cm^2 and 144 cm^2 was possible. The device performance was not compromised by the presence of the NPs at the interface up to a surface coverage of about 30 %.

The lead halide perovskite materials are equally suitable for photovoltaic and light emitting applications. With methylammonium lead halides, the light emitting color can be tuned in the full visible range from red over green to blue. To engineer white light for lighting applications, blue emitters are necessary, but usually, they are the most complex to be processed or highly unstable. In this thesis, we solution-processed blue-emitting perovskite-based LEDs. With the use of lead acetate precursor, we developed a synthesis approach for homogeneous but very thin perovskite films with bromide-chloride mixtures. This way, we produced very cost-efficient LEDs with low turn-on voltages. Another intriguing feature of these LEDs is the sharp, color-pure electroluminescence (EL), which is of interest for display applications.

In this thesis, we have examined the fundamental factors controlling the morphology and microstructure of perovskite polycrystalline thin films in optoelectronic devices. Additionally, the findings in the present thesis offer easy but powerful solutions for interface engineering without altering the perovskite crystallization or even to enable upscaling of optoelectronic devices to make them commercially more attractive. In particular, to push the photovoltaic device performance further towards the Shockley-Queisser limit, the perovskite thin film

morphology should approach the quality of single crystal wafers. In addition, matching interfaces need to be targeted according to the specific crystal facet alignment for most efficient charge extraction to the electrodes.

9 EXPERIMENTAL

9.1 PEROVSKITE SYNTHESIS

9.1.1 Synthesis Methods in Chapter 3

PEROVSKITE DEPOSITION: CH_3NH_3Br was synthesized by reacting 8 mL of hydrobromic acid (48 vol% in water) with 24 mL of methylamine (33 vol% in methanol, Sigma-Aldrich) in ethanol in a round-bottom flask at room temperature for 1 h. To recover the precipitates, solvent evaporation at 60 °C at a pressure of 200 mbar was used and the products were recrystallized in ethanol, filtered and dried with diethyl ether and under vacuum afterwards.

BD: A 1.2 M solution of the perovskite precursors $PbBr_2$ and MABr (1:1 ratio) was prepared in a solvent mixture of γ-butyrolactone (GBL) and dimethylsulfoxide (DMSO) in a 7:3 (GBL:DMSO) ratio. The precursor solution was deposited in a 3-step spin-coating program. The first step of the program was at 500 rpm for 5s, the second step was at 1000 rpm for 40 s and the third step was at 5000 rpm for 50 s. At the beginning of the last step, toluene was dripped onto the substrate. Afterwards the films were annealed at 100 °C for 10 min.

VASP: In the vapor-assisted-solution process first the lead bromide precursor layer was deposited. The $PbBr_2$ was dissolved in DMF (a 1 M solution) and preheated together with the substrates at 60 °C before spin-coating the layer at 3000 rpm for 15 s. Afterwards the $PbBr_2$ was dried at 60 °C for 10 min and converted in a closed vial to the perovskite in MABr vapor for 2 hours at 150 °C.

CSD: The perovskite layer was deposited on a substrate kept at room temperature via dynamically spin-coating 50 µL solution (1.5 $Pb(Ac)_2$ + 4.5 M MABr in DMF) per 9 cm^2 of substrate dimension at 5000 rpm for 3 min. The samples were then annealed at 100 °C for 2 min with a glass lid covering the substrate in order to avoid defects caused by gas circulation.

9.1.2 Perovskite Synthesis Methods in Chapter 4

The perovskite synthesis was performed in a nitrogen-filled glovebox. In all cases a 62 wt% perovskite precursor solution was used. $PbAc_2$ x 3 H_2O (99.995 % purity, Sigma Aldrich) was mixed with methylammonium iodide (MAI, Dyesol) at a molar ratio of 1:3. The main solvent used was dimethylformamide (DMF, Sigma Aldrich) and the additive used was tetrahydrothiophene-1-oxide (THTO, Alfa Aesar). For the solution preparation, it is very important to first add both precursors into the same vial and mix them until the mixture turns

yellow to form the intermediate phase (IP) before dissolving it. The mixture can be easily dissolved at RT and should not be heated at any time, since heat destroys the IP very fast, which changes the crystallization mechanism. For perovskite deposition, the solution was spin-coated dynamically at 5000 rpm for 3 min. Here, it is very important to use the minimum amount of solvent to cover the substrate. In our case, we used 50 µL for substrate dimensions of 9 cm^2. After spin-coating the film appeared bright yellow and after 10 min of staying at RT, the films turned to the bright orange IP. After the IP was formed, the film was transferred to the hotplate and annealed at 130 °C for 5 min to crystallize the perovskite. We note that the purity of the atmosphere in the glovebox is crucial for perovskite nucleation and crystal growth. For example, vapors of antisolvents like chlorobenzene (CB) can induce faster perovskite nucleation and lead to smaller grain sizes.

9.1.3 Perovskite Synthesis Methods in Chapter 5

In all cases a 62 wt% perovskite precursor solution with $PbAc_2$ and MAI in a 1:3 molar ratio was prepared in different solvent mixtures (see *Table 9 – 1*)and spin-coated for 3 min at 5000 rpm. After spin-coating the film appears yellow and transparent and turns orange-brown when the intermediate phase is pre-crystallized at RT to form the perovskite. After pre-crystallization, the substrate was transferred to the hotplate and annealed at 130 °C for 5 min. To achieve pure orientation in (200) direction, either a solvent mixture of DMSO/DMF was used with 20 vol% DMSO or a mixture of THTO/DMF with 13 vol% THTO. To achieve high preference in (002) direction a solvent mixture of DMSO/DMF was used with 10 vol% DMSO. Equally strong preference in (200) and (321) direction was achieved with 15 vol% DMSO. No preference in crystal orientation was obtained with pure DMF.

	Solvent Mixture		
Crystal orientation	**DMF / vol%**	**DMSO / vol%**	**THTO / vol%**
(200)	80	**20**	0
(200)	87	0	**13**
(200)+(321)	85	**15**	0
(002)	90	**10**	0
No pref.	**100**	0	0

Table 9 - 1: Solvent mixtures.

9.1.4 Synthesis procedures in Chapter 6

NANOPARTICLE SYNTHESIS: The SiO_2 nanoparticles were synthesized following Bogush [38] using fixed amounts of ethanol (2.71 ml), ammonia (101 µl) and tetraethyl orthosilicate (TEOS,

114 µl) and varying H_2O amounts (see *Table 9 – 2*) for 3 mL of a 1.2 wt% dispersion. The solution was stirred at 30° C for 3 hours.

SiO_2-NP size / nm	H_2O / µl	NH_3 / µl	Ethanol / µl	TEOS / µl
20	27	101	2717	114
40	67.5	101	2717	114
60	108	101	2717	114

Table 9 - 2: Synthesis mixtures.

LARGE GRAIN SIZED PEROVSKITE SYNTHESIS: The perovskite synthesis was performed as described in [39]. A 62 wt% perovskite precursor solution with $PbAc_2$ x 3 H_2O (99.995 % purity, Sigma Aldrich), mixed with methylammonium iodide (MAI, Dyesol) in a molar ratio of 1:3. The precursor mixture was dissolved in 87 vol% dimethylformamide (DMF, Sigma Aldrich) and 13 vol% tetrahydrothiophene-1-oxide (THTO, Alfa Aesar. To deposit the perovskite, the solution was spin-coated dynamically at 5000 rpm for 3 min. A volume of 50 µL for substrate dimensions of 3 cm x 3 cm and 500 µm for substrate dimensions of 12 cm x 12 cm were used. After spin-coating the film was pre-crystallized for 8 min at RT for substrate dimensions of 9 cm^2 and for 20 min in the case of 144 cm^2 substrate sizes. Afterwards the films were transferred to the hotplate and annealed at 130 °C for 5 min to crystallize the perovskite.

9.1.5 Perovskite Synthesis Methods in Chapter 7

3:1 Molar Starting Ratio Precursor Mixture Solutions

$CH_3NH_3PbBr_3$ precursor solution was synthesized by mixing CH_3NH_3Br and $Pb(CH_3COO)_2$ in a 3:1 molar stoichiometric ratio in DMF to obtain a 0.5 M solution. Similarly, the $CH_3NH_3PbCl_3$ precursor solution was synthesized by mixing CH_3NH_3Cl and $Pb(CH_3COO)_2$ in a 3:1 molar stoichiometric ratio in a mixed solvent comprising DMSO and DMF in the ratio of 40:60 (v/v) to get a 0.5 M solution. To prepare the desired $CH_3NH_3Pb(Br_xCl_{1-x})_3$ [$0 \leq x \leq 1$] precursor solutions, the above-mentioned $CH_3NH_3PbBr_3$ and $CH_3NH_3PbCl_3$ precursor solutions were mixed together in the required stoichiometric ratios.

5:1 Organic-to-Inorganic Molar Starting Ratio Precursor Mixture Solutions

$CH_3NH_3PbBr_3$ precursor solution was synthesized by mixing CH_3NH_3Br and $Pb(CH_3COO)_2$ in a 5:1 molar stoichiometric ratio in DMF to obtain a 0.5 M solution. Similarly, the $CH_3NH_3PbCl_3$ precursor solution was synthesized by mixing CH_3NH_3Cl and $Pb(CH_3COO)_2$ in a 5:1 molar stoichiometric ratio in a mixed solvent comprising DMSO and DMF in the ratio of 40:60 (v/v) to get a 0.5 M solution. To prepare the desired $CH_3NH_3Pb(Br_xCl_{1-x})_3$ [$0 \leq x \leq 1$] precursor

solutions, the above-mentioned $CH_3NH_3PbBr_3$ and $CH_3NH_3PbCl_3$ precursor solutions were mixed together in the required stoichiometric ratios.

9.2 DEVICE FABRICATION

SUBSTRATE PREPARATION: Fluorine-doped tin oxide (FTO, Pilkington, 7 Ω/sq) substrates were etched with 2 M HCl and zinc powder and cleaned in 2 % Hallmanex detergent, acetone, ethanol and were plasma-cleaned in nitrogen plasma before deposition of charge transport layers.

9.2.1 Photovoltaic Devices in Regular Architecture

A sol-gel approach was used to deposit the TiO_2 layer with a solution containing 0.23 M titanium isopropoxide (Sigma-Aldrich, 99.999 %) and 0.013 M HCl in isopropanol (IPA). The 250 µL of solution was spin-coated dynamically on top of a 36 cm^2 large substrate at 2000 rpm for 45 s, dried at 150 °C for 10 min and annealed at 500 °C for 45 min. Afterwards, the substrates were transferred to a glovebox. To prepare devices with a C_{60}-interface, a monolayer was deposited from a 0.5 mg/mL solution of 4-(1',5'-dihydro-1'methyl-2'H-[5,6]fullereno-C_{60}-I_h-[1,9-c]pyrrol-2'-yl)benzoic acid (C_{60}-SAM) dissolved in chlorobenzene (CB). 50 µL of the resulting solution were dynamically spread on top of a 9 cm^2 large substrate with 2000 rpm for 30 s and then annealed at 100 °C for 5 min. To achieve a better wetting and nucleation of the perovskite solution, a 0.2 wt% IPA solution of Al_2O_3 nanoparticles (Sigma-Aldrich, < 50 nm particle size, 20 wt% in IPA) was deposited on top of C_{60} at 2000 rpm for 30 s and dried at 130 °C for 5 min.

The perovskite was deposited on top and a Spiro-OMeTAD (99.6 % purity, Borun New Materials Technology Ltd.) layer afterward. We used a 75 mg/mL Spiro-OMeTAD solution in CB with 3 vol% of 170 mg/mL bis(trifluoromethane)sulfonimide lithium salt (Li-TFSI, Sigma-Aldrich) in acetonitrile (Sigma-Aldrich, anhydrous, 99.8%) and 1 vol% 4-*tert*-butylpyridine (TBP, Sigma-Aldrich, 96%). 75 µL of the solution was spin-coated on top of a 9 cm^2 large substrate at 1500 rpm for 45 s. The devices were stored for one day in a desiccator to oxidize the Li-TFSI additive in Spiro-OMeTAD. To finalize the devices, a 40 nm thick Au counter electrode was thermally evaporated under high vacuum conditions (<10^{-7} mbar) through a metal aperture leading to devices in the range of 0.10 cm^2. The specific active area was determined with a 0.083 +/- 0.001 cm^2 metal aperture.

9.2.2 Photovoltaic Devices in Inverted Architecture

As hole-transport layers either a PEDOT:PSS or a NiOx layer was used:

A poly(3,4-ethylenedioxythiophene)-poly(styrenesulfonate) (PEDOT:PSS, Heraeus Clevios, Al 4083, 1.0-1.3 % concentration by weight) solution was diluted with MeOH at a ratio of 1:2, treated in an ultrasonication bath for 10 min and filtered. 250 µL of the solution was spin-coated on top of a 36 cm^2 large substrate at 4000 rpm for 45 s and the substrate was annealed at 150 °C for 10 min. Afterwards, it was immediately transferred to the glovebox.

A NiOx hole-transporter was deposited via ALD after a procedure described in [1] with a final thickness of 7 nm. In short, nickelocene precursor was oxidized with oxygen plasma ant atomic layers were grown at 250 °C with a growth rate of 0.042 nm per cycle. To fully oxidize the NiOx layer, we annealed it at 300 °C for 1 h at ambient conditions.

On top of each layer, 100 µL of a 0.2 wt% Al_2O_3 nanoparticle solution in IPA was deposited on top of a 9 cm^2 large substrate at 2000 rpm for 30 s and annealed at 130 C for 5 min. The perovskite layer was deposited on top. [6,6]-Phenyl C_{61} butyric acid methyl ester ([60]PCBM, solenne, >99.5%) was used as electron transport material with a 20 mg/mL solution concentration in CB, which was spin-coated with 50 µL at 1800 rpm for 30 s and annealed at 100 °C for 5 min. 100 µL of a 0.5 mg/mL bathocuproine (BCP, Sigma-Aldrich, 99.99%) solution in IPA, spin-coated at 4000 rpm for 30 s, was used as an interfacial layer between ETM and the electrode. To finalize the devices, a 100 nm thick Ag counter electrode was thermally evaporated under high vacuum conditions (<10^{-7} mbar) through a metal aperture leading to devices in the range of 0.10 cm^2. The specific active area was determined with a 0.083 +- 0.001 cm^2 metal aperture.

9.2.3 Light Emitting Device Fabrication

Prepatterned ITO substrates were cleaned using an ultrasonic bath in acetone followed by isopropanol for 15 min each (see *Figure 9 – 1*). The cleaned substrates were subjected to oxygen plasma cleaning for 1 min. Magnesium-doped zinc oxide films (ZnO:Mg) were deposited at 150 °C using an atmospheric pressure spatial atomic layer deposition (AP-SALD) reactor operating in chemical vapor deposition (CVD) conditions. [2] First, 50 nm of ZnO was deposited onto these substrates, followed by 10 nm of $Zn_{0.56}Mg_{0.44}O$ on top. We used previously reported flow conditions for these depositions. [3] After deposition, the films were cleaned by soaking in acetone for 1 h, followed by 3 min of sonication in ethanol. All films were annealed at 400 °C for 15 min in air. Further, a 5 nm PEI layer was deposited using a 0.4 wt % solution in 2-methoxyethanol followed by annealing for 10 min at 100 °C. Desired perovskite precursor mixture solutions were spin-coated and annealed in a nitrogen-filled glovebox at 100 °C for 5 min. The resulting thickness of the perovskite film was in the range of 125–150 nm. We then

spin-coated a 25 nm thin layer of CBP from a chlorobenzene solution. This was followed by thermal evaporation of 15 nm of MoOx and 100 nm of gold, which forms the top electrode.

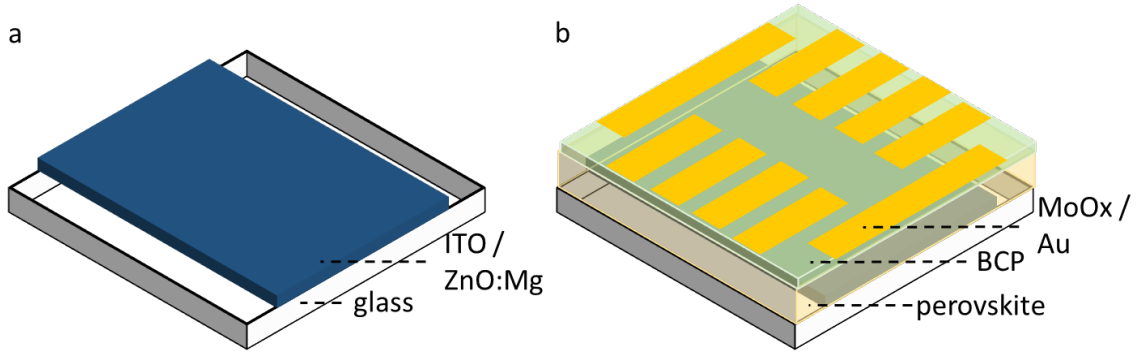

Figure 9 - 1: Schematic of : a) substrate pattern; b) full device stack.

9.3 CHARACTERIZATION

9.3.1 X-ray diffraction (XRD)

Every XRD analysis was operated with a Cu K_α X-ray source. Films were deposited on TiO_2-coated FTO-coated glass and scans were obtained using a Bruker D8 Discover X-ray diffractometer with a position-sensitive detector (LynxEye) in Bragg-Brentano geometry. *2θ* scans for powder X-ray diffraction (PXRD) were obtained with a STOE Stadi MP diffractometer equipped with a DECTRIS MYTHEN 1 K solid-state strip detector.

9.3.2 Grazing Incidence Wide Angle X-ray Scattering (GIWAXS)

GIWAXS data of the perovskite films were acquired with a Ganesha 300XL SAXS-WAXS system with a Cu K_α X-ray source. The incident angle was set to 0.4 °, which is well above the critical angle of $MAPbBr_3$ and $MAPbI_3$ so that the X-ray beam can penetrate the entire film. The measurement time was 10 h if not stated otherwise and the scattering signal was recorded with a Dectris Pilatus 300 k pixel detector with automatic flat field correction, positioned 106 mm behind the sample. Data treatment and reduction including solid-angle, efficiency, and polarization correction and reshaping of 2D images was conducted with the Matlab software GIXSGUI by Argonne National Laboratory. [4] The applied corrections include the solid angle correction, the efficiency correction and the polarization correction in Chapter 3 and 5. [5,6] In Chapter 5, further corrections as suggested in the literature were not applied, [5,6] which we explain in the following: The highly oriented samples presented in the present work gave us the opportunity to measure intensities of (002) and (110) peaks individually. For non-oriented samples, the Debye-Scherrer rings for these planes overlap and are not distinguishable. Here, they could be identified by their slightly differing q values. The intensity for the (110) reflex

should be higher than the intensity of the (002) peak, and this relation is reversed by applying Lorentz corrections, so simple Lorentz factors for in-plane powders are not applicable to these $MAPbI_3$ films.

9.3.3 Scanning Electron Microscopy (SEM)

A scanning electron microscope (FEI Helios NanoLab G3 UC) was used to acquire SEM images of perovskite layers prepared on TiO_2-coated FTO/ ITO glass for top-view images and complete devices for cross-sections.

9.3.4 Transmission Electron Microscopy (TEM)

TEM was performed on an FEI Titan Themis equipped with a field emission gun operated at 300 kV.

9.3.5 Contact Angle Measurements

A customized setup was used to take photographs of contact angles inside a nitrogen-filled glovebox. For evaluation of the data and contact angle fitting, program ImageJ [7] was used with the contact angle measurement tool by Marco Brugnara. [8]

9.3.6 Light absorption

The absorbance of the perovskite films on TiO_2-coated FTO glass was measured with a Lambda 1050 UV/Vis spectrometer (Perkin Elmer) using an integrating sphere.

Linear absorption spectra of thin films deposited on quartz substrates were measured using a Hewlett-Packard 8453 UV–vis spectrometer with blank substrate correction.

The photothermal deflection spectroscopy (PDS) technique was used for the absorption measurements. Films spun on quartz substrates were used for the measurements. PDS is a highly sensitive scatter-free surface averaged absorption measurement technique capable of measuring absorbances down to 10^{-5}. A detailed description of the PDS setup can be found in Sadhanala et al. [9]

9.3.7 Photoluminescence (PL)

Steady-state and time-correlated single photon counting measurements of the perovskite films coated on non-conductive glass were performed with a Fluotime 300 Spectrofluorometer (Picoquant GmbH); the excitation wavelength was fixed to 510 nm with a pump fluence of ~0.3 μJcm^{-2} and the emission was monitored at the maximum at 550 nm, the maximum intensity of the steady state photo emission.

Time-resolved photoluminescence measurements were taken with a gated intensified CCD camera system (Andor iStar DH740 CCI-010) connected to a grating spectrometer (Andor SR303i). Excitation was performed with femtosecond laser pulses which were generated by a home-built setup by second harmonic generation (SHG) in a BBO crystal from the fundamental output (pulse energy 1.55 eV, pulse length 50 fs) of a Ti:sapphire laser system (Spectra Physics Soltstice). The laser pulses generated from the SHG had a photon energy of 3.1 eV, pulse length ~100 fs.

9.3.8 Time-of-Flight Measurement (TOF)

The generation of charges in the $MAPbI_3$ films was induced upon low-intensity pulsed laser excitation at 540 nm with 1 J per pulse, 20 Hz repetition rate with a power of 20 W. The laser system consists of an optical parametric oscillator (LeCroy), pumped by a solid-state Nd: YAG laser (Innolas) with a repetition rate of 20 Hz and a pulse width of 7 ns. Perovskite thin films, contacted with a lateral electrode architecture (see *Figure 9 - 1*) and top-coated with a thin PMMA layer to prevent moisture-induced degradation, were illuminated from the semi-transparent glass/gold side at the edge of one contact by focusing the laser through a microscope objective (spot diameter approximately 2 µm). An external DC field was applied through the Au electrodes exclusively during the measurement of the transient (time frame of approximately 1 s). Photocurrent transients at bias voltages between 1.2 and 3.0 V were recorded in steps of 200 mV to confirm the applicability of *Equation 9 – 2* to the determined transit times.

$$\mu = \frac{d}{E\tau} \qquad \textit{(Equation 9 - 1)}$$

μ= carrier drift mobility; E = applied electric field; τ = transit time; d = electrode spacings

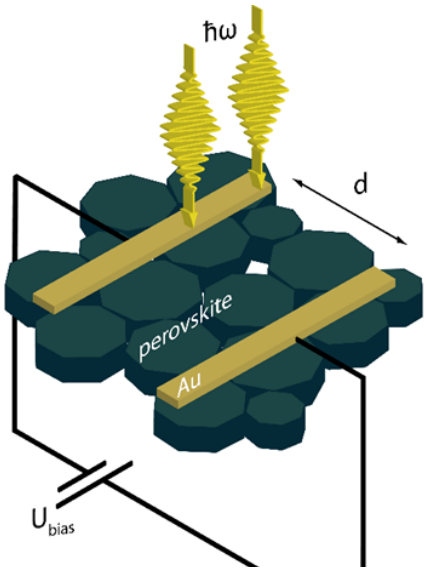

Figure 9 - 2: Lateral device architecture.

9.3.9 Photovoltaic Device Characterization

Photovoltaic device performance was measured with a Keithley 2400 source meter in the air at 25 °C under illumination by a Newport Oriel Sol2A solar simulator, which was calibrated to 100 mW/cm^{-2} with a Fraunhofer ISE certified silicon cell with a mismatch factor of 1.01. The active area of the solar cell was defined with a square metal aperture mask of 0.0831 cm^2. The devices were pre-biased at 1.5 V for 5 sec and measured with a scan speed of 0.2 V/s from 1.5 V to 0 V and back to 1.5 V.

To calculate the short circuit current from the EQE measurements, the AM 1.5G reference irradiance spectrum provided by the American Society for Testing and Materials was used (ASTM G173-03).

9.3.10 LED Characterization

Current-voltage (*I–V*) characteristics were measured using a Keithley 2400 source measure unit. The photon flux emitted during the scan was measured using a calibrated silicon photodetector, and the external quantum efficiency (EQE) was calculated assuming a Lambertian emission profile. The electroluminescence spectra were measured using an optical fiber connected to a calibrated Ocean Optics USB 2000+ spectrometer. An Oxford instruments flow cryostat was used to perform the LED measurements at low temperature with liquid helium as a cooling medium. At low temperatures, the LED was driven by manually changing the device bias and by coupling the EL output into a gated intensified CCD camera system (Andor iStar DH740 CCI-010) connected to a grating spectrometer (Andor SR303i).

9.4 LITERATURE

(1) Hufnagel, A. G.; Henß, A.-K.; Hoffmann, R.; Zeman, O. E. O.; Häringer, S.; Fattakhova-Rohlfing, D.; Bein, T. *Advanced Materials Interfaces*, *0*, 1701531.

(2) Hoye, R. L. Z.; Muñoz-Rojas, D.; Musselman, K. P.; Vaynzof, Y.; MacManus-Driscoll, J. L. *ACS Applied Materials & Interfaces* **2015**, *7*, 10684.

(3) Hoye, R. L. Z.; Chua, M. R.; Musselman, K. P.; Li, G.; Lai, M. L.; Tan, Z. K.; Greenham, N. C.; MacManus-Driscoll, J. L.; Friend, R. H.; Credgington, D. *Adv. Mater.* **2015**, *27*, 1414.

(4) Jiang, Z. *J. Appl. Crystallogr.* **2015**, *48*, 917.

(5) Baker, J. L.; Jimison, L. H.; Mannsfeld, S.; Volkman, S.; Yin, S.; Subramanian, V.; Salleo, A.; Alivisatos, A. P.; Toney, M. F. *Langmuir* **2010**, *26*, 9146.

(6) DeLongchamp, D. M.; Kline, R. J.; Herzing, A. *Energy Environ. Sci.* **2012**, *5*, 5980.

(7) Schneider, C. A.; Rasband, W. S.; Eliceiri, K. W. *Nature methods* **2012**, *9*, 671.

(8) Brugnara, M.; Volpe, C. D.; Siboni, S.; Zeni, D. *Scanning* **2006**, *28*, 267.

(9) Sadhanala, A.; Deschler, F.; Thomas, T. H.; Dutton, S. E.; Goedel, K. C.; Hanusch, F. C.; Lai, M. L.; Steiner, U.; Bein, T.; Docampo, P.; Cahen, D.; Friend, R. H. *J. Phys. Chem. Lett.* **2014**, *5*, 2501.

10 PUBLICATIONS AND PRESENTATIONS

10.1 LIST OF PUBLICATIONS

[18] A. Biewald, N. Giesbrecht, T. Bein, P. Docampo, A. Hartschuh, R. Ciesielski, Temperature dependent ambipolar charge carrier mobility in large crystal hybrid halide perovskite thin films. *Just accepted in ACS Applied Materials Interfaces* **2019**.

[17] F. Ruf, M. F. Aygüler, N. Giesbrecht, B. Rendenbach, A. Magin, P. Docampo, H. Kalt, M. Hetterich, Temperature-dependent studies of exciton binding energy and phase-transition supression in (Cs,FA,MA)Pb(I,Br)$_3$ perovskites. *APL Materials* **2019**, 7, *031113*.

[16] N. Giesbrecht, M. Schultes, J. Kueffner, E. Ahlswede, P. Docampo, T. Bein, M. Powalla, Universal Nanoparticle Wetting Agent for Upscaling Perovskite Solar Cells. *ACS Applied Materials Interfaces*, **2019**, 11, *12948*.

[15] R. Cielsielski, F. Schäfer, N. F. Hartmann, N. Giesbrecht, T. Bein, P. Docampo, A. Hartschuh, Grain Boundaries Act as Solid Walls for Charge Carrier Diffusion in Large Crystal MAPbI$_3$ Thin Films. *ACS Applied Materials Interfaces* **2018**, *10*, 7974.

[14] N. Giesbrecht, J. Schlipf, I. Grill, P. Rieder, V. Dyakonov, T. Bein, A. Hartschuh, P. Müller-Buschbaum, P. Docampo, Single-crystal-like optoelectronic properties of MAPbI$_3$ perovskite polycrystalline thin films. *Journal of Materials Chemistry A* **2018**, *6*, 4822.

[13] M. L. Petrus, J. Schlipf, C. Li, T. P. Gujar, N. Giesbrecht, P. Müller-Buschbaum, M. Thelakkat, T. Bein, S. Hüttner, P. Docampo, Capture the sun: Challenges and perspectives of perovskite solar cells. *Advanced Energy Materials* **2017**, *7*, 1700264.

[12] S. P. Senanayak, B. Yang, T. H. Thomas, N. Giesbrecht, W. Huang, E. Gann, B. Nair, K. Goedel, S. Guha, X. Moya, C. R. McNeill, P. Docampo, A. Saghanala, R. H. Friend, H. Sirringhaus, Understanding charge transport in lead iodide perovskite thin-film fieldeffect transistors. *Science Advances*, **2017**, *3*, 1601935.

[11] I. Grill, K. Handloser, F. C. Hanusch, N. Giesbrecht, T. Bein, P. Docampo, M. Handloser, A. Hartschuh, Controlling crystal growth by chloride-assisted synthesis:

Towards optimized charge transport in hybrid halide perovskites. *Solar Energy Materials and Solar Cells* **2017**, *166*, 269.

[10] L. Oesinghaus, J. Schlipf, N. Giesbrecht, L. Song, Y., Hu, T. Bein, P. Docampo, Toward Tailored Film Morphologies: The Origin of Crystal Orientation in Hybrid Perovskite Thin Films. *Advanced Materials Interfaces*, **2016**, *3*, 1600403.

[9] N. Giesbrecht, J. Schlipf, L. Oesinghaus, A. Binek, T. Bein, P. Müller-Buschbaum, P. Docampo, Synthesis of Perfectly Oriented and Micrometer-Sized $MAPbBr_3$ Perovskite Crystals for Thin-Film Photovoltaic Applications. *ACS Energy Letters*, **2016**, *1*, 150.

[8] K. Bader, N. Giesbrecht, T. Bein, P. Docampo, M. Handloser, A. Hartschuh, Contactless visualization of fast charge carrier diffusion in hybrid halide perovskite thin films. *ACS Photonics*, **2016**, *3*, 255.

[7] A. Sadhanala, S. Ahmad, B. Zhao, N. Giesbrecht, P. M. Pearce, F. Deschler, R. L. Z. Hoye, K. C. Goedel, T. Bein, P. Docampo, S. E. Dutton, M. F. L. De Volder, R. H. Friend, Blue-green colour tunable solution processable organolead chloride-bromide mixed halide perovskites for optoelectronic applications. *Nano Letters*, **2015**, *15*, 6095.

[6] F. Fahrnbauer, S. Maier, M. Grundei, N. Giesbrecht, M. Nentwig, T. Rosenthal, G. Wagner, G. J. Snyder, O. Oeckler, Heterostructures of skutterudites and germanium antimony tellurides– structure analysis and thermoelectric properties of bulk samples. *Journal of Materials Chemistry C*, **2015**, *3*, 10525.

[5] J. Schlipf, P. Docampo, C. J. Schaffer, V. Körstgens, L. Bießmann, F. Hanusch, N. Giesbrecht, S. Bernstorff, T. Bein, P. Müller-Buschbaum, A Closer Look into Two-Step Perovskite Conversion with X-ray Scattering. *The Journal of Physical Chemistry Letters* **2015**, *6*, 1265.

[4] P. Docampo, F. C. Hanusch, N. Giesbrecht, P. Angloher, A. Ivanova, T. Bein, Influence of the orientation of methylammonium lead iodide perovskite crystals on solar cell performance. *APL Materials* **2014**, *2*, 081508.

[3] F. C. Hanusch, E. Wiesenmayer, E. Mankel, A. Binek, P. Angloher, C. Fraunhofer, N. Giesbrecht, J. M. Feckl, W. Jaegermann, D. Johrendt, T. Bein, P. Docampo, Efficient Planar Heterojunction Perovskite Solar Cells Based on Formamidinium Lead Bromide. *The Journal of Physical Chemistry Letters* **2014**, *5*, 2791.

[2] T. Schröder, T. Rosenthal, N. Giesbrecht, S. Maier, E.-W. Scheidt, W. Scherer, G. J. Snyder, W. Schnick, O. Oeckler, TAGS-related indium compounds and their thermoelectric properties - the solid solution series (GeTe)xAgInySb1-yTe2 (x = 1-12; y= 0.5 and 1). *Journal of Materials Chemistry A* **2014**, *2*, 6384.

[1] T. Schröder, T. Rosenthal, N. Giesbrecht, M. Nentwig, S. Maier, H. Wang, G. J. Snyder, O. Oeckler, Nanostructures in Te/Sb/Ge/Ag (TAGS) Thermoelectric Materials Inducedby Phase Transitions Associated with Vacancy Ordering. *Inorganic Chemistry* **2014**, *53*, 7722.

10.2 ORAL PRESENTATIONS

[4] Nadja Giesbrecht, Eline Hutter, Irene Grill, Johannes Schlipf, Peter Müller-Buschbaum, Achim Hartschuh, Tom Savenije, Pablo Docampo , Crystal Facets: Do They Matter? *PSCO Conference* in **September 2017** in Oxford.

[3] Nadja Giesbrecht, Johannes Schlipf, Irene Grill, Achim Hartschuh, Peter Müller-Buschbaum, Pablo Docampo , Tuneable $MAPbI_3$ Perovskite Crystal Alignment and Their Impact in Optolectronic Applications. *ABXPV17* in **March 2017** in Valencia.

[3] N. Giesbrecht, J. Schlipf, L. Oesinghaus, A. Binek, T. Bein, P. Müller-Buschbaum, P. Docampo, Influence of Crystal Order and Size on Photocurrent in $MAPbBr_3$ Perovskite Solar Cells. *DPG Conference* in **March 2016** in Regensburg.

[2] N. Giesbrecht, J. Schlipf, L. Oesinghaus, A. Binek, T. Bein, P. Müller-Buschbaum, P. Docampo, Influence of Crystal Order and Size on Photocurrent in $MAPbBr_3$ Perovskite Solar Cells. *PSCO Conference* in **September 2015** in Lausanne.

[1] N. Giesbrecht, J. Schlipf, L. Oesinghaus, A. Binek, T. Bein, P. Müller-Buschbaum, P. Docampo, Influence of Crystal Order and Size on Photocurrent in $MAPbBr_3$ Perovskite Solar Cells. *E-MRS Fall Meeting* in **September 2015** in Warsaw.

10.3 POSTER PRESENTATIONS

[6] Nadja Giesbrecht, Eline Hutter, Irene Grill, Johannes Schlipf, Peter Müller-Buschbaum, Achim Hartschuh, Tom Savenije, Pablo Docampo , Crystal Facets: Do They Matter? *MRS Fall Meeting* in **November 2017** in Boston.

[5] Nadja Giesbrecht, Eline Hutter, Irene Grill, Johannes Schlipf, Peter Müller-Buschbaum, Achim Hartschuh, Tom Savenije, Pablo Docampo , Crystal Facets: Do They Matter? *SolTech Meeting* in **October 2017** in Munich.

[4] Nadja Giesbrecht, Irene Grill, Johannes Schlipf, Peter Müller-Buschbaum, Achim Hartschuh, Pablo Docampo, Single-Crystal-Like Optoelectronic-Properties of Perovskite Polycrystalline Thin Films. *PSCO Conference* in **September 2017** in Oxford.

[3] Nadja Giesbrecht, Johannes Schlipf, Thomas Bein, Peter Müller-Buschbaum, Pablo Docampo, Tunable Perovskite Crystal Alignment and Morphology. *Next Generation Solar Energy Meets Nanotechnology* in **October 2016** in Erlangen.

[2] Nadja Giesbrecht, Johannes Schlipf, Thomas Bein, Peter Müller-Buschbaum, Pablo Docampo, Tunable Perovskite Crystal Alignment and Morphology. *PSCO Conference* in **September 2016** in Genua.

[1] Nadja Giesbrecht, Johannes Schlipf, Thomas Bein, Peter Müller-Buschbaum, Pablo Docampo, Tunable Perovskite Crystal Alignment and Morphology. *SolTech Meeting* in **April 2016** in Munich.